Development of new volcano-shaped microelectrodes for single cell electrochemistry, electrophysiology and impedance studies.

Nicolas Grégoire MAÏNO

École
polytechnique
fédérale
de Lausanne

2023

Remember that your dream
is your only skin.
— Curtis Mayfield

To my parents…

Acknowledgements

This work would not have been possible without the advice, help and support from many people.

My first and foremost thanks goes to **Philippe Renaud** who gave me this incredible opportunity. I can say that you have redefined my idea of leadership. I will always remember how the trust you put into people and unwavering optimism have allowed me, like many before, to strive and take confidence in ambitious scientific undertakings. Since I was part of the last row of PhD student, I thank you for lending me the shared honor of concluding the LMIS4 long lasting story of innovation and I wish you all the best in your future projects!

To my co-supervisor **Arnaud Bertsch**, I want to address my gratitude and admiration for his critical thinking. I am really grateful that you took the time and effort to look into the details of my project in order to propose sound advice. I have learnt so much from you about the hows of science and I am happy to know that your invaluable skills will translate to another laboratory. Good luck and go easy on the poor PhD students!

To **Benoît Desbiolles**, I express my deepest gratitude for being a great friend and an unformal supervisor. I am forever indebted to you for your everlasting patience and help. It was not easy for me to start in a new field and I often felt embarrassed that you got paired with such a rookie as I was. During our two overlapping years in the lab, you provided me with so many advice and support that I can never fully repay you. Still, while advising me, you never failed to listen to my opinion and managed to make me part of the project. For that and many other things, like your fanatical optimism, I thank you a thousand times and hope to return you the favor one day.

My next acknowledgement goes to the members of my jury: **Patrick Barth, Andrew Ewing, Serge Lemay and Ralf Schneggenburger**. I am so grateful for the challenging yet warm discussion during the exam. After many years of uncertainty, it was truly exciting to go head-to-head with expert in the field. I thank **Patrick Barth** for taking the responsibility of being the jury president, **Andrew Ewing** for sharing his views on the exocytosis literature, **Serge Lemay** for the critical discussion about redox cycling and **Ralf Schneggenburger** for his advice on electrophysiology data presentation and knowledge on the use of cadmium as an inhibitor of exocytosis. I can say that I learnt a lot from the exam so thank you for putting the time and effort. A special thanks goes to **Serge Lemay** for coming all the way to EPFL!

Acknowledgements

While being superbly advised scientifically, I was very lucky to be able to count on **Christine Vuichoud** for her help on admin matters. I'd like to thank you for your support and patience along the years. I wish you all the best in your new lab(s). I'd like to thank **Sonja Bodmer** from the EDBB doctoral program as well for being not only helpful but also considerate for the anxious PhD students.

Moving on to the realm of friendly chat and pranks in the workspace, I am very pleased to acknowledge all my colleague from the Microsystems laboratory 4.
I'd like to start with my office mates: **Margaux Duchamp, Albert Leroy, Alexandre Huber and Mohammad Matin Behzadi**. To all of them, I want to say thank you for your friendliness and sorry for the occasional grumpiness on my side. **Margaux**, I had a lot of fun sharing the first-year clean room frustration with you and fighting to keep a glimpse of order in the cell lab. **Albert**, it was good to have someone to share the electrochemistry trauma with. **Alexandre**, thank you for continuing the electrochemistry bigotry started previously with Albert. **Matin**, thank you for being yourself and an awesome office mate. I feel very lucky that I was able to get a glimpse of the so rich Persian culture without moving out of my office. I am sure you will soon brilliantly complete your own thesis!
To my comrade of hardship: **Clémentine Lipp, Joan Teixidor and Jiande Zhou**. We went through the PhD experience together and found ourselves really bounded by its end so I'd like to thank you in particular for the good time we shared in and out of the lab. **Clémentine**, I still believe we are on track to become elite athletes. We just need to buy more gears. Thank you for the good laugh, the cat meme/video and the occasional procrastination opportunity. **Joan**, thank you for being such a cool, evil pranker in disguise and sharing the very elaborate trash talking you use on the soccer field. I am but a humble disciple of your legendary deceitfulness. **Jiande**, I am sure we'll make it to own a KOM somewhere insignificant together. Thank you for your sport enthusiasm and the deep discussion about life. I hope you manage to take it easy sometime!

Next, I offer a tribute to the wisdom of the past and more recent post-docs and scientific collaborators of the lab. **Lucas Yerly**, thank you for sharing the frustration of the dirty dishes situation in the chemistry room. I wish you all the best in your career of young dad. **Miguel Solsona**, I feel like we shared so much by having similar experience in our own projects while never finding the occasion to collaborate. No matter, I had a super good time biking, chatting and clean rooming along with you. **Nadya Ostromohov**, thank you for being the terrible person I can make terrible joke with. Also thank you for realizing all our silly cartoons with your great artist skills. **Evgenii Glushkov**, thank you for being the best event/get together catalyst. We owe a lot of the good lab atmosphere to you. I also really enjoyed being around your curious, outgoing personality. All the best settling with your girlfriend. **Daniel Migliozzi**, thank you for being a relentless defender of proper culinary practice as well as being always looking for a chat. **Thamani Dahoun**, thank you for trying to help my hopeless neuron experiments. It was good not to struggle alone but even more so with your fun, lively help. **Jonathan Cottet**, thank you for your help on DEP and sharing your experience of the post-doc life and struggle. **Sébastien "Seb" Jiguet**, thank you for being the omnipresent sportsman of the lab. Always

ready, always looking to get the PhD students out of the lab for some well needed exercise. It was so nice to have you around and I want to thank you specially for making me and any newcomer welcome. To **Weida Chen and Antoine Herzog**, thank you for contributing to the socializing in the lab but also patting the PhD students on the shoulder after group meeting. It was nice to get a glimpse of the startup life through your own experience, all the best with your company. **Clarisse Vailler**, thank you for being my cell culture guru. You efficiently gave a cell lab crash course which served me well for the next 5 years, thank you! **Stefano Varricchio**, we had the bet that whatever the outcome of my thesis, I would keep you accountable for it. Now I can safely conclude this bet by thanking you. My experience with you as a master student and our discussion before starting the PhD were really helpful in that I knew exactly what to expect and to prepare for.

Moving on to the underground lair of the CMi. I want to address special thanks to the staff of the EPFL clean room. As I came without any training in microfabrication, I truly owe all of you for teaching me everything from scratch. In particular, I want to thank the photolitho team: **Niccolò Piacantini, GAR and Julien Dorsaz**. Many thanks for supporting my uncanny addiction to the VPG. The etching team: **Joffrey Pernollet and Cyrille Hibert**. Thank you for your patience of gold, which should never be placed in and RIE/ICP etcher. The thin film team: **Rémy Juttin, Blaise Cuénod and Yoan Troillet**. I have stuck the evaporator and PECVD way too many times so thank you for your patience and help. Finally, thank you to the special Dummy support team: **Giovanni Monteduro, Vivigan Sinnathamby, Adrien Toros and Gatera Kumuntu** who fixed countless of my blunder at odd time of the day and night.

In and around EPFL, I was lucky to receive help from many talented scientists. From the LMNN, I want to warmly thank **Anne-Laure Mahul, Lorène Aeschbach and Soma Jagannath**. You helpedd us tremendously with neuron experiments. I feel sorry that nothing came out of it but you can rest assure that they were a critical help in understanding the issues in my initial project. So again, many, many thanks for your help. On a similar topic, I'd like to thank **Rodrigo de Campos Perin** from the LNMC for landing his Olympic patch clamping skills to characterize our neurons in culture. This experiment was definitely helpful in my project so thank you again. From the LSYM, I want to thank **Olexiy Kochubey** for looking into my early exocytosis experiments. I wish I had more time to explore this part of my project but nonetheless It was invaluable to get an expert's opinion early on. Finally, I want to address a huge thanks to **Luc Stoppini, Adrien Roux and Laetitia Nikles** from the Tissue engineering laboratory in Geneva. Although our electrophysiology experiments were not successful, they were pivotal in the progress of my thesis as they revealed to me that I needed to be more ambitious and further develop the technology I inherited from Benoît rather than stick to it blindly. For this invaluable input and your warm welcome in the group, thank you!

Of course, the support I received at work would not have been enough without the presence of my closest friends and family. I'd like to thank first my friends from high school: **Hugo, Boris Trapp, Pierre-Louis Ronat, Nicolas Richoz, Ted Baldwin, Maxime Rochaz and Alexis Baron**. Our gatherings have allowed me to release some steam by playing dumb and making silly

jokes. I thank **Hugo and Boris** in particular for the good flat sharing time. I have such good memories of the time we spent in Prilly and can say that you definitely helped me get along in life by disconnecting from work at home. Thank you, **Pierre-Louis**, for allowing me to crash at your place when needed, for the sport discussion and for the fun time online! It was also important for me to be around during your early career steps and I can say that I learnt many things for myself from your experience. To **Nicolas**, although we didn't have much time to meet lately, it was inspiring to see you moving closer to your passion for photography. To **Ted and Maxime**, thank you for taking us out to the same old bar and the good laugh. Thank you **Maxime**, for your board game frenzy and crushing me mercilessly at every game. **Alexis**, thank you for keeping in touch and for filling me with story of today's world and its challenges. A special thanks goes to **Valentin Rhonat**. I am proud and inspired to see you living your dream and I value your contrasted perspective on life very much.

À ma famille, je vous remercie pour votre soutien et votre bienveillance sans limite. **Marina, Loïc, Gabrielle et Andréa**, je suis si heureux de voir votre famille s'agrandir tout en restant toujours aussi proche l'un de l'autre. J'ai appris beaucoup en vous côtoyant. Votre sang-froid de parent à tout épreuve ainsi que votre regard calme et confiant sur la vie m'ont permis de prendre du recul face à mes petites pérégrinations. Pour cela, votre soutient et votre bienveillance, merci ! Je souhaite aussi remercier **Alexandra, Elodie et Jean-Baptiste** pour leurs encouragements et leurs visites. **Luc, Catherine, Nicole et Daniel**, je vous remercie pour votre sollicitude, nos discussions sur la vie de doctorant et ses aspects amusant/pénible.

Coming to the end of the acknowledgements, I am concluding with very special people, that have had an extraordinary impact in my life.

Xiaoyan Qian, you are so important in my life today that I can simply state that I couldn't have done it without you. Life would have been so dull without your cheering, good mood, and entertainment and hence you are truly part of my success. For this, for your realistic yet contagiously positive outlook on life, I thank you and acknowledge the irreplaceable influence you have had over my lifestyle, passions, and work.

Pour conclure, je souhaite remercier et rendre crédit à mes meilleurs atouts dans la vie, mes parents : **Danièle et Éric**. Rien n'aurait été possible sans votre aide. Le travail de ces quatre dernières années n'aurait pas été possible sans le travail en amont, depuis mes premiers pas dans la vie, jusqu'au diplôme de Master. Vous m'avez toujours soutenu dans les études sans pour autant me pousser afin de respecter mon caractère têtu tout en m'encourageant à poursuivre d'autres passions. Grace à cela, j'ai pu développer autant mes compétences intellectuelles que mon goût de la vie. Pour toutes ces raisons, je vous remercie et vous dédie ce travail dont au fond vous êtes un peu les instigateurs. Merci !

Lausanne, 7 December 2022   N. M.

Abstract

Micro- nano-electrodes have demonstrated superior performances in measuring attenuated intracellular action potentials from electrogenic cell cultures compared to traditional multi-electrode arrays. Yet, the understanding of the critical electrode features enabling intracellular access are limited by a lack of appropriate tools to characterize the cell/electrode interface. Consequently, the translation of these micro- nano-electrodes from cardiac to neuronal electrophysiology is difficult with only a few technologies successful for the latter so far. This is a common pitfall that supports a mounting consensus in the field that nanostructures need to be pitched to the cell of interest to enable intracellular access.

This thesis, address this limitation by presenting the implementation of an impedance spectroscopy method to resolve the interface of cells with nanostructures in a multi-site, scalable manner while remaining label free and harmless to the cell. This method allows to rationalize the impact of various electrode features (*e.g.*, geometry, chemical functionalization) on the cell/electrode coupling and is implementable for any micro- nano-electrode with moderate impedance.

In a second time, this thesis exploited the knowledge gathered in the field of electrophysiology to adapt a volcano-shaped nanostructure for parallelizable electrochemical measurements. The sensor developed allows the longitudinal study of exocytosis from neuron-like cells within a confined volume and over multiple sites. Interestingly, the kinetics of exocytosis registered at the volcano-shaped structure was faster than expected which suggests a possible role for nanotopography to regulate exocytosis; a possible fundamental discovery never reported so far.

On the long term, the device developed for electrochemical study is envisioned to allow scalable, longitudinal intracellular sampling from single cells for *in situ* detection of neurotransmitter by redox cycling.

Key words: Multielectrode array, single-cell electrochemistry, impedance spectroscopy, intracellular measurement, redox cycling, cell/electrode interface, nanofabrication, nanovolcano, catecholamine

Résumé

Les micro- nano-électrodes ont démontrées leurs avantages lors de la mesure de potentiels d'actions atténués originant de cultures de cellules électrogéniques comparées aux matrices d'électrodes traditionnelles. Cependant, la compréhension des facteurs critiques permettant à une électrode de pénétrer l'espace intracellulaire reste limitée dû au manque d'outils adaptés à la caractérisation de l'interface électrode/cellule. En conséquence, l'adaptation de micro-nano-électrodes développées pour l'électrophysiologie cardiaque vers l'électrophysiologie neuronale est difficile comme suggéré par le peu de technologies ayant achevées ce but. Cet obstacle rencontré par beaucoup suscite l'émergence d'un consensus dans le domaine suggérant que l'électrode doit être adaptée pour chaque type de cellule.

Cette thèse vise à résoudre ce problème en proposant une méthode de spectroscopie d'impédance permettant de caractériser l'interface de cellules avec des nanostructures selon une approche extensible, pouvant être opérée sur plusieurs sites en parallèle tout en restant inoffensive pour la cellule et ne demandant pas de marquage moléculaire. Cette méthode permet de rationaliser l'impact de différentes propriétés de l'électrode (par exemple sa géométrie ou sa fonctionnalisation chimique) sur l'interface cellule/électrode et peut être mise en oeuvre par toutes micro- nano-électrodes ayant une impédance raisonnable.

Dans un second temps, cette thèse a exploité les connaissances acquises dans le domaine de l'électrophysiologie afin d'adapter une nanostructure en forme de volcan en vue de permettre des mesures électrochimiques parallélisables. Le senseur développé a permis l'étude au cours du temps de l'exocytose suscité à la membrane de pseudo-neurones dans un volume confiné et sur plusieurs sites à la fois. Surprenamment, la cinétique des événements d'exocytoses mesurés était beaucoup plus rapide qu'attendue ce qui suggère un possible rôle de la nanotopographie environnante sur les procédés menant à l'exocytose ; une découverte insoupçonnée à ce jour.

Sur le long terme, ce senseur développé pour l'électrochimie est envisagé de pouvoir permettre la mesure de neurotransmetteurs au sein même de la cellule de façon inoffensive et répétée ainsi que sur plusieurs sites en parallèles.

Mots clefs : Matrice d'électrode, électrochimie de cellules individuelles, spéctroscopie d'impédance, mesure intracellulaire, oxidoréduction cyclique, interface cellule/électrode, nanofbrication, nanovolcan, catécholamine

Contents

Contents

Contents

List of Figures

List of Abbreviation

Ag/AgCl	Silver/silver chloride reference electrode
DIC	Days in culture
DIW	Deionized water
EAP	Extracellular action potential
EIS	Electrochemical impedance spectroscopy
CFE	Carbon fiber electrode
FEM	Finite element model
FWHM	Full width at half maximum
CMOS	complementary metal-oxide-semiconductor
HEK	Human embryonic kidney cells
IDE	Interdigitated electrodes
MEA	Multi-electrode array
MPA	Mercaptopropionic acid
NV	Nanovolcano
PECVD	Plasma enhanced chemical vapor deposition
PEDOT:PSS	poly(3,4-ethylenedioxythiophene) polystyrene sulfonate
PC12	Pheochromocytoma 12 cell line
PDL	Poly-D-Lysine
Pt	Platinum
ROc	RedOx Cycling
RT	Room temperature
SEM	Scanning electron microscope
SNR	Signal-to-noise ratio
VSE	Vertically stacked electrodes

1 Introduction

1.1 Context of the thesis

1.1.1 Technology and scientific discoveries throughout human history

Understanding how biological matter organizes and functions is a main subject of questioning of mankind and studies on the subject can be traced back to 1600 BCE in ancient Egypt. Anatomical treaties like the Edwin Smith and Ebers Papyrus reveal that knowledge of the human body and way to treat trauma and afflictions were already actively sought by presumably dedicated scholars. These written records hardly constitute the earliest evidence of physicians being part of organized labor within human society. In fact prehistoric anatomical evidence of human surgery suggest that mankind was well versed in anatomical knowledge by 29 000 BCE (Maloney et al., 2022). Natural curiosity, along with practical necessities, have hence fostered the development of scientific inquiry well before written records could be used as medium of communication. Still, the accelerated rate of scientific progress from ancient Mesopotamian society onwards seems to indicate that dissemination of ideas through time and space thanks to writing systems was an enabling factor. Such technologically driven advancements can be observed throughout all of human history. As another example, the invention of the printing press in the 15th century by Gutenberg was pivotal in the further progression of the anatomy field as it was to all scientific endeavors at the time. Anatomical science had peaked with the description of animal anatomy by Galen in the third century CE that was in some part erroneously applied to human anatomy. In the absence of an efficient means to propagate knowledge and critical opinions, his views remained unchallenged for 1300 years. In 1543, Andreas Vesalius published his work *De Humani Corporis Fabrica*. Thanks to the printing press that was 100 years old at the time, his book reached a wide audience, propagating new conceptions of the human anatomy and the function of organs.

Again and again, technology was to find a central role in the development of all natural sciences, biology among them. While anatomy enjoyed the ease of dealing with the macroscopic organization of organism in organ and organ in tissues observable to the naked human eye, understanding of the building block of tissues, cells, remained elusive until the development

of the compound microscope around 1620. This enabling technology allowed the study of living matter at an unprecedented scale, breaking down tissue organization into individual units: the cell; famously coined by Robert Hooke in 1665 as an analogy of the cork cell wall to the honeycomb (Figure 1.1, A)(Mazzarello, 1999). Although Hooke did not recognize these cells as alive, others like him made use of the light microscope to unravel the significance of his discovery. This led to the postulation of the cell theory in 1839 usually credited to Theodor Schwann and Matthias Jakob Schleiden stating that the cell is the most basic unit of life and that all plants and animals are composed of cells.

1.1.2 The neuron theory and drive towards single-cell investigations

The development of the light microscope in the 17th century gave way to the discipline of histology that shed light on the organization and heterogeneity of tissue at the microscopic level. The conception of the scale at which the biological matter can organize to create function was redefined as with the discovery of capillaries that allowed Marcello Malpighi to refute the open ended conception of the circulatory system inherited from Galen over a millennium ago. Despite such findings and the recent discovery of the cell, the idea that complex behavior like learning or memory formation could stem from the connection of individual cells would have seemed unfathomable all throughout the 18th century. This view came to change with the groundbreaking work of famous neuroscientist, the first of his kind, Santiago Rámon y Cajal in the 19th century. Cajal study of birds brains using the Golgi staining led him to believe that cells in the brain were contiguous instead of continuous (Figure 1.1, B) (López-Muñoz et al., 2006). His study of the growth cone also led him to believe that cells of the brain could form connections dynamically. This latter point was put forth as a possible origin of learning in his address to the Royal Academy of London in 1894 (Higgins & George, 2019). From there on, holistic conceptions of the nervous system were gradually abandoned and a drive to study individual nervous cells through staining or other means began to pick up speed. In parallel, fundamental understanding of nerve cell excitability and communication was attracting more and more attention.

1.1.3 From frog legs to single molecule patch clamp electrophysiology

As discussed, histology was able to move on to single-cell investigations thanks to improvement of the light microscope as early as the mid 17th century which culminated in the elaboration of the cell theory in the mid 18th century and the neuron theory at the turn of the century. On the other hand, the measurement of the electrical currents and potentials associated with nerve cell functions would take several more decades to reach single-cell precision. The emergence of bioelectricity is historically associated with Luigi Galvani who conducted electrophysiological experiments on frog legs in the second half of the 18th century (Figure 1.1, C). To move on from the study of prepared tissue (frog leg) to individual nerve cells would take about a century marked by gradual improvement of the instrumentation. As early as 1868, the differential rheotome of Julius Bernstein allowed measurement on a few millisecond time
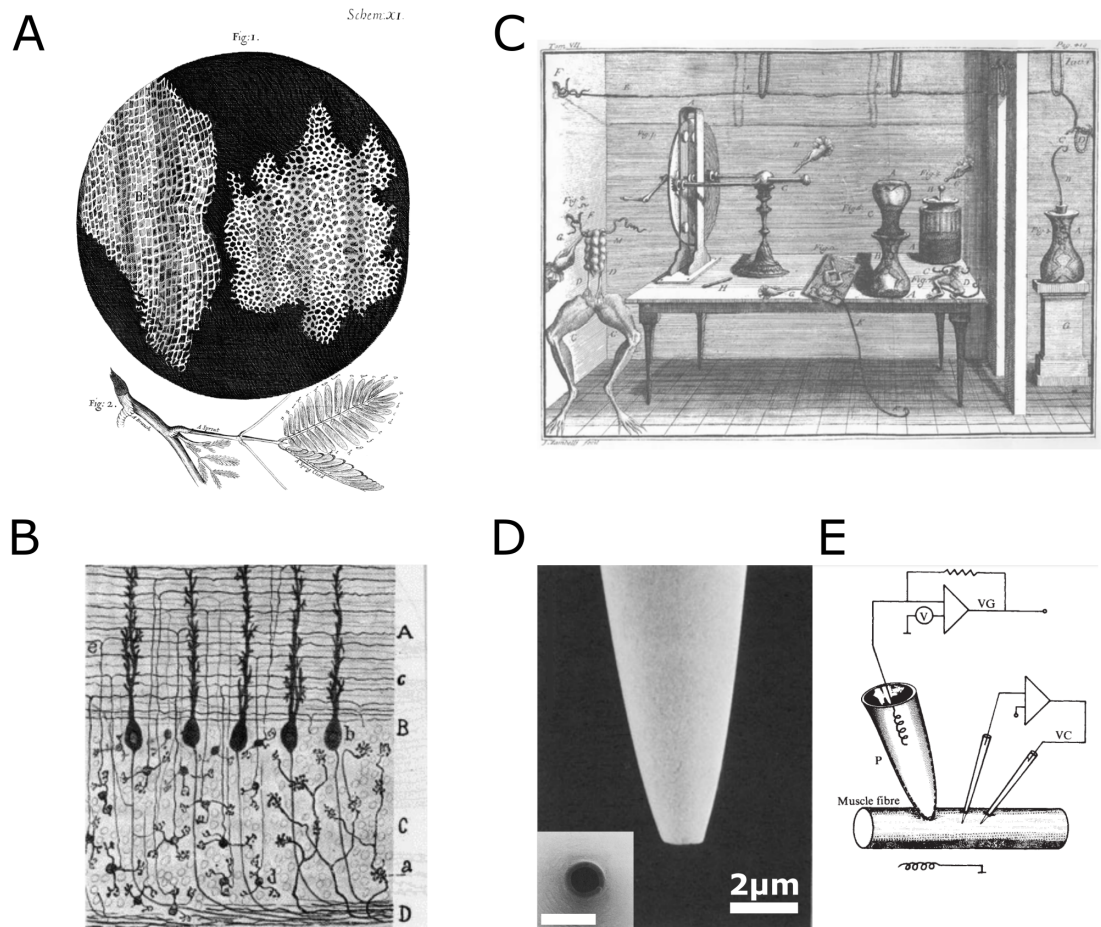
Figure 1.1: Technological advancements and their impact on scientific progress. (A) Depiction of a cork specimen observed by Hooke under his compound microscope and published in his book *Micrographia* in 1665. (B) Annotated depiction of the chick cerebellar circumvolution published by Cajal (Cajal, 1888). The resolution of finer cellular details was made possible by improved light microscopes and staining procedures. (C) Frog preparation and electric machine of Galvani from his *Commentarius* of 1791. (D) Microforge pulled glass micropipette reproduced from (Sakmann & Neher, 1983). Both scales bars are 2 μm. (E) Voltage clamp circuitry reproduced from (Neher & Sakmann, 1976). Similarly as for (A) and (B), the progression from the electric machine of Galvani (C) to the patch clamp technology represents the aggregation of decades of scientific endeavors. All reproduced with permission.

scale allowing to already resolve the resting potential and sign reversal during action potential (Carmeliet, 2019). The temporal resolution of the differential rheotome was striking for its time but the interfacing of electrodes with single cells and adaptation of the electrical circuitry constituted challenge that remained to be solved. As often is the case, insurmountable technical challenges in science can be alleviated thanks to the diversity of size and shape found in Nature. Electrophysiology was lucky to find in the squid giant axon a convenient model that would carry on to be inextricably linked to the development of modern electrophysiology instruments from its discovery by John Z. Young onward (Young, 1936). Thanks to its large dimensions of about 1 mm across for up to a meter long, electrode size requirement was much easier to meet. Advancements of electrophysiology methods would proceed increasingly faster from there on, with the development of the voltage clamp electrical circuitry by Cole and Marmonts (Cole, 1949; Marmont, 1949), the works of Hodgkin and Huxley (Hodgkin & Huxley, 1952; Hodgkin et al., 1952) leading later to the development of the eponymous mathematical model for action potential and finally the development of the gigaohm seal by Neher and Sakmann (Figure 1.1, D-E) (Hamill et al., 1981) . Neher and Sakmann went on to be awarded the Nobel prize in physiology or medicine in 1991. The condensed succession of advances presented here is of course a summary of a global effort taking place over a century and involving hundreds of investigators. In this time period, electrophysiologists moved from studying tissue preparations, to single cells and finally single ion channels. This brief historical review focusing on critical times and a few brilliant minds has also highlighted the concurrent technological developments that prompted many breakthroughs.

1.2   Modern electrophysiology methods

1.2.1   Limitations of the patch clamp for today's scientific questions

Today, neuron excitability is a fundamental process that is well understood and captured by physical models based on the functioning of single molecules (ion channels) acting together. This understanding was built in part thanks to the patch clamp technique that remains today the gold standard in electrophysiology. While the patch clamp is unarguably the tool restituting the electrophysiological signals with the greatest fidelity, it suffers from three considerable drawbacks. First , the patch clamp approach is not well suited to simultaneous recordings over multiple sites. Because some of today's foremost questions in neuroscience include how neurobiological networks result in cognition and how their dysregulation leads to pathological states, patch clamp has given way to other means of investigations more suited to the scale and complexity of the problem. Electrophysiology still holds its place in this new framework of investigations alongside high-throughput molecular screening, magnetic resonance imaging and cell staining but under the form of new methods that all rely on offering multiple sites from which functional electrophysiological activity can be recorded from. Secondly, intracellular recording with a patch clamp set up (*i.e.*, whole cell configuration) necessarily results in cell deaths within a few tens of minutes due to excessive dilution of the cell cytosol. This is especially limiting for investigations of pathological states development

and longitudinal studies in general (*i.e.,* monitoring a parameter repeatedly over time). Lastly, patch clamp studies are inherently slow and the throughput is consequently low as well. This is relevant in particular for therapeutic or toxicology screening. Altogether, these limitations have stimulated the emergence of other technologies for electrophysiology that seek to address one or several of the patch clamp shortcomings.

1.2.2   Other electrophysiology techniques and their trade-off

Multi-electrode arrays emerged in the early 1970 as an alternative to patch clamp electrophysiology (Pine, 2006). The electrodes in MEAs are typically inlaid disk electrodes patterned on a substrate at high density using semiconductor fabrication methods (Figure 1.2, A). Cells are then cultured directly on top of the electrode array. MEAs offer parallel recording over multiple sites and their fabrication is scalable. As such, MEAs have remained for long the method of choice for throughput and scalability with as many as a tens of thousands of recording sites today thanks to complementary metal-oxide-semiconductor (CMOS) integration (Figure 1.2, B) (Dragas et al., 2017). This advantage comes as a trade off as the electrode resides outside of the electrogenic cell. In this configuration, only action potentials can be measured while other important electrophysiological features are indiscernible (synaptic inputs, membrane oscillations, sub-thresholds potentials). On the other hand, the extracellular configuration has the advantage of being harmless to the cells allowing long-term experiments.

Microfabrication technology together with microfluidics also drove the apparition of planar patch clamp arrays which improves the throughput of the patch clamp approach using hydrodynamic traps in microfluidic channels (Pantoja et al., 2004). As for the MEA, the silicon-chips are built using largely scalable semiconductor techniques. Today, automated patch clamp set ups using conventional glass micropipettes or planar patch chips using microfluidics are both commercially available (Figure 1.2, C) (Dunlop et al., 2008). While these techniques address scalability and/or throughput issue of conventional patch clamp, they take dissociated cells as input and still eventually kills cells within minutes still precluding longitudinal studies.

Finally, optical methods for electrophysiology are growingly more attractive. In particular, the emergence of optogenetic has made optical methods more attractive since a single set up (microscope) can both stimulate and record single unit electrophysiological data (Scanziani & Häusser, 2009). Optical methods rely on voltage sensitive dyes (Palmer & Stuart, 2009) genetically encoded voltage indicators (Hochbaum et al., 2014), calcium sensitive chemicals (Sabatini et al., 2002) or genetically encoded calcium indicators (Figure 1.3, A, B,C and D respectively) (Grienberger & Konnerth, 2012). Optical methods offer more streamlined approach and are amenable to reasonable throughput. Voltage indicators are generally molecules that insert in the cell plasma membrane and emit fluorescence according to the electrical potential across the membrane. Voltage indicators were among the first optical electrophysiology methods described but suffer from limited signal-to-noise ratio (SNR) and photobleaching (Bando et al., 2019). For these reasons, they have declined over the last decade in favor of calcium
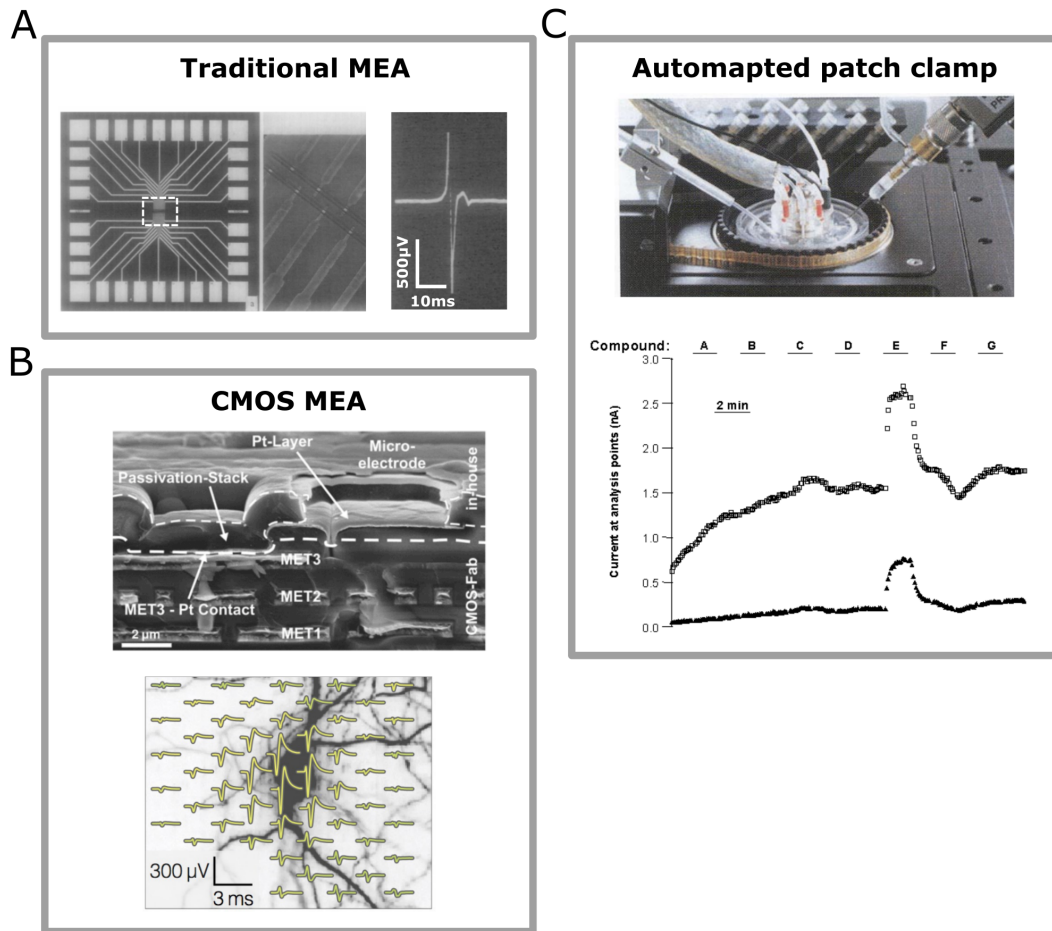
Figure 1.2: Multi-electrodes array (MEA) and automated patch clamp electrophysiology. (A) Top view of a traditional MEA chip. Traditional MEA are machined over silicon substrates using techniques from the semiconductor industry (Thomas et al., 1972). Dashed white box on the left image is viewed with a scanning electron microscope (SEM) showing an array of individual electrodes. Traditional MEA typically record action potentials extracellularly from single units (right). (B) MEA integrated on complementary metal-oxide-semiconductor (CMOS) are built directly on the recording circuitry (top image, cross section viewed with SEM) allowing decreased recording noise and increased electrode density (Hierlemann et al., 2011). CMOS MEA record action potential with sub-cellular resolution (bottom image) (Radivojevic et al., 2017). (C) Automated patch clamps perform intracellular measurement with glass micropipettes without human intervention for micropipette and sample exchange (top image). Automated and planar patch clamp (see text for distinction) focus on compound screening for ion channels drugs discovery (bottom image) (Asmild et al., 2003). All reproduced with permission.

indicators owing to the latter's larger SNR. Calcium indicators are bioluminescent proteins, calcium chelators with fluorescing domains or recombinant proteins with one fluorescing domain or sometimes two (as for fluorescence resonant energy transfer). In most central nervous system neurons, action potentials traveling down the axon will back propagate to the cell body and apical dendrites resulting in voltage-gated calcium channel opening, which is the origin of the increase of intracellular fluorescence of calcium indicators during action potentials (Grienberger & Konnerth, 2012; Kaiser et al., 2001). While calcium indicators enjoy higher SNR compared to direct voltage indicators, their kinetic is slow and doesn't allow to resolve the shape of action potentials. It is noteworthy that while optical methods allow for interrogations of many cells, the recording from an increasing number of cells *in vivo* will necessarily come with a decrease of sampling rate. This is due to the necessity of focusing to different planes to observe cells in their native 3D environment. For example, measurement of firing rates for 10000 cells by two-photon imaging *in vivo* allows for sampling rate of individual cells at about 3 Hz (Pachitariu et al., 2017).

In this discussion, we limited ourselves to methods aiming to measure single units. Single units is a term used to refer to an electrophysiological recording capturing activity from a single neuron typically through monitoring of action potentials. Other methods like electroencephalography look at the activity of ensembles of neurons. This is also the case for other non-electrophysiologic methods like magnetic resonance imaging which investigates cognition at the network level. Since the central nervous system is home to nearly 10^{11} neurons (Herculano-Houzel, 2012) and about 10^{15} synapses, whole brain single units recording is unrealizable and consequently both approaches are complementary in trying to understand the organization and functioning of neurobiological networks at different scales.
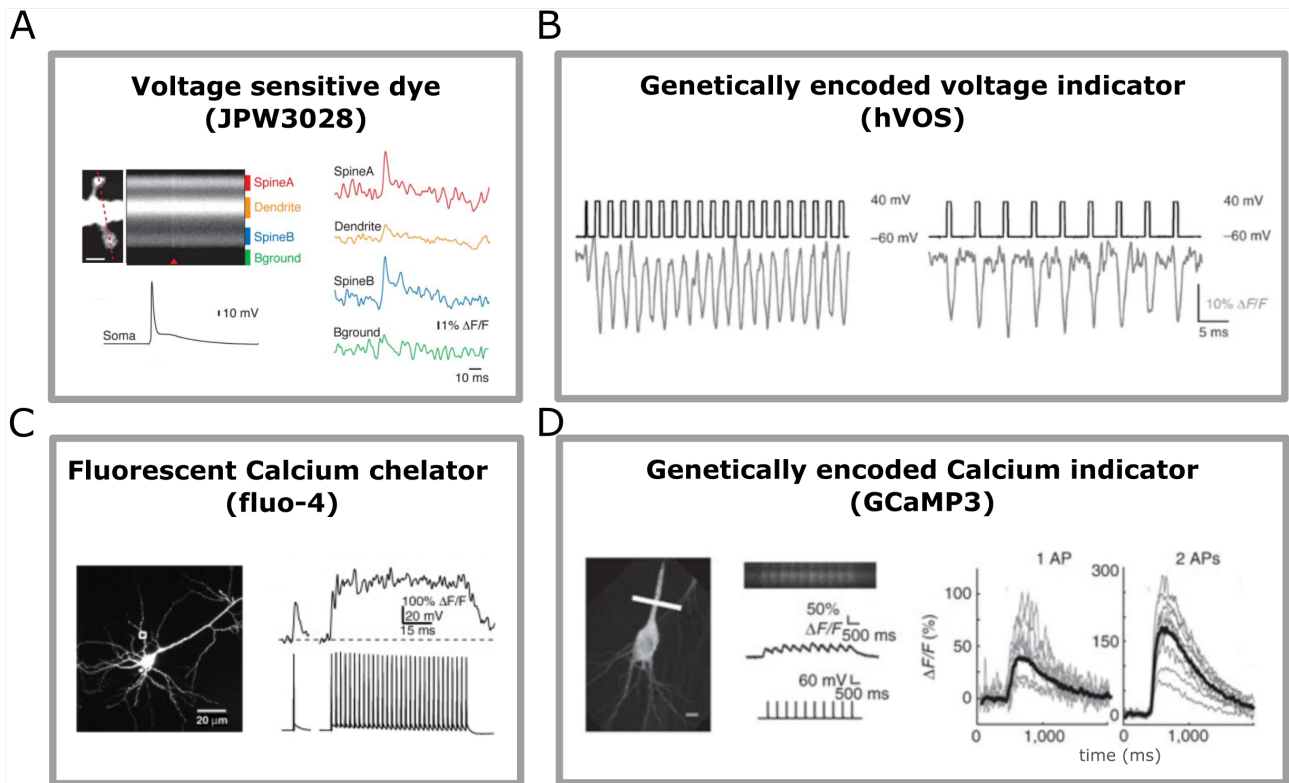
Figure 1.3: Optical electrophysiology methods. (A) Voltage sensitive dye insert in the membrane and response to change of the transmembrane potential. Action potentials initiated in the soma (left, bottom trace) travel through dendrites and can be sensed all the way to individual spines (left image) with good temporal accuracy (relative fluorescence change, right traces) although inhomogeneous fluorescence and low signal-to-noise ratio can make voltage sensitive dye challenging to work with (Palmer & Stuart, 2009). (B) Genetically encoded voltage indicators function similarly but have demonstrated superior signal-to-noise-ratio (Chanda et al., 2005). (C) Fluorescence calcium chelators are small molecules that reside in the cytosol and fluoresce stronger upon binding divalent cations. Response at a dendrite (white box on left image) to single and train of action potential (right) show increased signal amplitude compared to voltage indicators but at the cost of decreased temporal resolution (Sabatini et al., 2002). Genetically encoded calcium indicators are typically peptide chain fused to a chromophore that change protonation state and fluorescence intensity upon calcium biding (L. Tian et al., 2009). (D) Neuron axon (left image) change of fluorescence over time in response to action potential train (center) result in build up of the fluorescence level (measured over a line scan indicated by white bar on left image). Trial averaging shows that fluorescence level originating from one or two action potentials (or more) can be distinguished (right). All reproduced with permission.

1.2.3   Multi-site intracellular electrophysiology using nanotechnology

In the last two decades, novel micro- nano-electrodes designed to sample electrophysiological signals intracellularly have started to emerge. As for MEAs, these electrodes are fabricated at high density using top-down semiconductor fabrication approaches. Integration with CMOS technology can even further increase the density of recording sites (Abbott et al., 2017). The micro- nano-electrodes developed have a variety of shapes: pillars, nanowires, nanotube, mushroom shaped microelectrodes. Most of them are passive elements (electrodes) while there exist only a few descriptions of field effect transistor based recording systems (Gao et al., 2012; B. Tian et al., 2010). As for MEAs, the electrogenic cells are cultured directly on top of the electrode array. In most cases the probes can establish a very tight extracellular contact with the cell but do not spontaneously cross the plasma membrane to contact the intracellular space. Different strategies have been used to breach this last obstacle: electroporation(Abbott et al., 2020; Desbiolles, de Coulon, et al., 2020; Jahed et al., 2022; Lee et al., 2022; VanDersarl & Renaud, 2016; Xu et al., 2022), engulfment promoting surface functionalization (Gao et al., 2012; Hai et al., 2010; Qing et al., 2014; B. Tian et al., 2010), optoporation (Dipalo et al., 2017) and extreme sharpness (R. Liu et al., 2017; R. Liu et al., 2022) (Figure 1.4, A, B, C and D respectively). Intracellular recording using micro- nano-electrodes enables intracellular measurement of attenuated action potentials and in some cases synaptic inputs (Abbott et al., 2020; Hai et al., 2010; R. Liu et al., 2022).

A Electroporation
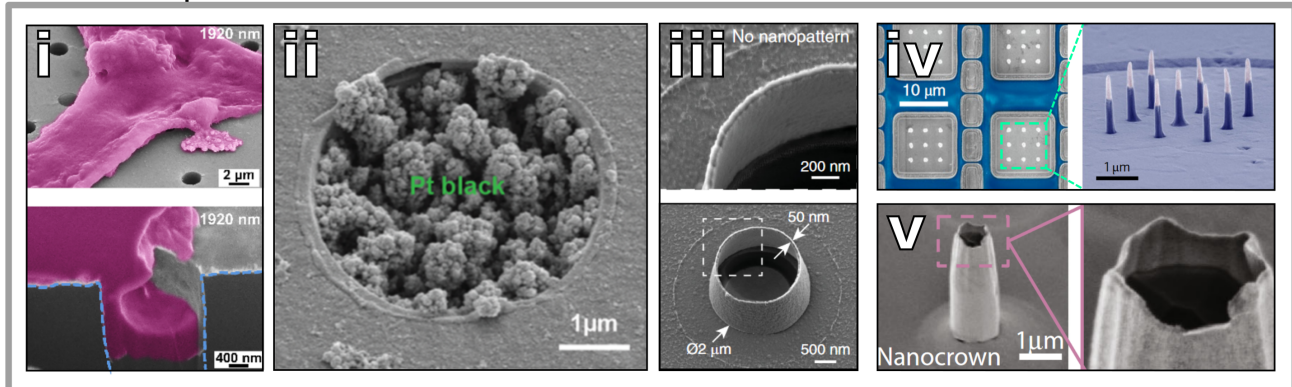
B Chemical functionaliaztion
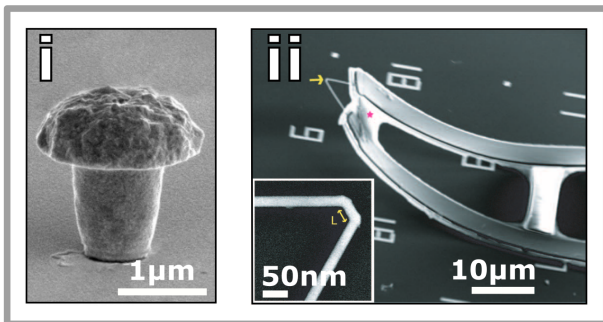
C Optoporation
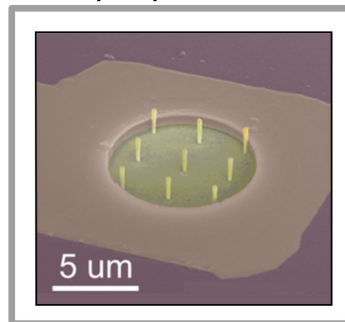
D Sharpness
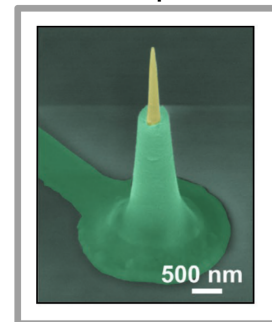
Figure 1.4: Micro- nano-electrodes for intracellular electrophysiology and their respective strategy to enable intracellular access. (A) Intracellular access through electroporation. i) Cardiomyocyte coloured pink is seen to protrude in the nanoporous PET membrane electrode. ii) Electrodeposited platinum black within recess integrated on CMOS. The platinum black has topography features on the nanoscale. iii) Nanovolcano electrode with insulating/conductive outer/inner wall. The wall is 50 nm in thickness. iv) Platinum black electrodeposited nanowire arrays and nanowire array before deposition (right). (v) Nanopillar wrapped with platinum and platinum nanocrown on top (Abbott et al., 2020; Abbott et al., 2017; Desbiolles, de Coulon, et al., 2020; Jahed et al., 2022; Lee et al., 2022; Xu et al., 2022). (B) Intracellular access through chemical functionalization. i) Gold micromushroom functionalized with a engulfment promoting peptide. ii) Flexible field effect transistor probe fabricated with a kinked nanowire gate (inset) functionalized with phospholipids for robust anchorage across the cell membrane (Ojovan et al., 2015; B. Tian et al., 2010). (C) Intracellular access through optoporation of gold plasmonic antenna (Dipalo et al., 2017). (D) Intracellular access through spontaneous insertion owing to extreme sharpness of platinum coated silicon nanowire (R. Liu et al., 2022). All reproduced with permission.

1.2.4 Optimization for micro- nano-structures intracellular access and tools available

Comparing the performances of the different strategies for intracellular access shows that not all micro- nano-electrodes are equal in recording quality and stability (Appendix, Figure 1, signal amplitude, duration and yield). A striking point is the fact that a given micro/nano-electrode results in recording of vastly different quality depending on the cell type recorded from (Figure 1.5). This observation highlights the significant yet little studied effect of the cell physicochemical properties such as stiffness, cytoskeleton arrangement and adhesion processes. It is known for example that the viscosity of the cell membrane and overall stiffness will determine the minimum force needed for penetration by a nanowire (Xie et al., 2013). Still, experimental studies of the parameters affecting the quality of intracellular recording from micro- nano-electrodes are lacking due to the limitations of the few methods available.
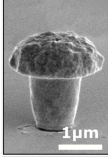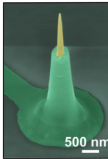
Electrode geometry	Cell tested	Signal amplitude (mV)	Reference
Micromushroom	Rodent CMCs	6	Fendyur and Spira, 2012
	Rodent hippocampal neurons	5	Shmoel *et. al.*, 2016
	Applysia neurons	25	Hai *et al.*, 2010
nanowire	Rodent cortical neurons	0.1-99	Liu *et. al.*, 2017
	HiPSC derived dopaminargic neuron	0.1-35	Liu *et. al.*, 2017
	iPSC CVPCs	5 mV	Liu *et. al.*, 2022

Figure 1.5: Micro- nano-electrodes recording from different cell types result in different recording quality. In the first row, micromushroom show signal amplitude varying by 5 fold depending on the cell under study. Similarly, the signal amplitude recorded by individual nanowires from different cell type spreads over an order of magnitude.

A common strategy to rationalize the quality of an electrophysiological recording from micro-nano-electrode is the use of lumped element models. In such model, the cell/electrode interface is modeled in term of electronic elements (*e.g.*, resistance and capacitor) that can be quantified in order to gain an understanding of the interface. A simple model of a cell on a nano-electrode can let us know that the quality of an electrophysiological recording is in great part dictated by the ratio of the seal resistance to the junctional membrane impedance (Figure 1.6). Seal resistance is defined as the resistance from the point of contact of the micro- nano-electrode to the bulk of the extracellular bath. It originates from the electrolyte filled tortuous cleft between the cell's plasma membrane and its substrate. This parameter is equivalent to the seal resistance of a patch clamp pipette to a cell and directly affects the quality of the electrophysiological recording. The junctional membrane impedance (also called access resistance) is the resistance encountered by the micro- nano-electrodes when injecting

current across the portion of cell membrane it is facing. For intracellular measurement, this portion of membrane (usually called junctional membrane as opposed to the remaining non-junctional membrane) needs to be permeabilized typically by electroporation. While typical electrophysiological recordings from electrode arrays are made with voltage follower passing zero current (ideally), this access resistance is also present and results in attenuation of the transmembrane potential measured as detailed further below. In this model the effect of the stray capacitance and ratio of the electrode impedance to amplifier input impedance also play a role but are within the control of investigator. On the other hand, the seal resistance and junctional membrane impedance arise from the interaction of the cell with the electrode and is hence unknown until resolved experimentally.
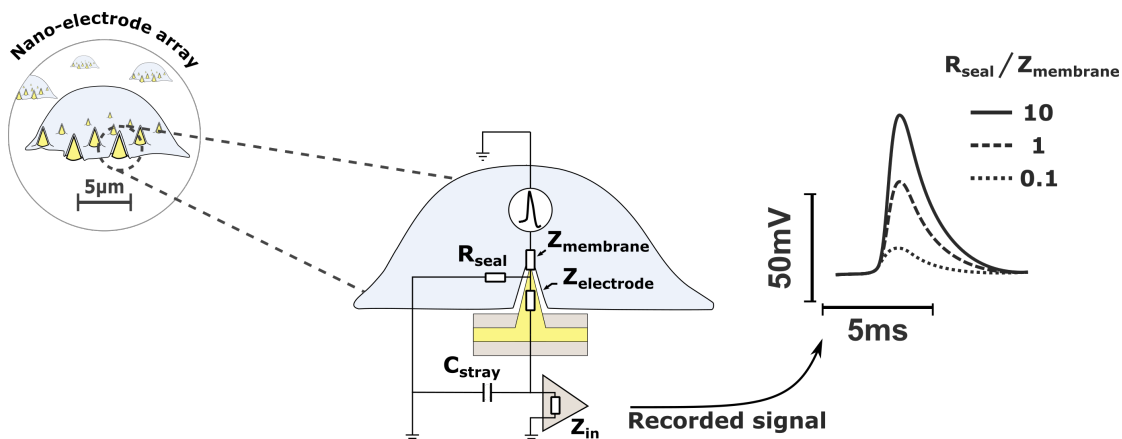
Figure 1.6: Lumped element model of the cell/electrode interface during intracellular recording from a nano-electrode. $Z_{electrode}$ is the impedance of the electrode, $Z_{membrane}$ is the impedance of the portion of the cell membrane facing the electrode, R_{seal} is the sealing resistance arising from the electrolyte filled cleft between the cell and its substrate, C_{stray} is the stray capacitance of the electrode leads to ground and Z_{in} is the amplifier input impedance. The encircled waveform within the cell symbolizes the transmembrane potential fluctuation during an action potential. The bath is connected to the ground of the amplifier typically through an Ag/AgCl electrode. The ratio of the seal resistance to junctional membrane impedance is determinant for the fidelity of the signal recorded.

Naturally, all micro- nano-electrodes designed for intracellular electrophysiology seek to optimize these two parameters; maximize seal resistance and minimize access resistance. Methods capable of resolving these parameters are hence highly desirable in order to i) understand the basis for intracellular access susceptibility in different cell type and ii) pitch the electrode used to the cell studied in order to obtain an optimal cell/electrode interface and hence recording quality. The methods available to probe these parameters include electron microscopy, fluorescence microscopy and electrical characterization with patch clamp (Figure 1.7, A-C).
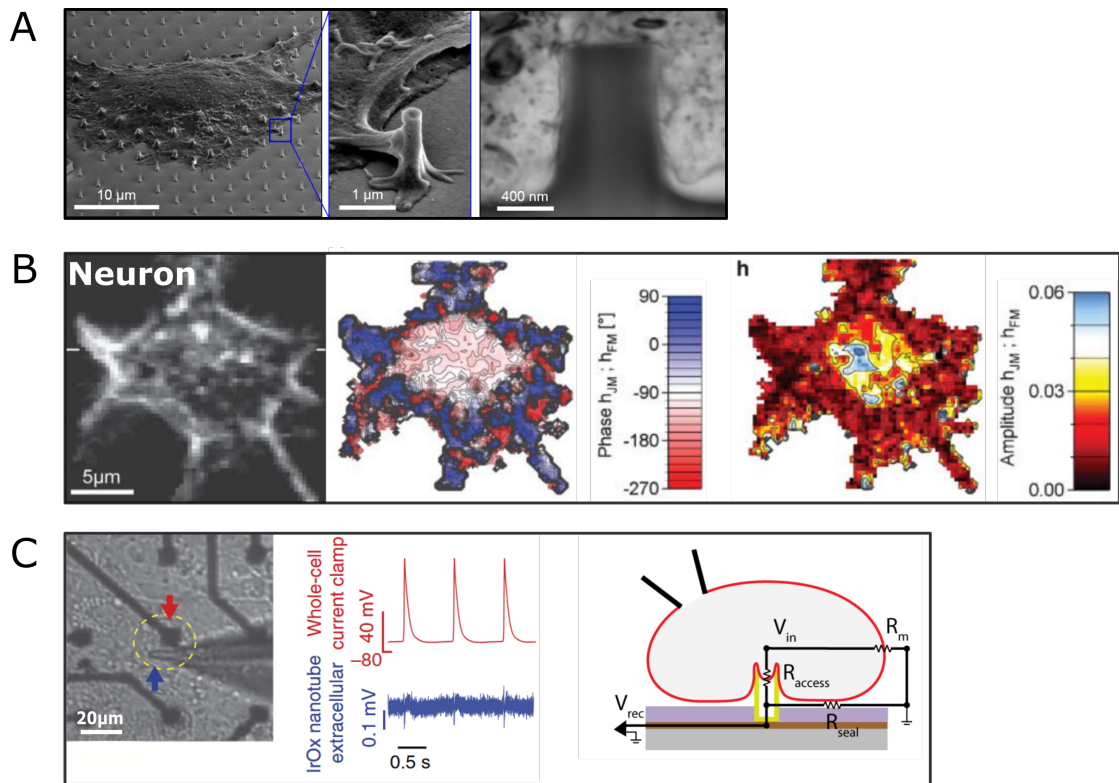
Figure 1.7: Methods for imaging the cleft between cells and their substrate or electrode. (A) Electron microscopy rely on delicate sample preparation and sectioning techniques. The cleft can be imaged down to fractions of nanometers. (B) Optical imaging using voltage sensitive dye. (C) Simultaneous recording from a cell using a whole cell patch clamp and an underlying nano-electrode. The seal resistance and access resistance can be estimated by comparing the holding current before and after establishing the whole cell configuration. All reproduced with permission from Braun and Fromherz, 2004; Lin et al., 2014; Santoro et al., 2017.

Clever sample preparation for electron microscopy have demonstrated the feasibility of imaging the cleft between the cell and its substrate with high contrast down to a couple of nanometers (Hai et al., 2009; Santoro et al., 2017; Wrobel et al., 2007). However, this approach is essentially a snapshot at a fixed time precluding any dynamic study and requires skilled operator for the complex sample fixing, cross-section preparation, imaging and is in general very time consuming.

Imaging of the cell/substrate cleft using membrane fluorescent tags is an alternative that benefits from allowing live, multi-site interrogation. Still, implementation described may result in phototoxicity since they are either based on voltage sensitive dye (Braun & Fromherz, 2004) or confocal imaging (Berthing et al., 2012). Seal resistance can be estimated from the electrolyte conductance and cleft geometry but this method accuracy will rely on the microscopy resolution which may become limiting for the few tens of nanometers of cell/substrate cleft obtained from cells on nanotopography (Zeck & Fromherz, 2003) and necessitates non-trivial

image analysis.

Finally, concomitant recording from a cell with a patch clamp and a micro- nano-electrode has been described (Lin et al., 2014; Robinson et al., 2012). This method has the advantage of measuring directly the parameters of interest but suffers from the inherent throughput limitation and eventual cell death resulting from the use of whole cell patch clamp measurement. Consequently, this approach is more suited to characterize an already well performing micro- nano-electrode rather than helping in its development.

Consequently, all approaches available today are limited either due to low throughput or limited resolution in resolving the cell micro- nano-structure interface which precludes to our understanding of the cell/electrode interface.

1.3   Parallel to electrochemistry

1.3.1   Intracellular biomolecules analysis

Establishing contact with the intracellular space of a single cell is a daunting task that met its goal in electrophysiology after decades of research. Hence it is no surprise that the patch clamp method found interest across many disciplines outside of electrophysiology. Analysis of biomolecules within a single cell has seen many implementations using glass micropipette similar to those used in patch clamp. Examples include electrochemical neurotransmitter analysis (Mosharov et al., 2003), metabolites and drugs mass spectrometry (Pan et al., 2014), electrochemical nicotinamide adenine dinucleotide quantification (Ying et al., 2018), all sampled using a micropipette. In all cases, experimental throughput and cell death preclude the application of these methods to larger scale and/or longitudinal studies. The impact on cell viability can be alleviated using nanoelectrodes mounted on micromanipulator however this kind of study requires labelling (P. Sun et al., 2008) or is limited to biomolecules with large concentrations close to the millimolar range (*e.g.*, glucose) (Liao et al., 2019) or spatially concentrated as with neurotransmitters packaged in vesicles (Omiatek et al., 2010). Finally, the manipulation of a nanoelectrode mounted on a micromanipulator is slow and retains the throughput and scalability limitation of patch clamp approaches. There is accordingly a similar need in electrochemistry and electrophysiology for scalable, multi-site intracellular sensing. When sensing in the intracellular space is desired, nanotechnology can provide solutions similar to the sharp micro- nano-electrodes used for intracellular electrophysiology. This approach also comes with the advantage of reduced cell damage compared to micropipette based methods which should allow for longitudinal monitoring. In this context, measurement schemes using electrochemical methods are attractive for being label free and allowing translation of the knowledge developed in micro- nano-electrodes electrophysiology.

1.3.2 Collection efficiency in electrochemical detection at the cell vicinity

Another problematic situation that may arise in single-cell measurement is the collection of a molecule of interest being released at the cell's membrane as during exocytosis of neurotransmitters. The traditional approach uses carbon fiber microelectrodes (CFE) encased within a glass micropipette to oxidize electroactive neurotransmitters which can be quantified through Faraday's law (Wightman et al., 1991). It has recently been suggested that pressing the CFE against the cell is not enough in preventing the neurotransmitter molecule from escaping detection which could result in significant underestimations (McCarty et al., 2022). Interestingly, isolating the electrode in contact with the cell from the extracellular bath using a recessed electrode allowed to recover a larger fraction of the released quanta. Because this approach was demonstrated using a glass micropipette, it is not well scalable. Accordingly, a substrate integrated electrode reproducing the geometry of the glass micropipette with recessed electrodes could constitute an improvement over the CFE in terms of throughput and collection efficiency.

1.4 Nanovolcano as a gateway to the the intracellular space

Recently, a volcano-shaped microelectrode with superior performance for intracellular cardiac electrophysiology was described (Figure 1.4, A, iii) (Desbiolles, de Coulon, et al., 2019; Desbiolles, de Coulon, et al., 2020). In another work linked to this thesis, the rate of intracellular access obtained through electroporation of primary cardiomyocytes was optimized to reach up to 76% (Desbiolles, de Coulon, et al., 2020). This high yield makes the nanovolcano technology very promising for other applications as well. For this reason, this thesis makes use of the nanovolcano extensively in order to interface single cells for electrophysiology or electrochemistry.

Today, the fabrication process of the nanovolcanoes enjoys high scalability and wide process compatibility thanks to the mild thermal processing steps it includes (maximum 160°C). However, the fabrication of the volcano-shaped tip results in the inner wall of the nanovolcano necessarily connected to the underlying electrode. While this can be an advantage in certain cases (*e.g.*, large surface area electrodes), it would be practically more convenient to have the fabrication of the volcano-shaped insulating tip independent of the electrode fabrication itself. With such a process, the nanovolcano could be used as an independent, intracellular-enabling feature, part of a greater device where the sensing mechanism and intracellular access mechanism are separately controlled.

1.5 Goals and structure of the thesis

In the discussion above we have identified current limitations in the field of electrophysiology and electrochemistry and consequently concluded that at the start of this thesis several investigation leads presented themselves.

First, the establishment of intracellular access by micro- nano-electrodes and the ensuing quality of electrophysiological recording is poorly characterized and few tools, all with drawbacks, exist. Therefore, the first goal pursued in this thesis was to develop a scalable method to characterize the cell/micro- nano-electrode interface in view of improving electrophysiological recording. **Chapter 2** presents the development of a new nanovolcano capable of measuring the seal resistance using impedance spectroscopy. The method is demonstrated to discriminate difference in seal resistance for human embryonic kidney cells and primary rodent neurons cultured on microelectrodes of different geometries and functionalized with different chemical cues.

Secondly, we have identified that there currently exists few solutions for intracellular electrochemical sensing; none of which is scalable. Accordingly, the second goal pursued in this thesis was the development of an electrochemical sensor capable of intracellular sensing over multiple sites without impairing cell function. In **Chapter 3** the design and characterization of a new nanovolcano harnessing redox cycling is presented. The requirements and design of the sensor are discussed in detail and a proof-of-concept measurement in cell lysate is reported.

Third and last, we took note of the limitations highlighted for amperometric detection of neurosecretion. In particular, the possible underestimation of quantal size using CFE and the lack of scalability of micropipette based approaches. Henceforth, the third goal of this thesis was the application of the nanovolcano electrode to the measurement of exocytosis hypothesizing that the enclosed volume created by the cell covering the nanovolcano should confine the release of neurotransmitter to the sensing electrode. **Chapter 4** presents results of exocytosis recorded at the nanovolcano/nanogap electrode developed in **Chapter 3**. This work discusses a possible fundamental discovery: the faster rate of catecholamine release during exocytosis from plasma membrane with large curvature induced by nanotopography.

The results are finally summarized in the **Perspectives and Conclusion**. The significance and limitations of each work are discussed. Finally, future opportunities arising from the thesis outputs are considered.

2 Impedance spectroscopy of the cell/nanovolcano interface enables optimization for electrophysiology

This thesis chapter is adapted from our recently submitted manuscript: N. Maïno, A. Bertsch, P. Renaud, "Impedance spectroscopy of the cell/nanovolcano interface enables optimization for electrophysiology", *Submitted*, 2022.

2.1 Introduction

In the last decade, the emergence of nano- micro-electrodes for intracellular recording of the transmembrane potential is a formidable advancement that is poised to supplant traditional extracellular recordings with planar multi-electrode arrays (MEA). This technology aims to allow the recording of the whole electrophysiological repertoire, not only action potential, while retaining the advantages of MEA: multi-site sensing for high-throughput experiments and long term monitoring thanks to reduced cell damage compared to patch clamp techniques (Spira et al., 2019). Nonetheless, the establishment of intracellular access by the probe (*(i.e.)*, nano- micro-electrode) is a process that remains elusive and hard to study. A simple approach consists in measuring the yield of intracellular access as the percentage of probes that register an electrophysiological signal with intracellular features (polarity, timescale, amplitude). However this assessment method is time consuming as most electrogenic cell cultures take time to mature (*(e.g.)*, 2-3 weeks for primary neurons) and requires that intracellular access is a consistent, if rare, event. Alternative methods include concomitant patch-clamp and nano- micro-structure characterization of the cell/probe interface (Lin et al., 2014; Robinson et al., 2012), optical microscopy (Berthing et al., 2012; Braun & Fromherz, 2004) and electron microscopy (Hai et al., 2009; Santoro et al., 2017; Wrobel et al., 2007). Unfortunately, the patch clamp method suffers from an inherent throughput limitation. Microscopy techniques are an indirect measurement of the feature of interest, the electrical coupling of the cell and probe, that may fail to capture the true degree of fitness of a given probe for intracellular access and electrophysiology. There is consequently a need for a method that could directly assess the electrical properties of the cell-probe interface at high throughput. We hereby

present an impedance spectroscopy method that allows to optimize the interface of cells based on nanovolcano (NV) electrodes. The impedance spectrum of individual cells cultured on arrays of NVs are measured and the seal resistance, a critical parameter to intracellular electrophysiology recordings, is assessed. The value of seal resistances measured are found to correlate well with electrophysiological recording quality. This method is label-free, scalable and harmless for cells and does not necessitate the cell to be electrogenic. The last point is a critical advantage considering the present experimental bottleneck of electrogenic culture maturation. Finally this method can be implemented for any hollow microstructures (*(e.g.)*, nanostraw, nanotubes) owing to a novel fabrication process that decouples the nanostructure from the underlying electrode.

2.2   Results

2.2.1   Fabrication of low impedance nanovolcanoes

The NV have been previously employed for intracellular recordings of action potentials from primary cardiomyocyte cultures (Desbiolles, de Coulon, et al., 2019; Desbiolles, de Coulon, et al., 2020). However, the NV in their previous implementation are not amenable to seal resistance measurement because of their large impedance as discussed in the supplementary materials (Supp. information, section 2.6.1).

We thus developed a new fabrication process to lower the impedance of NVs over two-orders of magnitude (for fabrication details, see Materials and Methods and Supp. Figure 2.1). A top view, cross-section and collapsed view of the finished device is depicted in Figure 2.1, A-B. The key feature of this device is the platinum ring electrode of 17 μm in diameter covered by a layer of poly(3,4-ethylenedioxythiophene) polystyrene sulfonate (PEDOT:PSS). PEDOT:PSS is a conductive polymer characterized by a large specific capacitance that can be electrodeposited *in situ* and has long been used to lower the impedance of MEA (Cui & Martin, 2003).

The electrodeposition of PEDOT:PSS is performed as the last step of the fabrication process and is easily monitored under an optical microscope (Figure 2.1, C). Thanks to the ring-shaped platinum electrode, it is possible to stop the deposition process early so as to leave the portion of substrate below the nanovolcano transparent. This allows optical inspection of all NVs during cell culture in order to assess which NV should be considered for seal measurement (covered by a cell) and which should not (not covered).

It should be noted that the probe itself (*i.e.*, the NV) is independent of the underlying electrode, a feature that we put to use below to alter the NV geometry (diameter and height; as highlighted in Figure 2.1, D) in order to obtain higher seal resistance while maintaining constant electrode impedance for direct comparison. The electrodeposition process results in a decreased impedance below 10 kHz that reaches up to two decades (Figure 2.2).
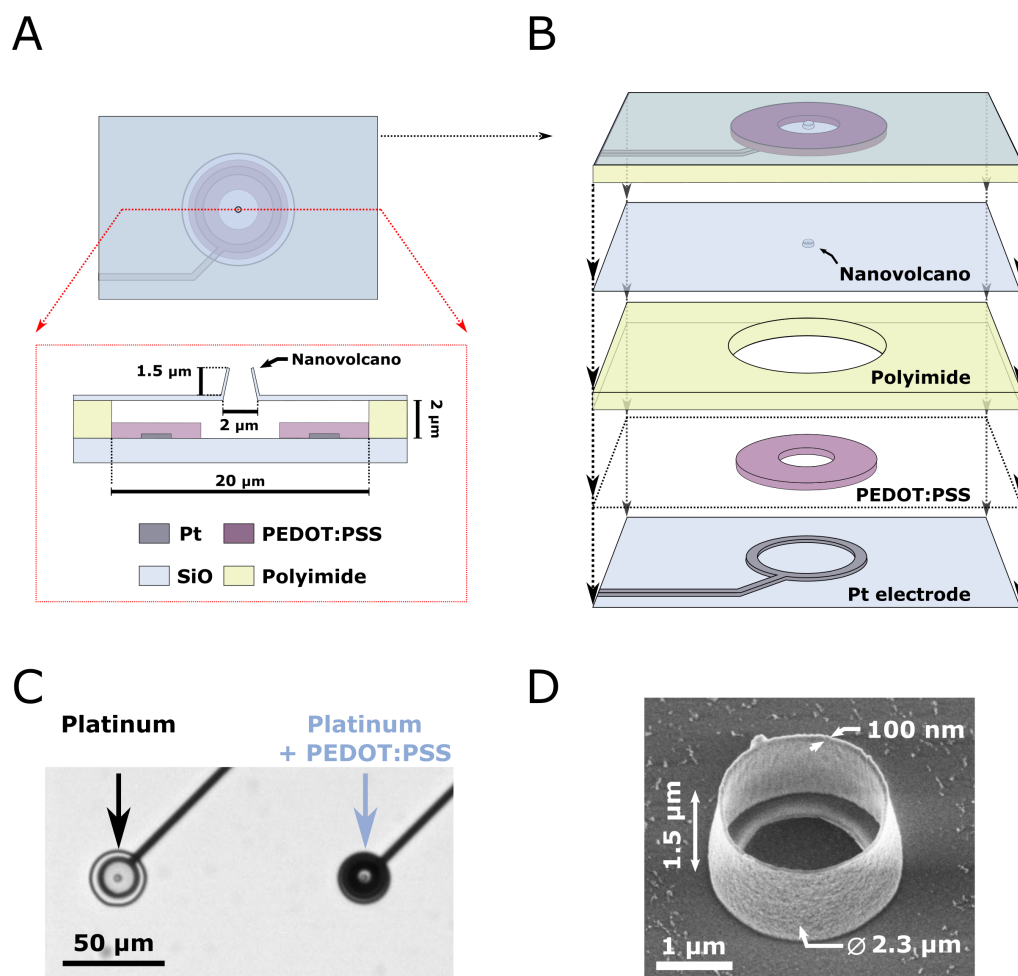
Figure 2.1: Device description. (A) Top view and cross section of the device to scale. The nanovolcano is standing on top of a cavity whose floor is patterned with a platinum electrode covered by a layer of poly(3-4,ethylenedioxythiophene) polymer doped with polystyrene-sulfonate (PEDOT:PSS). (B) Device collapsed view showing the different layers to scale. From bottom to top: platinum electrode on fused silica substrate, PEDOT:PSS ring, polyimide insulation with cavity etched into it and SiO_2 insulating layer into which the nanovolcano is patterned. (C) Optical micrograph of the platinum electrode before and after *in situ* electrode-position of PEDOT:PSS. Although the electrode is enlarged, the nanovolcano is still readily imageable thanks to the ring geometry and the transparent fused silica substrate. (D) Scanning electron micrographs of the finished device viewed with a tilt. Nanovolacnoes of various height and diameter were fabricated in this study.
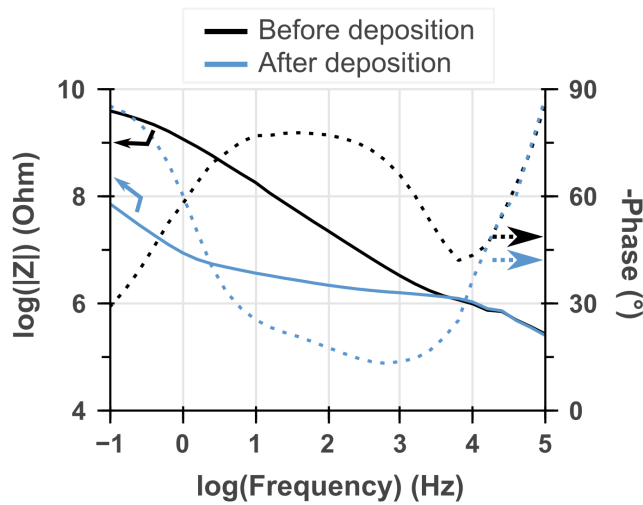
Figure 2.2: Bode plot in magnitude and phase of the electrode impedance before and after electrodeposition of PEDOT:PSS. The impedance magnitude is decreased significantly in the range of the seal resistance measurement between 1 Hz and 1 kHz. The impedance decrease above 10 kHz characterized by a -90° phase arises from the stray capacitance of the printed circuit board used to interface the devices. Between 10 kHz and 100 Hz the impedance is dominated by the spreading resistance, between 100 and 10 Hz a transition occurs from the spreading resistance to the PEDOT:PSS capacitance with a transitory regime characterized with a -45° phase arising from the diffusion of cations through the polymer (see Supp. Figure 2.8 for the equivalent circuit and theoretical model).

2.2.2 Measurement *Modus Operandi*

The seal resistance of a cell adhered on top of a NV is measured by electrochemical impedance spectroscopy (EIS). In a typical experiment, the cells are plated on a device housing an array of 60 NVs and allowed to adhere to the substrate for 24h. During the measurement session, the device is connected to a potentiostat in a three electrode configuration (working electrode: NV's Pt/PEDOT:PSS electrode, counter electrode: Pt wire and reference electrode: silver/silver-chloride (Ag/AgCl) pellet).

From the impedance spectra, the seal resistance is taken as the averaged real part of the impedance over a decade centered at the point of minimum phase after subtraction of the same metric from a NV that is not covered by a cell. Alternatively, the impedance spectrum of NVs covered by a cell can be fitted to an equivalent circuit to extract the seal resistance. Both methods were found to yield similar results (Supp. Figure 2.9) so we used the former method which allows for simpler data processing.

2.2.3   Impact of chemical functionalization on the seal resistance

As a demonstration of our method's ability to sense the impact of chemical functionalization, we assessed the effect of different adhesion promoters on the seal resistance of human embryonic kidney cells (HEK) cultured on NVs. HEK cells were cultured on substrates that were either bare, functionalized with Poly-D-Lysine (PDL) alone, or PDL and collagen sequentially. It is apparent from optical inspection of cells cultured on bare or PDL/collagen functionalized chips that they adhere to the substrate in different ways as evidenced by the difference in cell body shape (Figure 2.3, A-B). Qualitatively, this is also visible from the impedance spectrum reaching larger values for HEK cells cultured with adhesion promoters (Figure 2.3, C). For quantitative analysis, the seal resistances are extracted and displayed as box plots where each datapoint represents a measurement originating from a single cell (Figure 2.3, D).

In these data, the spread of the distributions arises primarily from biological variability and random cell/NV pairing as opposed to variability due to noise in the measurement (Supp. Figure 2.10). From our data, we can conclude that PDL together with collagen provide a better seal resistance than PDL alone and that compared to the bare substrate, the seal resistance is increased from 500 kΩ to 10 MΩ on average; a 20-fold improvement.

2.2.4   Variation of the nanovolcano geometry

Having demonstrated the ability of our method to discriminate changes in seal resistance, we looked to alter the NV geometry with aim of increasing the cell/NV coupling. We fabricated NV of varying diameter and height (Figure 2.4, A). We also fabricated NV of equal dimensions but with a different roughness of the NV wall (rough vs smooth; Figure 2.4, A, i vs ii). Finally, we included chips with holes instead of NV (Figure 2.4, A, vi). After culturing HEK cells on all NV geometries, we measured the seal resistance as described above and compared their distribution across all geometry (Figure 2.4, B). During experiments with HEK cells, we performed all measurements 24h after plating cells at a low density of 31500 cells/cm^2. We have characterized the impact of both plating density and time of recording and concluded that seal measurements should be compared at a similar time point after plating and that high plating densities reflect the properties of cell-sheets rather than those of single cells (Supp. Figure 2.11 and 2.12).

The most notable difference in seal resistance is observed for NV with very short wall height or no wall at all (Figure 2.4, B, vi). From this result, we conclude that the NV wall results in an increased average value of seal resistance and narrower distribution around the mean. Unfortunately, none of the geometry considered could significantly improve the seal resistance as compared to the original NV design (Figure 2.4, B, i). While the seal resistance measured is on average slightly larger and the distribution narrower for smooth compared to rough NV wall, the difference is not significant (Figure 2.4, B, i vs ii). This suggests that contrary to the geometry investigated here, taller nanostructures with larger pitch are desired to better interface HEK cells. Nonetheless, we conclude that the method presented is able to resolve
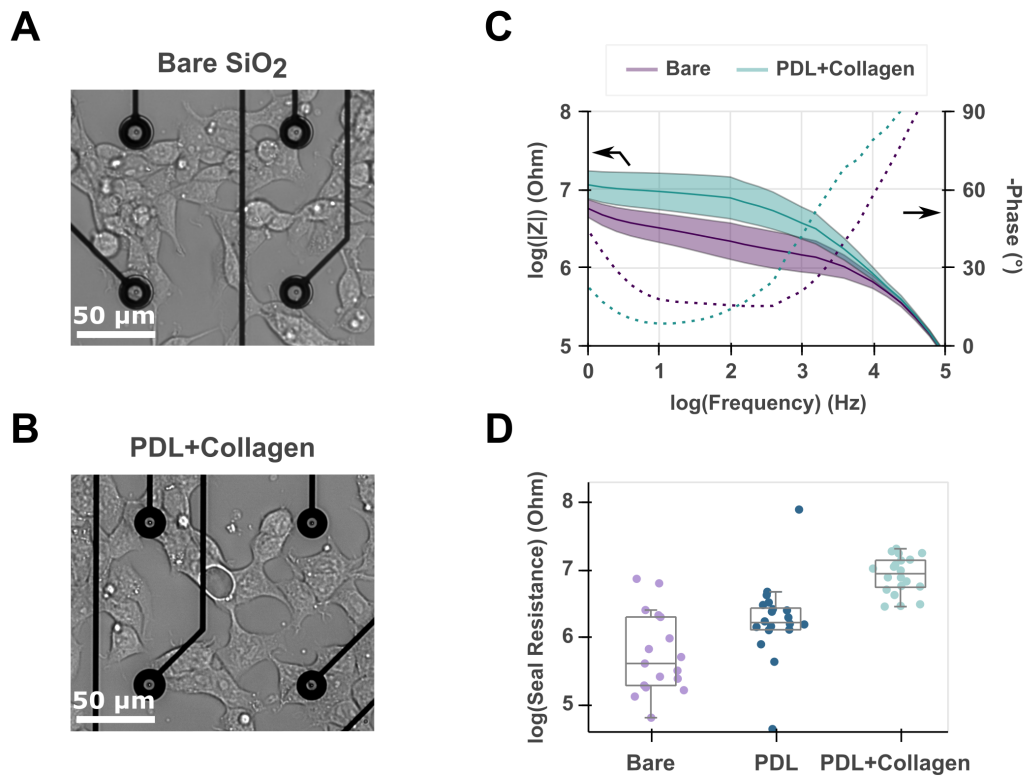
Figure 2.3: Impact of chemical functionalization on seal resistance. (A) optical micrograph of human embryonic kidney cells (HEK) 24h after plating on bare glass substrate show elongated features with little spreading over the substrate. (B) In comparison, cells plated on glass substrate functionalized with poly-D-Lysine (PDL) and collagen assume a flatter cell body configuration by spreading more on the substrate due to improved adhesion. (C) Impedance spectra displayed as a bode plot of the magnitude (solid line) and phase (dashed line) for cells plated on bare and PDL+collagen functionalized substrate. The impedance magnitude is represented by the mean of the sample of cells interrogated ± one time the sample standard deviation represented by the colored area. Sealing resistances are obtained from the resistive portion of the spectra characterized by a minimum in the impedance phase (phase ~0°; see text for detail). (D) Comparison of seal resistances for samples of HEK cells cultured on bare glass (n=17), PDL (n=20) and PDL+collagen (n=20).

A

B
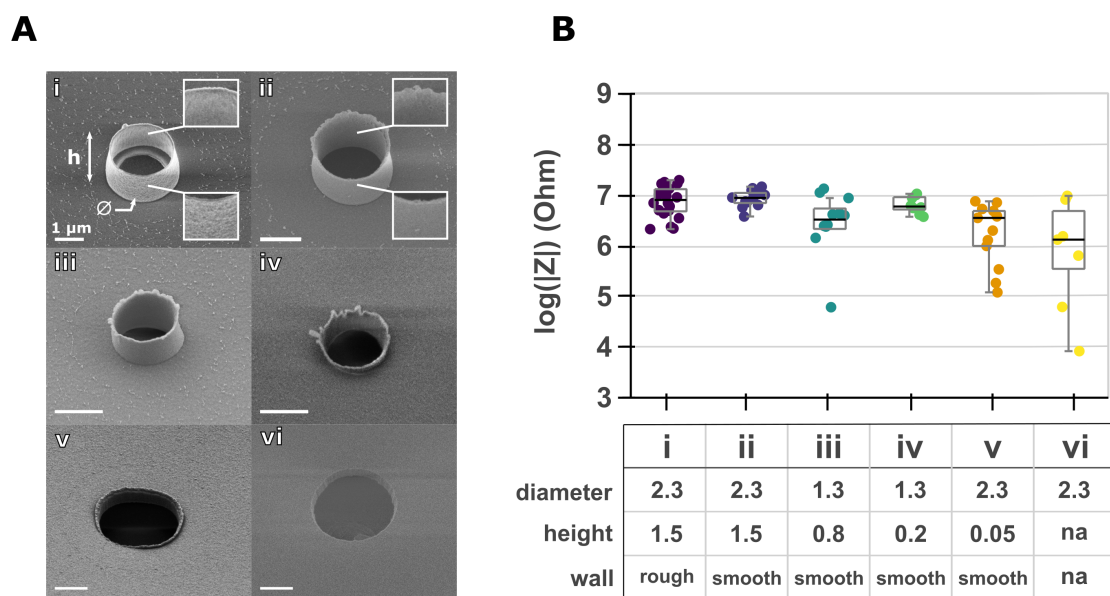
Figure 2.4: Impact of nanovolcanoes geometry on seal resistance. (A) Scanning electron micrograph of the different nanovolcano geometries fabricated. All scale bars correspond to 1 μm. Probe i) and ii) are 2.3 μm in diameter and 1.5 μm in height however i) has walls with nanoscale roughness compared to ii) smooth walls (insets). iii) and iv) are 1.3 μm in diameter but with decreasing wall height. v) and vi) are 2.3 μm in diameter with walls 50 nm high (v) or without walls (vi). For a summary of the geometrical parameters see table in (B) where diameter and height are in units of microns. (B) Seal resistance of human embryonic kidney cells 24h after plating on the nanovolcanoes of different geometries.

change in cell/probe coupling given that the seal resistance of HEK cells on NVs with shorter walls can be distinguished from ones with taller walls.

2.2.5   Electrophysiology recordings from primary cortex neurons

Having ascertained our method can differentiate the impact of chemical and geometrical cues on cells seal resistance, we looked to apply our method to optimize the coupling of primary rodent cortex neurons to NV. We used different NV geometries as above which we functionalized with PDL and laminin sequentially. The cells were allowed to mature for 16 days before performing the experiment at which point each culture was inspected optically to identify the NVs covered by cells. The impedance spectrum of each NV covered by a cell was acquired as described above followed by recording of spontaneous electrophysiological activity. We expect that probe geometries/functionalization yielding large seal resistance should result in better electrophysiological recording. The quality of the electrophysiological signal was assessed by the signal-to-noise ratio (SNR) of action potentials measured extracellularly (EAP). Intracellular access is often too low and yields too few data to enable a quantitative comparison hence the extracellular signal was preferred. Below, we report the distribution of measured SNR as individual data points overlaid with boxplots that summarizes the distribution features. Each data point corresponds to a measurement originating from a single cell (*i.e.*, average SNR of all the spikes recorded from a given cell).

As for HEK cells, the different geometries of NV investigated resulted in mostly similar seal resistance (Figure 2.5, A). Similarly, the median of the EAP SNR was equivalent across all NV with values between 10-15 (Figure 2.5, B). We also assessed the impact of different adhesion promoters on the coupling of neurons to NV. We measured the seal resistance for neurons cultured on NVs functionalized with PDL alone or PDL and laminin sequentially and found that PDL plus laminin resulted in seal resistance median 2.3 times higher (Supp. Figure 2.16).

The motivation of the method we present in this study is that impedance spectroscopy predicts well the quality of electrophysiological recording and can thus be used as a substitute for the latter which is time consuming. When we plot the averaged SNRs against seal resistances we observe a reasonably good fit to a linear regression defined by $SNR = 4R_{seal} + 6.5$ with R_{seal} expressed in MΩ (Figure 2.5, C). If we consider only NV that registered EAP with average SNR equal or above 20, the coefficient of correlation and determination of the two variables are improved (Pearson coefficient=0.95, coefficient of determination 0.91; Figure 2.5,D).
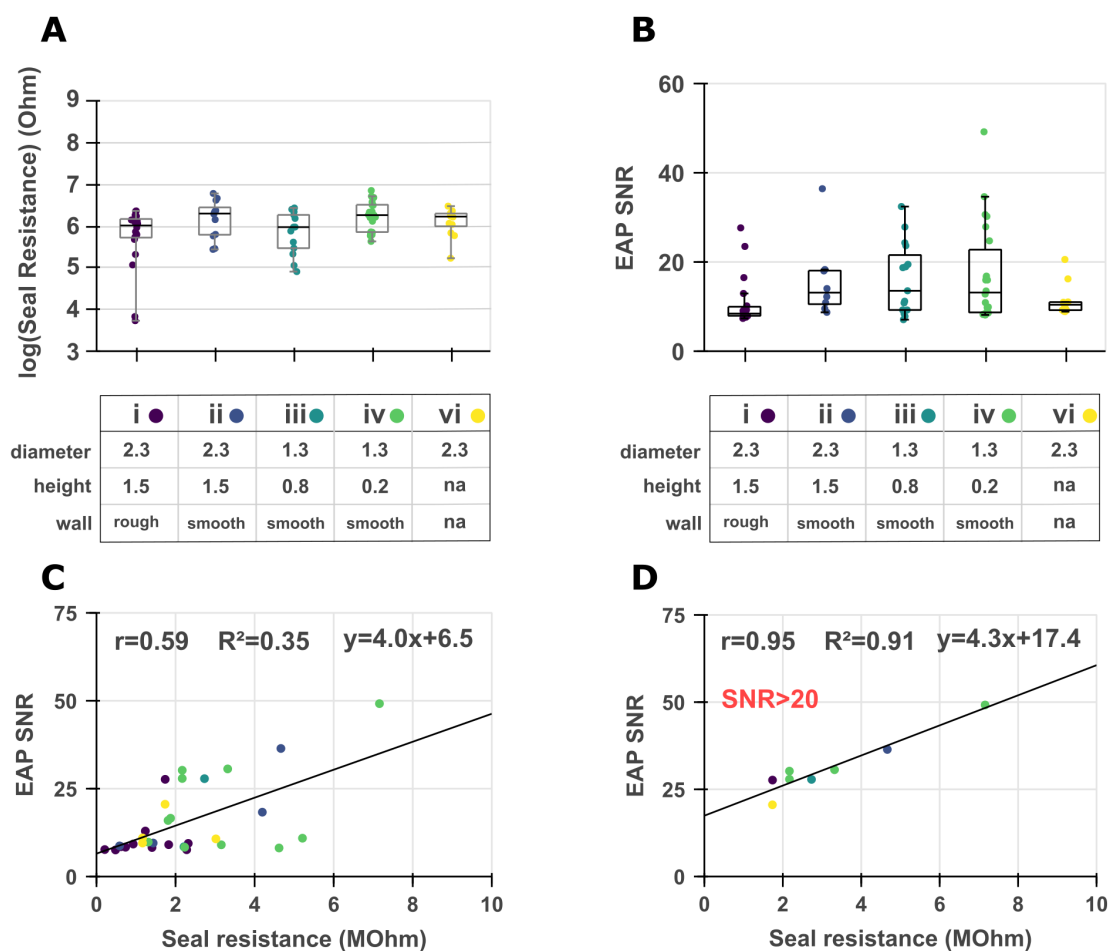
Figure 2.5: Seal resistance, extracellular action potentials (EAP) signal-to-noise ratio (SNR) and their comparison for primary rodent cortex neurons after 16 days in culture. (A) Seal resistance of neurons on nanovolcanoes of different geometries. Groups i) to vi) are as in Figure 2.4. (B) average SNR of spontaneous EAP measured from neurons on nanovolcanoes of different geometries. In (A) and (B), each data point corresponds to a single cell and the boxplots summarize the sample distribution for a given geometry. (C) Plot of the average EAP SNRs against seal resistances for all cells. The line is a linear regression characterized by the equation at the top of the plot, Pearson coefficient r and coefficient of determination R^2. (D) Same as in (C) but only for cells whose average EAP SNRs was above 20.

2.3 Discussion

2.3.1 Fabrication and characterization of low impedance nanovolcanoes

The consistency of the deposition process was very satisfactory (Supp. Figure 2.7). Optical inspection during electrodeposition allowed to leave the center of the ring electrode undeposited and thus optically transparent. The optical transparency of the cell/probe interface

could allow multiplexed recordings such as electrical and fluorescence measurement for the development of voltage-sensitive dye and recombinant proteins.

We have analyzed the impedance spectrum of the Pt/PEDOT:PSS electrode following the model of Cui and Martin (Cui & Martin, 2003) for electrodeposited PEDOT:PSS films (Supp. Figure 2.8). In this model, the bulk electronic capacitance of the polymer is coupled (in series) with the diffusion of ionic charge carriers (cations) within the film and the spreading resistance of the electrode. The model fits well the experimental impedance spectrum considering the complexity of charge transfer within conducting polymers.

Based on the impedance spectrum after deposition and the noise level in our experiments, we can estimate the lower and upper bound of seal resistance measurable with our approach as $1\,k\Omega$ and $20\,G\Omega$. These lower and upper bounds originate from the spreading resistance across the NV and our PCB stray impedance respectively. The seal resistance of cardiomyocyte or neuron cells range from couples of megaohms on flat substrate (Braun & Fromherz, 2004) up to a few hundreds of megaohms on nanotopography (Lin et al., 2014; R. Liu et al., 2017; Robinson et al., 2012).The dynamic range of our method is hence well suited to the study of adherent cells seal resistance. Additionally, the decreased impedance is expected to benefit the SNR of electrophysiological recordings thanks to the lower thermal noise of the electrode.

2.3.2 Impact of chemical functionalization on the seal resistance

The seal resistance arises from the tortuous cleft between a cell's plasma membrane and the substrate surrounding the electrode. It has long been known that chemical functionalization can alter the dimension of this cleft to values ranging from tens to a few hundreds of nanometers (Zeck & Fromherz, 2003). It is a logical consequence that a narrower cleft results in a larger seal resistance and accordingly the minimization of cell/substrate distance by mean of chemical functionalization has been a common strategy to enable intracellular access. An illustrative example of this approach is the internalization of micrometer sized gold protrusion functionalized with RGD peptides by Aplysia neurons (Spira et al., 2007). Such strategies have led to state-of-art intracellular electrophysiological measurement by MEA (Hai et al., 2010). Furthermore, others have rationalized these findings by modeling the penetration of the cell plasma membrane by vertical nanowires and concluded that adhesion forces are pivotal to enable intracellular access (Xie et al., 2013). In this context, a methodology that would enable the assessment of chemical functionalization impact on seal resistance in a quantitative, high-throughput manner is highly desirable.

Our results for HEK cells on NVs are in close agreement with the $10\,M\Omega$ seal resistance reported for HEK cells cultured on planar substrate as assessed by fluorescence imaging of a voltage-sensitive fluorescent dye (Braun & Fromherz, 2004). This suggests that the NV doesn't raise the seal resistance significantly compared to a planar substrate in the case of HEK cells. On the other hand, our previous results with cardiomyocytes in which intracellular action potential were measured allowed for an estimation of the seal resistance around $300\,M\Omega$ (Desbiolles, de

Coulon, et al., 2020). This discrepancy between cardiomyocytes and HEK cells highlights the importance of another factor on seal resistance: the interplay between the probe's geometry and the stiffness of the cells. As discussed in another research study (Xie et al., 2013), cells with stiffer plasma membranes (*i.e.*, larger Young modulus) need taller nanostructures with a larger pitch between nanostructures to bring the same amount of membrane deformation as for a cell with a plasma membrane of lower Young modulus. Although the Young modulus of HEK and primary cardiomyocytes plasma membranes are unknown, one can consider a related parameter: the overall cell stiffness calculated from indentation experiment which suggests that HEK cells are stiffer than cardiomyocytes derived from human-induced pluripotent stem cells (5-7.5 kPa vs 1 kPa respectively) (Pires et al., 2019; P.-C. Zhang et al., 2001).

This comparison supports our observation of lower seal resistance for HEK cells compared to cardiomyocytes when cultured on NV and suggests that the NV geometry is not well adapted to interface HEK cells (with the aim of establishing intracellular access). Our previous work with NVs fabricated on an AFM tip is in agreement with this conclusion as the impedance of a NV engaged on adherent cells resulted in larger impedance increase for cardiomyocytes than for HEK cells (Desbiolles, Hannebelle, et al., 2020). Since in this study the NV was brought into contact with the cell, the contribution of adhesion forces can be ruled out and hence the difference of seal resistance must arise from physicochemical properties of the plasma membrane being different for different cell types. Finally, we note that others have reported seal resistance of HEK cells on vertical nanowires in the range of 100 to 500 MΩ for nanowires with diameters of 150 nm and 3 μm in height (Robinson et al., 2012). Consequently, we conclude that an optimization of the probe geometry is desired on a cell type basis for best performance.

2.3.3   Variation of the nanovolcano geometry

The most notable difference in seal resistance is observed for NV with very short wall height or no wall at all (Figure 2.4, B, vi). From this result, we conclude that the NV wall results in an increased average value of seal resistance and narrower distribution around the mean. Unfortunately, none of the geometry considered could significantly improve the seal resistance as compared to the original NV design (Figure 2.4, B, i). While the seal resistance measured is on average slightly larger and the distribution narrower for smooth compared to rough NV wall, the difference is not significant (Figure 2.4, B, i vs ii). This suggests that contrary to the geometry investigated here, taller nanostructures with larger pitch are desired to better interface HEK cells.

2.3.4   Electrophysiology recordings from primary cortex neurons

A noteworthy feature of the extracellular recordings on the new generation of NV is that they mostly picked up signals from only one cell, sometimes two but never more. This situation is reminiscent of small electrodes of subcellular size that interface single cells. With such

electrodes however, the SNR of the EAPs are typically decreased due to a larger electrode impedance (Viswam et al., 2019) which was not the case with our large, buried electrodes. Furthermore, a given EAP was always registered by one electrode only (Supp. Figure 2.13) which is expected for arrays with large electrode-to-electrode pitch. These combined features made the analysis of EAP trivial with spike sorting only needed for a few channels and facilitated from having at most two candidates during classification (Supp. information Section 2.6.6 and Supp. Figure 2.14).

Although the median of EAP SNR and seal resistance are not statistically different across the NV geometries investigated, the distributions of EAP SNR for NVs with smooth walls, shorter heights and diameters have more outliers with large SNR (Figure 2.5, B; ii,iii and iv). This is also apparent from the averaged EAP waveforms for each cell (Supp. Figure 2.15) showing a prevalence of EAP with higher amplitude for smooth NVs and smooth NVs with shorter height and diameter. It thus seems that NVs with smooth walls and shorter height and diameter are preferred to interface primary mammalian neurons. We believe that this observation denotes the different regimes of adhesion a cell can undergo when covering a NV to different degrees. For a cell completely covering a nanostructure and contacting the substrate all around it, adhesion forces are expected to decrease cell/substrate distance leading to higher seal resistance. On the other hand, a cell covering a nanostructure may contact its surrounding substrate only partially which would result in asymmetrical loading of the plasma membrane and failure to induce membrane tension and deformation. According to this hypothesis, a strategy that would allow to position the cell optimally over the nanostructure should drastically improve seal resistance and EAP SNR.

The correlation between impedance and seal resistance in our data was better if considering only NV which recorded EAP SNR higher than 20 (Figure 2.5, D). This observations could be explained by some NVs being obstructed by cell debris while being covered at the same time by an active neuron. The presence of dead, yet substrate adhering, cell bodies/debris was routinely observed in our culture due to our use of frozen neurons which results in about 50% cell death after thawing and plating. In such case, the seal resistance may be high due to the debris and live cell above the NV while the EAP SNR would be decreased by the raised spreading resistance between the electrode and the live cell. Furthermore, the absence/presence of glial cells should be ascertained through immunostaining as 2D neuronal cell culture often spontaneously organize as carpet of glial cells on top of which neurons reside (Limongi et al., 2013). In our experiments we tried to limit the presence of glial cells by using only pre-natal neurons from the cortex of embryo sacrificed at the 18 days of development at which time differentiation of neural progenitors to glial cells has yet to begin. Based on these two plausible explanations, it could be argued that only NVs registering EAP whose SNR are above a certain threshold represent truly the scenario of interest: a neuron in direct contact with a NV. This hypothesis should be ascertained with live/dead staining and immunostaining of glial and neuronal markers (*e.g.*, glial fibrillary acidic protein and microtubule-associated protein 2 respectively).

Still, the method presented here allowed us to resolve seal resistance with ease, at large throughput and without harm to the cell, which is the main object of this study and should allow incremental optimization procedures for electrophysiology.

2.4   Conclusion

In this study we presented a novel approach for the characterization of cell/probe interfaces. We demonstrated that the measurement of the seal resistance through impedance spectroscopy captures well the degree of coupling between cell and nanostructures. Furthermore, this measurement correlates well with the quality of electrophysiological recording. The measurement is able to resolve physiologically relevant patterns in cell/substrate adhesion even for very low values of the seal resistance (down to fractions of MΩ).

The data obtained show the critical role of chemical functionalization for the establishment of a tight cell/probe interface. On the other hand, the impact of the various probe geometries investigated so far resulted in modulations of the seal resistance of lower magnitude. Taken together these observations suggest that adhesion processes are more potent than topography-induced membrane deformation although a more exhaustive range of probe geometries should be considered to ascertain this conclusion.

In a broader perspective, the new implementation of NV described were characterized by better quality of electrophysiological recordings in terms of noise and SNR due to their decreased impedance. Furthermore, we discovered that the new NV configuration with the electrode buried within the insulating substrate results in electrophysiological recordings that are fairly robust to background activity originating from distant neurons. Together with the discussed possibility of measuring access resistance after permeabilization of the cell membrane, this truly single-cell framework could foster the development of bi-directional measurement methods. In such methods, the coupling of the cell to the underlying electrode could be assessed in term of seal and access resistance during concomitant electrophysiological recording. These readouts could be used to i) maintain a consistent access resistance (*e.g.,* by applying electroporation when the access resistance falls below a set threshold) and ii) correct the registered signal for signal attenuation at the cell/electrode interface on a cell-to-cell basis.

A critical advantage of the decoupled electrode and nanostructure configuration as we used in this study is the resulting ability to alter the nanostructure alone over an arbitrary range of dimension while maintaining unaffected electrodes properties. This feature is broadly appealing since other nanostructures developed by other investigators (*e.g.,* nanotube, nanostraw, nanopore) could be fabricated on top of the buried electrode in a straightforward fashion. The use of a cell positioning strategy (*e.g.,* dielectrophoresis (Zhou et al., 2015), chemical patterning (X. Liu et al., 2011) or nanotopgraphy (M. Huang et al., 2018) could further improve the throughput of our method.

In conclusion, the impedance sensing of the electrode/cell interface described in this study

constitutes a significant step toward the systematic and rational optimization of micro- nano-electrodes for intracellular electrophysiology. Yet, we suggest that this measurement modality is not constrained to the characterization/optimization of probes dedicated to electrophysiology but is also appealing for the development of new cell adhesion factors, fundamental investigations of cellular mechanosensing and toxicology studies.

2.5   Materials and Methods

2.5.1   Fabrication of the device

The fabrication process flow is depicted step by step in the supplementary materials (Figure 2.6). Before starting the process, fused silica substrates are cleaned in two consecutive piranha baths (three part sulfuric acid 97% one part 30% hydrogen peroxide) for 5 min each followed by thorough rinsing in two consecutive ultra-pure deionized water (DIW) bath before spin-drying. In step A) a stack of thin metal layers consisting of Ti/Pt with thickness 10/240 nm is evaporated using an EVA760 (Alliance Concept, France) e-beam evaporator. In step B) the ring electrodes, leads and contact pads are patterned in the metal layers.This is achieved by spin-coating the substrate with a 600 nm thick AZ ECI 3007 i-line photoresist (MicroChemicals, Germany) with an ACS Gen 3 automated spin-coater (Süss MicroTec, Germany). The desired pattern is then exposed using a MA6GEN3 mask aligner (Süss MicroTec, Germany) in i-line mode (365 nm) with a dose of 165 mJ/cm^2 and developed with the same automated coater starting with a 60 s post-exposure bake with a proximity of 100μm to a hotplate set to 110°C , cooling down for 15 s on a cool plate and subsequent development in AZ MIF726 developer with a total contact time of 27 s. Before etching the resist is reflown by direct contact with a Sawatec HP200 hot plate (Sawatec, Switzerland) set to 125°C for 60 s. The metal layer is then etched using Ar$^+$ ion bombardment using a IBE350 (Veeco, USA) set to 500 V acceleration voltage, 800 mA beam current and with a stage tilt with respect to the incident beam of -30°. The stage tilt during etching is used to limit redeposition of the etched material on the photoresist sidewalls which would result in fences. The etching is monitored using an integrated secondary ion mass spectrometer (SIMS) and stopped 10 s after the appearance of the silicon signal originating from etching of the fused silica substrate. The photoresist is then removed thoroughly by subjecting the substrate to a long oxygen plasma etching at 500 W with an oxygen flow of 400 mL/min for 7 min using a TePla 300 microwave plasma system (PVA TePla, USA). When stripping the resist in this manner the wafers were positioned vertically using a quartz holder. In step C) a 2μm thick layer of polyimide is spin coated and cured before plasma enhanced chemical vapor deposition (PECVD) of a layer of silicon carbide and silicon dioxide. Before polyimide coating, the substrates were dehydrated for 10 min in a convection oven set at 150°C. A quick oxygen plasma with the same parameter as in step A) was applied to remove any organic contaminants. The substrate were then immediately spin coated (WS-650,Laurell Technologies, USA) by manual dispensing of 3 mL over static substrate with a solution of aminopropyl triethoxysilane silane (VM-652 adhesion promoter; HD Microsystems, USA) before spinning for 30 s at 3000 RPM under nitrogen stream. PI2610

polyimide (HD Microsystems, USA) was spin coated (LSM-200; Sawatech, Switzerland) at 3000 RPM for 40s to obtain a final thickness (after curing and hard bake) of 2μm. After spin coating the polyimide was cured by direct contact of the substrates with a hotplate (HP-401Z, Sawatech, Switzerland) at 65°C for 3 min and 105°C for 3 min. The polyimide was hard baked in a convection oven (T6060; Heraeus, Germany) for 1 hour at 300°C under nitrogen atmosphere above 200°C. Before the PECVD deposition the substrates were exposed to a mild oxygen plasma 100 W with an oxygen flow of 400 mL/min for 1 min to roughen the polyimide surface in order to improve adhesion. Robust adhesion of the silicon based dielectric to polyimide is critical to the final device stability especially for experiments involving weeks-long cell cultures in aqueous saline conditions. A thin adhesion layer of silicon carbide was thus deposited (35 nm; chamber pressure of 1000 mTorr, gaz flow of 750 sccm of 2% SiH4 in Ar and 70 sccm of CH4, 20 Watts RF) before silicon dioxide (320 nm; chamber pressure of 1000 mTorr, gaz flow of 400 sccm of 2% SiH4 in N2 and 710 sccm of N2O, 20 Watts RF) using a Oxford Plasmalab System 100 (Oxford Instruments, UK) with a with deposition chamber temperature set to 300°C. In step D) the NVs are defined as described previously (Desbiolles, de Coulon, et al., 2019). A 2μm thick layer of AznLoF2020 photoresist (MicroChemicals, Germany) is spin coated and 2.25μm diameter openings are defined by exposure with a VPG200 direct laser writer (Heidelberg, Germany) with a 355 nm UV light dose ranging from 9 to 15 mJ/cm^2 depending on the nanovolcano geometry. To obtain photoresist straight wall, the manufacturer exposure dose recommendation for a 2 μm thick layer of AznLoF2020 is 80 mJ/cm^2 but we found that optimal values to obtain the desired pattern lateral dimension were significantly different on glass substrate as well as dependent on the pattern dimension. Thereby the exposure dose used in this step should be optimized on a substrate/design basis. The post-exposure bake is conducted at 110°C with 100μm proximity gap for 75 s followed by 51 s contact time development with AZ MIF726. The substrates are then subjected to ion beam etching as described above but with 0° incidence angle. Etching is stopped 2 min after the disappearance of the silicon signal on the SIMS detector. The photoresist is removed and the cavity below the NV is formed with oxygen plasma as described in step B) except that the wafer was lying flat in the chamber (for better homogeneity) and that the etching time was prolonged for a total duration of 20 min or until the under-etching of the polyimide reached a diameter of 20μm. SEM images were acquired using a Merlin SEM (Zeiss, Germany) with an extraction voltage of 1.5 kV and a beam current of 30 pA and a secondary-electron detector. The wafers were diced on a DAD321 (Disco, Germany) with a resinoid blade of 70μm width under 25000 RPM rotation moving at 1 mm/s from the top side of the wafer. A glass O-ring was glued on top of the individual chips using PDMS and cured overnight at 60°C in a convection oven.

2.5.2 Electrodeposition of PEDOT:PSS

Electrodeposition was performed from a filtered aqueous solution of 20 mM 3,4-ethylene dioxythiophene (EDOT, 483028; Merck, USA) and 1 wt % poly(sodium 4-styrenesulfonate) of molecular weight 70,000 g/mol (PSS, 243051; Merck). The electrodeposition was performed according to the protocol developed by others (Rothe et al., 2017). The devices were first

cleaned with a 3 min oxygen plasma (100 W, 650 mTorr; Diener Electronic, Germany) followed by immediate filling of the culture chamber with pure ethanol to ensure proper wetting of the inside of the NVs. The culture chamber content was then exchanged with deionized water (DIW) 6 times making sure to each time leave a thin layer of water in order to keep the cavity below the NV filled with liquid. DIW was then exchanged two times with the EDOT:PSS solution and the device was connected to a Stat.h bipotentiostat (Ivium, The Netherlands) in a three electrode configuration. We used a silver-silver chloride electrode in saturated NaCl (MF-2052; BASI, USA) as a reference electrode and a platinum wire as a counter electrode. Electrodeposition was achieved by chronoamperometry, alternating between 0.23 V and 1.05 V for 800 ms and 200 ms respectively and total number of cycles between 400 and 600 depending on the NV geometry. The process was monitored under an optical microscope and stopped when the ring electrode enlargement left a transparent circular surface area of diameter 7μm. The culture chamber content was finally exchanged with deionized water (DIW) 6 times.

2.5.3 Cell culture

During all liquid exchange of the cell culture chamber a thin layer of liquid was always left in order to prevent the cavities below the NVs to fill with air. In some cases, the devices were functionalized with adhesion promoters before cell pating. When PDL (A-003-E; Merck) was used an aqueous solution of 500μg/mL was incubated over the device at room temperature (RT) for 2 hours before rinsing with DIW 3 times and cell plating. If and additional adhesion promoter was used, the PDL functionalization was carried out on the day before plating in the same way and followed with overnight incubation at 4°C with either collagen reconstituted in aqueous acetic acid 2% (v/v) at 100μg/mL (11179179001; Roche, Switzerland) or laminin at 100μg/mL in PBS (10010023; ThermoFisher, USA). In both cases, the adhesion promoter solutions were washed off with three rinsing with PBS before cell plating. HEK cells (CRL-1573) were obtained from ATCC. All experiments with HEK cells correspond to culture between passage 5 and 15. HEK cells were kept in DMEM supplemented with Glutamax (10566016, ThermoFisher), 10% fetal bovine serum (F9665, Merck) and 0.4% penicillin/streptomycin (P4333, Merck) solution within a 37°C incubator under 5% CO2 and 100% humidity atmosphere. Before plating, a 80% confluent culture was collected by trypsinization (1084440001, Merck) for 5mn at 37°C followed by mechanical dislodgement by repetitive pipette dispensing over the cells. Cells were centrifuged 2 min at 0.3 RCF and resuspended in culture medium after the supernatant was discarded. We plated 30000 cells per chip (0.95 cm^2) and conducted experiments 24h after passaging unless stated otherwise. Primary rat cortex neurons from day 18 embryo (A36511, ThermoFisher) were received frozen, thawed for 2 min in a 37°C water bath and diluted slowly in Neurobasal cell culture media (A3582901, ThermoFisher) in order to avoid osmotic shock. We found that centrifugation of the cell solution to remove the freezing solvent resulted in higher viability thus the cells were spun at 0.3 RCF for 2 min. The supernatant was discarded and the cells resuspended in Neurobasal supplemented with 100X Glutamax (35050061, ThermoFisher), B27 supplement (A3582801, ThermoFisher) and 0.4% penicillin/streptomycin (P4333, Merck). 200 000 cells were plated per chip (0.28 cm^2)

unless specified otherwise. Half of the culture medium was exchanged every second day and experiments were performed on the 14 day after plating.

2.5.4 Electrochemical impedance spectroscopy and seal resistance measurement

Electrochemical impedance spectroscopy (EIS) was performed with a Stat.h bipotentiostat (Ivium, The Netherlands) in a three electrode configuration. We used a silver-silver chloride pellet (E205; Multichannel Systems, Germany) as a reference electrode and a platinum wire as a counter electrode. The impedance spectrum was acquired from 200 kHz to 1 Hz (100 mHz for characterization of the electrode) under sinusoidal excitation waveform of 10 mVrms and 0 V DC bias. The application of a fixed DC bias rather than the open circuit potential is preferable as different levels of the conductive polymer oxidation can result in different bulk capacitance. The measurement was performed within a faraday cage to limit electromagnetic noise interference. From the impedance spectrum the seal resistance was extracted from one of the two following approaches. The seal resistance was obtained from finding the point of minimum phase across the spectrum. For the NV presented in this study this corresponded to frequency typically between 10 Hz and 1 kHz. The real part of the impedance was averaged over a decade around that frequency and this metric was subtracted from the same value obtained from NVs not covered by any cell to obtain the seal resistance. Alternatively, an equivalent lumped element circuit model was fitted to the experimental impedance spectrum from which the seal resistance was obtained. Both approaches are depicted and compared in the supplementary information Supp. Figure 2.9.

2.5.5 Electrophysiology recordings and analysis

Before recordings, the cell culture medium was exchanged for recording buffer (in mM; 125 NaCl, 5.5 KCl, 1.8 CaCl2, 0.8 MgCl2, 20 HEPES, 24 glucose, and 36 sucrose at pH 7.3, osmolarity adjusted to 315 mOsm with sucrose). The device was interfaced with a custom PCB and placed within an incubator set to a temperature of 37°C. CO2 perfusion was not necessary with our recording solution buffered with HEPES. The recording amplifier used was a HS-36 headstage (1 TΩ, 2 pF input impedance) connected to a Digital Lynx SX acquisition system (Neuralynx, USA). The signal ground of the amplifier was connected to a silver-silver chloride pellet immersed in the cell culture bath and the chassi ground of the amplifier was connected to the inner metal lining of the incubator. Spontaneous neuronal activity was sampled at 32 kHz over a range of ± 10 mV. The signal was bandpass filtered between 1 and 5000 Hz for visualization and 300 and 3000 Hz for spike analysis. Spikes were extracted from the filtered signal given that their maximum absolute voltage reached was superior to 2.3 times the value of the median absolute deviation for that particular channel. In most recordings, the median absolute deviation was close to 10µV. The SNR was calculated as the absolute of the ratio of spike peak voltage to the value of the median mean deviation for that channel.

2.6 Supplementary Materials

2.6.1 Comparison to previous nanovolcanoes generation for seal resistance measurements

The ability of resolving difference of seal resistance through impedance spectroscopy as presented in this study was modeled with an equivalent circuit of the cell/NV interface (Supp. Figure 2.17). Specifically, we looked at the ability of the new and former NVs ability to i) resolve minute change of the seal resistance and ii) the dependence of the measured signal on properties of the cell membrane in contact with the NV. We first conclude that although theoretically possible, the measurement of seal resistance with the previous implementation of NV necessitates rigorous fitting given that the impedance spectrum shape changes markedly for modest increase in seal. This is in opposition to the new NV presented in this study whose impedance spectrum keeps the same shape while being merely scaled up by increasing sealing resistance allowing for easy and unambiguous assessment. Still, the application of the previous generation of NV to seal measurement is further impaired by the impact of the nearby cell membrane capacitance. Because of the large impedance of the previous NV, the measurement would need to be taken at higher frequencies (10-100 kHz). Although the capacitance of the portion of cell membrane in contact/close proximity of the electrode is very small (in the range of fraction of picofarads), the use of such high frequencies results in shunting of the seal resistance by capacitive current through the cell. This poses a significant problem considering that the impedance of this portion of membrane may vary from cell to cell and for different experimental conditions thereby resulting in the same sealing resistance yielding a different impedance spectrum. In comparison, seal measurements with the NVs presented in this study are insensitive to the nearby cell membrane impedance owing to the decreased electrode that allows measurements over lower frequencies range (typically 0.01-1 kHz).

2.6.2 Comparison of nanovolcanoes noise levels

We compared the performance of the new NV with respect to their original implementation in terms of noise and seal resistance measurement capability. The noise amplitude spectral density (ASD) was inferred from the thermal noise of NVs using the real part of the impedance spectrum according to the following formula: $R_{thermal} = \sqrt{4kT\Re(Z_{elec})f}$ (Supp. Figure 2.18). The root-mean-square value of the noise in bandwidths relevant to electrophysiology reveals that the NV presented in this study are superior with a 1.03 against 9.88μVrms previously for a 1-300 Hz bandwidth relevant to slow electrophysiological processes (*(e.g.)*, synaptic inputs, membrane oscillation) and 8.72 and 12.06 μVrms over a 0.3-5 kHz bandwidth relevant to action potentials.

2.6.3 Opportunity for access resistance measurements

The conclusion of this comparison is thus that the NV presented in this study are mostly insensitive to the capacitance of the cell over the frequency range of the measurement. Interestingly, it follows that since little capacitive current will flow through an intact cell membrane there should be a large, easily readable change after permeabilization of the membrane; for example with electroporation. Since most probes described in the literature relies on some form of membrane perforation technique (*(e.g.*), electro- (Lin et al., 2014; Robinson et al., 2012),(Lin et al., 2014; Robinson et al., 2012) opto- poration (Dipalo et al., 2017)) of the cell membrane to establish intracellular contact, it would be highly beneficial to be able to measure the resistance of the patch of membrane itself (*(i.e.*), access resistance). Since the flow of current through the cell is necessarily shunted by the seal resistance it follows that access resistance can only be measured given they are on the same order of magnitude as the seal resistance. Values reported for the junctional cell membrane resistance, the portion of cell membrane interface by the probe, are typically in the order of 100 $G\Omega$ (Ojovan et al., 2015) for an intact membrane and a few hundreds of $M\Omega$ for an electroporated membrane (Lin et al., 2014; Robinson et al., 2012). According to our simulations based on the equivalent circuit depicted in Supp. Figure 2.19, it is reasonable that access resistance of a few GOhm can be resolved with the NV described in this study. This could open up a promising bi-directional framework where the access resistance is controlled, *(e.g.*), by re-applying electroporation when its value falls below a certain set point due to membrane resealing, meanwhile an intracellular electrophysiological signal is recorded and corrected for the amplitude drop/temporal deformation resulting from access resistance and cell/probe interface characteristics.

2.6.4 Equivalent circuit model and defining equations of the electrode and nano-volcano

The equivalent circuit model is characterized by the following elements. The finite-length Warburg element represents the diffusion resistance of cations through the polymer film according to equation 2.1:

$$Z_{warburg} = \frac{(\frac{\tau_D}{C_D})coth(j\omega\tau_D)^{1/2}}{(j\omega\tau_D)^{1/2}} \tag{2.1}$$

Where D is the diffusional time constant, C_D the diffusional pseudocapacitance. The ratio of τ_D/C_D defines a diffusional resistance R_D associated with cations diffusion from the polymer/electrolyte interface into/out of the polymer film as the polymer changes its oxidation (doping) state. This impedance element is named differently (finite space Warburg, open Warburg element, finite-length Warburg with reflective boundary) in different researche articles/textbook/fitting software. Here we consider the case of a diffusional impedance arising from the diffusion of cations through a nanoporous material (*i.e.*, the polymer layer) that is terminated by a reflective boundary (*i.e.*, the noble metal electrode). This gives rise to the $coth$ function which replaces the $tanh$ function used in the case of a transmissive boundary.

Equation 2.1 is also often expressed in terms of admittance Y_0 which is the admittance at an angular frequency of 1 (rad/s) and a characteristic time $B = \frac{\delta}{\sqrt{D}}$.

The constant phase element is defined by equation 2.2):

$$Z_{CPE} = \frac{1}{C_b(j\omega)^n} \tag{2.2}$$

Where C_b is the bulk electronic capacitance (unit of s^n/Ω hence not a capacitance in the traditional sense) and n is the phase constant parameter. In their modeling of electrodeposited PEDOT:PSS film, (Cui & Martin, 2003) used a capacitor instead of a phase element as we did here. The phase angle of our Pt/PEDOT:PSS electrodes impedance at low frequencies deviated significantly from that of a pure capacitor an we found that a constant phase element resulted in significantly better fit. Although the fitting of the low frequency end of the impedance spectrum had little effect on the accuracy of the spreading resistance fitting (the parameter of interest), we report here on the improved agreement of our model and experimental data using a constant phase element. We hypothesize that this deviation from the model of (Cui & Martin, 2003) may arise from different packing level of the polymer originating from different electrodeposition condition. Constant phase elements are traditionally associated with roughness or fractality of the electrode as proposed by (Mulder et al., 1990). Another possible explanation could be thickness or composition variation of the polymer film as discussed by (Schiller & Strunz, 2001)

The impedance associated with C_{stray} is defined by equation 2.3:

$$Z_{stray} = \frac{1}{j\omega C_{stray}} \tag{2.3}$$

The stray capacitance was dominated by our PCB stray capacitance since the stray capacitance of the electrodes leads on the chip was only 0.24 pF. When performing electrophysiology measurement we used a different high impedance PCB to prevent signal attenuation from the stray capacitance (Desbiolles, de Coulon, et al., 2020).

Hence the total impedance is as in equation 2.4):

$$Z_{total} = \frac{Z_{stray}(Z_w + Z_{CPE} + Z_{spread})}{Z_{stray} + Z_w + Z_{CPE} + Z_{spread}} \tag{2.4}$$

2.6.5 Equivalent circuit model and defining equations of the cell-covered electrode and nanovolcano

The equivalent circuit model is characterized by the following elements. The junctional and non-junctional cell impedance are defined following equation 2.5 and 2.6 respectively:

$$Z_{junctional} = \frac{R_j (1/j\omega C_j)}{R_j + (1/j\omega C_j)} \tag{2.5}$$

$$Z_{non-junctional} = \frac{R_{nj} (1/j\omega C_{nj})}{R_{nj} + (1/j\omega C_{nj})} \tag{2.6}$$

R_{nj}, C_{nj}, R_j and C_j were taken as 100 MΩ, 30 pF(Robinson et al., 2012), 100 GΩ and 0.1 pF (from a specific capacitance of 1 μF/cm^2 and surface area of 12.6 μm^2 corresponding to the NV inner surface area). All other components are as in supplementary Section 2.6.4 and Figure 2.8. The new total impedance is given by equation 2.7:

$$Z_{total} = \frac{Z_{stray}(Z_w + Z_{CPE} + R_{spread} \frac{R_{seal}(Z_j + Z_{nj})}{R_{seal} + Z_j + Z_{nj}})}{Z_{stray} + Z_w + Z_{CPE} + R_{spread} \frac{R_{seal}(Z_j + Z_{nj})}{R_{seal} + Z_j + Z_{nj}}} \tag{2.7}$$

2.6.6 Analysis of channels registering action potentials from more than one cell

Most electrodes in our data registered extracellular action potentials (EAP) from only one cell. In some rare cases some channels picked up signals from two different cells. The process of classifying EAPs as originating from different cells is called spike sorting and is a well studied problem that grows increasingly difficult with the number of units (*(i.e.)*, firing cells) registered by a single electrode. In our recordings, classification of channels detecting several units was however relatively easy because those channels picked up spikes from at most two cells. Such a channel is displayed in supplementary Figure 9. Spike sorting was achieved with a minimalistic strategy that was yet good enough to cluster spikes belonging to different units effectively. The collection of spikes from the considered channel was normalized and subjected to principal component analysis. Classification was performed by k-means clustering by taking only the first two principal components where the number of clusters was adjusted manually by the user. Although one of the cells in the data presented in supp. Figure 2.14 is bursting frequently, the family of classified spikes show a satisfactory homogeneity. We believe the reason that we rarely observe channels with two units and no channels with three or more units is a consequence of the burrowed electrode configuration of our multi-electrode array (MEA). In a traditional planar MEA, the electrodes are on the same plane as the cells and typical register spikes originating from many units. It is known that smaller electrodes will pick up signals from fewer units than larger electrode which makes analysis easier and less error-prone but comes with the tradeoff of electrode with higher impedance and lower SNR (Harris et al., 2016; Viswam et al., 2019). The NV implementation presented in this study has the merit of
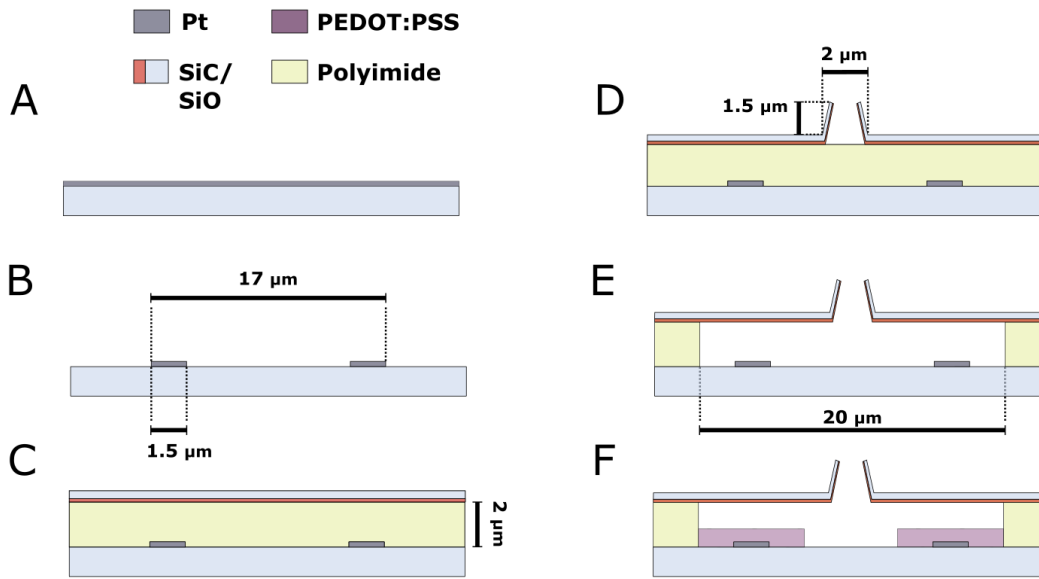
Figure 2.6: Nanovolcano fabrication process flow. See Materials and Methods for detailed description (A) Metal evaporation, (B) electrode and leads patterning, (C) polyimide spin-coating and curing followed by plasma enhanced chemical vapor deposition of silicon carbide + silicon dioxide, (D) patterning of nanovolcanoes and access holes to contact pads, (E) cavity etching by isotropic oxygen plasma, (F) electrodeposition of PEDOT:PSS.

having low impedance thanks to the large ring electrode surface area while maintaining a small footprint on the substrate plane resulting on interfacing by mostly one and at most two cells.
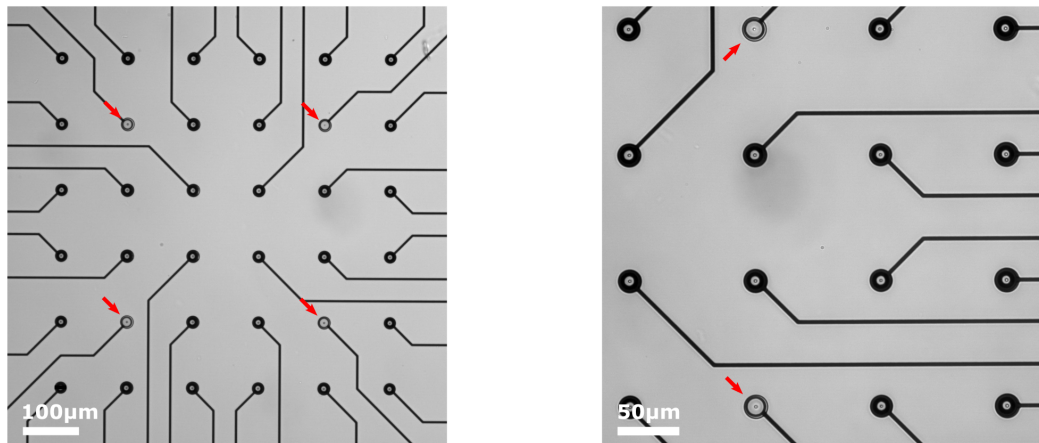
Figure 2.7: Optical micrograph of a portion of the multi-electrode array after electrodeposition of PEDOT:PSS. On the left and right image the red arrows indicate electrodes that were not deposited for comparison. During electrodeposition the ring shape of the electrode is seen to enlarge progressively until it covers most of the cavity as best visible on the magnified image (right). As can be seen the deposition homogeneity was very satisfactory with all 60 electrodes of the array covered in a similar way.
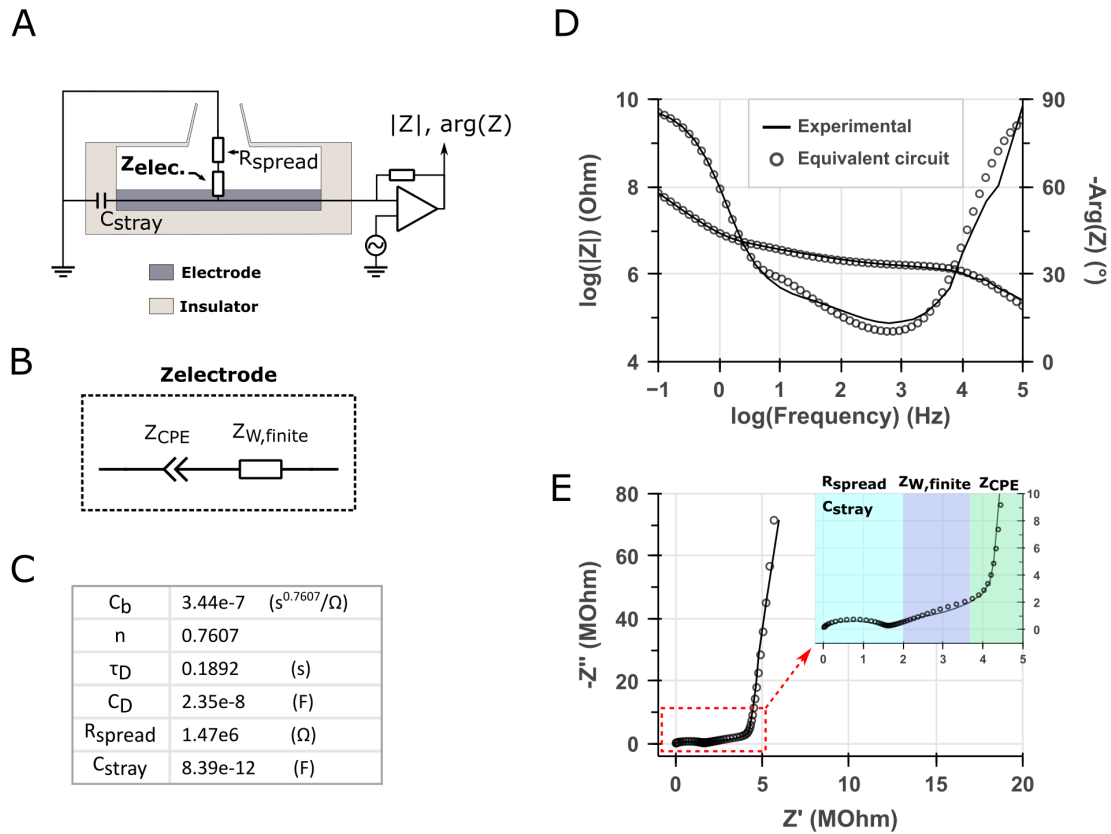
Figure 2.8: Equivalent circuit of the electrode/NV and modeling of the experimental impedance spectrum. (A) The electrode/NV was modeled as a two branch circuit composed of i) the electrode impedance $Z_{electrode}$ in series with the spreading resistance R_{spread} which is in parallel with ii) the stray capacitance of the electrode leads and printed circuit board tracks C_{stray}. (B) $Z_{electrode}$ the electrode impedance is modeled according to (Cui & Martin, 2003) as a finite-length Warburg element in series with a constant phase element. The equations for each elements and the total impedance are given above in the Supplementary information Section 2.6.4. (C) Fitted parameter using the model in (A). (D) Fitting the equivalent circuit model to the experimental results show a good agreement of our model as evidenced by the almost overlapping curve on the Bode and (E) Nyquist plots. A deviation was often apparent around 1 Hz which arises from the bulk capacitance rising faster than the finite Warburg impedance. In (E) the inset highlights the different regime of the impedance spectrum and the corresponding dominating circuit element over that frequency range.
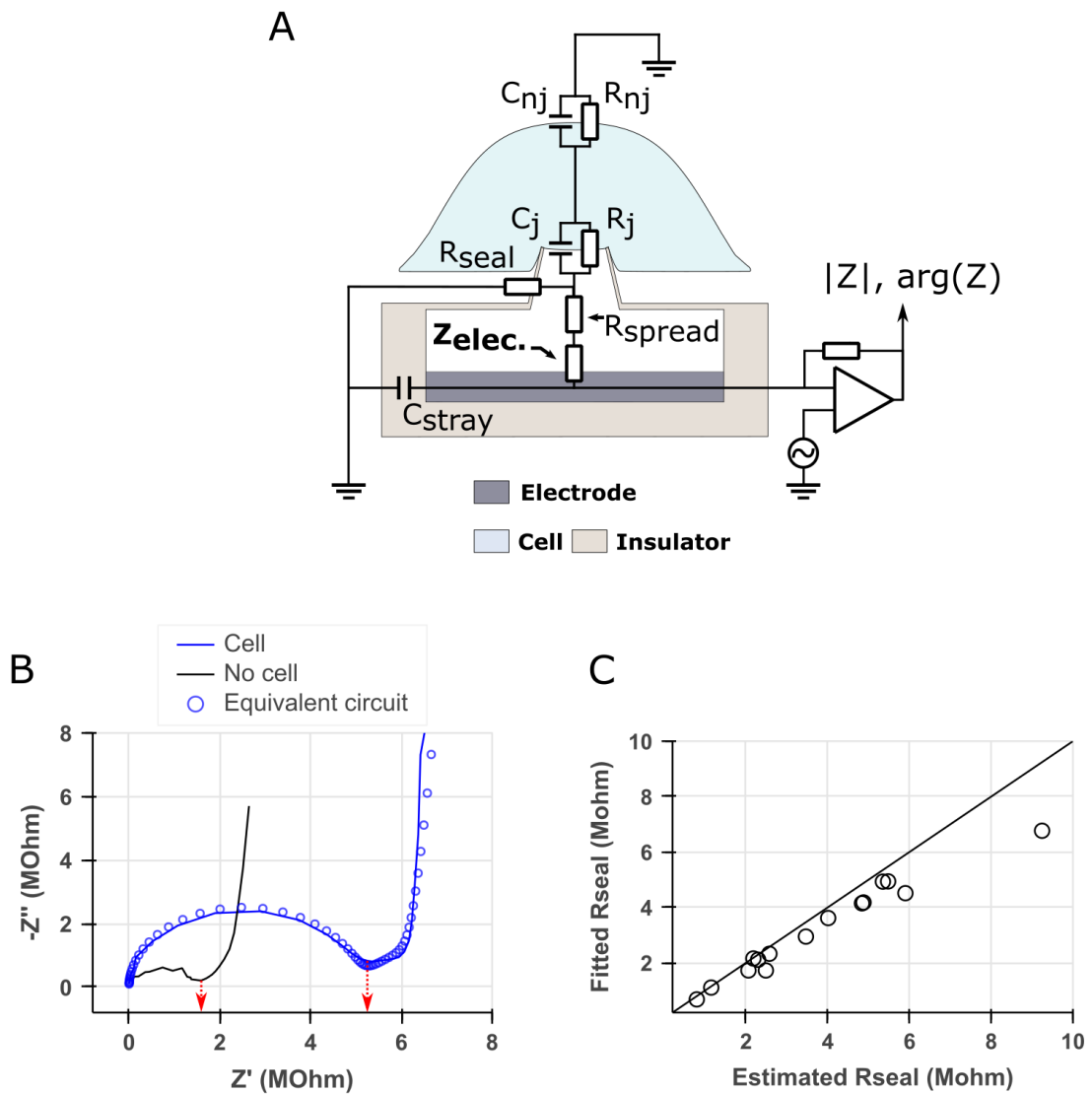
Figure 2.9: Estimation and fitting of the seal resistance. (A) An equivalent circuit model of the cell on top of the nanovolcano can be fitted to the experimental data to extract the sealing resistance. (B) Alternatively, sealresistance can be estimated from the impedance spectrum without fitting. The impedance spectrum of two NV is displayed on a Nyquist plot. One NV is covered by a HEK cell (confirmed by optical inspection). The difference across the spectra arises from the seal resistance added by the cell. The seal resistance can be estimated reliably by taking the difference of the projection of the spectra on the real axis at the point of minimum phase (highlighted by red arrows). (C) Comparison of the two methods. Seal resistances fitted or estimated as in (A) or (B) are similar as evidenced by a coefficient of determination $R^2 = 0.97$.
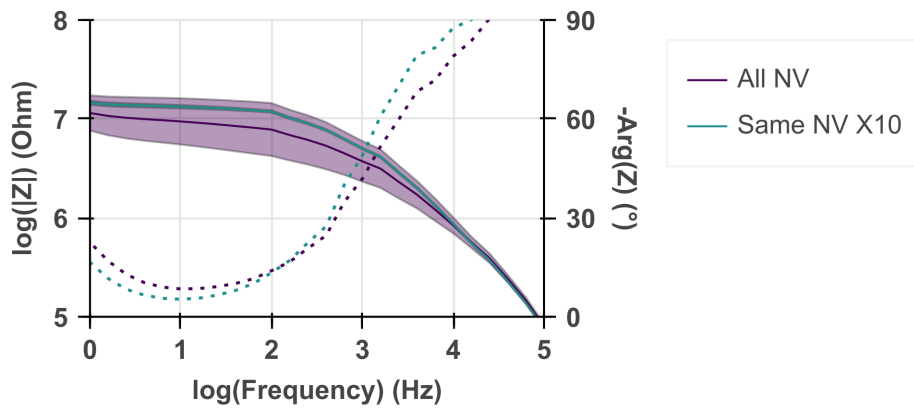
Figure 2.10: Noise in the measurement in comparison to variability of the data. The distribution of impedance spectra for human embryonic kidney cells (HEK) on NV is displayed as a bode plot in magnitude (solid line) and phase (dashed line). The distribution is displayed as a colored band of ± one time the sample standard deviation centered around the mean. In the legend, "All NV" refers to the distribution of spectra obtained from n=20 HEK cells whereas the "Same NV X10" corresponds to a single HEK cell whose impedance spectrum was measured ten times in a row. Accordingly, the precision of the measurement was good enough that the variability in samples of many cells arises from the distribution of seal resistance, not noise.
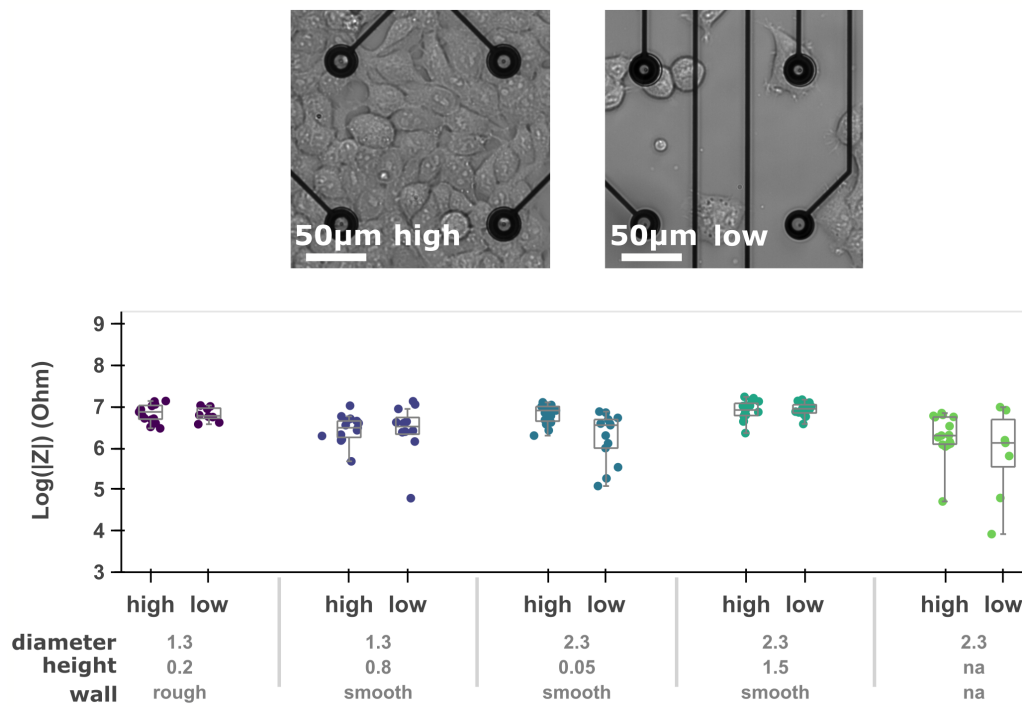
Figure 2.11: Effect of plating density on seal resistance measurement. Human embryonic kidney cells (HEK) were plated at different densities on NV of different geometries and allowed to attach to the substrate for 24h before measurement of the seal resistance. Although the seal resistances were rather similar in both cases, we noted a tendency for the seal resistance to be higher when measurement from dense cultures. We hypothesize that this arises from cells forming a continuous monolayer at higher densities in which case the seal resistance measured might represent the sealing resistance of several cells in series.
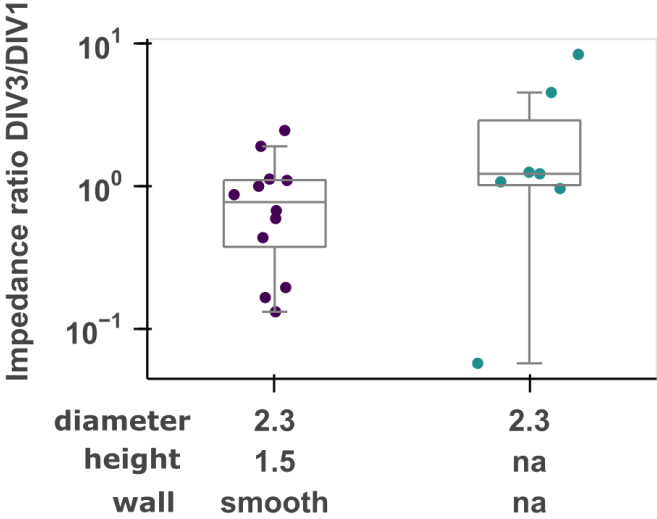
Figure 2.12: Effect of day post plating on seal measurement. HEK cells were plated on NV of different geometries and their sealing resistance was measured after 24h or 72h. The seal resistance of the same cells was found to vary by as much as 20 fold between those two time points. In consequence only seal measurements carried out in the same half-day were compared to one another in this study. This also highlights the need for a harmless, longitudinal measurement method as the value seal resistance is fluctuating along the culture lifespan.
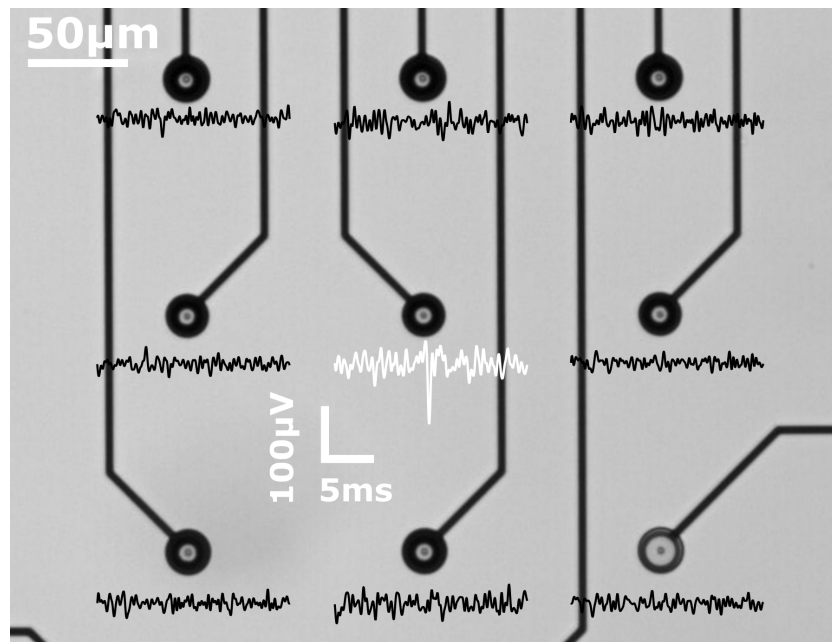
Figure 2.13: Parallel electrophysiological recordings of neighboring electrodes displayed on a dummy optical image of the electrode array. The recordings were obtained from a culture of primary rodent cortex neurons 14 days after plating. All signal traces correspond to the same time window. An extracellular action potential is registered on the center electrode but is not detected on neighboring electrodes. This is expected for multi-electrode arrays of pitch equal and above 100 μm (Harris et al., 2016) which makes analysis much easier given that action potentials emitted by a given cell are picked up by only one electrode at most.

A

B

C

D

E

F
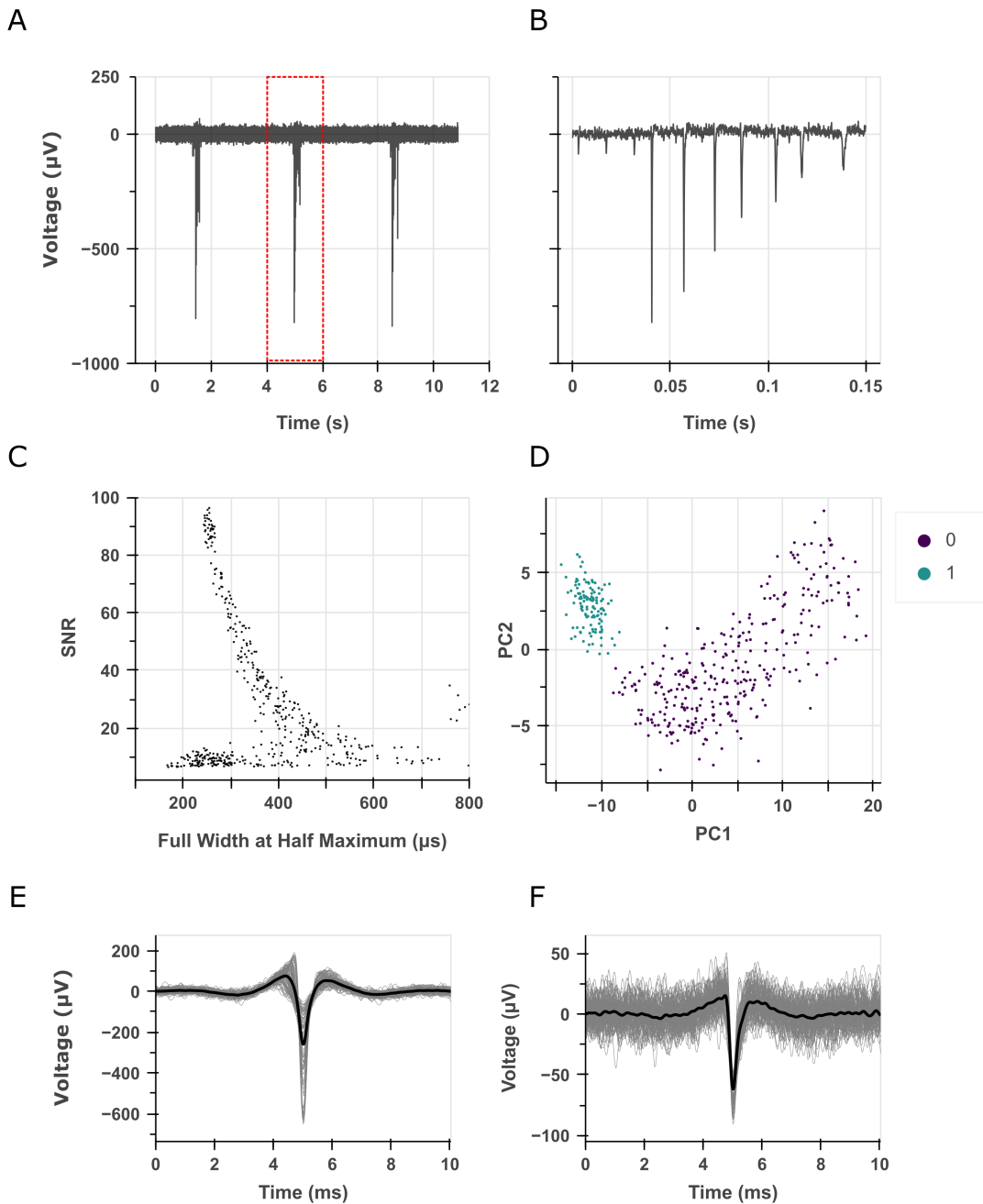
Figure 2.14: Analysis of channels with more than one unit (A) Electrophysiological trace showing extracellular action potentials (EAP) originating from two different cells, one of which is bursting frequently. (B) Magnified view of the dashed red box in (A). Spikes of less than 100 μV in amplitude from one cell are visible prior to the burst followed by the burst itself originating from another cell emitting several action potentials in a row of decreasing amplitude. Bursting cells can be difficult to analyze as the decreasing amplitude of the spikes can lead to misclassification and are typically met with complex analysis methods (Pouzat et al., 2004). In our data however, classification is easily achieved based on the large dissimilarity of the waveforms. (C) This dissimilarity is already obvious in the two dimensional space of spike SNR versus full width at half duration. (D) Following a simple analysis (see supplementary information section 2.6.6), spikes are readily classified by k-means clustering. (E) and (F) the corresponding classified waveforms show good intra-class homogeneity.
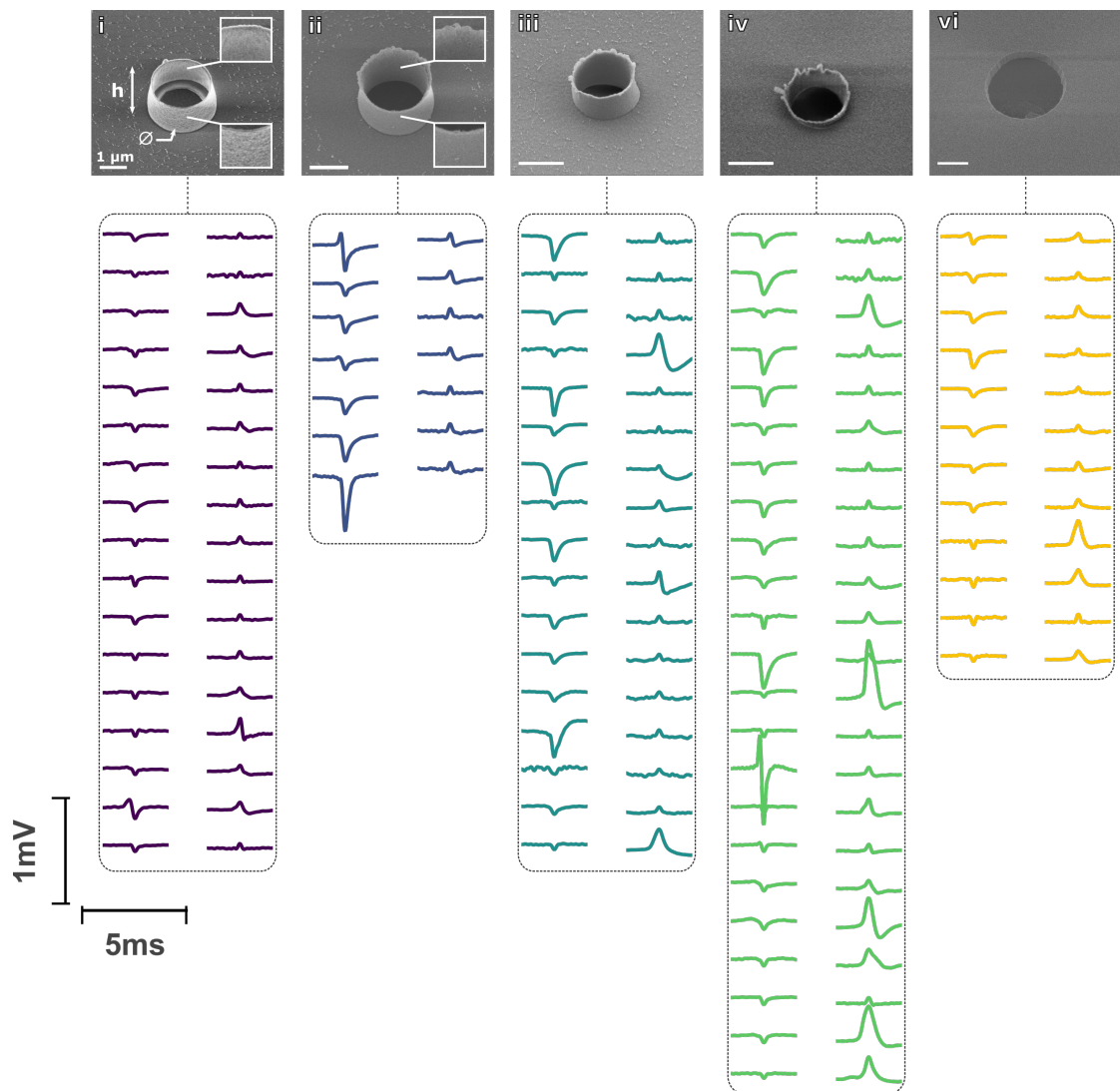
Figure 2.15: Averaged waveforms of spontaneous extracellular action potentials (EAP) registered at nanovolcanoes of different geometries from primary rat cortex neurons culture 16 days after plating. Traces sharing the same colour and enclosed within one box were obtained from cells cultured on NVs of the same geometry (displayed above the box). Each trace is the averaged EAP from a single recording site: the average of all the EAP measured from a single NV (100 EAPs minimum). NV geometries i, ii, iii, iv and vi are the same as depicted on figure 4. The averaged EAP were either monophasic hyperpolarization corresponding to EAP generated close to the soma, biphasic swings originating from axons and monophasic depolarization tentatively corresponding to attenuated intracellular action potentials.
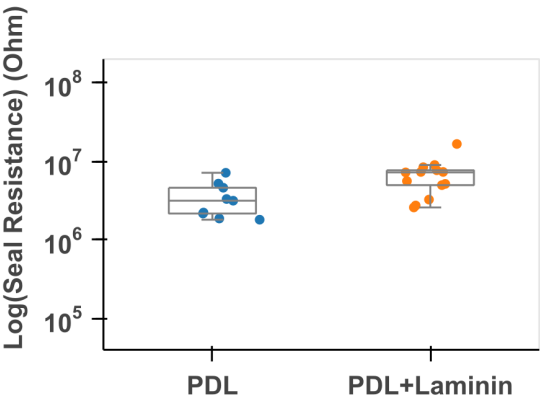
Figure 2.16: Impact of chemical functionalization on seal resistance for primary rat cortex neurons culture 16 days after plating. Neurons were plated on NV functionalized with either poly-D-Lysine (PDL) alone or with PDL and laminin sequentially. Neurons on PDL and laminin had a 2.3 times larger seal resistance compared to those plated on PDL alone (7.24 MΩ and 3.15 MΩ respectively).
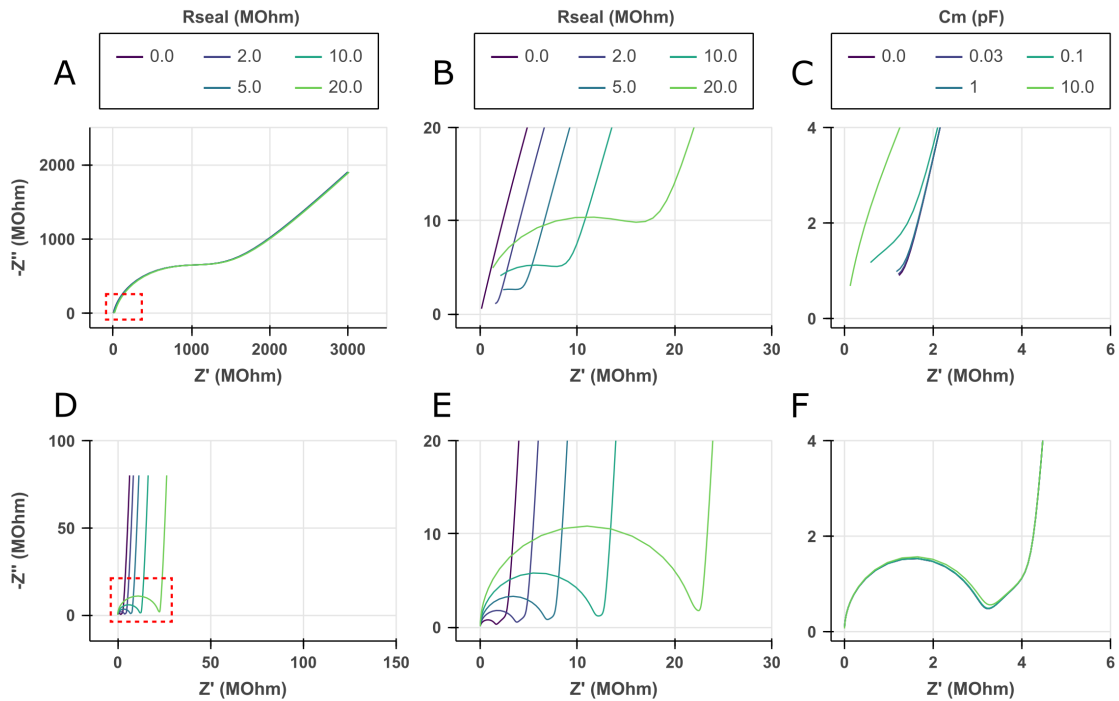
Figure 2.17: Comparison of the previous generation of NV (Desbiolles, de Coulon, et al., 2020) to the new NVs presented in this study for the measurement of seal resistance. (A) and (D) are simulated impedance spectra displayed on a Nyquist plot for increasing value of seal resistance. (A) Corresponds to the measurement performed with the previous generation of NV and (D) to the one presented in this study. The legend in (A) also apply for (D). The model used in this simulation is as in supplementary Figure 2.9. (B) and (E) are magnification of the dashed red box in (A) and (D) respectively. (C) and (F) are the impedance spectra simulated for a constant seal resistance of 1.5 MΩ but with varying junctional cell membrane capacitance for the previous and new generation of NV respectively. In the former case (C), the impedance spectrum is largely dependant on the exact value of the junctional membrane capacitance in the range of 30 fF (plasma membrane sitting flat on top of the NV), 100 fF (plasma membrane protruding inside the NV), 1 pF (partially porated plasma membrane by *(e.g.)*, electroporation) and 10 pF (perfectly disrupted plasma membrane; the resulting capacitance then corresponds to the non-junctional membrane capacitance). On the other hand, the spectrum simulated for the new generation of NV (F) is independent of the capacitance of the cell junctional area.
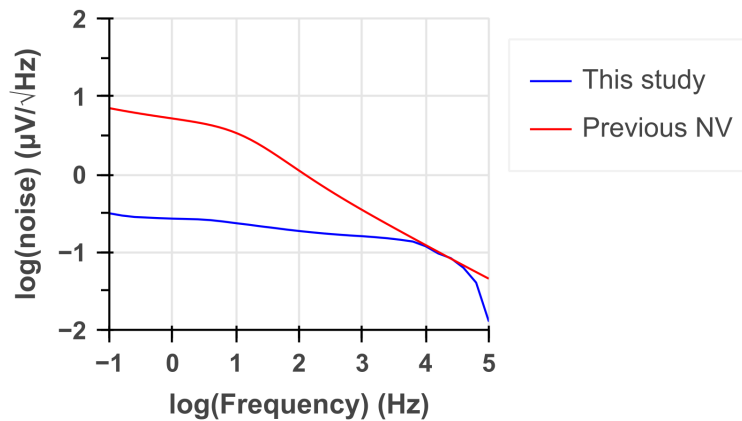
Figure 2.18: Inferred noise of the previous generation of NV (Desbiolles, de Coulon, et al., 2020) and the new NVs presented in this study. The inferred noise was obtained from the electrodes impedance spectrum as described in the supplementary information section 2.6.2.
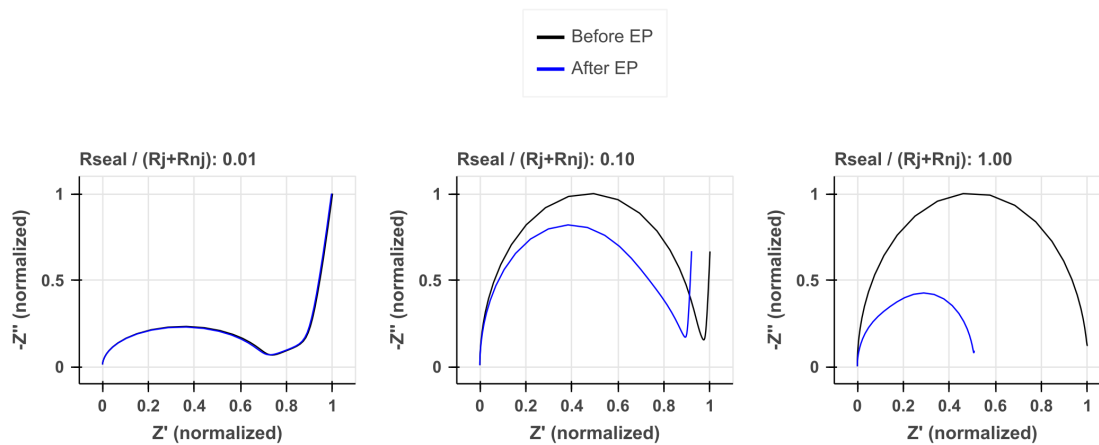
Figure 2.19: Simulation of the impedance spectrum before and after electroporation for increasing value of $\frac{R_{seal}}{R_j + R_{nj}}$. The model used in this simulation is as in supplementary Figure 2.9. The black and blue curves (before/after electroporation respectively) correspond to a junctional membrane resistance of 100 GΩ and 100 MΩ respectively with the later being a typical value reached after electroporation (Lin et al., 2014). For a seal resistance no less than one tenth that of the sum of junctional and non-junctional membrane resistance, the access resistance could be estimated from the decrease in the real part of the impedance at the point of minimum phase and a theoretical value of R_{nj}.

3 Design and implementation of a scalable intracellular electrochemical sensor

This chapter discuss the design and development of an electrochemical redox cycling sensor for the multi-site, longitudinal, intracellular measurement of neurotransmitter. As a proof-of-concept, the device developed was tested using whole cell lysate from catecholamine containing cell with success. The intracellular measurement of catecholamine was not yet achieved and should be the object of future work.

3.1   Introduction

Detection of small bio-molecules like glucose or neurotransmitters within single-cells is a difficult challenge characterized by the complex nature of the sample as well as minute sample volume. Advanced analytical methods for single-cell analysis include high performance liquid chromatography with electrochemical detection, mass spectrometry or co-localization fluorescence assay. Of course single-cell analysis is further complicated if longitudinal sampling is required: the sampling from the same cell along time which implies that the technique used has to preserve the cell viability. This problem can arise for example in the monitoring of a bio-molecule of interest during pathogenesis. An unsatisfactory approach consists in parallel replicates that will be assessed at different time points but unfortunately results in smudging of the phenomenon of interest with sample-to-sample variability. Optical microscopy methods with harmless labeling or even label-free are naturally very attractive for this prospect but have been established for only a limited number of molecules. In the case of neurotransmitters, most labeling techniques available are related to tracing neurosecretion (Gubernator et al., 2009; Kruss et al., 2017; Leopold et al., 2019) while very few solutions for cytosolic neurotransmitter monitoring have been described (Jeng et al., 2020; Qian et al., 2015).

Another promising approach is the use of electroanalytical methods that benefit, in the case of some critical electroactive neurotransmitters like catecholamines, from being label-free. With the help of micro- nano-fabrication technology, electrodes of subcellular sizes can be
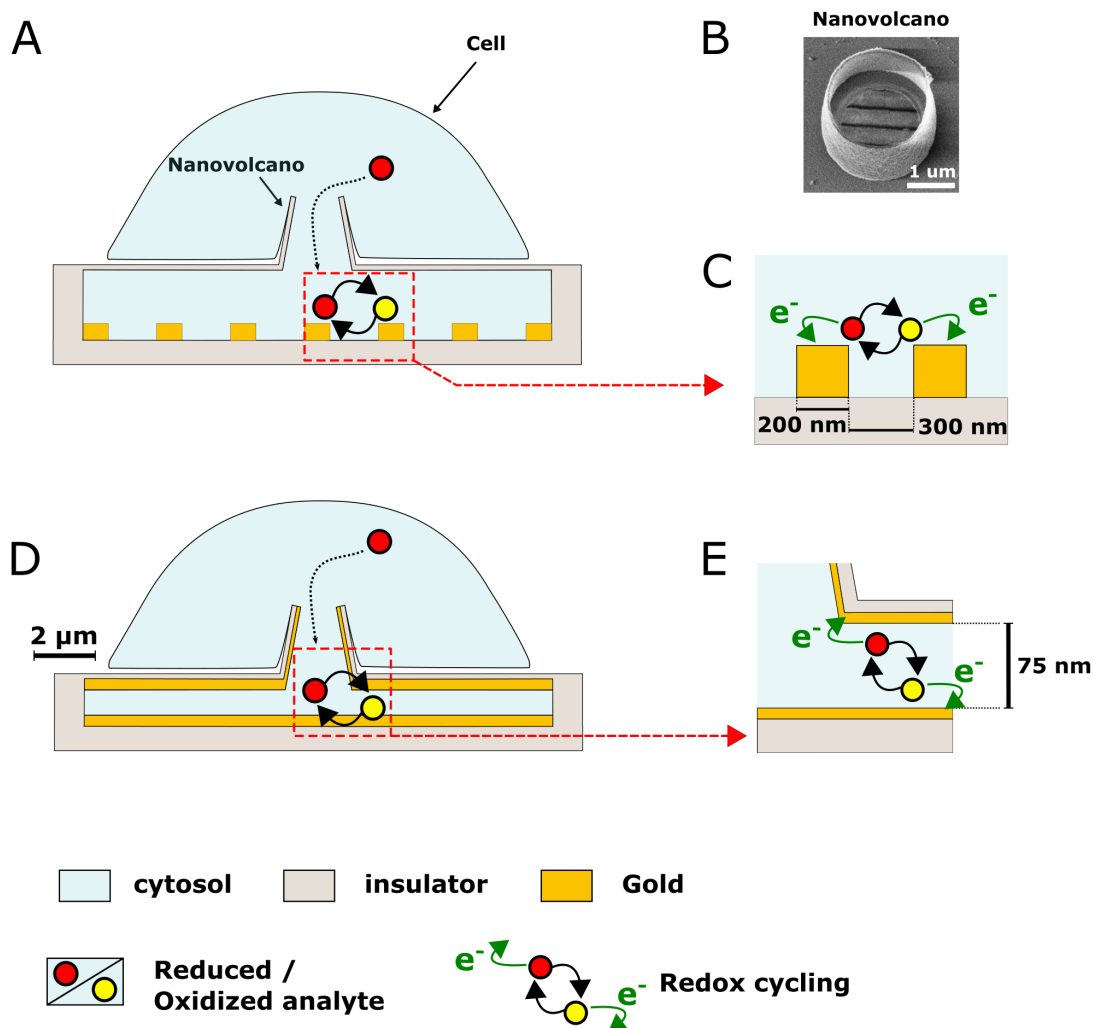
Figure 3.1: cross-section of devices implementing the proposed scheme of intracellular analyte detection using electrochemical redox cycling and nanovolcanoes. (A) A cell is depicted on top of a nanovolcano which allows local disruption of the cell plasma membrane above it by electroporation. Analytes molecules diffuse in the sensor cavity where they meet with the electrode pair used in redox cycling detection. (B) Scanning electron microscope image of a nanovolcano.(C) The electrode pair in (A) is depicted under a closer view with typical dimensions highlighted. The two individually addressable electrodes are set to potentials symmetrically apart from the analyte formal reduction potential thereby allowing analyte molecules to be successively oxidized and reduced at the corresponding electrode in a process known as electrochemical redox cycling (D) Same as (A) but for another implementation of the electrode pair used for redox cycling.(E) Enlarged view of the redox cycling within the sensor cavity in (D). The legend at the bottom of the figure applies to (A), (C), (D) and (E).

fabricated and used for single-cell investigations. However, most of these methods rely on the manipulation of a micropipettes or nano-electrode with a micromanipulator to penetrate the cell interior (Mosharov et al., 2003; P. Sun et al., 2008; Y. Wang & Ewing, 2021), an approach that is inherently slow and unscalable. On the other hand, the use of planar multi-electrode arrays (MEA) for analytes that are secreted by cells, and thereby do not require intracellular access, are commonplace for example in the investigation of neurotransmitter release (P. Chen et al., 2003; M. Huang et al., 2018; X. Liu et al., 2011; Spégel et al., 2007; X. Sun & Gillis, 2006; J. Wang & G. Ewing, 2014). There is accordingly a gap to bridge between electroanalytical methods that allow either scalable extracellular measurements on one hand, or intracellular but slow measurements on the other.

In this study, we present an electrochemical sensor design tailored for scalable, single-cell, intracellular electrochemical measurement of neurotransmitters. The envisioned sensor is based on a volcano-shaped tip to interface and sample repeatedly from individual cells while an underlying electrochemical redox cycling nanogap provides a stable and selective signal. We present technological development towards this goal, analytical pitfalls and proof of concept of neurotransmitter sensing in complex samples. This study paves the way towards substrate integrated nano- micro-electrodes for intracellular sensing.

3.2 Results and Discussion

3.2.1 Sensor design considerations

Problem definition

In order to make longitudinal intracellular measurements of bio-molecules possible, three critical aspects have to be addressed. First, there must be an efficient and reliable way to bring the sample in contact with the sensor. Second, the detection itself needs to be sensitive, specific and stable enough over the time course of the experiment. Third, the measurement needs to be harmless to the cell if it is to be used for monitoring of the molecule of interest over several days. Finally, the goal of this study is to enable multi-site measurements so the solution proposed needs to be scalable. We will detail the strategies put to use to address each of these requirements below.

Among the class of electroactive bio-molecules, neurotransmitters are of particular interest owing to their pivotal role in neural pathway communication at the synaptic level and wider implication in prominent pathological conditions like Parkinson's disease. Hence, we propose to develop our sensor for the cytosolic measurement of catecholamines as the dysregulation of this class of neurotransmitter's homeostasis has been linked to cell death in the scope of Parkinson's disease(Mosharov et al., 2009).

Chapter 3. Design and implementation of a scalable intracellular electrochemical sensor

Nanovolcanoes for repeated intracellular sampling

The first challenge is the reliable sampling of cytosolic bio-molecules. While others have described the use of nanowires (P. Sun et al., 2008; Y. Wang & Ewing, 2021) and micro-pipettes (Mosharov et al., 2003) for intracellular electrochemical sensors, these approaches are not scalable as they require extensive work to reposition the electrode in between measurements. Furthermore, in the latter case the cell is destroyed in the process. In the field of electrophysiology, the use of MEA has become predominant and in the last decade the employment of micro- nano-structures allowed attenuated intracellular measurements from MEA (Spira et al., 2019). An example of such nano-structures is the nanovolcano (NV) which is a volcano-shaped substrate-integrated tip housing a conductive electrode. This nano-structure has demonstrated state-of-art intracellular electrophysiology recordings from primary cardiomyocytes by mean of electroporation of the cell membrane (Desbiolles, de Coulon, et al., 2019). We therefore propose to use the NVs as a tool to permeabilized the cell membrane by electroporation and funnel the effluxing molecules toward the underlying sensor. Because mild electroporation amplitudes produce transient pores that reseal within minutes, this approach is essentially a discrete measurement. We have previously demonstrated that electroporation of primary cardiomyocytes with NVs was repeatable and yielded high rate of intracellular access (Desbiolles, de Coulon, et al., 2020). Accordingly, this approach is a good solution to enable longitudinal intracellular sensing while limiting viability issues due to dilution of the intracellular space with extracellular solution; a common problem in patch clamp experiments.

Electrochemical redox cycling for stable and sensitive measurement

In order to propose a scalable sensor, detection on site is highly desirable. Others approach for intracellular sampling with downstream *ex situ* analysis have been proposed (Cao et al., 2017; Guillaume-Gentil et al., 2016) but suffer from limited throughput due to the extra sample handling required and have only been demonstrated for nucleic acid so far.

The concentration and total amount of catecholamines within the cytosol of central nervous system neurons is still subject to investigations. In the case of dopamine, it is clear that most of it is stored within vesicles (Chien et al., 1990) and that its cytosolic concentration is very low, somewhere below 100 nM which is the limit of detection of intracellular patch electrochemistry (Mosharov et al., 2009). Other commonly used cell models for neurosecretion like pheochromocytoma cells have also been reported to hold sub-micromolar cytosolic catecholamine level, below the detection limit of tools available (Mosharov et al., 2006). It is noteworthy that there exists other cell types with higher endogenous cytosolic catecholamine concentration. For example, chromaffin cells are known to have intracellular concentration of catecholamine in the range of 10-20 μM (Mosharov et al., 2003). Such cell type could constitute a convenient fall back model allowing to benchmark electrochemical measurements of cytosolic catecholamine concentration.

Yet because the level of cytosolic catecholamines has not yet been measured for cells of the central nervous system or relevant cell models, it is difficult to define a target limit of detection and ensuing sensor design to meet this limit. As a first approach, one may assume a particularly stringent case to allow for some leeway. For a cell of 12 μm in diameter and hence about one picoliter in volume, a cytosolic concentration of 10 nM makes up a total of 6000 dopamine molecules in the cytosol. The detection of 6000 molecules from an enclosed volume of one picoliter can thus be set as a semi-empirical target.

This poses a first constraint on the sensitivity of the sensor envisioned. If a standard amperometric detection is used, the number of molecules reaching the electrode at any given time following electroporation is very low and result in a transient signal decaying to zero but never exceeding a few femto-amps (Appendix figure 2, A-C). While there exists reports of atto-amps current range measurements in electrochemical set ups (Grall et al., 2021), such approaches rely on cutting edge instruments that are costly and thus not widely available as well as being not well scalable towards parallel measurements. These considerations are important since a technology is useful and meets a demand only if it can be implemented by others. A reasonable assumption as to the limit of quantification for a widely available amplifier (*e.g.*, patch clamp amplifier) using averaging is 1 pA. With this constraint, it follows that it would unfortunately prove very difficult to implement our proposed electroporation-based sampling method and on site electrochemical measurement with the standard NV electrode (Desbiolles, de Coulon, et al., 2019).

A way to tackle the issues of low signal magnitude and transient response is the use of electrochemical redox cycling (ROc). In this approach, a molecule of interest able to undergo a reversible oxidoreduction reaction is cycled between its oxidized and reduced form by a set of closely spaced electrodes biased to potentials set symmetrically apart from the formal potential of the redox couple. The effect on the measured current is an amplification of hundreds to thousands of times as predicted by the time required for shuttling (*i.e.*, diffusion) of the molecule of interest back and forth between the two electrodes. In chronoamperometry, current per molecule of 7 fA has been reported by Kang et al., 2013 using an electrochemical nanogap. With such an electrochemical nanogap built below a NV (Appendix figure 3, A-B), redox cycling allows the amperometric signal to reach magnitude in the tens of pico-amps still considering an initial 6000 molecules within the cell initially (Appendix figure 3, C). More interestingly perhaps, the signal is now a initial transient followed by a steady-state response.

It follows that ROc is an attractive technique to quantify concentrations from small, finite sample volumes even in the complex case of mass-transport through nanometric pores as envisioned by our electroporation-based sampling. While the redox cycling current is expected to reach a steady-state, in practice it will be desirable to reach this steady-state in a reasonable timescale to account for possible escape of molecules from the NV toward the extracellular bath. Accordingly, the level of membrane disruption brought by electroporation needed to result in sufficiently fast mass-transport should be optimized experimentally. This is not addressed in this study and should be the object of a work of its own in the future.

Chapter 3. Design and implementation of a scalable intracellular electrochemical sensor

Electrochemical redox cycling for enhanced specificity and self-assembled monolayer for better sensor stability

Another critical parameter for meaningful measurement is the specificity of the sensor. In the complex environment of the cell cytosol, a large number of molecules are known to interfere with the oxidation of catecholamines. In particular, ascorbic acid, 3,4-dihydroxy-L-phenylalanine (levodopa), 3,4-hydroxyphenyl ethylene glycol (DOPEG), 3,4-dihydroxyphenyl acetate (DOPAC) and homovanillic acid. Accordingly, the electrochemical reactions at the electrode needs to be made selective in order to yield a reliable signal that truly reflects the concentration of the analyte of interest. Fortunately, the use of ROc comes with another advantage which is that only molecules undergoing a reversible redox reaction are susceptible to signal amplification.

ROc detection of dopamine in a large background of ascorbic acid has already been demonstrated by Zhu et al., 2011 although not applied to single-cell intracellular sensing. At the same time, dopamine precursor interferrents have been reported to undergo much slower oxidation reaction at carbon electrodes compared to catecholamines (Mosharov et al., 2003). Their contribution to the measured current can be subtracted although this requires to know the expected concentration in the sample and hence constitutes an imperfect solution that should be addressed eventually.

Lastly, the sensor has to be able to perform measurements over a long period of time (days) to be able to monitor the evolution of neurotransmitter homeostasis. This can be particularly difficult to achieve for electroactive molecules whose oxidation product may undergo polymerization as is the case for dopamine (Schindler & Bechtold, 2019). To tackle this issue we decided to make use of mercapto propionic acid (MPA) which readily assembles as a monolayer on noble metals and improves the reversibility of catecholamine redox reaction (Spégel et al., 2007). Fortunately, the use of this self assembled monolayer has already been characterized as compatible with ROc although at the cost of a modest decrease in current density (Singh et al., 2011). Furthermore, ROc at MPA covered gold microelectrodes have been recently harnessed to monitor extracellular levels of dopamine in organoid cultures thereby demonstrating its stability in complex samples (Zanetti et al., 2021).

Redox cycling limits bio-molecule consumption during measurement

To achieve harmless electrochemical detection, the consumption of the analyte has to be taken into account. For example, passing a current of a single pico-amp of current to oxidize molecules at a concentration of one micromolar within a single-cell of volume taken as one picoliter will result in full depletion of the analyte in less than one second (McCormick & Dick, 2021). Such total depletion of a cell metabolite is likely to challenge the cell viability and needs to be taken into consideration. Thankfully, the use of ROc also helps in that regard since the analyte of interest can be returned to its original state at the end of a measurement cycle. Still, while the majority of the current registered is accounted for by molecules undergoing

redox cycling, it is likely that other molecules undergoing irreversible redox reaction are being oxidized/reduced but contribute only fractions of pico-amps. These molecules are "consumed" and their reaction to another molecule may have deleterious impacts on the cell. Accordingly, the measurement should be performed as quickly as possible and the surface of the sensor should ideally be minimized although that would come as a trade-off with the magnitude of the ROc signal measured as described below. We also discussed below the impact of cell dilution which can lead to cell viability impairment.

3.2.2 Proposed implementation

Figure 3.1 depicts cross-sections of the proposed nanogap ROc sensor integrated with the NV needed to obtain intracellular access (not to scale). The cell is depicted over the NV and the cell cytosol is shown to fill the sensor cavity which would be achieved by electroporation of the cell membrane covering the NV. We propose two approaches to build an electrochemical nanogap. One relies on planar interdigitated electrodes (IDE) in which the nanogap is defined as the lateral separation between the digits of the IDE (Figure 3.1, A). The NV is depicted on the cross-section and displayed on a scanning electron microscope (SEM) image (Figure 3.1, B). Another approach relies on self-aligned nanogaps built from vertically stacked electrodes (VSE) separated by a sacrificial layer (Figure 3.1, D; the sacrificial layer removed before sensor operation is omitted). The operation of the electrodes is depicted for the IDE and VSE (Figure 3.1, C and E respectively) but essentially follows the same principle. The two individually addressable electrodes are set to potential symmetrically apart from the molecule of interest's formal potential. For a molecule undergoing a reversible redox reaction, ROc will arise. The dimensions of the nanogaps are chosen within the plausible limits of the corresponding manufacturing methods.

3.2.3 Scaling laws and numerical simulation of the proposed sensors

As mentioned above, ROc scales with the reciprocal of the nanogap dimension. Formally, if the shuttling time is governed by diffusion only, an analyte molecule may shuttle back and forth across a distance d as fast as:

$$\tau = 2\frac{d^2}{2D} \quad (s) \tag{3.1}$$

where τ is the time for shuttling, D is the molecule's diffusion coefficient and the factor two on the numerator arises from traveling the distance d twice. The current per molecule is then:

$$i_{perN} = \frac{zq}{\tau} = \frac{zqD}{d^2} \quad (A) \tag{3.2}$$

where z is the number of electrons involved in the redox reaction and q is the elementary charge. For a ROc sensor forming a cavity the total current at a given concentration will be:

$$I = V c N_a i_{perN} = A d c N_a \frac{zqD}{d^2} = \frac{AczFD}{d} \quad (A) \tag{3.3}$$

and for the current density:

$$J = \frac{czFD}{d} \quad (A/m^2) \tag{3.4}$$

where V is the cavity volume, c the analyte concentration, Na the Avogadro number and after simplification the right hand term is obtained where A is the sensor surface area and F is the Faraday's constant. While the shuttling time τ scaled with the reciprocal of the nanogap dimension squared, the total current is only reciprocally scaling with it because the number of analyte molecules within the cavity (*i.e.*, available for sensing) is itself proportional to the nanogap dimension. From equation 3.3, we thus conclude that the ROc current will scale linearly with the sensor surface area and reciprocally with the nanogap dimension and that the total ROc current will increase linearly with analyte concentration.

Equation 3.3 is the exact theoretical ROc current however it may fail to account for the specific geometry of our sensor. In fact this equation is based on the assumption that mass transport solely occurs between the two electrodes, *i.e.* in a closed system, whereas in our sensors mass transport may also occur through the NV to and from the bulk which we define as the aqueous solution residing outside of the cavity and NV. Because the concentration of the oxidized and reduced form of the analyte will be higher at the electrode surfaces where they are produced compared to the bulk, some molecules will diffuse out of the cavity thereby decreasing the ROc current.

For this reason we performed numerical simulations based on finite element modeling (FEM) of our sensor to find the expected total ROc current given a specific design. We constructed 2D axisymmetric models corresponding to both sensor configuration (Figure 3.1, A and D) and imposed boundary conditions (symmetry axis, no flux, fixed concentration and oxidoreduction reaction at the electrodes surfaces) as highlighted in the supplementary materials (Supp. Figure 3.11). The oxidoreduction reactions taking place at the electrodes surfaces were defined by the Butler-Volmer equation (see Materials and Methods 3.4) and implemented in the simulation according to another research article (Lavacchi et al., 2009). Mass transport followed Fick's laws of diffusion as there was no convection and electromigration was negligible in the saline of physiological concentration used in this study. This approach has the advantage compared to the simpler spread-sheet implementation of random walk (Sulzer & Pothos, 2000) to allow us to vary the geometry of the sensor with ease.

For verification of the theoretical equation 3.3 we only performed simulation with the VSE configuration and obtained current densities that scaled with the reciprocal of the nanogap dimension as expected and fitted well to equation 3.4 up to a constant of 0.48 (Figure 3.2).

Phrased differently, the current densities obtained through the simulation are 0.48 times lower than predicted from equation 3.3). As mentioned above this discrepancy is due in part to the escape of molecules from the cavity into the bulk. In addition, it is known that dead volume in the sensor (regions where the two electrodes do not overlap due to misalignment or alignment tolerance during fabrication) will decrease the ROc current by a factor:

$$\chi_{deadvolume} = \frac{V_{active}}{V_{active} + V_{passive}} = \frac{A_{active}}{A_{active} + A_{passive}}$$ (3.5)

where V and A are volumes and area respectively, *active* denotes surface area where the two electrodes overlap thereby sustaining ROc whereas passive surfaces are the remaining electrode surface area. For the geometry used above which yielded 0.48 times the theoretical ROc current, the dead volume attenuation factor is equal to 0.51. The magnitude of this attenuation factor in the VSE device configuration is determined by the alignment leeway built into the design which is discussed below. Accordingly, we conclude that molecule escape from the sensor cavity will contribute only 3% to the decrease from the theoretical ROc current which is close to negligible compared to the effect of dead volumes.

An important parameter in the design of the sensor is the surface area. Because we aim to measure from the cytosol of a cell, the sample volume is limited. During measurement the cell membrane is first disrupted by electroporation following what the cytosol content diffuses into the cavity. It is common knowledge in the field of patch clamp electrophysiology that dilution of the cell cytosol with the patch pipette solution will lead to cell death within tens of minutes. On the other hand micro-scale devices have demonstrated that cell recover well from sampling of a significant fraction of their cytosol, up to a few picoliters (Cao et al., 2017; W. Chen et al., 2022). Accordingly, it is desirable for cell viability purposes to limit the volume of the cavity to dimensions on the same scale as the cell (picoliters).

On the sensing point of view, a large sensor volume is preferable. Considering a cell of volume V_{cell} holding a number N of analyte molecules of interest, when that cell cytosol is made continuous to the cavity housing the sensor with volume V_{sensor} the redistribution of the analyte molecules will dictates that at equilibrium the number of analyte molecules residing in the cavity will be given by:

$$N_{inSensor} = N\frac{V_{sensor}}{V_{sensor} + V_{cell}} = cV_{cell}Na\frac{V_{sensor}}{V_{sensor} + V_{cell}}$$ (3.6)

This is assuming no leakage at the NV/cell interface which we ignored for simplicity. The total ROc current that would be obtained in that case is given by multiplying equation 3.2 and 3.6:

$$I = I_{perN}N_{inSensor} \quad (A/m^2)$$ (3.7)

In which both terms depend on the radius of the electrode's surface area, height of the sensor cavity and the cell volume. We compared the ROc current predicted from equation 3.7 with numerical simulations of a cell of radius 5 μm on top of a VSE sensor of increasing radius but

constant nanogap dimension of 75 nm and found a very good agreement (Figure 3.2, B) The theoretical equation and numerical simulation agree closely and the total ROc current follows a sigmoid curve rising with increasing sensor radius. This is a consequence of more and more molecules residing within the sensor cavity, i.e. over the sensor and available for detection, as the cavity volume is increased with respect to the cell's volume. There is hence unfortunately a trade-off between the magnitude of the ROc readout and the dilution of the cell content which may be harmful to the cell. Above a certain sensor radius there is however no further gain. We can thus use this model to find what is the minimum sensor radius that will obtain optimal ROc current defined as the radius needed to reach an arbitrary fraction of the sigmoid asymptote. Since this value is impacted by the volume of the cell as well, we simulated ROc current for increasing sensor and cell radius (Figure 3.2, C). We conclude that if sensing is prioritized above all, a sensor radius of 50 µm will result in optimal ROc current for cells of diameter up to 10 µm which corresponds to an upper limit of mammalian cell dimension.

Having identified the scaling law at play with the sensing mechanism chosen and the trade-off arising from device design, we devised the final sensor dimensions. With both approaches the nanogap dimension was taken as the smallest reachable with the fabrication technique employed as detailed further in the next sections. The radius of the IDE and VSE electrodes were taken as 10 µm and 60 µm respectively resulting in 0.63 pL and 0.85 pL. With both sensor implementations having cavities of volume close to those of a typical cell, we expect that about half of the molecule contained in the cell cytosol will diffuse to the sensor which was chosen as a compromise between ease for sensing and limited cell impairment. In the case of dopamine, for a cytosolic concentration of 10 nM that would amount to 3000 molecules reaching the sensor cavity.

A

B

C
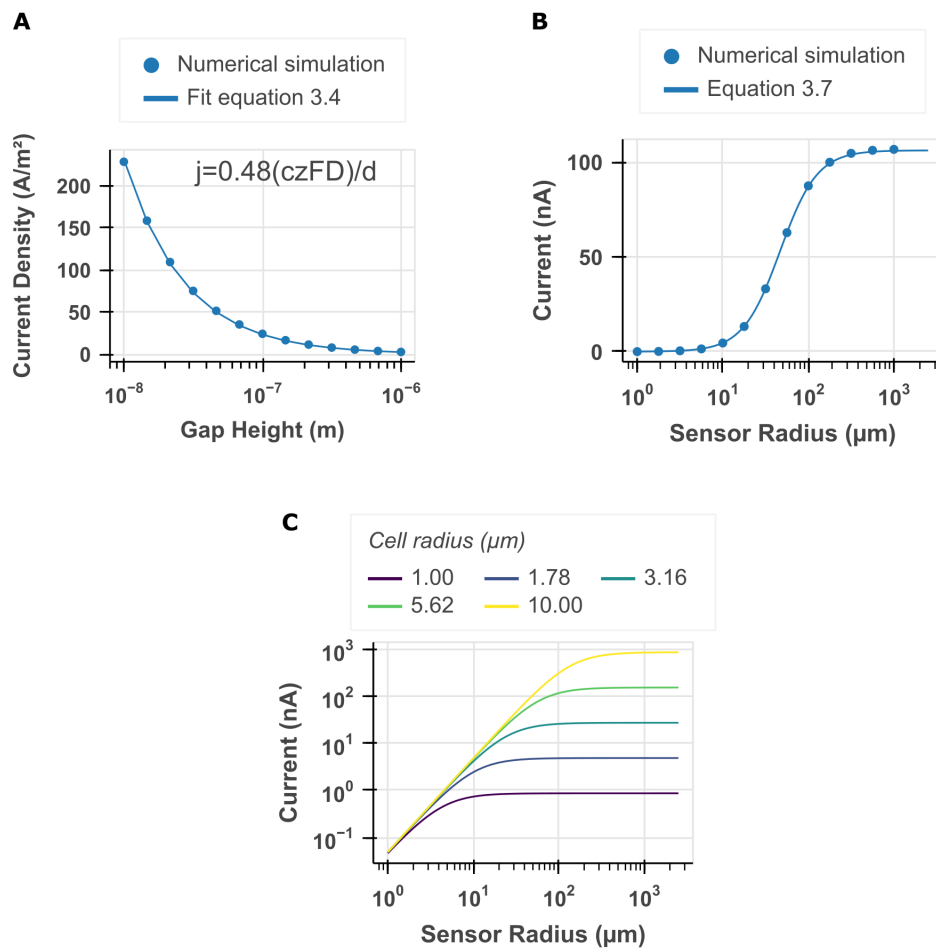
Figure 3.2: Scaling of the redox cycling current with electrode separation, electrode radius and cell size. (A) Redox cycling current obtained from numerical simulation using a finite element model of the device in figure 3.11, (D) with decreasing inter-electrode distance (*i.e.*, gap height). Redox cycling current scales with the reciprocal of the inter-electrode distance. The data from the numerical simulation is fitted to the theoretical equation 3.4 of the redox cycling current density *j*. The initial pre-factor of 0.48 corresponds to the deviation of the model to the theoretical redox cycling current, mostly due to dead volumes and escape of molecules from the sensor cavity as described in the main text. (B) A cell of finite dimension and volume whose cytosol is freely communicating with the sensor cavity is added to the model. For increasing electrode radius and hence cavity volume, an increase of the redox cycling current is observed due to more analyte molecules residing within the sensor cavity at equilibrium. (C) Same as in (B) but for cells of increasing radius. For cells up to 10 μm in diameter, a sensor radius of 50 μm will result in close to optimal redox cycling current.
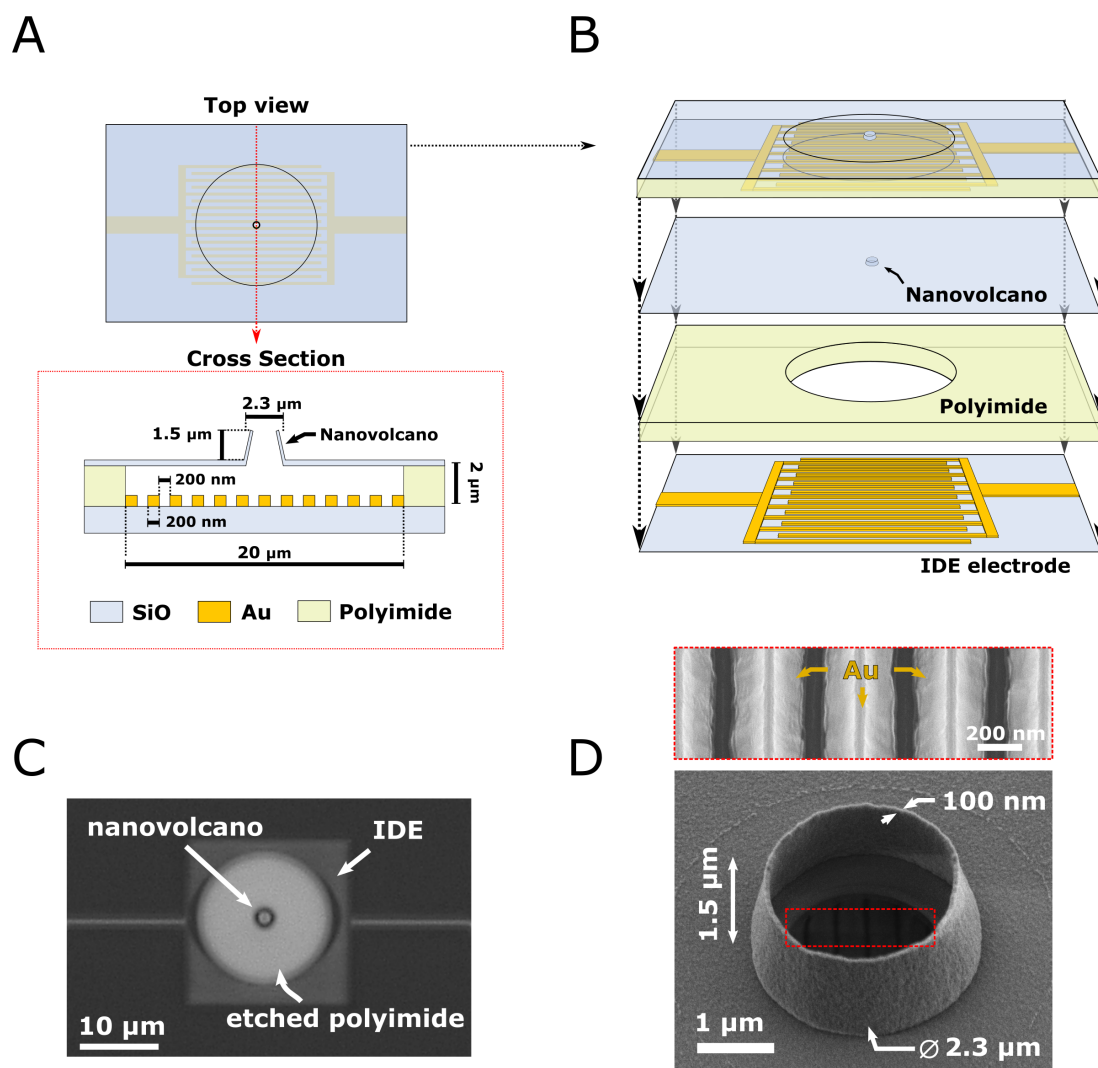
Figure 3.3: Interdigitated electrode (IDE) sensor description. (A) Top view and cross-section of the device (not to scale). The nanovolcano is standing on top of a cavity whose floor is patterned with a pair of gold IDE. (B) Device collapsed view showing the different layers. From bottom to top: gold IDE on fused silica substrate, polyimide insulation with cavity etched into it and SiO_2 insulating layer into which the nanovolcano is patterned. (C) Optical micrograph of the finished device. The IDEs appear as a blurry rectangle because of their sub-diffraction dimension and pitch. (D) Scanning electron micrographs (SEM) of the finished device viewed with a tilt showing the nanovolcano. The IDEs are visible through the nanovolcano and the highlighted dashed red box is shown on another SEM above at an intermediate stage of the fabrication process. The IDEs have a tapered shape due to the etching method used.

3.2.4   Interdigitated electrodes (IDE) fabrication and characterization

Fabrication of the IDE device

The fabrication process developed for the IDE sensor is based on deep ultraviolet (DUV) lithography, ion beam etching and isotropic plasma etching. The process flow is detailed in the Materials and Methods section 3.4.2 and Supp. Figure 3.12. A top view, cross-section and collapsed view of the finished device is depicted in Figure 3.3, A-B. The IDE are patterned from gold which is the noble metal most suited for the electrochemical detection of catecholamine. Each digit of the IDE is 200 nm wide and 250 nm thick with a pitch of 400 nm (200 nm nanogap). Each electrode is contacted with its own lead (*i.e.* electrical connection) and is therefore individually addressable. An optical micrograph shows a top of view of the device where the NV, the underlying cavity and IDE are highlighted (Figure 3.3, C). The digits of the IDE are not discernable with optical microscopy because of their sub-diffraction width and pitch and appear as a slightly blurry rectangle. The NV itself is well defined and the exposed portion of the IDE electrodes are clean without polyimide residues (Figure 3.3, D). A SEM image shows the IDE more clearly at an intermediate stage of the fabrication process (Figure 3.3, D; upper SEM image).

The key feature of this device is the inter-electrode distance between digits of the IDE. This is achieved thanks to the enhanced resolution achievable by DUV lithography. In DUV lithography a KrF source emits light at a wavelength of 248 nm which, with advanced image formation techniques, can pattern photoresist with a resolution down to 150 nm. While electron beam lithography is a possible alternative, DUV lithography has the advantage of considerably higher throughput as it was typically implemented on step-and-repeat exposure tools for the semiconductor industry up to the late 80s. The overall fabrication process was achieved in two days for batches of a few four inches substrates (typically four).

The patterning of the metal itself into the IDE was performed with etching instead of lift-off to be able to use a metal layer of 250 nm in thickness.Thick IDE digits are preferable as electrode surface area increases accordingly. A distinct feature of the IDEs is their tapered shape (Figure 3.3, D; upper SEM image). This shape arised from the ion beam etching used. Ion beam etches material through physical sputtering which leads to possible redeposition of the etched material on the photoresist side walls. This phenomenon is increasingly problematic with narrower mask dimensions and can only be counteracted by tilting the incident beam of ions thanks to angle specific sputtering (Jeon et al., 2010). Interestingly, this leads to a tapered etching profile which results in much narrower dimensions at the foot of the taper than originally patterned in the photoresist. With this approach we could pattern nanogaps with dimensions down to 60 nm at the foot of the taper and we have assessed through energy dispersive X-ray analysis that the etching was complete even at this small gap dimension (Figure 3.4, A).

Lastly, a critical requirement was to ensure the proper adhesion of the top silicon dioxide (from which the NV is built) to the polyimide. This is especially critical for the application of the

sensor to longitudinal sensing under prolonged aqueous saline solution (cell culture medium) exposure. Silicon dioxide adhesion to polyimide was unsatisfactory with delamination occurring under mild stress like spin coating (data not shown) so this issue was circumvented by i) roughening the polyimide with a short oxygen plasma prior to deposition and ii) depositing a thin adhesion layer of silicon carbide before silicon dioxide. Finally the NV could be patterned in the same way as described in our previous work (Desbiolles, de Coulon, et al., 2020).

Characterization of the IDE sensing performance

The performance of the IDE sensor was assessed in terms of ROc current from an aqueous saline solution (100 mM KCl) of ferrocenemethanol and compared the obtained current densities to those obtained from our numerical simulation (Figure 3.4, B). We found a good agreement between the experiment and the simulation with a sensitivity of 0.24 pA/(μm^2.μM) or 38.64 pA/μM for this specific IDE geometry. From SEM inspection we estimated the active electrode surface area to 128 μm^2 and a cavity volume of 0.63 pL from optical inspection. This leads to a current per molecule of 0.1 fA per molecule of ferrocenemethanol. Note that due to the large volume of the cavity only a fraction of the molecules interacts with the electrode at a given time so the current per molecule is necessarily lower than the one observed for other electrode configurations like the VSE.

Nonetheless, this metric allows a representative estimate of the current obtained from having N molecules within the sensor cavity. As discussed above, a cell with a typical initial dopamine concentration of 10 nM would equilibrate with the sensor cavity to yield around 3000 dopamine molecules within the cavity and hence we could expect 300 fA of current from the IDE sensor in ideal conditions. This falls just short of the set goal of obtaining a current reading in the picoamps range in order to be compatible with amplifiers of reasonable availability, cost and therefore measurement scalability. On the other hand this is a satisfactory outcome of the design process that was undertaken and the final measurement feasibility could still be sought with a model system, for example chromaffin cells which have cytosolic catecholamine concentration in the micromolar range (Mosharov et al., 2003). The limit of detection (LOD) was taken, here and throughout the rest of this study, as the value of a blank sample plus 3.2 times the standard deviation obtained from 10 measurements of the same blank sample and dividing the result by the sensitivity.

In this characterization experiment the LOD was mostly determined by the very large standard deviation of the measurements which was larger than the noise specification of our instruments (Ivium stat.h; Ivium, The Netherland) and that this variability grew worse over time as discussed in the next section.
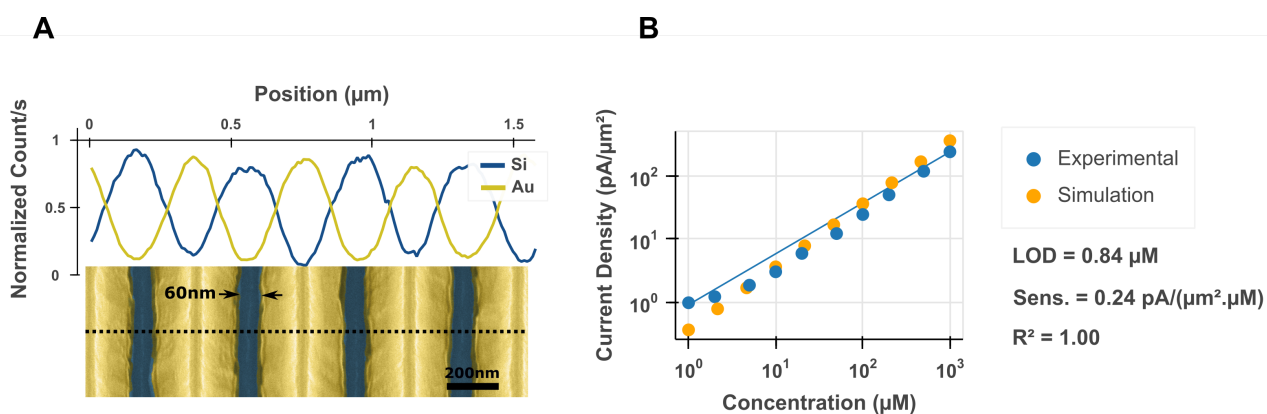
Figure 3.4: Characterization of the interdigitated electrodes (IDE) and performance of the finished sensor. (A) Energy dispersive X-ray analysis of the IDE shown as normalized counts per seconds for the cross-section indicated by the black dashed line on the scanning electron micrograph (SEM) below. The SEM was false-colored in post processing according to the composition of the line scan above with dark blue corresponding to silicon dioxide and yellow to gold. (B) Calibration curve of the redox cycling current sustained by the IDE sensor in a solution of aqueous saline with decreasing amount of ferrocenemethanol and comparison to the numerical simulation of the same sensor. LOD stands for limit of detection, Sens. for sensitivity and R^2 is the coefficient of determination for the linear regression of the experimental data corresponding to the solid blue line.

Failure overtime of the IDE devices

Furthermore we found that the device yield (% of device with individually addressable electrode) was very unsatisfactory in that i) the as fabricated device yield was low around 15% and ii) individual IDE were found to fail after repeated use. The latter problem is especially limiting for longitudinal interrogation. We have ascribed the cause of this failure over repeated use to dielectric breakdown resulting in arcing and shorting of the two electrodes. This hypothesis was supported by several observations of a given IDE becoming shorted during inter-electrode resistivity measurement with probing voltage as low as 500 mV (data not shown). For a dielectric breakdown of distilled water taken at 65 MV/m (Haynes, 2016) and a voltage of 500 mV, breakdown may occur for electrode distances of 7.7 nm and less. It should be noted that breakdown may occur at lower voltage for aqueous saline solution. Although the average distance between electrodes for the IDE fabricated was around 60 nm, a significant line roughness was apparent in the electrode probably due to different etching speed of the cores versus boundaries of the polycrystalline gold (C. Zhang et al., 2020). We hypothesized that due to line roughness, there may be regions where the inter-electrode distance is below the average value of 60 nm and nucleates dielectric breakdown. The application of the IDE sensor to cytosolic catecholamine was not further pursued as increasing the nanogap distance to prevent breakdown would also decrease the already too low sensitivity of the device.

In conclusion, the IDE configuration has the merit of a high throughput fabrication process

with a final device composed of only three layers. This ROc sensor may still be well suited to the detection of analytes in the hundreds of micromolar range for which the nanogap distance requirement would be less stringent and breakdown less likely to occur.

3.2.5 Vertically stacked electrodes (VSE) fabrication and characterization

Fabrication of the VSE device

The fabrication of the VSE device was inspired by the self-aligned nanogaps fabrication method developed by Kang et al., 2013. The step-by-step description of the fabrication process is detailed in the Materials and Methods section 3.4.3 and supplementary materials (Supp. Figure 3.13). The device is composed of two stacked gold electrodes covering the wall and ceiling of a cavity accessed through the NV. A top view and cross-section of the device (Figure 3.5, A; not to scale) depicts the two gold electrodes and NV. The NV measures 2.3 μm in diameter, the top electrode 100 μm in diameter and the bottom electrode 120 μm in diameter. The nanogap separation between top and bottom electrodes is only 75 nm yet they never come into contact across their whole surface. Each electrode is contacted with its own lead (*i.e.* electrical connection) and is therefore individually addressable. A collapsed view of the device (Figure 3.5, B; not to scale) allows to see the top and bottom electrodes and the middle layer of silicon dioxide which houses a critical feature of our design: four insulating pillars keeping the gold electrodes separated. Scanning electron micrographs (SEM) (Figure 3.5, C) are showing different views of the device at real scale. The NV is encircled by the egress out of the substrate resulting from the underlying silicon dioxide pillars (Figure 3.5, C; i). The NV itself is 1.5 μm tall with walls only 100 nm thick (Figure 3.5, C; ii).
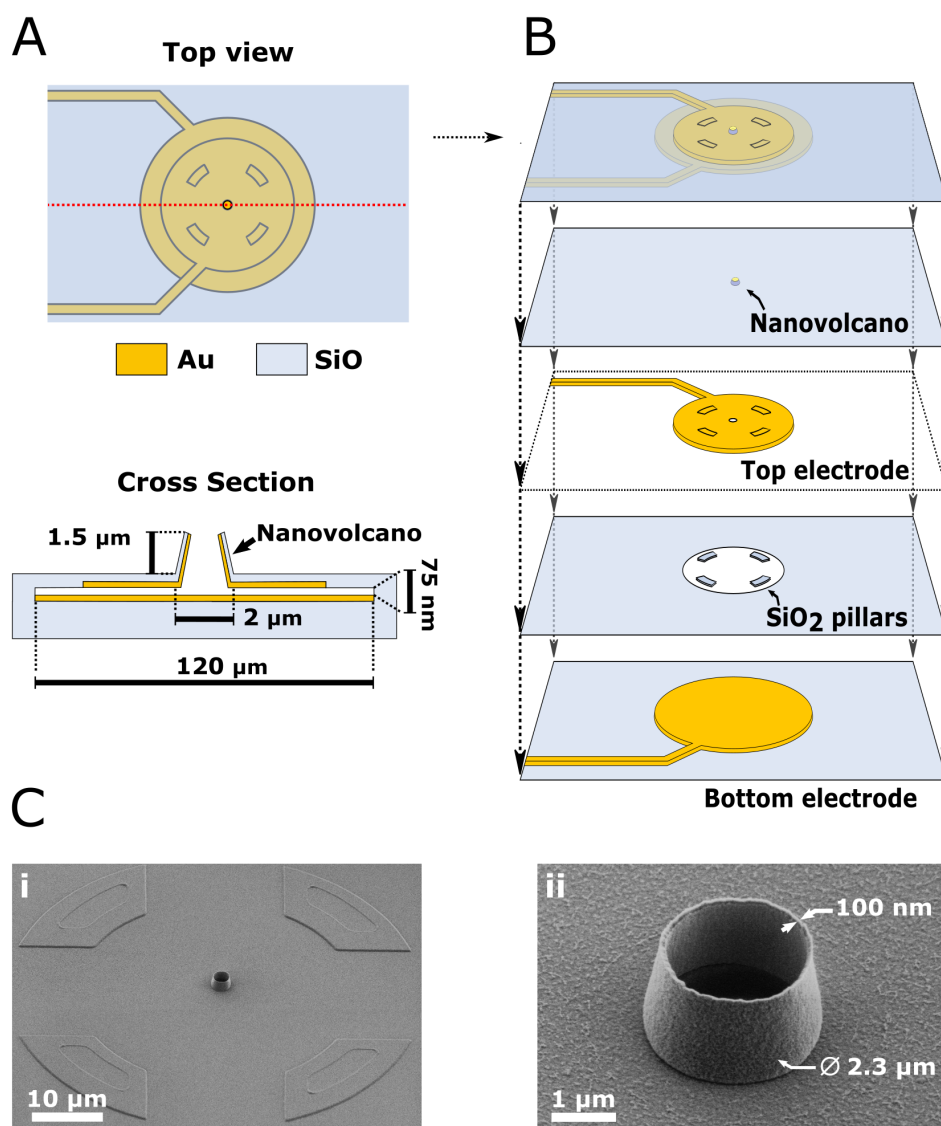
Figure 3.5: Vertically stacked electrodes sensor description. (A) Top view and cross-section of the device (not to scale). The nanovolcano is standing on top of a cavity whose floor and ceiling is covered by a set of individually addressable electrodes. The inter-electrodes distance is 75 nm. (B) device collapsed view showing the different layers (not to scale). The SiO$_2$ pillars ensure the two electrodes never come into contact. (C) Scanning electron micrographs of the finished device viewed with a tilt. i) Shows the nanovolcano surrounded by the egress from the substrate caused from the underlying SiO$_2$ pillars. ii) Shows an enlarged view of the nanovolcano.

During fabrication, the two electrodes are evaporated on the substrate with a sacrificial layer of chromium in between them. This sacrificial layer is removed at the end of the fabrication process by potential assisted wet etching as described by Sparreboom et al., 2008 (Supp. Figure 3.14). The device yield assessed by counting out the NVs whose pair of electrodes were shorted was always over 85% with at least 24 out of 28 devices per chip operational.

The fabrication process developed is largely independent of residual stress in the different layers. This is achieved through the incorporation of the silicon dioxide pillars in between the two electrodes that ensures that the electrodes remain separated after removal of the chromium layer (Figure 3.5, B). This issue was previously addressed by others (Kang et al., 2013) by balancing the stress of the thin dielectric films deposited, notably by alternating layers of compressive silicon dioxide and tensile silicon nitride deposited by plasma enhanced chemical vapor deposition. This elegant approach however suffers from an irremediable drawback when working with glass substrates. Under the same deposition conditions, silicon nitride deposited on silicon and fused silica substrate by PECVD have respectively large tensile and compressive residual stress. The origin of this difference stems from different epitaxial growth depending on the substrate as evidenced by stress measurements after depositions on different substrates (Supp. Figure 3.15).

Our design incorporating silicon dioxide pillars between the electrodes is hence a work-around for this issue that has the merit of being applicable to any geometry and allows one to vary the thickness/material of the electrodes and dielectric layer without having to match stresses between layers. The robustness of our fabrication methods allowed us to build nanogaps with electrode overlap of 7000 μm^2. This is over ten times larger than other electrochemical nanogaps presented in the scientific literature (Kang et al., 2013). On the other hand, our nanogap vertical dimension is about twice as large and, given that microelectrode noise in amperometric measurements scales with the electrode surface area (Yao & Gillis, 2012), our implementation is adapted to physiological concentration range but would be unable to achieve single-molecule electrochemical detection as was achieved by Kang et al., 2013.

Characterization of the VSE sensing performance

The performance of the VSE device was evaluated in terms of ROc current from an aqueous saline solution (100 mM KCl) of ferrocenemethanol. The cyclic voltammogram obtained from scanning only the top electrode while keeping the bottom electrode at 0 V shows a well behaved sigmoid curve (figure 3.6, A). The sensitivity obtained in amperometry is 0.29 pA/($\mu m^2.\mu M$) or 577.3 pA/μM for this specific VSE geometry (the device under test had an electrode of 25 μm in radius). The active electrode surface area is 1963 μm^2 and hence a cavity volume of 0.287 pL (with dead volumes). This leads to a current per molecule of 1.45 fA per molecule of ferrocenemethanol. Compared to the current densities obtained from our numerical simulation (Figure 3.6, B), we find a good agreement from the experiment although with a systematic reduction of 0.32 times. While it has been shown that ferrocenemethanol molecules spend up to 82% of their time adsorbed on the electrode in an electrochemical nanogap (Singh

A

B
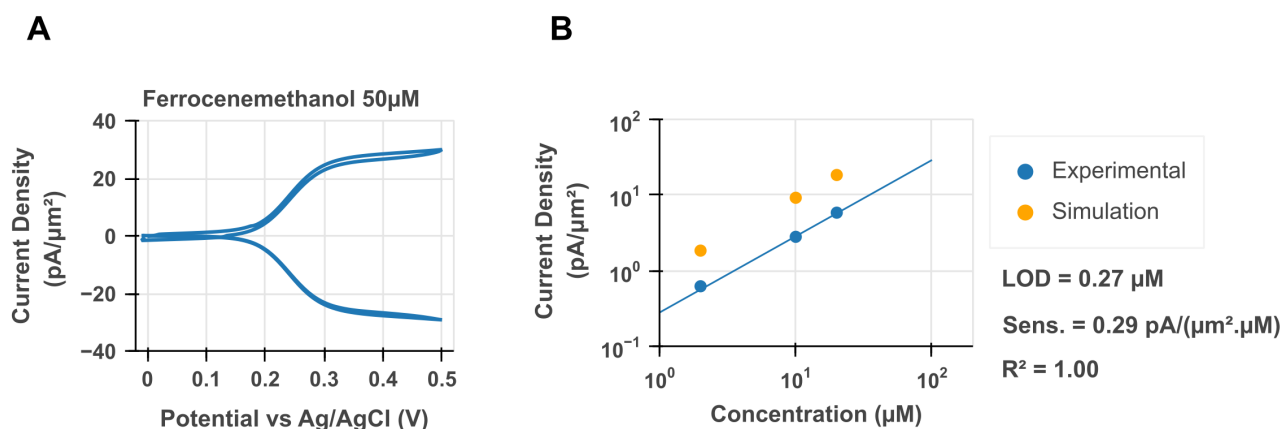
Figure 3.6: Characterization and performance of the vertically stacked electrode (VSE) sensor. (A) Typical cyclic voltammogram obtained from a VSE sensor in an aqueous saline solution of ferrocenemethanol. The two curves seemingly mirrored over the horizontal axis are obtained from the two electrodes of the sensor as they support redox cycling, one of which is scanned from 0 V to 0.5 V and back (anodic upper trace) and the other is kept at 0 V (cathodic bottom trace). The sigmoid shape is characteristic of microelectrodes. (B) Calibration curve of the VSE sensor for decreasing concentration of ferrocenemethanol and comparison to the numerical simulation of the same sensor. LOD stands for limit of detection, Sens. for sensitivity and R^2 is the coefficient of determination for the linear regression of the experimental data corresponding to the solid blue line.

et al., 2011), this factor should not be perceptible when measuring from a sample of large volume (*i.e.*, a local decrease in concentration within the nanogap due to molecules transiently adsorbing onto the electrode can be counteracted by influx of new molecule from the bulk where the concentration is constant). Instead, it seems more reasonable that this discrepancy arises from the very high surface area of the sensor which makes it prone to blocking from surface impurities thereby altering the electrode active surface area and total ROc current. If this hypothesis is correct, it would follow that about two third of the nanogap electrode surface area is blocked and unable to sustain ROc.

The LOD of the VSE was found to be 0.27 µM corresponding to a measured ROc current (background substracted) of 53 pA. While measuring sub micromolar concentration and blank samples with our instrument (Ivium stat.h; Ivium, The Netherland), the noise level of the VSE was close to 15 pA$_{rms}$; double the accuracy rating of the instrument (7 pA$_{rms}$+0.025% current range). This was also the case when operating only one electrode and increased when shorting the two electrodes (data not shown). We believe that this large noise level is due to fluctuations of the amplifier bias voltage which results in capacitive current flowing through the electrode/-electrolyte double layer. This is a recurrent problem in voltammetric measurements that is expected to scale linearly with the electrode surface area, the measurement bandwidth and the amplifier bias voltage (Yao & Gillis, 2012). For electrode larger than a couple thousands squared microns, this capacitive-loading is expected to be the main contributor to noise (Yao & Gillis, 2012).

Because the goal of this study is to demonstrate the feasibility of intracellular ROc measurement, we deemed this LOD as sufficient as some cells have level of catecholamine in the micromolar range endogenously (chromaffin cells) (Mosharov et al., 2003) or upon exogenous loading with a precursor (neuronal cells and cell line derived from pheochromocytoma)(Mosharov et al., 2009; Pothos et al., 1996). In the future, detection/quantification of samples with sub-micromolar concentration will require to perform a thorough electrochemical cleaning of the electrodes (*e.g.*, sweep in potassium hydroxide (Fischer et al., 2009)) and to use a set of low-noise current amplifier (*e.g.* patch clamp amplifier).

Improvement of sensor stability with self-assembled monolayer of mercapto propionic acid

As mentioned above, stability of the electrochemical sensor is pivotal if longitudinal monitoring is desired. This is particularly complicated when dealing with target analytes that tend to foul the electrode by polymerization after oxidation (Schindler & Bechtold, 2019) and/or adsorption (Jill Venton & Cao, 2020) both of which dopamine does at noble metal electrodes.

Fouling of our ROc sensor was apparent from the decrease in amplitude of successive cyclic voltammograms of dopamine (Figure 3.7, A). Others have addressed the problem of fouling with cleaning waveform applied to the electrode in between measurements (Manica et al., 2003), nanostructuring of the electrode (Patel et al., 2013) and finally there exist an extensive literature of coatings, polymer films and membranes devised to reduced electrode fouling (Hanssen et al., 2016). In the case of dopamine, an approach that was undertaken to reduce fouling is to functionalize the gold electrode with a monolayer of alkanethiols with a positively charged end group (Singh et al., 2011; Spégel et al., 2007). This approach was found to result in less adsorption of the analyte to the electrode and in increased reversibility of the dopamine oxidation at gold electrodes.

After functionalization by formation of a SAM of MPA, we observe less drift in the ROc signal over successive cyclic voltammograms (Figure 3.7, B). This comes at the cost of decreased faradaic current and a shift of the formal potential of the dopamine/quinone couple toward higher voltage (0.17 V and 0.25 V vs saturated Ag/AgCl respectively). Nonetheless, this functionalization improves the sensor stability and was demonstrated to behave well under detection of dopamine with interferents and in complex samples (Zanetti et al., 2021) which is desirable for our application. Hence the results presented from this point onward correspond all to VSE gold electrodes functionalized beforehand with MPA unless specified otherwise.
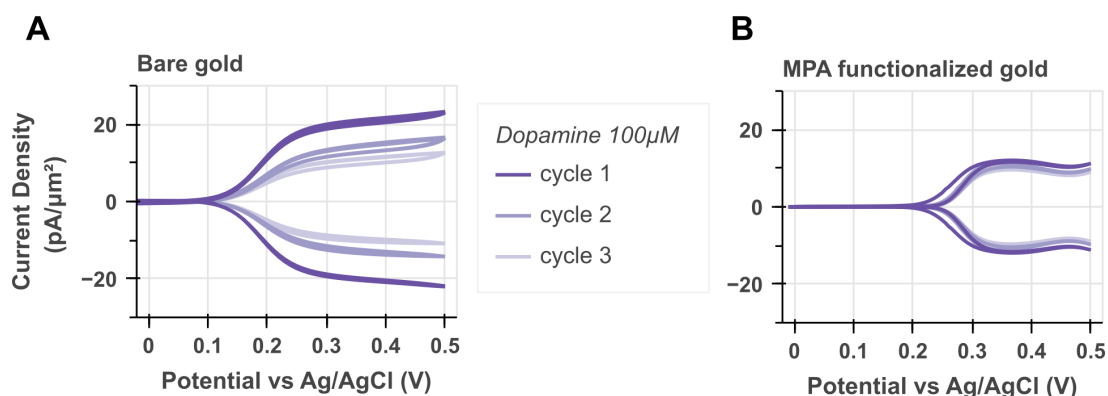
Figure 3.7: Mercapto propionic acid (MPA) reduces fouling of the VSE electrode. (A) Successive cyclic voltammogram obtained from redox cycling of dopamine. The amplitude falls to 50% of its original value after only 3 cycles. (B) Functionalization of the VSE electrode with a self-assembled monolayer of MPA results in i) decreased electrode fouling, ii) shifting of the formal potential from 0.17 V to 0.25 V and decrease of the current densities by 50%.

Sensitivity to interferent and precursor molecules

Oxidation of catecholamine unfortunately takes place at a voltage also imparting oxidation of other common bio-molecules; the most common example of which being ascorbic acid and dopamine precursors like levodopa. As mentioned above, ROc cycling was demonstrated to increase the specificity of electrochemical detection of dopamine with respect to ascorbic acid by Zhu et al., 2011. On the other hand, the precursors of dopamine are expected to also undergo ROc although at a decreased rate which should hopefully limit their interference (Mosharov et al., 2003). We found that ascorbic acid resulted in close to background ROc current at our sensor while levodopa is detected although with four times less sensitivity than dopamine (Figure 3.8, A). Furthermore, the detection of dopamine by ROc was largely

insensitive to ascorbic acid (Figure 3.8, B).
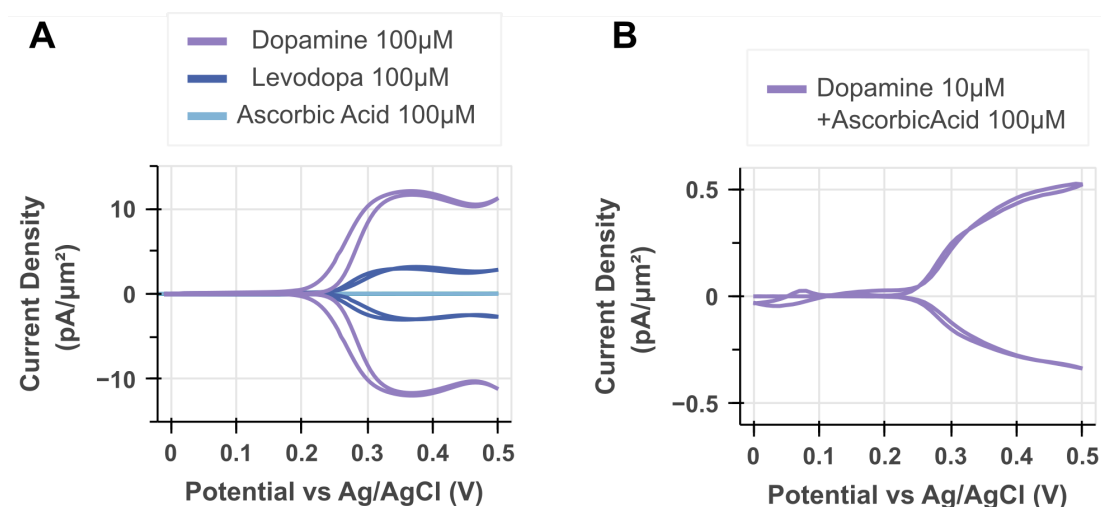
Figure 3.8: Selectivity of redox cycling current at the VSE sensor for dopamine over levodopa and ascorbic acid. (A) Ascorbic acid is a degradation product of dopamine and a common interferant for dopamine electrochemical detection but results in close to background level of redox cycling current. Levodopa, a precursor of dopamine, results in a modest redox cycling current that is however four times smaller than that obtained from a solution of dopamine of equal concentration. (B) Background substracted detection of dopamine in presence of ascorbic acid with a 1:10 ratio. The rise in current above 0.25 V can safely be attributed to dopamine rather than ascorbic acid given that ascorbic acid do not undergo reversible oxidoreduction reaction while the anti-correlation of the top and bottom current curves can only arise from the redox cycling of a necessarily reversible redox reaction.

Degradation of performance under prolonged aqueous saline conditions

Aside from fouling and adsorption of the molecule of interest, complex biological samples contain a large number of other biomolecules that may affect the electrode performance by permanently adsorbing to it. We tested the stability of the ROc signal over 24 hours while kept in a typical cell culture media which includes salts, sugars, amino acids, protein and antibiotics. The measurement was carried out directly in the cell culture media which may also impart further fouling from other biomolecules oxidation. Our results show that the ROc current decreased to two thirds of its initial values within 24 hours (Figure 3.9). This is unfortunately a caveat that will limit the applicability of the proposed sensing strategy for longitudinal sampling. Although this sensitivity drift could be characterized and corrected for, this constitutes a non-ideal situation that may suffer especially when detecting concentration of analytes close to the detection limit in which case the measurement might go to become unfeasible from a certain time point. This is clearly a limitation of the current sensor and should be addressed in further works.
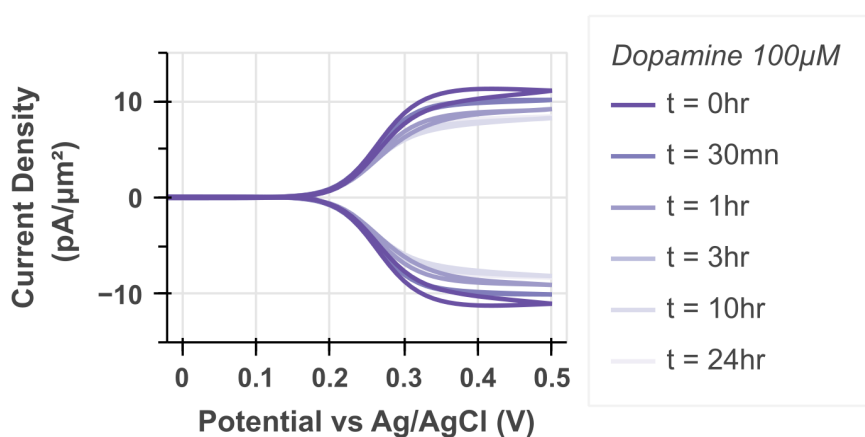
Figure 3.9: Degradation of the VSE sensor sensitivity to dopamine over prolonged storage in cell culture medium. The amplitude of the voltammograms is seen to decrease overtime. In this experiment, a solution of dopamine in cell culture medium was measured from at regular intervals. The solution was exchanged for a freshly prepared one before each measurement to ensure an equal concentration of dopamine.

Detection in complex sample proof-of-concept

In order to test the VSE sensor ability to detect catecholamine in complex samples, we performed an experiment where rat pheochromocytoma cells (PC12 cells) were lysed and the lysate dispensed over the sensor. This approach was undertaken in order to eliminate the impact of intracellular access on the measurement. As mentioned above, intracellular access by electroporation arises from pores of nanoscale dimension. The level of membrane disruption needed to result in sufficient diffusion of molecules out of the cells into the sensor cavity should be optimized which should be the object of a work of its own. Because cells were lysed in this experiment, it is important to remember that the measured catecholamine content will be the sum of the cytosolic and intravesicular catecholamines. Accordingly, it is not an estimate of the cytosolic level of catecholamine in PC12 cells.

We started by studying the behavior of ROc in the buffer used for cell lysis In the following experiments we did not functionalize the VSE with MPA since the detergent present in the lysis buffer would probably interfere with alkanethiols SAMs. Additionally, we operated the VSE electrodes in differential cyclic voltammetry. This technique differs from the result presented above in that both electrodes potentials are scanned rather than keeping one at a constant potential. This is used in order to obtain a cyclic voltammogram that presents anti-correlated peak features centered at the formal potential of the molecule susceptible to ROc present in the sample under study. This mode of operation is advantageous when working in complex samples where unforeseen interferents may be present since they would result in separate peaks given that their formal reduction potential is different from that of the target molecule. This approach was used by van Megen et al., 2012 for multiplexing and is exemplified in the supplementary materials (Supp. Figure 3.16).

We did not observe any peak features in the cyclic voltammogram in pure lysis buffer (Figure 3.10, A; cyclic voltammograms are offset for clarity) and found only a modest response to levodopa and ascorbic acid (Figure 3.10, B-C). The detection of dopamine in the lysis buffer in presence of excess ascorbic acid was found to result in a well resolved anti-correlated peaks on the top and bottom electrodes current trace (Figure 3.10, D).

We then collected the lysates from one million PC12 cells with or without pre-incubation with levodopa. Incubation with extracellular levodopa was shown to raise catecholamine quantal size in vesicles (Pothos et al., 1996). For one million cells the total content of catecholamine was below the detection limit of the sensor as shown by the featureless cyclic voltammogram (Figure 3.10, E) given that the sample was heavily diluted in the lysis buffer. On the other hand, cells incubated with levodopa before lysis had a detectable total amount of catecholamine as evidenced by the anti-correlated peak centered at 0.17 V versus an Ag/AgCl reference electrode; similar to that of the lysis buffer spiked with dopamine (Figure 3.10, D). By comparing the peak currents at this potential we can extrapolate that the levodopa incubated cells lysate had a concentration of 6.67 μM catecholamine. Taking into consideration dilution and the precise number of cells, our measurement suggests that PC12 incubated with levodopa holds 4.00
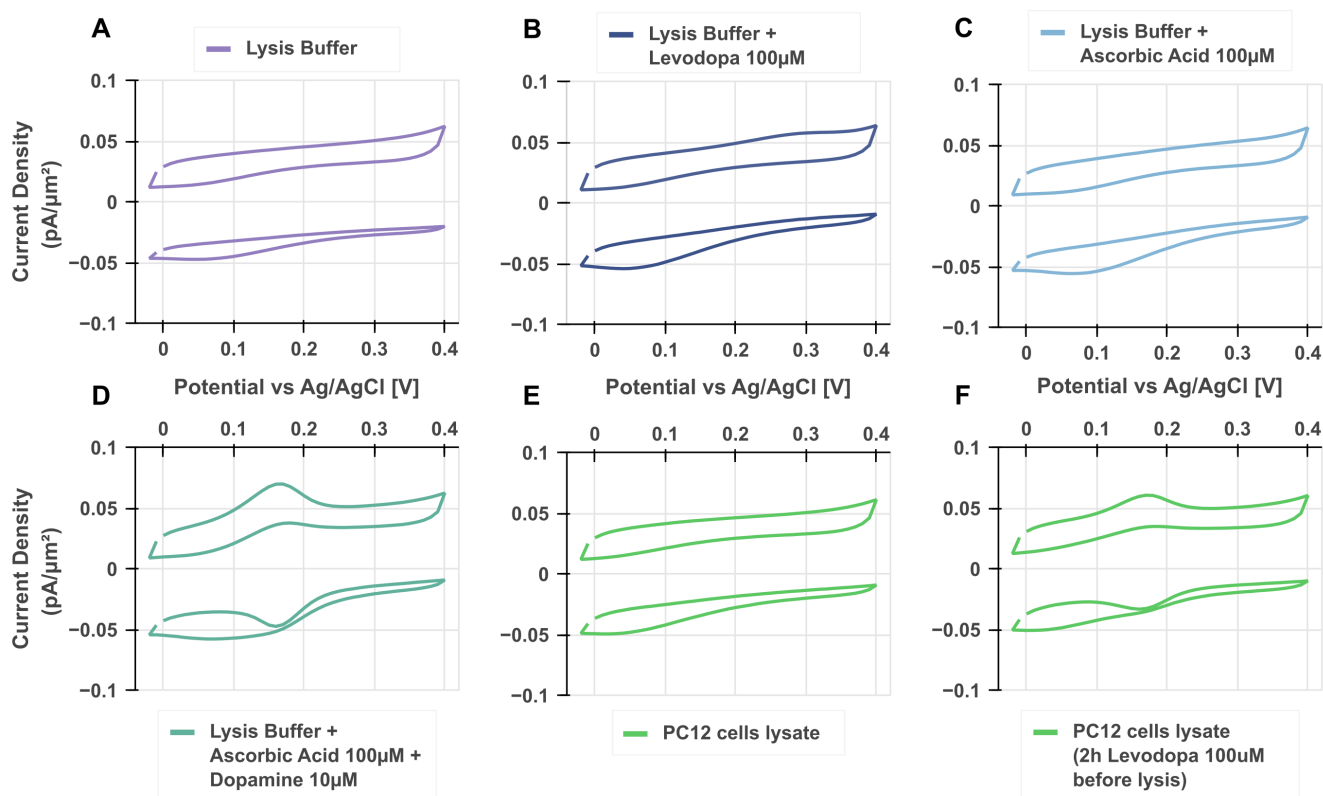
Figure 3.10: Detection of dopamine by the VSE sensor in whole cell lysate. (A) Differential cyclic voltammogram obtained in pure cell lysis buffer. The top and bottom electrodes of the VSE were scanned at the same time but with an offset of 100 mV. The top and bottom curves on the plot were offset by ±0.05 pA/μm^2 for clarity and correspond to the electrode with leading and trailing potential respectively. (B) and (C), assessment of the interference of levodopa and ascorbic acid on redox cycling in the lysis buffer respectively. (D) Dopamine is readily detected in the lysis buffer as evidenced by the anti-correlated peaks centered at 0.17 V (the MPA functionalization was omitted in this experiment due to the presence of detergent in the lysis buffer). (E) Analysis of a sample of rat pheochromocytoma cells (PC12) lysate. The absence of anti-correlated peaks indicates that the level of catecholamine is below the detection limit of the VSE. (F) Same as in (E) but for PC12 cells incubated with levodopa before lysis to increase their total content of dopamine. The cyclic voltammograms show anti-correlated peaks with similar formal potential to that observed for dopamine in (D).

femtomoles of catecholamine per cell. This is close to the value of 5 femtomoles reported by using high performance liquid chromatography with downstream electrochemical detection of catecholamine(Greene & Rein, 1977). Although the latter study did not increase the catecholamine content by levodopa incubation, the number of cell per sample was loosely estimated between one and five millions hence it is possible that the reported value of 5 femtomoles per untreated cell is overestimated by as much as 500%.

In an independent experiment, we have ascertained the origin and amount of the electroactive species present in PC12 cell lysate through a fluorometric assay according to a published article (Supp. Figure 3.17) (X. Liu et al., 2019). Based on the reported selectivity of this assay to catecholamine we conclude that the electroactive specie in PC12 cell lysate is indeed catecholamine (most likely dopamine) and found a similar per cell amount of catecholamine of 1.5 femtomoles and 3.36 femtomoles for untreated and levodopa treated cells respectively.

Altogether, we conclude that detection of catecholamines in whole cell extract by ROc is feasible with our approach. Furthermore the resulting cyclic voltammogram shows no other features which suggest that the measurement specificity is satisfactory.

3.3 Conclusion

In this study we present the initial steps towards the development of an electrochemical redox cycling sensor dedicated to the scalable, single-cell, intracellular monitoring of neurotransmitters. We started out by carefully identifying the challenge associated with the proposed measurement and devised theoretical and numerical models to guide us in the sensor design. In a first implementation, we described the fabrication of interdigitated electrodes aimed at the detection of analytes concentrations in the hundreds of micromolar. Such IDEs benefit from a simple, high-throughput manufacturing process.The final strategies we adopted allowed us to fabricate vertically stacked individually addressable electrodes separated by only 75 nm with ease and great reliability. The result is a multi-electrode array (MEA) on top of which adherent cells can be cultured to enable multisite sensing.

The redox cycling detection scheme proved successful in amplifying the signal of interest (*e.g.*, neurotransmitter oxidation) up to a current per molecule of 1.5 fA. Even for central nervous system neurons holding but a few thousands of neurotransmitter molecules within their cytosol this sensitivity should result in a large readout current in the picoamps range which is an improvement compared to other intracellular electrochemical measurement techniques (Mosharov et al., 2003; Rawson et al., 2015). We found that electrode functionalization with a mercapto propionic acid self-assembled monolayer was a convenient solution to limit the fouling of the electrode during detection of dopamine by redox cycling. The resulting sensor was capable of detecting dopamine in a 1:10 background of ascorbic acid and was found to be four times more sensitive to dopamine than one of its precursors: levodopa. Finally, the sensor was capable of detecting the presence of catecholamine in a complex sample composed of whole cell extract.

The sensor was integrated with a nanostructure that is envisioned to enable intracellular penetration and thereby should allow measurement of the intracellular cytosolic levels of relevant biomolecules. This very promising lead of investigation should grant investigators with a new tool that builds upon the previous descriptions of conventional MEA dedicated to extracellular measurement of neurosecretion on one hand (P. Chen et al., 2003; M. Huang et al., 2018; Spégel et al., 2007; X. Sun & Gillis, 2006) and harnessing of nano-electrodes/micropipette for intracellular sensing on the other hand (Larsson et al., 2020; P. Sun et al., 2008). In merging the critical features of both approaches, scalability plus longitudinal monitoring and intracellular access respectively, the proposed device will enable a new workflow of electrochemical investigations of single-cells over multiple sites and prolonged period of time.

3.4 Materials and Methods

3.4.1 Numerical simulation

Finite element modeling of the electrochemical ROc sensors was performed with COMSOL Multiphysics®. The sensors geometry was reproduced in a 2D axisymmetric space to limit computation cost (Supp. Figure 3.11). Mass transport followed the Fick's laws of diffusion given that there was no convection nor electromigration as charges are well screened in aqueous saline solution with physiological salt concentration as were used in this study. The oxidoreduction reactions at the electrode surfaces were modeled as fluxes whose magnitude were determined from evaluating the Butler-Volmer equation at the surface of the electrodes according to:

$$J = -cke^{\frac{\alpha zF\theta}{RT}} \quad (mol/m^2.s) \tag{3.8}$$

where J is the flux of molecules per seconds, c the molecule concentration at the electrode surface in mol/m^3, k the heterogeneous reaction rate was set to 0.1 cm/s, α the symmetry factor was set to 0.5, F is the faraday constant, θ the overpotential, z the number of electrons involved in the reaction, R is the gas constant, T the temperature was set to 298.15 Kelvin. To obtain redox cycling, the overpotential was set to 0.15 volt for one electrode (*i.e.* 0.3 volt versus Ag/AgCl for the oxidation of ferrocenemethanol at a gold electrode) and -0.15 volt for the second electrode (*i.e.* 0 volt versus Ag/AgCl). Current at the electrodes was obtained by integrating equation 3.8 multiplied with the Faraday constant over all electrodes surfaces after rotation of the axisymmetric model. When studying the impact of cell size on redox cycling current, a spherical domain was used to model the cell. The spherical domain was made continuous with the sensor cavity thus representing a perfect intracellular access (no hindrance from partially permeabilized plasma membrane and no leakage to the extracellular bath). The mesh elements were taken as triangular. Meshing of the geometry was carefully optimized with refinements along all electrodes surfaces, corners and edges. We performed a mesh refinement sweep until no changes of the step amperometric response were observed leading to meshes with about 300 000 elements for the IDE and 500 000 for the VSE sensors.

3.4.2 Interdigitated electrodes sensor fabrication

The fabrication process flow is depicted step by step in the supplementary materials (Supp. Figure 3.12). Before starting the process, fused silica substrates are cleaned in two consecutive baths of piranha solution (three-part sulfuric acid 97% one-part 30% hydrogen peroxide) for 5 min each followed by thorough rinsing in two consecutive ultra-pure deionized water (DIW) bath before spin-drying. A stack of thin metal layers consisting of Ti/Au with thickness 20/250 nm is evaporated using an EVA760 (Alliance Concept, France) e-beam evaporator. The IDEs are patterned through a DUV lithography and ion beam etching process. The substrates are first spin-coated with a 45 nm thick layer of bottom anti-reflective coating (BARC) baked at 195°C for 60s (proximity 100 µm, DS-K101-304; Brewer Science, USA) followed by 250 nm of positive tone M108Y DUV resist baked at 130°C for 90s on a TEL ACT-8 track automated coater (Tokyo Electron Limited, Japan). The photoresist pattern was defined on an ASML PAS 5500/350C stepper (ASML, The Netherlands) with exposure parameters of 34 mJ/cm^2, -0.3 µm defocus. The pattern on the mask used corresponded to an IDE of 200 nm width and 200 nm gap but the dose of the exposure was optimized to obtain width and gap of the photoresist digits of 120 nm and 280 nm in order to account for pattern enlargement during ion beam etching. Development of the photoresist and BARC was performed with a post-exposure bake of 90s at 130°C followed by development in TMA238WA (JSR Corporation, Japan) for 60s puddle contact time. Gold is then etched using Ar$^+$ ion bombardment using a IBE350 (Veeco, USA) set to 500 V acceleration voltage, 800 mA beam current and with a stage tilt with respect to the incident beam of -5°. The etching is monitored using an integrated secondary ion mass spectrometer (SIMS) and stopped 19s after the appearance of the titanium signal. Because titanium etches considerably slower than gold under Ar$^+$ ions bombardment, it was etched for 20s with a separate inductively coupled plasma process using Cl_2/BCl_3 chemistry (STS Multiplex ICP; SPTS Technologies, UK) in order to prevent excessive shrinking of the pattern. The tapered shape of the IDE digits originates from the beam incidence tilt used during ion beam etching . This tilt is necessary to avoid redeposition of the sputtered material which at 0° beam incidence was found to occasionally result in shortening of the IDEs. On the other hand, excessive Ar$^+$ ion etching resulted in shrinking of the tapered electrode. Balancing the DUV photoresist patterning and the two subsequent etching steps is the most sensitive part of the process although easily reproducible.The photoresist and BARC are then removed thoroughly by subjecting the substrate to a long oxygen plasma etching at 500 W with an oxygen flow of 400 mL/min for 7 min using a TePla 300 microwave plasma system (PVA TePla, USA). When stripping the resist in this manner the wafers were positioned vertically using a quartz holder. In the next step, a 2 µm thick layer of polyimide is spin coated and cured before plasma enhanced chemical vapor deposition (PECVD) of a layer of silicon carbide and silicon dioxide. Before polyimide coating, the substrates were dehydrated for 10 min in a convection oven set at 150°C. A quick oxygen plasma with the same parameter as above was applied to remove any organic contaminants. The substrate were then immediately spin coated (WS-650,Laurell Technologies, USA) by manual dispensing of 3 mL over static substrate with a solution of aminopropyl triethoxysilane silane (VM-652 adhesion promoter;

HD Microsystems, USA) before spinning for 30s at 3000 RPM under nitrogen stream. PI2610 polyimide (HD Microsystems, USA) was spin coated (LSM-200; Sawatech, Switzerland) at 3000 RPM for 40s to obtain a final thickness (after curing and hard bake) of 2 μm. After spin coating the polyimide was cured by direct contact of the substrates with a hotplate (HP-401Z, Sawatech, Switzerland) at 65°C for 3 min and 105°C for 3 min. The polyimide was hard baked in a convection oven (T6060; Heraeus, Germany) for 1 hour at 300°C under nitrogen atmosphere above 200°C. Before the PECVD deposition the substrates were exposed to a mild oxygen plasma 100 W with an oxygen flow of 400 mL/min for 1 min to roughen the polyimide surface in order to improve adhesion. Robust adhesion of the silicon based dielectric to polyimide is critical to the final device stability especially for experiments involving weeks-long cell cultures in aqueous saline conditions. A thin adhesion layer of silicon carbide was thus deposited (35 nm; chamber pressure of 1000 mTorr, gaz flow of 750 sccm of 2% SiH4 in Ar and 70 sccm of CH4, 20 Watts RF) before silicon dioxide (320 nm; chamber pressure of 1000 mTorr, gaz flow of 400 sccm of 2% SiH4 in N2 and 710 sccm of N2O, 20 Watts RF) using a Oxford Plasmalab System 100 (Oxford Instruments, UK) with a deposition chamber temperature set to 300°C. In step D) the NVs are defined in a similar way as in chapter 2 section 2.5.1. A 2 μm thick layer of AznLoF2020 photoresist (MicroChemicals, Germany) is spin coated and 2.25 μm diameter openings are defined by exposure with a VPG200 direct laser writer (Heidelberg, Germany) with a 355 nm UV light dose ranging from 9 to 15 mJ/cm^2 depending on the nanovolcano geometry. As discussed in chapter 2 section 2.5.1, the optimal exposure dose resulting in straight photoresist side walls had to be optimized. The post-exposure bake is conducted at 110°C with 100 μm proximity gap for 75s followed by 51s contact time development with AZ MIF726. The substrates are then subjected to ion beam etching as described above but with 0° incidence angle. Etching is stopped 2 min after the disappearance of the silicon signal on the SIMS detector. The photoresist is removed and the cavity below the NV is formed with oxygen plasma as described in step B) except that the wafer was lying flat in the chamber (for better homogeneity) and that the etching time was prolonged for a total duration of 20 min or until the under-etching of the polyimide reached a diameter of 20 μm. SEM images were acquired using a Merlin SEM (Zeiss, Germany) with an extraction voltage of 1.5 kV and a beam current of 30 pA and a secondary-electron detector. The wafers were diced on a DAD321 (Disco, Germany) with a resinoid blade of 70 μm width under 25000 RPM rotation moving at 1 mm/s from the top side of the wafer. A glass O-ring was glued on top of the individual chips using PDMS and cured overnight at 60°C in a convection oven.

3.4.3 Vertically stacked electrodes sensor fabrication

The fabrication process flow is depicted step by step in the supplementary materials (Supp. Figure 3.13). Before starting the process, fused silica substrates are cleaned in two consecutive piranha baths (three-part sulfuric acid 97% one-part 30% hydrogen peroxide) for 5 min each followed by thorough rinsing in two consecutive ultra-pure deionized water (DIW) bath before spin-drying. In step A) a stack of thin metal layers consisting of Ti/Au/Cr with thickness 7/50/70 nm is evaporated using an EVA760 (Alliance Concept, France) e-beam evaporator.

In step B) The sacrificial chromium layer is patterned into disks of 100 μm of diameter with bean-shaped openings that will define the SiO_2 pillars. This is achieved by spin-coating the substrate with a 600nm thick AZ ECI 3007 i-line photoresist (MicroChemicals, Germany) with an ACS Gen 3 automated spin-coater (Süss MicroTec, Germany). The desired pattern is then exposed using a MA6GEN3 mask aligner (Süss MicroTec, Germany) in i-line mode (365 nm) with a dose of 165 mJ/cm^2 and developed with the same automated coater starting with a 60s post-exposure bake with a proximity of 100 μm to a hotplate set to 110°C , cooling down for 15s on a cool plate and subsequent development in AZ MIF726 developer with a total contact time of 27s. Before etching the resist is reflown by direct contact with a Sawatec HP200 hot plate (Sawatec, Switzerland) set to 125°C for 60s. This step together with the use of a thin photoresist layer and a tilt of the stage during the next etching step is critical to prevent fences formation along the pattern by redeposition of the etched material during ion beam etching. Chromium is then etched using Ar^+ ion bombardment using a IBE350 (Veeco, USA) set to 300 V acceleration voltage, 500 mA beam current and with a stage tilt with respect to the incident beam of -30°. The etching is monitored using an integrated secondary ion mass spectrometer (SIMS) and stopped 5s after the appearance of the Au signal. The photoresist is then partially removed by carefully subjecting the substrate to a short oxygen plasma etching of 100 W with an oxygen flow of 400 mL/min for 1 min using a TePla 300 microwave plasma system. Without initial dry etching, the photoresist layer is unremovable using wet resist stripping alone. This is because the top layer of photoresist has become hardened from ion implantation during Ar^+ ions bombardment in the previous step. This hardening effect is proportional to ion beam acceleration voltage, beam current and total etching time hence the use of a moderate acceleration voltage above. Short time of oxygen plasma etching with moderate power did not result in etching of the chromium underneath as evidenced by features dimension unaffected within the resolution afforded by optical microscopy. Finally, the bulk of the photoresist layer is removed by immersion in two consecutive baths of 70°C Remover 1165 (Dow Chemical Company, USA) for 5 min each before rinsing in two consecutive DIW baths and spin-drying. In the following steps C), E) and G) the same workflow for photolithography and etching is used with the same machine and materials (*i.e.* Az ECI 3007). Accordingly, in step C) the underlying Au electrode, leads and contact pads are defined by photolithography, etching and careful resist removal as described above. In step D) a 200 nm layer of SiO_2 is deposited by plasma enhanced chemical vapor deposition (PECVD), see supplementary figure 3.15 for detailed deposition parameters, on an Oxford plasmalab system 100 (Oxford Instruments, UK). In step E), the SiO_2 layer is patterned to open the contact area to the chromium layer. In this step the bean-shaped openings in the chromium layer that were filled by SiO_2 in the previous step are protected from etching by the photoresist mask thereby creating the SiO_2 pillars. In step F) a stack of thin metal layers consisting of Cr/Au/Ti with thickness 5/60/7 nm is sputtered using a DP650 (Alliance Concept, France). The use of sputtering over evaporation is to ensure good step coverage of the underlying SiO_2 pattern. In step G) the metal stack is patterned as in step C) and E). At this point the resistivity from one electrode's contact pad to the second forming the electrode pair can be measured to verify the good inter-layer contact and was between 3 and 4 kΩ with our design. In step H) a second layer of SiO_2 of

300 nm thickness is deposited by PECVD as described above. In step I) the NVs are defined starting with a 2 μm thick layer of AznLoF2020 photoresist (MicroChemicals, Germany) is spin coated and 2.25 μm diameter openings are defined by exposure with a VPG200 direct laser writer (Heidelberg, Germany) with a 355 nm UV light dose of 13 mJ/cm^2, again different from the manufacturer's recommended dose as described in chapter 2, section 2.5.1. The post-exposure bake is conducted at 110°C with 100 μm proximity gap for 75s followed by 51s contact time development with AZ MIF726. In this step the photoresist reflow is omitted and substrates are immediately subjected to ion beam etching as described above but with 500 V beam acceleration voltage, 800 mA beam current and 0° incidence angle. Etching is stopped 1min10s after the appearance of the chromium signal or as soon as the Au signal arising from the bottom electrode etching appears. Photoresist is removed as described above. SEM images were acquired using a Merlin SEM (Zeiss, Germany) with an extraction voltage of 1.5 kV and a beam current of 30 pA and a secondary-electron detector. The wafers were diced on a DAD321 (Disco, Germany) with a resinoid blade of 70 μm width under 25000 RPM rotation moving at 1 mm/s from the top side of the wafer. A glass O-ring was glued on top of the individual chips using PDMS and cured overnight at 60°C in a convection oven.

3.4.4 VSE device Preparation

Individual VSE devices were cleaned with a 3 min oxygen plasma (100 W, 650 mTorr; Diener Electronic, Germany) followed by immediate filling of the glass chamber with pure ethanol to ensure proper wetting of the inside of the NVs. The glass chamber content was then exchanged with DIW 6 times and chromium wet etchant 2 times (TechniEtch Cr01, MicroChemicals, USA). The etching of the chromium layer was accelerated by biasing the electrode to oxidizing potentials as described by Sparreboom et al., 2008. All NVs of the device were shorted and connected to the working electrode of a Stat.h bipotentiostat (Ivium, The Netherlands). The counter electrode used was a platinum wire and the reference electrode was a saturated Mercurous/Mercurous sulfate electrode (OGR011; Origalys, France). The working electrodes were biased by +150 mV with respect to the open circuit potential and the current and charge passed was monitored for 2 min (Supp. Figure 3.14). Completion of the chromium etching was assessed by the charge passed reaching a plateau (1.33 mC for our design). From this point onward, the glass chamber was never dried and any liquid exchange was performed by leaving a small amount to ensure the device would not dry which could result in sticking of the electrodes pair due to surface tension (not tested).The glass chamber content was exchanged 6 times with DIW. When applied, 3-mercaptopropionic acid (M5801, Merck, USA) functionalization was carried out from a 100 mM solution in pure ethanol for 24h at room temperature. The glass chamber was rinsed twice with ethanol and 6 times with DIW to wash off the excess MPA. Before characterization, the glass chamber was rinsed 2 times with a solution of KCl 250 mM and the device yield was assessed at this point by biasing the electrodes of a given NV to different potentials (*e.g.* 0 mV top electrode and +500 mV bottom electrode) and counting out the NV whose electrodes were shorted as evidenced by current overload.

3.4.5 Thin Film Stress Measurements

Residual stress measurements of PECVD deposited thin films of SiO_2 and Si_3N_4 were carried out on different four inches 525 μm thick substrates: <100> p-type silicon, <100> p-type silicon with 500 nm wet oxide and fused silica. The substrate radius of curvature was measured before and after deposition using a FLX 2320-S (Toho Technology, USA) and the thin film stress was found using the Stoney equation.

3.4.6 Cell culture

Rat pheochromocytoma 12 cells were obtained from the European Collection of Cell Cultures. Cells from passage 10 to 15 were used. The cells were kept in RPMi-1640 supplemented with Glutamax (61870036, ThermoFisher, USA), 10% heat-inactivated donor equine serum (26050070, ThermoFisher), 5% fetal bovine serum (F9665, Merck) and 0.4% penicillin/streptomycin (P4333, Merck) solution within a 37°C incubator under 5% CO2 and 100% humidity atmosphere.

3.4.7 Cell lysate preparation for on-chip ROc analysis

PC12 cultures were washed twice in ice-cold PBS and cells collected by pipette dislodgement from their substrate. The number of cells was assessed by counting on an automated hemocytometer (TC20^{TM}; Bio-Rad, USA) after trypan blue staining. The cell suspension was centrifuged at 2000 g for 2 min. The supernatant was discarded and the cells resuspended and incubated in Cell lytic (C3228, Merck) lysis buffer with 125 μL per millions of cells. The lysate was centrifuged for 10 min at 15 g and the supernatant was used for on-chip analysis

3.4.8 Catecholamine Fluorometric Assay

Quantification of catecholamine in PC12 cultures was carried out with a fluorometric measurement following the reaction of catecholamine with 3-hydroxyphenyl boronic acid (X. Liu et al., 2019). We used a different lysis protocol with a homemade lysis buffer of known composition. We expect the estimate of total catecholamine per cell using this lysis method to be more accurate thanks to protein denaturation from trichloroacetic acid (TCA). The PC12 cells culture were prepared and a cell suspension was obtained as described above. After centrifuging at 2000g for 2 min, the supernatant was discarded and the cells resuspended in 100 μL PBS to which we added 100 μL of TCA at 0.5 M and sonication at room temperature for 10 min. The TCA was neutralized by addition of 22.8 μL of KOH 2M and the resulting solution was serial diluted to obtain three samples diluted according to a semi-log scale. The three diluted samples per culture were pipetted into a 94-well plate together with concentration standards of dopamine used as calibration. All culture and calibration samples were then mixed with 160 μL of 25 mM Na_2CO_3 (pH = 10.5) and 200 μL of 8 mM 3-hydroxyphenyl boronic acid and imaged after 10 min incubation at room temperature protected from light. Samples were

excited at 417 nm and fluorescence measured at 464 nm with a bandpass of 10 nm on both filters. The optimal gain was assessed on the calibration samples of highest concentration and kept constant throughout all readings. The calibrations yielded the following regression equation: concentration $(\mu M) = 0.0244 F/F0 + 1.71$ where F is the fluorescence intensity at 464 nm and $F0$ is the background fluorescence of a blank sample. The regression determination coefficient R^2 was equal to 0.996.

3.4.9   Sensors characterization

For characterization purposes devices were flushed with an aqueous saline solution (250 mM KCl) of ferrocenemethanol (335061, Merck), dopamine hydrochloride (H8502 Merck), levodopa (D9628, Merck), ascorbic acid (A92902, Merck) alone or combined as specified in the text. The devices were connected to a Ivium stat.h bipotentiostat (Ivium, The Netherlands) together with a platinum wire used as a counter electrode and a KCl saturated reference silver/silver chloride electrode (MF-2056; BaSi, USA) serving as reference electrode. Cyclic voltammograms were acquired at scan rates of 10 to 50 mV/s. Amperometric step responses were acquired with a sampling period of 1 ms. Both cyclic voltammograms and amperometric responses were low-pass filtered at 10 Hz to decrease noise. For the long term effect of cell culture media on the sensor performance, VSE devices functionalized with MPA were filled with RPMI medium supplemented as described above and kept in an incubator under a 37°C, 5% CO2 and 100% humidity atmosphere.

3.5   Supplementary Materials
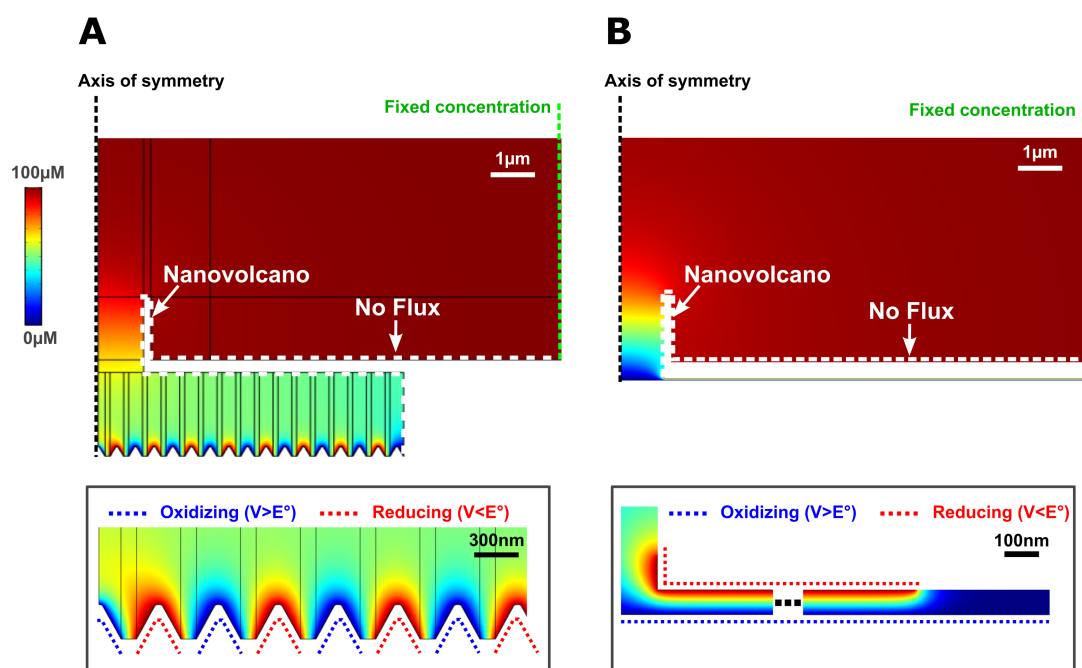
Figure 3.11: Finite element models of the IDE and VSE sensors performing redox cycling in an aqueous solution containing 100 μM of an electroactive molecule after equilibrium was reached. The concentration scale bar in (A) applies to both graphs. The models are cropped vertically. On both graphs, the black dashed line indicates the axis of symmetry around which the 2D model is rotated to obtain current densities per unit of squared meter. The implementation of heterogeneous reaction taking place at the electrodes (oxidation/reduction) was modeled as fluxes across the electrodes surface, flowing out of the domain for the consumed reactants and into the model for products, whose magnitudes were defined according to the Butler-Volmer equation evaluated at the electrodes surface. This approach has the advantage of being implementable on any finite element modeling software without the need for additional subscription-based packages. The regions of the models defined as electrodes (hence where the Butler-Volmer condition was imposed) are highlighted in (A) and (B) within the black box. Dashed blue and dashed red lines indicate electrodes set to a potential above (oxidizing) or below (reducing) the formal potential of the electroactive molecule. The white dashed lines correspond to solid boundaries consisting of insulating material (*e.g.,* silicon dioxide) hence across which flux is prohibited. The green dashed lines correspond to the limit of the model where a constant concentration of the electroactive molecule is imposed, reflecting the influence of the solution bulk. This boundary is also imposed on the top of the model cell but is not visible in these images (cropped). In (A) the black solid lines are the geometrical delimitation of the domains which were used for adaptive meshing but have no influence on the simulation of mass transport. For electrodes set to potentials sufficiently apart from the electroactive molecule's formal potential, oxidoreduction rates at the electrode surface are negligible and the simulation boils down to a mass transport problem influenced only by i) the molecule diffusion coefficient and concentration and ii) the geometry of the model; the nanogap distance in particular. In the simulations, mass transport follows Fick's laws of diffusion as there was no convection and the physiological concentration of salt used in this study precluded electromigration. Visually, the gradient of color in between electrodes of opposing potentials represents the gradient of concentration. Steeper gradients result in faster mass transport and increased redox cycling current.

84
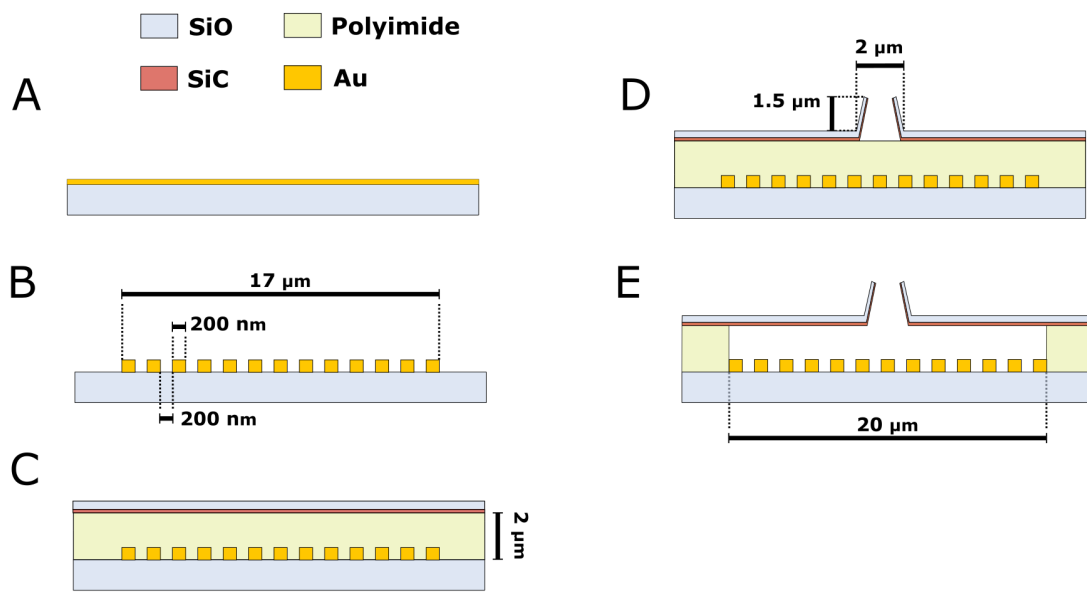
Figure 3.12: Interdigitated electrodes sensor fabrication process. See Materials and Methods for detailed description (A) Metal evaporation, (B) electrode and leads patterning, (C) polyimide spin-coating and curing followed by plasma enhanced chemical vapor deposition of silicon carbide + silicon dioxide, (D) patterning of nanovolcanoes and access holes to contact pads, (E) cavity etching by isotropic oxygen plasma.
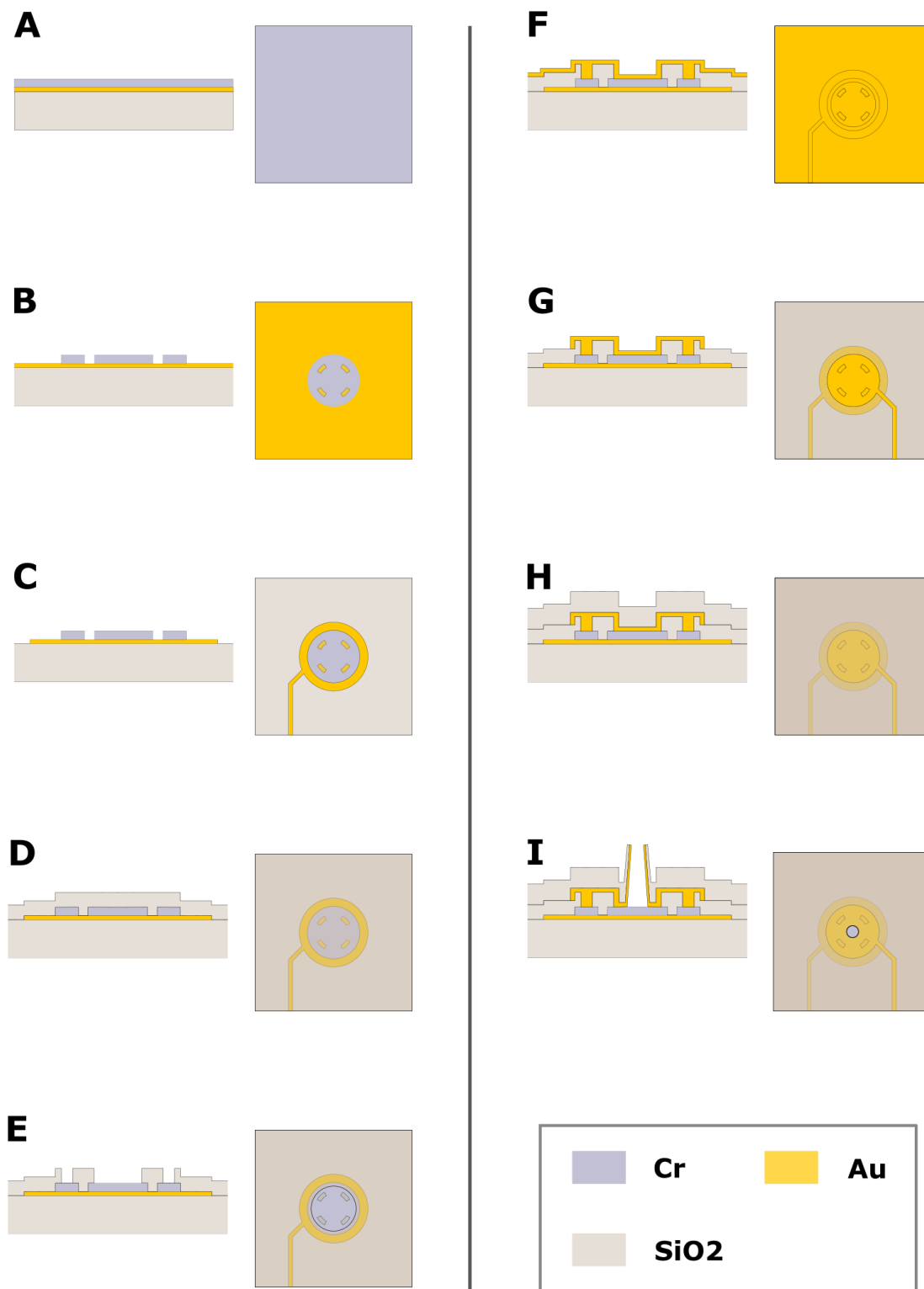
Figure 3.13: Vertically stacked electrodes sensor fabrication process. See Materials and Methods for detailed description (A) Metal evaporation, (B) sacrificial chromium layer patterning, (C) bottom electrode, lead and contact pad patterning, (D) plasma enhanced chemical vapor deposition (PECVD) of silicon dioxide, (E) patterning of the silicon dioxide, (F) top electrode metal sputtering, (G) top electrode, lead and pad patterning, (H) second PECVD of silicon dioxide and (I) patterning of nanovolcanoes and access holes to contact pads.
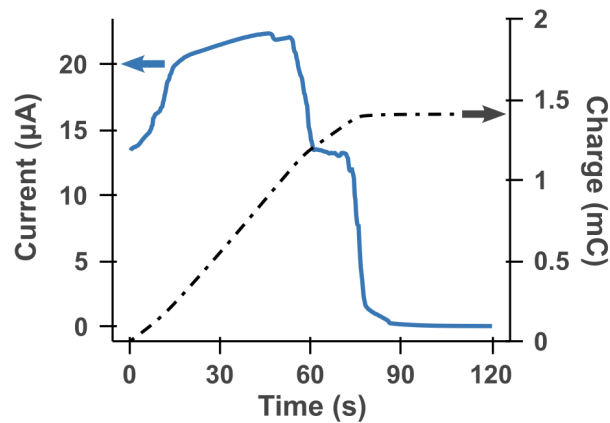
Figure 3.14: Sacrificial chromium layer removal by potential assisted wet etching. The graph displays the current passed (left y-axis) and total charge (right y-axis) monitored over the whole etching process lasting 2 min for a device housing 28 sensors. The current is seen to decrease abruptly at 60s and a second time at 85s since this design included two versions of the VSE sensor: one with silicon dioxide pillars and one without (14 devices of each design). Completion of the chromium etching is visible from current dropping below tens of nanoamps and the charge passed reaching a plateau (1.33 mC in this case).

Wafer N°	Substrate	Machine	Material deposited	Temp. (C)	Time (mn,s)	Thickness (nm)*	SiH4/N2 (sccm)	N2O (sccm)	NH3 (sccm)	Pressure (mTorr)	RF power (W)	measured stress 0° (MPa)**	measured stress 90° (MPa)**
	Silicon												
WSi25	Si test	Oxford Instrument Plasmalab System (PECVD)	SiO	300	1mn40	100	400	710	0	1000	20	-301.62	-377.15
WSi23	Si test	Oxford Instrument Plasmalab System 100	SiN	300	6mn27	200	1000	0	15	800	40	192.85	207.12
WSiWOX1	Si test + 500nm Wet Oxide	Oxford Instrument Plasmalab System 100	SiO	300	1mn40	100	400	700	0	1000	20	-272.1	-319.91
WSiWOX2	Si test + 500nm Wet Oxide	Oxford Instrument Plasmalab System 100	SiN	300	3mn20	100	1000	0	15	800	40	206.45	211.62
			* Thickness from theoretical deposition rate, not m										
			** Measurement: Wafer bend (Stoney equation), Machine: Toho FLX-2320-S Wafers were rotated to have main flat facing South (0°) or West (90°) to obtain two measurements										
	Glass												
WFS17SiO	Fused Silica	Oxford Instrument Plasmalab System 100	SiO	300	3mn20	200	400	710	0	1000	20	-621.38	-618
WFS15SiN	Fused Silica	Oxford Instrument Plasmalab System 100	SiN	300	6mn27	200	1000	0	15	800	40	-229.88	-230.82

Figure 3.15: Stress measurement of silicon dioxide and silicon nitride deposited by PECVD on different substrates as assessed by wafer bow. Despite equal deposition parameters the resulting residual stresses are markedly different between silicon substrate (with or without oxide) and fused silica substrate which arise from different epitaxial growth. Silicon nitride is often used in conjunction with silicon dioxide to obtain stress free membranes by alternating layers of each material.The measurements reported here show that this approach is however not possible on fused silica substrate as silicon nitride has a large compressive stress.
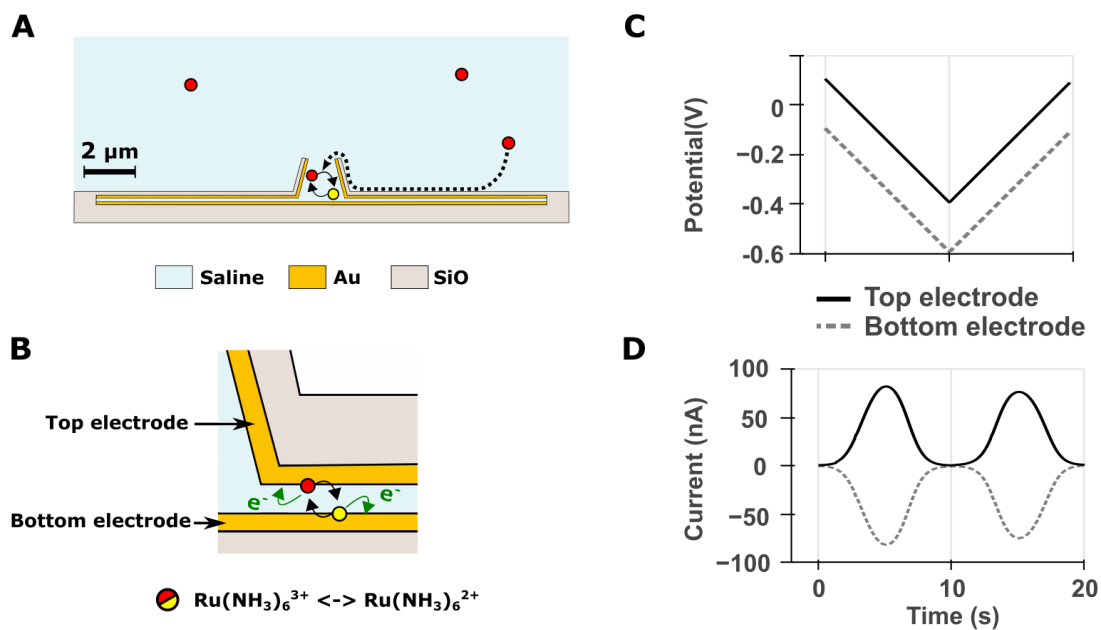
Figure 3.16: Differential cyclic voltammetry detection scheme. (A) Depiction of the VSE sensor in an aqueous saline solution containing a redox probe (B) Enlarged view of the nanogap sketching the redox cycling amplification mechanism. (C) Potential waveform applied to each electrode and (D) Resulting currents measured for a solution of 100 μM hexaammine(III) ruthenium.

A

Expectation (Greene and Rein 1977)		
moles per cell [moles]	Cell number	Total catecholamine [moles]
5.00E-15	1.00E+06	5.00E-09

B

	This study		
Well label	moles per cell [moles]	Cell number	Total catecholamine [moles]
A1	1.73E-15	1.67E+06	2.89E-09
A2	1.27E-15	1.69E+06	2.16E-09
average	**1.50E-15**	**1.68E+06**	**2.52E-09**
B1 (LD 1h30)	3.80E-15	1.89E+06	7.18E-09
B2 (LD 1h30)	2.92E-15	1.68E+06	4.90E-09
average	**3.36E-15**	**1.78E+06**	**6.04E-09**

Figure 3.17: Result of the catecholamine quantification from PC12 cell cultures using a 3-hydroxyphenyl boronic acid fluorometric assay. Cells were lysed with or without pre-treatment with levodopa for 1h30 which is known to increase the total pool of catecholamine in PC12 cells. (A) Previous result of catecholamine quantification in PC12 cultures. (B) Results from catecholamine from PC12 cultures with or without levodopa pre-treatment. The result is in agreement with (A). As expected levodopa increased the catecholamine content per cell.

4 Rapid exocytosis kinetics measured by amperometry within nanovolcano electrodes

This thesis chapter is adapted from our recently submitted manuscript: N. Maïno, A. Bertsch, P. Renaud, "Rapid exocytosis kinetics measured by amperometry within nanovolcano electrodes", *Submitted*, 2022.

4.1 Introduction

Carbon-fiber microelectrodes (CFE) have long been the cornerstone of synaptic mechanisms investigations at the exocytosis level. In a typical experimental setup, the microelectrode is encased in a glass capillary and its tip is polished to expose the core of the fiber. The electrode is pressed against a cell and the release of neurotransmitters is then stimulated by application of a secretagogue through a second pipette while the CFE is biased to an oxidizing potential that will register a current spike for every release event. This method pioneered by Wightman et al., 1991 was first applied to chromaffin cells to record transients following catecholamine release from large dense core vesicles (LDCVs) containing up to several millions of catecholamine molecules released over tens to hundreds of milliseconds. This study and the many that followed making use of the same method have shed light on the mechanisms at play during synaptic or neuroendocrine release from single cells. The attractiveness of the method is threefold. First it achieves unequaled temporal resolution. As an example, the presynaptic bouton of neuron from the central nervous system neuronal cells is home to small synaptic vesicles (SSV) that contains less than 50 000 neurotransmitter molecules and give rise to release events on the sub-milliseconds timescale that could only be measured with the CFE technique so far (Staal et al., 2004). In contrast, optical methods like total internal reflection and super-resolution microscopy applied to vesicle imaging achieve acquisition periods of 1-10 ms at best (Nosov et al., 2020). Secondly, amperometry directly relates the measured signal to the experimental quantity of interest (*i.e.* the number of molecules released) through the Faraday law: $Q = \int i\,dt = nzF$ where Q, the electrical charge in Coulomb, is determined by integrating the current i over time and relates to the number of moles detected n multiplied

by z the number of electrons involved in the redox reaction and F the Faraday's constant. This considerably simplifies the experimental workflow as no calibration is needed. Lastly, amperometry of electroactive neurotransmitters (*i.e.*catecholamines) doesn't require labeling or mediator which again is in contrast with optical methods involving either fluorescent antibodies (Schroeder et al., 1994), membrane bound fluorescent tags (Leopold et al., 2019; Schmoranzer et al., 2000) or fluorescent false neurotransmitters (Gubernator et al., 2009). Unfortunately, the outstanding performance of the CFE technique suffers from two main limitations. First, there is a chance for the released molecules to escape detection at the microelectrode by diffusion away from the electrode. While modeling using random walk has concluded that collection efficiency should be virtually 100% all across the electrode diameter (Bruns, 2004), experimental data seems to indicate that the collection efficiency is worse than expected and leads to underestimation of the quantal size (McCarty et al., 2022). Secondly, the use of CFE with micromanipulator is very work intensive and poses a true limitation on throughput. Multi-electrode arrays (MEAs) fabricated using standard microfabrication techniques on the other hand have the advantages of allowing highly parallelizable experiments. MEAs have long been popular for electrophysiology investigations where measuring attenuated action potential across the intact cell membrane is sufficient, thereby sacrificing signal integrity for throughput. This figure of merit also applies in the scope of exocytosis investigations which has seen several implementations of MEAs dedicated to amperometric measurements of catecholamine releases (M. Huang et al., 2018; X. Liu et al., 2011; Spégel et al., 2007; X. Sun & Gillis, 2006; J. Wang & G. Ewing, 2014). Unfortunately the use of MEAs still suffers from the same limitation as the traditional CFE technique in terms of collection efficiency. In the typical MEA configuration, cells are cultured on arrays of inlaid disk electrodes. Because of this loose interface, the molecules of interest released by the cell tend to spread as they diffuse to the electrode which results in broadening of the signal registered or even loss of molecules. Interestingly, it has been demonstrated that nanostructures reduce the dimension of the cleft between the cell membrane and its substrate significantly (Santoro et al., 2017). Iridium oxide nanotube electrodes have also demonstrated that such nanostructure improve the seal resistance in electrophysiology measurements (Lin et al., 2014). These findings suggest that a disk electrode used for amperometric detection could theoretically improve its collection efficiency through the use of nanostructures to i) reduce the distance between the cell membrane and the electrode and ii) create a confined volume owing to the sealing of the cell/electrode interface.

In an attempt to adapt MEA for scalable yet faithful exocytosis quantification, we applied our sensor developed in chapter 3 composed of a volcano-shaped nanostructures (*i.e.*, the nanovolcano, abbreviated NV) and two underlying electrodes forming a nanogap. We hypothesized that the nanovolcano/nanogap device may improve over previous amperometric measurements of exocytosis by i) enabling high collection efficiency thanks to the confined volume formed by the cell/NV interface and ii) allowing parallelizable experiments by having cells cultured on chips with 28 sensing sites each. Furthermore, since each sensing site house two individually addressable electrodes, we could make use of electrochemical redox cycling

detection to characterize the cell/NV interface. We benchmarked the performance of our devices by amperometric measurements of triggered exocytosis from PC12 cells cultured on NVs. Our devices record quantal size close to the expected value found in the literature. Interestingly, the recorded amperometric spikes take place over a much smaller time scale compared to previous reports; within a single millisecond and down to a couple hundreds of microseconds. We hypothesize that this faster kinetics is the result of deformation of the plasma membrane brought by the nanotopography of the NV. Because the quantal size measured is preserved, we argue that our device is a well behaved sensor that reports the parameter of interest faithfully. Furthermore, it may be used as a novel tool to study the link between membrane mechanosensing ability and exocytosis opening new investigations opportunities.

4.2 Results

4.2.1 Device and mode of operation

The step by step description of the fabrication process is detailed in chapter 3 Materials and Methods section 3.2.5 and Supp. Figure 3.13). Briefly, the device is composed of two stacked gold electrodes covering the wall and ceiling of a cavity accessed through the NV. Figure 4.1 (reproduced from chapter 3) depicts the device components and geometry. A top view and cross-section of the device (Figure 4.1, A; not to scale) depicts the two gold electrodes and NV. The NV measures 2.3 µm in diameter, the top electrode 100 µm in diameter and the bottom electrode 120 µm in diameter. The separation between top and bottom electrodes, which we refer to as nanogap, is only 75 nm yet they never come into contact across their whole surface. Each electrode is contacted with its own lead (*i.e.*electrical connection) and is therefore individually addressable. The top electrode also covers the inner wall of the NV as is discussed later. A collapsed view of the device (Figure 4.1, B; not to scale) allows to see the top and bottom electrodes and the middle layer of silicon dioxide (SiO_2) which houses a critical feature of our design: four insulating pillars keeping the gold electrode separated. Scanning electron micrographs (SEM) (Figure 4.1, C) are showing different views of the device at real scale. The NV is encircled by the egress out of the substrate resulting from the underlying SiO_2 pillars (Figure 4.1, C; i). The NV itself is 1.5 µm tall with walls only 100 nm thick (Figure 4.1, C; ii).

The wafers are diced into individual chips and a glass ring is glued on top of each chip to delimitate a culture chamber using polydimethylsiloxane (PDMS). The chromium sacrificial layer in between the gold electrodes is removed by potential assisted wet etching as described in chapter 3 (section 3.4.4 and Supp. Figure 3.14). The device yield assessed by counting out the NVs whose pair of electrodes were shorted was always over 85% with at least 24 out of 28 devices per chip operational. We characterized the electrochemical behavior of the NV (Supp. Figure 4.6) and assessed the viability of cells cultured on NV (Supp. Figure 4.7) and found a viability of 98.17 ± 0.19% (n=10 field of views centered on different NV).
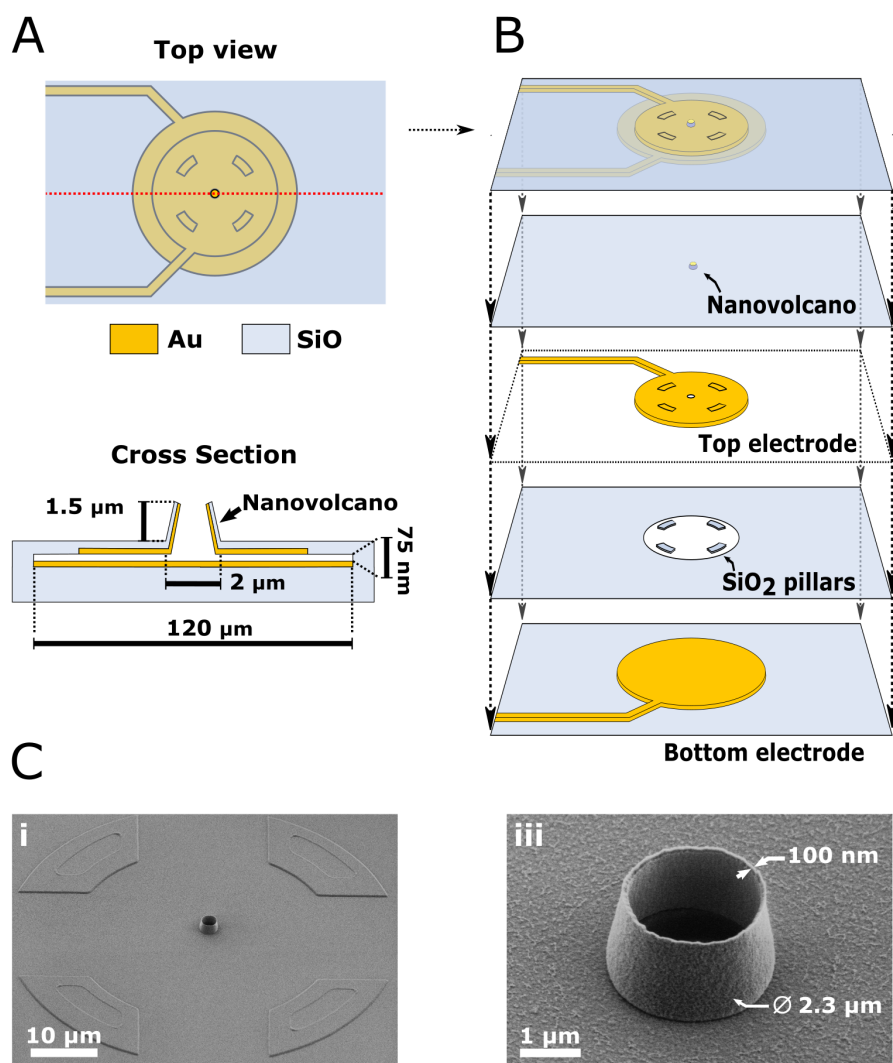
Figure 4.1: Device description. (A) Top view and cross-section of the device (not to scale). The nanovolcano is standing on top of a cavity whose floor and ceiling is covered by a set of individually addressable electrodes. The inter-electrodes distance is 75 nm. (B) device collapsed view showing the different layers (not to scale). From bottom to top: bottom electrode, SiO_2 insulating layer with pillars, top electrode, SiO_2 insulating layer with nanovolcano and all layers combined. The SiO_2 pillars ensure the two electrodes never come into contact. (C) Scanning electron micrographs of the finished device viewed with a tilt. i) Shows the nanovolcano surrounded by the egress from the substrate caused from the underlying SiO_2 pillars. ii) Shows an enlarged view of the nanovolcano.

Throughout most of this study, we used our devices in constant amperometry mode whereby the top and bottom electrodes are shorted and their potential set to an equal potential, positive with respect to the silver/silver chloride reference electrode, aimed at oxidizing the molecules of interest (Figure 4.2, A). Upon stimulation, cells undergo exocytosis and release catecholamines that diffuse to the electrode and are oxidized resulting in spikes in the amperometric trace (Figure 4.2, B). Spikes are then individually analyzed to retrieve their peak current, charge and full width at half maximum (FWHM) (Figure 4.2, C).

On the other hand, we also made use of the two electrodes being individually addressable to leverage a phenomenon known as electrochemical redox cycling to characterize the cell/NV interface. In the redox cycling mode, the potential of the two electrodes are set symmetrically apart from the formal potential of a redox mediator resulting in the mediator molecules undergoing oxidation and reduction up to several hundreds to thousands of times per seconds (Figure 4.2, D). When the two electrodes potential are scanned with an offset (Figure 4.2, E), the resulting current traces therefore show anticorrelated peaks centered at the formal potential of the mediator molecule (Figure 4.2, F).

4.2.2   Amperometric detection of stimulated exocytosis from PC12 cells

We cultured PC12 cells on NVs and conducted amperometric detection of catecholamine release upon stimulation with a recording solution altered to have a higher concentration of potassium (125 instead of 5.5 mM). In order to demonstrate the device's ability to capture biologically relevant fluctuations of exocytosis pattern, we stimulated and measured the resulting catecholamine release events at two different time points on the same culture: one day and three days after plating (Figure 4.3; DIC1 and DIC3 respectively).

Typical recording traces are presented at both time points (*i.e.*DIC1 and 3) over the initial 4 seconds of stimulation (Figure 4.3, A) and show strong, continuous amperometric spikes. Sample amperometric spikes from both time points are displayed over a 10 ms window (Figure 4.3, B). We plotted the distribution of each of these features at both time points on a separate graph over a logarithmic scale (Figure 4.3, C-H). Amperometric exocytosis data pooled from several cells are expected to follow a log-normal distribution (Mosharov & Sulzer, 2005) and were hence fitted with a normal distribution whose parameters (mean and standard deviation) are displayed on the corresponding graph.

4.2.3   Pharmacological manipulation of exocytosis

We then subjected a cell to cadmium, a voltage-gated calcium channel blocker (Shafer, 1998; Taylor & Peers, 1998), in order to assess the ability of our device to resolve pharmacological manipulation of exocytosis. Because adherent cells attach to their susbtrate through calcium dependant integrin (Loftus et al., 1994), we preferred cadmium over calcium chelator or calcium removal.
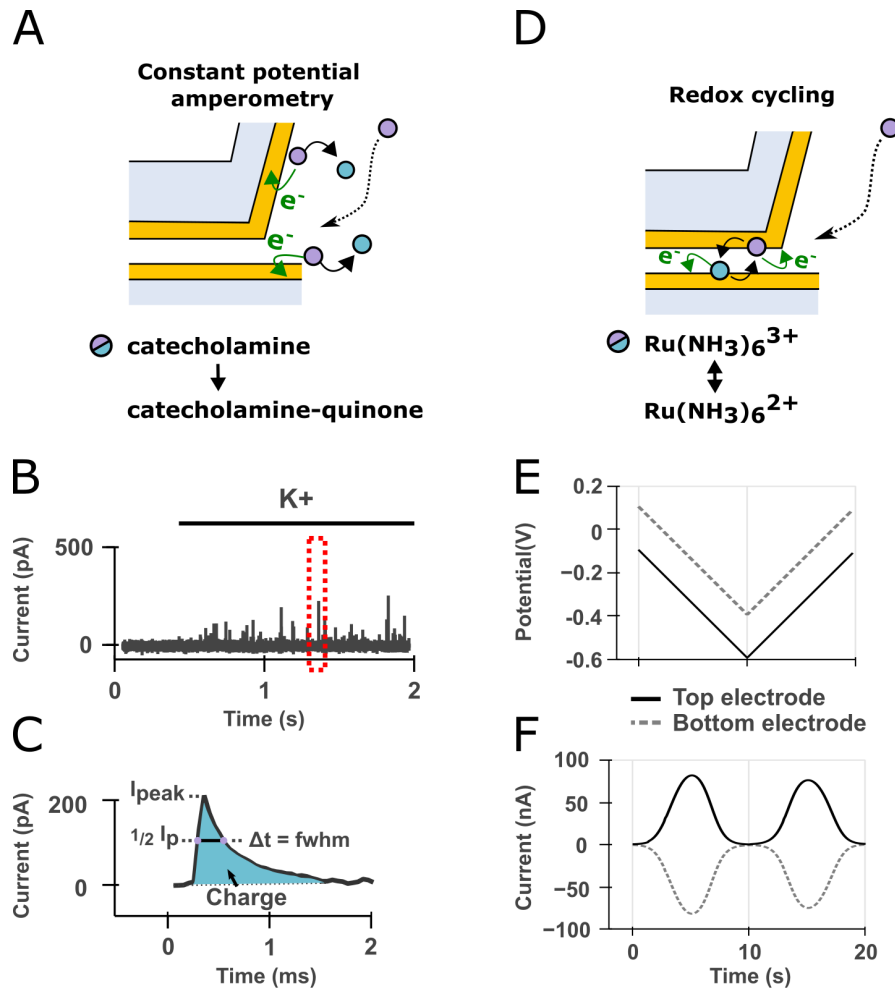
Figure 4.2: Device mode of operations sketched over a cross-section view of the device. (A) In constant amperometry mode the top and bottom electrodes are shorted and kept at a constant potential. Catecholamine molecules released by exocytosis at the cell membrane (not depicted) diffuse to the electrodes and are oxidized to catecholamine-quinones. (B) The oxidation of catecholamine packets originating from single vesicle fusion events are registered as individual spikes on the current trace during cell stimulation with high potassium recording solution. (C) Enlarged view of the dashed red box in (B). Spikes are analyzed individually to extract the total charge (*i.e.* from the area under the curve through Faraday's law (see text), peak current and full width at half maximum (FWHM). (D) In redox cycling mode, the potential of the top and bottom electrodes are set symmetrically apart from the formal potential of a redox mediator resulting in the mediator molecules undergoing oxidation and reduction up to several hundreds to thousands of times per seconds thereby amplifying the recorded current. (E) This can be achieved by scanning the potential of both electrodes with an offset. (F) The current traces will display anticorrelated peaks at the formal potential of the redox mediator.
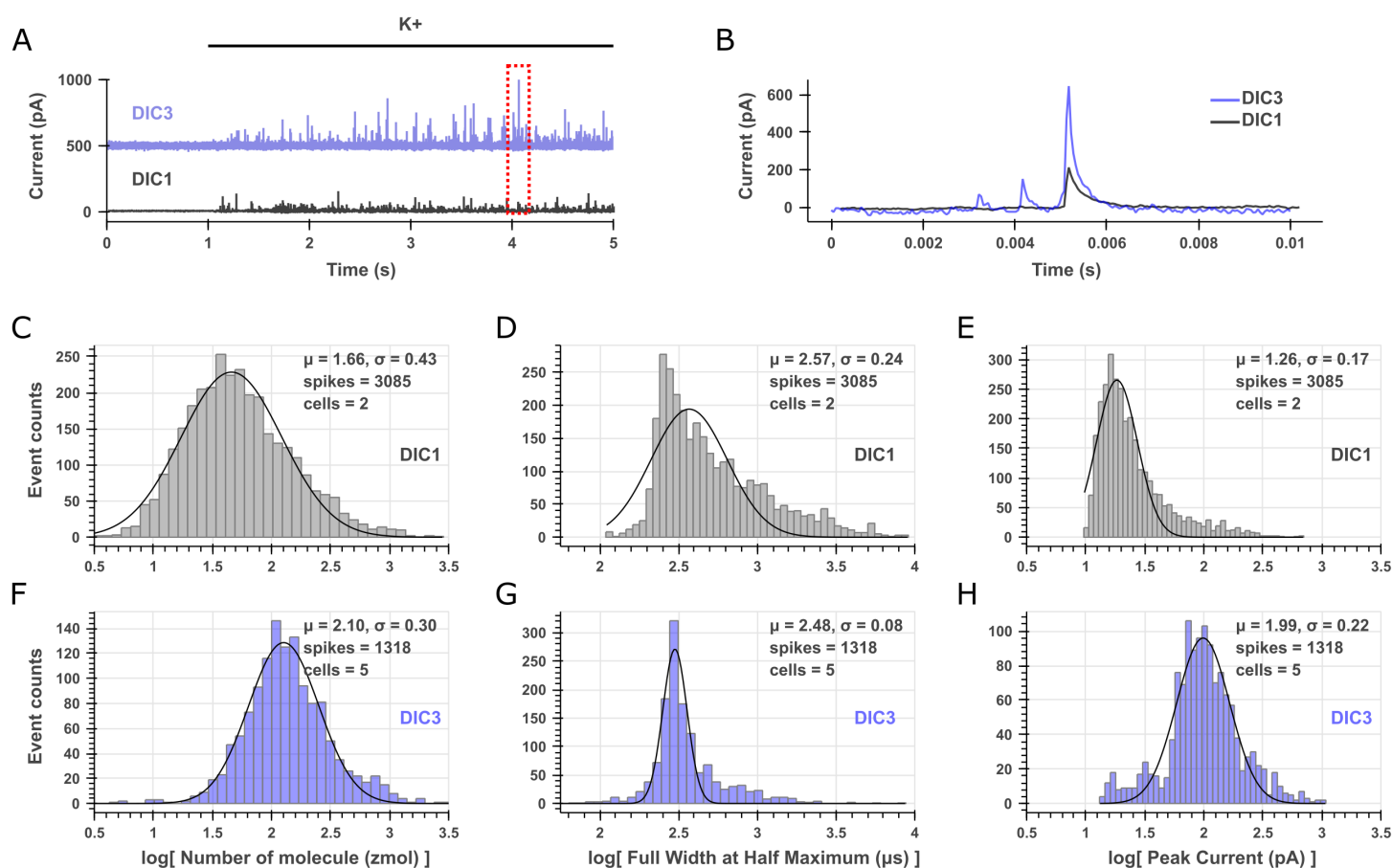
Figure 4.3: Amperometric measurement of potassium-stimulated exocytosis from PC12 cells on nanovolcanoes. (A) Application of an elevated potassium solution provokes exocytosis in PC12 cells although with different features at different time points in culture. (B) Enlargement of the amperometric spikes within the red dotted box in (A). Spikes at DIC3 (purple) are often seen to be larger although of roughly same duration compared to DIC1 (black). (C-E) Spike features distributions at DIC1 and (F-H) DIC3. Bars correspond to experimental data and curves to a log-normal distribution fit whose parameters (mean and standard deviation) are displayed on the same graph. Bin sizes were determined using the Freedman-Diaconis Estimator. (C,F) Distribution of the vesicle quantal size obtained through integration of the area under the curve and Faraday's law (See text). (D,G) Distribution of the spikes full width at half maximum defined as the time interval separating crossing of half the maximum current during the rising and falling phase. (E, H) Distribution of the spikes maximum current.
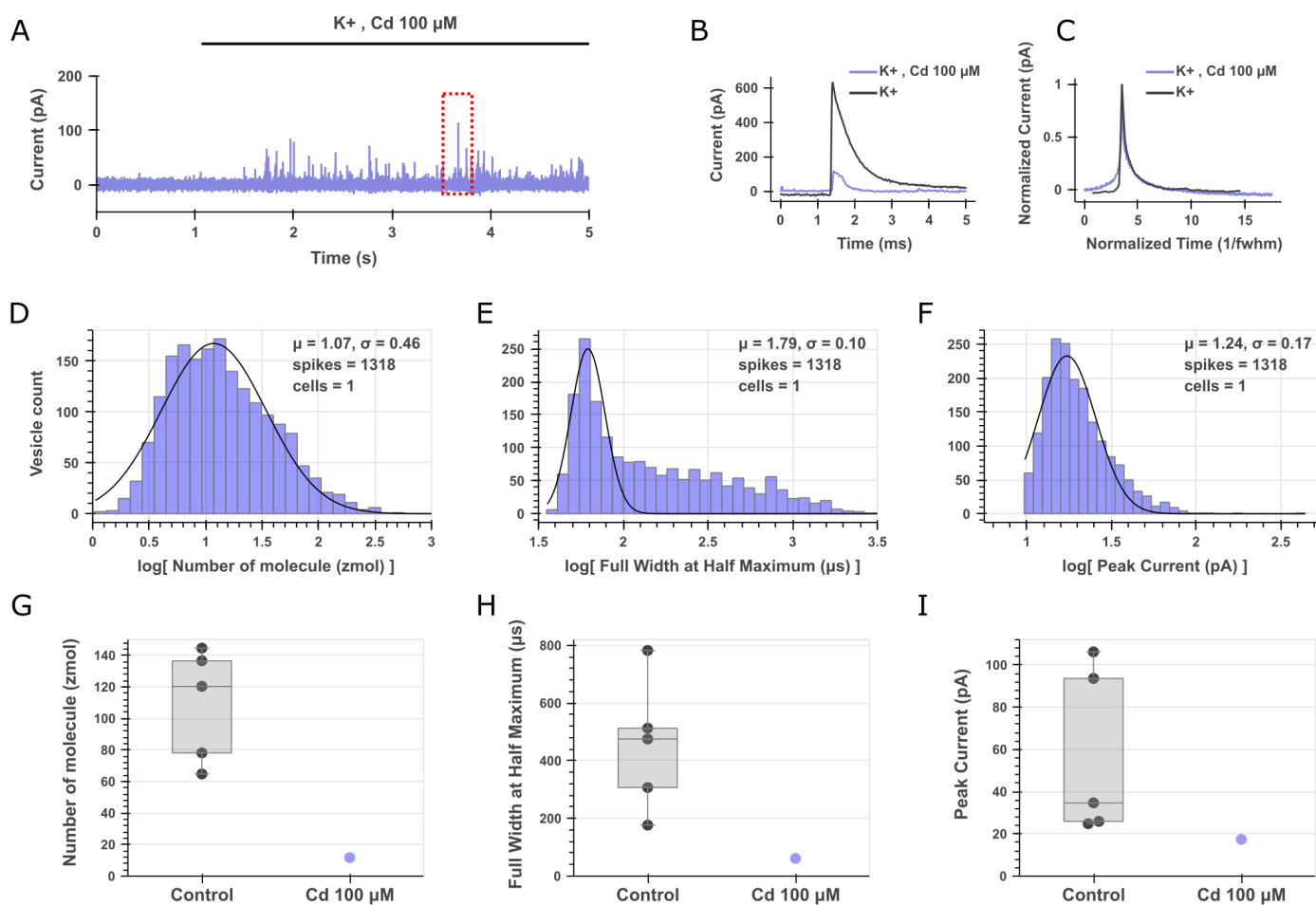
Figure 4.4: Amperometric measurement of stimulated exocytosis challenged with extracellular cadmium from PC12 cells on nanovolcanoes. (A) cadmium fails to inhibit potassium-stimulated exocytosis in a PC12 cell on a nanovolcano. (B) Enlargement of the amperometric spikes within the red dotted box in (A) displayed together with a spike from the previous experiment. (C) Average of the spikes recorded after potassium stimulation with (purple) or without (black) cadmium after normalization to spikes maximum current and full width at half maximum. The two families of spikes are similar in their decaying phase but the cadmium challenged spikes show a slower rising phase. (D-F) Distribution of spikes features during cadmium challenge. Bars correspond to experimental data and curves to a log-normal distribution fit whose parameters (mean and standard deviation) are displayed on the same graph. Bin sizes were determined using the Freedman-Diaconis Estimator. (G-H) boxplot comparing the per cell spikes features of potassium stimulation without (Control, black) or with 100 μM cadmium (purple).

Against our expectations, we observed continuous spiking during the entirety of the challenge. Sample amperometric spikes from the potassium stimulation with or without cadmium are displayed over a 10 ms window for comparison (Figure 4.4, B).The sample spikes displayed are clearly different in term of amplitude. However, spikes need to be normalized with respect to their peak current and FWHM to eliminate the variability due to quantal size difference for a rigorous comparison. Accordingly, all spikes from a given experiment were averaged after normalization in the case of potassium stimulation or potassium stimulation with cadmium and displayed over a time window of 15 times the FWHM (Figure 4.4, C).

Spikes features were computed as above and the distribution of spikes features is displayed on separate graphs over a logarithmic scale (Figure 4.4, C-H). As a summary, we compared spike features obtained from potassium stimulation with or without concurrent cadmium challenge using boxplot (Figure 4.4, H-I) where each data point is the average from one cell.

4.2.4 Finite element modeling of exocytosis within nanovolcanoes

In order to study the kinetics of the amperometric spikes measured, we performed finite element modeling (FEM) of catecholamine release from a vesicle, diffusion of the catecholamines and collection by amperometry within the NV. The simulation of fusion pore opening is a difficult problem given that the model has to be both time dependent and change its geometry over the course of vesicel fusion (Amatore et al., 2010). Accordingly, we took another approach in which we treated vesicle fusion as a total and instantaneous release making our model rely on diffusion and oxidation rate at the electrode only.

We constructed a 3D geometry representing the nanovolcano and closed its top surface with an impermeable boundary representing the cell membrane (Figure 4.5, A cross-section). The bottom (1), top (2) and wall (3) domains as labeled on the cross-section represent electrode surfaces that will oxidize catecholamine molecules (see Materials and Methods for detailed implementations of the electrodes boundaries). The vesicle was modeled as a spherical domain with a fixed concentration of 0.6 M of a molecule with diffusion coefficient of $4.1\text{x}10^{-8}$ cm^2/s inside the vesicle and $6\text{x}10^{-6}$ cm^2/s everywhere else which are typical of catecholamines in the vesicle matrix (Amatore et al., 2000) and aqueous medium respectively(Gerhardt & Adams, 1982). The quantal size was taken from our experimental results (Figure 4.3, F) as 125 zeptomol or 75 814 molecules. The position of the vesicle was varied along the radial axis but kept at a constant height, with its hemisphere across the no-flux boundary modeling the cell membrane.

We first looked to ascertain whether or not the NV inner wall is conductive and participating in the electrode active surface area. Previous electrochemical impedance spectroscopy data (Desbiolles, de Coulon, et al., 2019) and scanning electron microscope (SEM) images of NV cross-section (Desbiolles, Bertsch, et al., 2019) have demonstrated that the inner wall of the NV is covered with metal redeposited by secondary ion sputtering during fabrication. However in the current study the thickness of metal etched that generated secondary ion
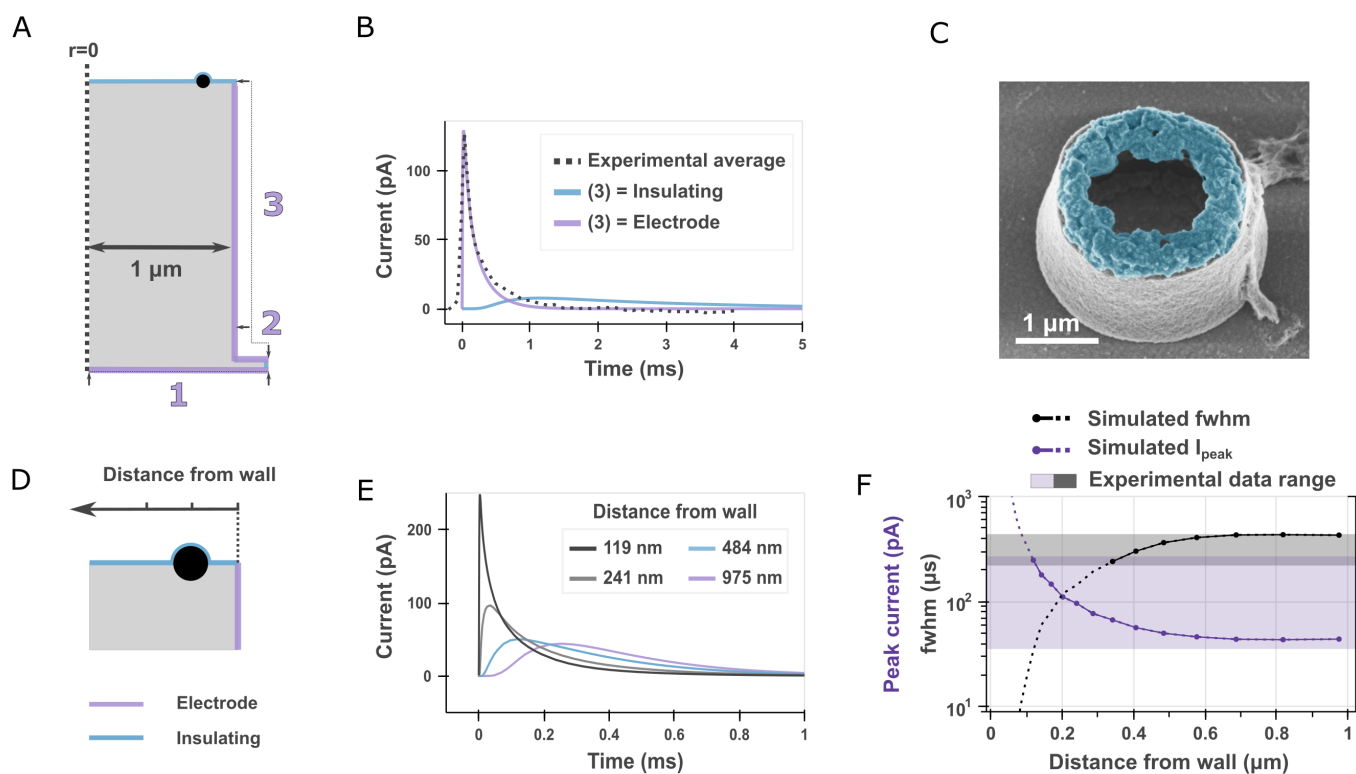
Figure 4.5: Finite element modeling suggests an accelerated vesicle fusion kinetics at the cell/nanovolcano interface. (A) Schematic depicting a cross-section of the simulation geometry (cropped at r=0). Boundaries in purple are modeled as electrode surfaces by imposing a Butler-Volmer boundary condition (See chapter 3, section 3.4.1) while boundaries in blue are no flux conditions. The vesicle is shown as a black sphere of defined concentration and quantal size. (B) Simulated amperometric spikes when domains 1 and 2 are set as electrodes while domain 3 is either taken as an electrode (purple) or insulating (blue) surface. The black curve is the average of the experimental spikes obtained during potassium stimulation. A good fit to the experimental data is observed when domain A is taken as an active electrode surface. (C) Scanning electron micrographs of a nanovolcano electrodeposited with platinum under a tilted view. The electrodeposited platinum was highlighted in blue in image post-processing. The circular outgrowth of platinum along the nanovolcano inner wall supports the results in (B). (D) Detailed view of the simulation geometry highlighting the vesicle position with respect to the nanovolcano wall. (E) Simulated amperometric spikes obtained from vesicles at different distances from the nanovolcano wall. (F) Simulated spike features (peak current in purple, full width at half maximum in black) as a function of vesicle distance from the nanovolcano wall. The dotted line corresponds to simulated spike features that fall outside the variability of the experimental data (displayed as brackets on the right y-axis).

sputtering is significantly thinner (50 nm gold + 10 nm titanium). It was therefore necessary to assess whether or not the inner part of the NV was part of the electrode active surface area to accurately simulate the diffusion processes.

We hence simulated amperometric spikes registered in the case of a conductive or insulating wall (Figure 4.5 A; domain 3 is set as an electrode or insulating boundary respectively) while keeping the vesicle at an arbitrary distance of 200 nm from the wall. The results seem in favor of a conductive wall with the corresponding spike closely matching the experimental average spike (Figure 4.5, B). To further support this outcome we performed platinum electrodeposition over the shorted electrodes of a NV with the hypothesis that in the case of conductive walls the electrodeposited platinum would be localized both on the NV bottom and walls. The SEM micrographs show a regular layer of platinum along the NV inner wall (Figure 4.5, C) providing further evidence of the NV inner wall being conductive.

Having established the electrode's active surface, we simulated the amperometric spikes resulting from vesicles at increasing distance from the wall (Figure 4.5, D). As the vesicle is positioned close to the wall, spikes become taller and narrower. In order to compare the experimental and simulated data, we shaded on the graph two areas that correspond to the range of the experimental data observed (taken as the experimental mean $\pm$ 2 x standard deviation from Figure 4.3, G-H). Put in another way, any simulated data point within the shaded area of corresponding color is within two standard deviations of the experimental mean.

4.3 Discussion

4.3.1 Yield and advantages of the device fabrication process

The merits of the novel fabrication process used to define the electrochemical nanogap were discussed in 3.2.5. Briefly, The fabrication of the device is exceptionally robust considering the pair of electrodes in each NV are separated by 75 nm only in the nanogap region. The yield obtained being consistently above 85% is a marked improvement to the 50% achieved before achieved by Kang et al., 2013 although our nanogap is almost twice as large. Nonetheless, our approach provides two considerable advantages. First, the transparent substrate used grants more flexibility for light microscopy along the cell culture lifetime. Although the NV are located at the center of the opaque metal electrode, transparent metal electrode materials like indium tin oxide could be used to obtain fully optically transparent chips.

Secondly, our fabrication process is largely independent of residual stress in the different layers. This is achieved through the incorporation of SiO_2 pillars in between the two electrodes that ensures that the electrodes remain separated after removal of the chromium layer (Figure 4.1, B).

The individually addressable electrodes pair obtained after removal of the chromium sacrificial

layer is another unique feature of our device. Although not achieved yet, their application to longitudinal, intracelluar electrochemical detection of neurotransmitters using redox cycling was discussed in chapter 3, section 3.2.1.

4.3.2   Exocytotic patterns are differents along PC12 cell maturation

The measurement of potassium-stimulated exocytosis at different time points after passaging were markedly different to one another. It is a common assumption that neuroendocrine secretion is a process that matures along cell development (Johnson et al., 2005). However this assumption is rarely motivated and our data are the first formal corroboration of this phenomenon in PC12 cells to our knowledge and demonstrate the ability of our sensor to resolve fine differences in exocytotic patterns.

In our data, the most striking features of this development are the increased quantal size and narrower FWHM distribution (Figure 4.3, C-D and F-G). In both cases, the FWHM observed were still well below the milliseconds mark (451 ± 91 μs DIC1 and 424 ± 19 μs DIC3; mean ± SEM) which is considerably smaller than the few/tens of milliseconds commonly reported in the literature for PC12 cells (Westerink et al., 2000). Nonetheless, the quantal size measured were in line with the admitted range of 100 000 molecules (Westerink et al., 2000) (30669 ± 3341 catecholamine molecules per spike at DIC1 and 65580 ± 8568 at DIC3; mean ± SEM) The conservation of a typical quantal size despite much shorter events is explained by the large peak currents observed (21.3 ± 1.1 pA DIC1 and 57.0 ± 15.8 pA DIC3; mean ± SEM) as compared to typical values around 10 pA obtained with a conventional CFE.

These atypical spikes features are not an effect of using microelectrodes per se as measurements on MEAs by others also reported FWHM clearly above the milliseconds mark at inlaid disk microelectrodes (X. Sun & Gillis, 2006) and recessed disk microelectrodes (P. Chen et al., 2003; M. Huang et al., 2018; X. Liu et al., 2011).

4.3.3   Cell membrane is accessible for pharmacological manipulation within the nanovolcano

The exocytotic releases were only partially dependent on calcium influx as evidenced by partial inhibition during cadmium challenge (Figure 4.4). The effect of cadmium on exocytosis is visible by comparing the time and current normalized spikes with or without cadmium (Figure 4.4, C). Although the decay phase is similar between both conditions, the initial rising phase shows a lag in the case of cadmium reflecting a mechanistic difference between exocytosis taking place with obstructed or pristine calcium influx. This fine difference in spike waveform is another demonstration of the temporal resolution affordable by our sensor. In terms of spike features, cadmium affects primarily the FWHM (Figure 4.4, E). The distribution of FWHM is markedly broadened although while quantal size and peak currents are reduced compared to the no cadmium condition (Figure 4.4, H-I).

A concern that may arise in that experiment is whether or not the cell-impermeant cadmium ions could reach the portion of membrane covering the nanovolcano. As was shown by transmission electron microscopy (TEM) (Santoro et al., 2017) and voltage sensitive dye imaging (Braun & Fromherz, 2004), the cleft between cells and their substrate range in the tens of nanometers which result in a tortuous diffusion pathway from the bulk of the culture chamber to the inside of the NV. Thanks our novel sensor design encompassing two electrodes operable in redox cycling mode, we were able to dismiss this possible issue by adding a redox mediator to the extracellular bath and performing differential cyclic voltammetry (Supp. Figure 4.8). In fact, the current obtained from the oxidation and reduction of hexaammine(III) ruthenium was found to be very close whether the NV was covered by a cell or not. This highlights that cell-impermeant molecules added to the cell culture bath will reach the inside of the NV eventually.

It could be argued that the redox mediator finding its way in one direction supposes that catecholamine molecules could escape the confined detection volume by diffusing the same way but in the opposite direction during exocytosis. However since the electrode oxidizes molecules almost instantly, the concentration of catecholamine within the NV remains negligible at all times; *i.e.* catecholamines do not accumulate at the electrode. Consequently, the flux of catecholamine escaping the NV through a nanometric slits necessarily has to be small in comparison to the unobstructed flux of molecules to the much larger electrodes of micrometric size.

4.3.4   Diffusion within the nanovolcano has sub-milliseconds timescale

An important question that arises from our data is the cause of the faster release kinetics observed. SSVs present at the neuronal synapse undergo flickering exocytosis with a time scale of hundreds of microseconds (Staal et al., 2004). However, PC12 are reported to essentially secrete catecholamine stored in LDCVs-like vesicles in response to potassium stimulation with a second small vesicle pool containing non-electroactive acetylcholine (Westerink & Ewing, 2008). We have previously analyzed the electroactive molecules found in the PC12 cells used in this study with 3-hydroxyphenyl boronic acid fluorometry and confirmed their catecholaminergic nature (chapter 3, section 3.4.8 and Supp. Figure 3.17). Hence we cannot attribute the release events we observed to another vesicle pool.

It could be hypothesized that the NV conical geometry forms a funnel from the release site to the electrode and that the confined volume of the nanovolcano results in less dilution and hence a steeper concentration gradient from the vesicle to the electrode. This hypothesis is however in disagreement with experimental results using recessed cavity carbon electrodes which register amperometric spikes of similar duration to those from a conventional CFE (McCarty et al., 2022). A significant difference of the NV however lies in the fact that the inner wall of the recess is itself conductive as evidenced by our simulated data (Figure 4.5, B) and *in situ* electrodeposition of platinum (Figure 4.5, C).

Under the assumption of a conductive inner wall of the NV, exocytotic release at varying distances from the wall results in a distribution of spikes of equal charge but varying peak currents and FWHMs (Figure 4.5,E) that captures well the variability of the experimental data (Figure 4.5, F). At large vesicle distance from the wall we see the experimental and simulated data converge to similar values of FWHM (436 μs) and peak current (35 pA). On the other hand, simulated data at vesicle distance from the wall below 500 nm predict faster, taller spikes which are not found within the experimental data. Instead experimental data reach a maximum/minimum in peak current and FWHM respectively that could be attributed to diffusion time becoming small compared to the opening of the vesicle fusion pore. In absence of an appropriate modeling of the fusion pore opening, this observation remains to be confirmed.

Additionally, the present simulation does not allow us to conclude whether exocytosis takes place preferentially from membrane portions close to the NV wall or rather at the center of the NV. In this scope, TEM imaging of the cell membrane conformation within the NV would prove very valuable and perhaps reveal prefenrential vesicle localization close to or far away from the NV wall rim. Still, the conclusion we draw from simulating the impact of vesicle position is twofold. First, simulated diffusion times within the NV are within the experimental bounds and hence do not challenge the plausibility of our data. Second, on top of diffusion being fast (sub-millisecond timescale), the kinetic of vesicle fusion needs to be faster as well since it usually takes place over a few milliseconds (Schroeder et al., 1996).

4.3.5   Hypothetical impact of nanovolcano on membrane tension and cytoskeleton arrangement

The factors influencing vesicle fusion kinetics can be broadly separated into two categories: physicochemical and biomolecular factors. An example of the former and latter could respectively be i) the impact of extracellular ionic composition (Jankowski et al., 1994) and ii) the hypothetical kinetics dependance on the numbers of v- and t- SNARE (soluble N-ethylmaleimide-sensitive factor attachment protein receptor) pairing prior to fusion (Mohrmann & Sørensen, 2012).

A plausible hypothesis to reconcile our observations with admitted vesicle fusion kinetics could be the impact of membrane curvature and tension arising from the sharp NV wall. It was observed by several investigators that hypotonic conditions result in faster, more frequent exocytosis while the converse is true for hypertonic conditions (Borges et al., 1997; Schroeder et al., 1996). The resulting spikes in hypotonic conditions are shorter in duration of both the rising and decaying phase of the spikes which are associated with rate of opening of the fusion pore and diffusion of catecholamine out of the vesicle matrix (Schroeder et al., 1996) yet with conserved quantal size (Amatore et al., 2003). Our experiments did not involve osmolarity manipulation yet a possible role of the plasma membrane tension in the fast exocytosis kinetics we observe is plausible since it was demonstrated that membrane deformation

brought by nanotopography induces membrane tension (Xie et al., 2013). Although the cell membrane was shown to be able to accommodate microscale vertical features from its substrate (Dipalo et al., 2018), the more subtle impact of local curvature on the nanoscale is believed to develop significant stress in the cell membrane (Capozza et al., 2018). It is thus reasonable to hypothesize a possible role of membrane deformation at the NV wall rim in the alteration of vesicle fusion mechanisms.

An ensuing argument is that the membrane deformation might alter the molecular composition of the membrane and/or cytoskeleton in the vicinity of the NV wall rim. This is supported by a vast literature on protein localization to curved membrane domains like α-synuclein (Jensen et al., 2011), complexin (Gong et al., 2016) and BAR domains-containing proteins in general (McMahon & Boucrot, 2015). In particular, nanotopography was demonstrated to induce the recruitment of FBP17, a membrane curvature sensing protein, leading to filamentous actin assembly (F-actin) through action of the neuronal Wiskott–Aldrich syndrome protein (N-WASP) in U2OS cells (Lou et al., 2019). Interestingly, independent findings revealed the role of F-actin polymerization, also mediated by N-WASP, in providing enough membrane surface tension to enable the merging of vesicles with the chromaffin cell membrane (Shin et al., 2018; Wen et al., 2016). Taken together the impact of nanotopography on membrane tension and cytoskeleton rearrangement substantiates the hypothesis that the NV wall sharpness alters exocytosis kinetics. This hypothesis gives away some very interesting investigation prospects since to our knowledge there only exists one report of nanotopography impact on lateral vesicle movement (J. Zhang et al., 2009) but none about exocytosis itself.

4.3.6   Comparison to patch amperometry

A possible caveat of our hypotheses is the consideration that patch amperometry as described by Albillos et al., 1997 would effectively result in a similar if not stronger membrane tension which by deduction should result in shorter events duration. Yet, amperometric spikes registered using this technique have features close to those reported by conventional CFE. It should be noted however that in patch amperometry the carbon electrode is separated from the tip of the pipette by typically 6-7 µm (Albillos et al., 1997). This separation results in convolution of the release kinetics with the subsequent diffusion to the electrode which should result in spikes duration in the tens of millisecond range. An interesting detail is the report that establishment of the gigaohm seal during patch amperometry results in spontaneous exocytotic releases (Albillos et al., 1997; Dernick et al., 2003). This observation and other reports on swelling-activated ion channels could propose a greater susceptibility of exocytosis at deformed region of the cell membrane yet remains to be investigated.

4.4   Conclusion

In this study we have described a new electrochemical sensor capable of multi-site, sensitive single cell measurement. This new sensor encompasses a robust fabrication process that

allows to outfit each NV with two individually addressable electrodes instead of one. The two electrodes are arranged in a nanogap configuration, a novelty that we put to use to shed light on the cell/microstructure interface thanks to a redox cycling detection scheme. The sensor applied to single-cell amperometry of exocytosis achieves sensitive detection that can resolve maturation in cellular mechanisms in culture and pharmacological manipulations.

A limitation of the current study is the small number of cells the data were collected from. Although our NV arrays like other MEAs allow a high number of simultaneous sensing sites, our experiment yield was limited by the random pairing of NV and cells and the use of a single channel amplifier. Others have addressed the former by defining zone of preferential attachment for cells around the microelectrodes (M. Huang et al., 2018; X. Liu et al., 2011) which could be implemented in the future together with other approaches like cell specific dielectrophoretic patterning (Zhou et al., 2015). Finally, CMOS integration as implemented by others (M. Huang et al., 2018) are a common strategy to parallelize recordings thereby increasing throughput.

The short time scale of the spikes observed led us to build a set of hypotheses relying on the increased membrane tension and cytoskeleton reshaping plausibly brought by the NV wall nanoscale-sharpness. There exists a vast literature about the impact of nanostructures on cell mechanisms like differentiation (Dalby et al., 2014), migration (Yang et al., 2017) and signaling (A. Zhang et al., 2021) yet their impact on exocytosis remains to be explored. Accordingly, NVs stand as an interesting platform to explore this question. A straightforward way to test our hypothesis could be to use pharmacological or genetic manipulations to perturb the hypothetical actin polymerization over the NV rim using latrunculin A or *Actb* knockout respectively. On the other hand, varying the NV geometry (*e.g.* wall thickness, height, diameter) could also be used to challenge or refine this hypothesis. Our current data offer a novel view of exocytotic behavior under membrane deformation and could foster further investigations of the impact of nanotopography on synaptic mechanisms and cellular mechanosensing.

4.5   Materials and Methods

4.5.1   Device fabrication and preparation

The fabrication and preparation of the device are described in chapter 3, section 3.2.5 and section 3.4.4 respectively. Briefly, four inches fused silica substrates were evaporated with Ti/Au/Cr of 7/50/70 nm which was patterned by i-line photolithography and ion beam etching to define the region of overlap of the two gold electrodes and silicon dioxide pillars. The bottom gold electrode itself was defined in subsequent photolithography/etching similarly. A 200 nm thick insulating layer of silicon dioxide was deposited by plasma enhanced physical vapor deposition (PECVD) and subsequently patterned by photolithography/etching to open an access to the chromium and define the silicon dioxide pillars. Cr/Au/Ti of 5/60/7 nm was sputtered and patterned to form the top electrode. A second 300 nm thick insulating layer

of silicon dioxide was deposited by PECVD and patterned by photolithography/etching to define the nanovolcano itself and access contact of the electrodes. The wafers were diced on a DAD321 (Disco, Germany) with a resinoid blade of 70 μm width under 25000 RPM rotation moving at 1 mm/s from the top side of the wafer. A glass O-ring was glued on top of the individual chips using PDMS and cured overnight at 60°C in a convection oven. The removal of the chromium sacrificial layer was carried out at this point by potential assisted wet etching followed by device yield assessment. The device electrochemical response was characterized in cyclic voltammetry and step chronoamperometry (Suplementary materials, section 4.6.1 and Supp. Figure 4.6).

4.5.2 Cell culture

The device culture chamber formed by the glass O-ring glued on top was incubated with Poly-D-Lysine (A3890401, ThermoFisher) for 1 h at room temperature. After rinsing 5 times with DIW, the culture chamber was filled with culture medium and kept at 37°C until cell plating. Pheochromocytoma 12 rat cells were obtained from the European Collection of Cell Cultures. Cells from passage 10 to 15 were used. We have previously analyzed the electroactive molecules found in the PC12 cells used in this study and confirmed their catecholaminergic nature (chapter 3, section 3.4.8 and Supp. Figure 3.17). During cell culture the cells were kept in RPMi-1640 supplemented with Glutamax (61870036, ThermoFisher), 10% heat-inactivated donor equine serum (26050070, ThermoFisher), 5% fetal bovine serum (F9665, Merck) and 0.4% penicillin/streptomycin (P4333, Merck) solution within a 37°C incubator under 7% CO2 and 100% humidity atmosphere. Before plating on the devices, a 80% confluent culture was collected by trypsinization (1084440001, Merck) for 5 min at 37°C followed by mechanical dislodgement by repetitive pipette dispensing over the cell. Cells were centrifuged 2 min at 0.3 RCF and resuspended in culture medium after the supernatant was discarded. We plated 150 000 cells per chip (0.95 cm$_2$) and conducted experiments on the third day after passaging or sixth day after passaging in the case of the cadmium challenge experiment. In another experiment we cultured Human Embryonic Kidney cells on our chip in a similar way except for the medium (DMEM supplemented with Glutamax; 10566016 ThermoFisher) and no equine donor serum but 10% fetal bovine serum. On the third day after passaging we assessed cell viability by calcein-AM/ethidium homodimer-1 assay (L3224; ThermoFisher) according to the manufacturer protocol. We analyzed 10 fields of view of 610 x 460 μm centered on a single NV. Using the CellProfiler (CellProfiler$_{TM}$, Broad Institute) methods "identifyPrimaryObjects" we identified, segmented and counted individual cells to obtain the ratio of live cells to total cells in a given field of view (Supp. Figure 4.7).

4.5.3 Amperometric measurement of exocytosis

On the third day after passaging, the medium culture was exchanged for a recording buffer (in mM; 125 NaCl, 5.5 KCl, 1.8 CaCl$_2$, 0.8 MgCl$_2$, 20 HEPES, 24 glucose, and 36 sucrose at pH 7.3, osmolarity adjusted to 315 mOsm with sucrose) and allowed to equilibrate for 10

min at room temperature during which time NV covered by a cell were identified using an epifluorescence microscope under bright field illumination. The device was placed inside a custom printed circuit board interface itself within a Faraday cage to limit electromagnetic interference. The selected NV were sequentially connected to the input of a Axopatch 200 B amplifier (Molecular Devices, USA) by shorting its pair of electrodes while the ground of the input amplifier was connected to a silver/silver chloride pellet (E-205; Multi Channels System, Germany) immersed in the culture chamber bath. The NV's electrodes were biased to +600 mV with respect to ground. The cells were stimulated using an elevated potassium solution (same as recording buffer but with KCl elevated to 125 mM and NaCl reduced to 5.5 mM dispensed by a Nemesys Base120 syringe pump (Cetoni, Germany). The tubing outlet connecting to the elevated potassium solution syringe was positioned 3 mm above the MEA and dispensed at a rate of 20 μL/s while another tubing positioned 6 mm above the MEA withdrew an equal volume at an equal flow rate. In the case of cadmium challenge the solution of elevated potassium was supplemented with 100 μM cadmium chloride. After stimulation or challenge the culture chamber was exchanged in a similar way using a third syringe filled with standard recording solution and the next recording (typically from another cell) was started after a 5 min break.

4.5.4   Data acquisition and analysis

Data were filtered with the built-in Axopatch 200B four-pole low-pass Bessel filter set to a cut-off frequency of 10 kHz and digitized at 100 kHz using a Powerlab 4/25 acquisition card (AD Instruments, Australia). The signal was also digitized on another channel after high-pass filtering using the acquisition card single-pole analog high-pass filter set to a cut-off frequency of 10 Hz. In the rest of data processing the 10 kHz low-pass,10Hz high-pass signal was used. Spikes above 3.75 to 5 times the standard deviation of the noise, depending on the specific recording noise level, were selected. The spike start and end used to compute total quantal size were found as the first occurrence of a sample below one time the noise standard deviation on a 3 sample rolling-averaged version of the signal. The spike features distributions are plotted on a log-scale and fitted by a log-normal distribution of parameter μ = mean and σ = standard deviation. All results in the text are reported as the mean ± standard error of the mean.

4.5.5   Redox Cycling detection on cell covered NV

At the end of an amperometric experiment, the recording solution was exchanged with a similar solution that was supplemented with 100 μM Hexaammineruthenium(III) chloride (262005, Merck). The cells were incubated in that solution for 15 min before recording. The top electrode of a given selected NV was connected to the first working electrode of the bipotentiostat (same as above) and the bottom electrode was connected to the second working electrode. The counter electrode was a platinum wire and the reference electrode a chlorinated silver wire. The potential of the two working electrodes were scanned simultaneously from -100 mV to -600 mV with an offset of +200 mV. This results in a transient centered at the formal

potential of the redox probe as was used for multiplexed electrochemical detection referred to as differential cyclic voltammetry. In our experiment, comparing the current trace obtained at NVs covered or not covered by a cell allows us to assess the ability of molecules to diffuse inside covered NVs (Supp. Figure 4.8).

4.6 Supplementary Materials

4.6.1 Electrochemical characterization of the device

For characterization purposes devices after chromium etching were filled with an aqueous solution of 1 mM ferrocenemethanol (335061, Merck) and 250 mM KCl. Both electrodes of the NV were shorted and connected to a Stat.h bipotentiostat (Ivium, The Netherlands) together with a platinum wire and KCl saturated reference silver/silver chloride electrode (MF-2056; BaSi, USA) serving as counter and reference electrode respectively. Cyclic voltammograms between +100 mV and +400 mV were acquired at a scan rate of 2 mV/s and the average of the last three cycles were taken. The cyclic voltammogram (Supp. Figure 4.6, A) shows a current trace close to a sigmoid curve as is expected for microelectrodes scanned at low scan rate (Compton & Banks, 2018). Amperometric traces were acquired in the same solution by stepping the NV electrodes potential from 0 to +600 mV and sampling the current every 10 ms. The currents obtained in amperometry are notably larger than the expected Cottrelian regime just after stepping the potential (Supp. Figure 4.6, B-C) (Bond et al., 1988), a feature we attribute to depletion of the cavity from the redox probe used for characterization.
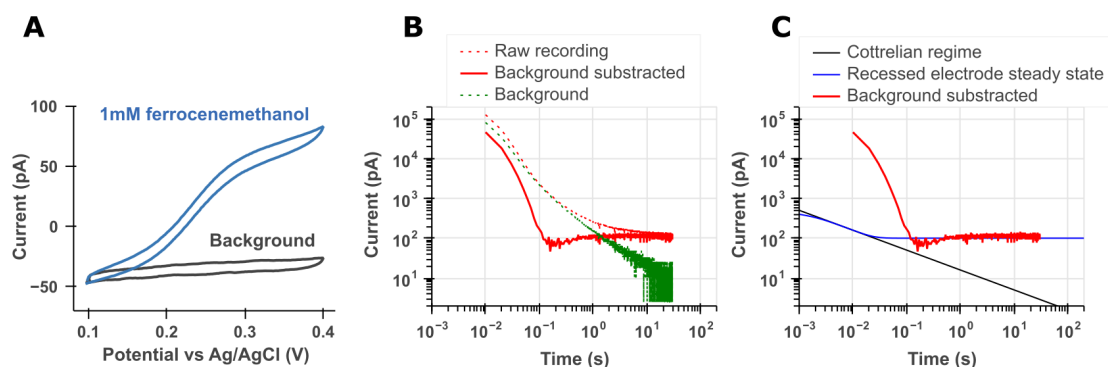
Figure 4.6: Cyclic voltammogram and step amperometry from a nanovolcano in an aqueous solution of 250 mM KCl without (Background) or with (Raw) 1 mM ferrocenemethanol. The nanovolcano electrodes were shorted together and their potential stepped to +600 mV. (A) Cyclic voltammogram of the shorted electrode from a single nanovolcano in an aqueous solution of 1 mM ferrocenemethanol and 250 mM KCl showing a sigmoid shape typical of microelectrodes. (B) Background, raw and background-subtracted current traces. (C) Comparison of the background subtracted trace to the theoretical current describing a recessed microelectrode of radius 2 μm positioned at the bottom of a recess of depth 5 μm. The theoretical current is approximated at short times (black) and follows a Cottrelian regime as for an inlaid microelectrode. The steady state current is obtained from an approximation at long times (blue) and describes the steady state current obtained once the depletion layer has outgrown the recess depth. The nanovolcano operated in step amperometry clearly diverges from the Cottrelian regime at short time (larger slope) but reaches a steady state value within 100 milliseconds. Note that this does not represent the time constant of the nanovolcano when measuring exocytotic packet as the settling time of the electrode toward steady state at 100 milliseconds probably arises from depletion of the nanocavity from the ferrocenemethanol molecules. A fitting of the experimental amperometric curve by the piece-wise theoretical model results in a poor fit that we explain by the NV electrode differing significantly in that the wall of the recess is itself conductive.
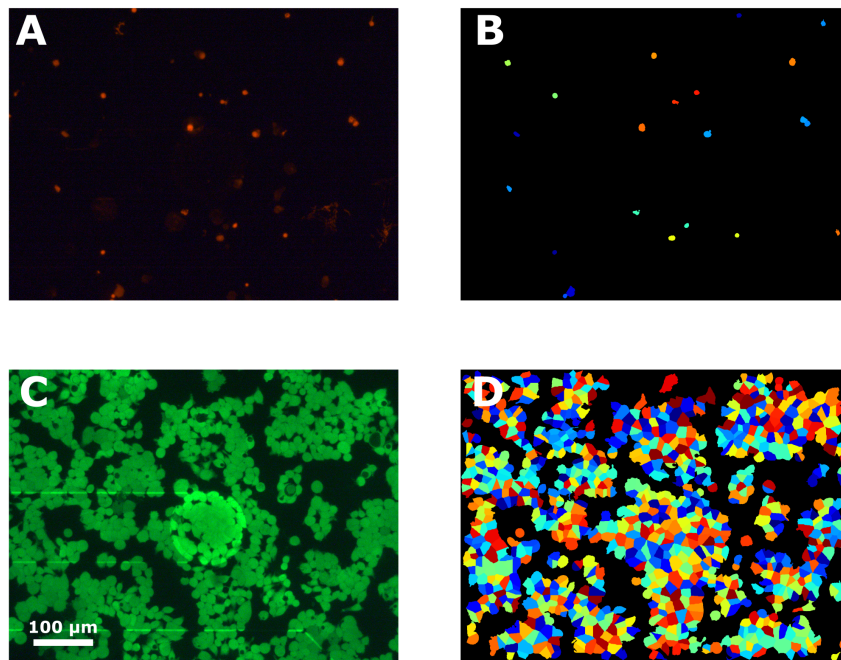
Figure 4.7: Live and dead human embryonic kidney cells revealed by calcein-AM and ethidium homodimer-1 staining respectively. (A) and (C) correspond to epifluorescence images of the dead and live stain respectively. (B) and (D) are the output of the CellProfiler pipeline used to identify, segment and count the dead and live cells respectively. Region of increased background fluorescence in (C) corresponds to electrode and electrical leads.
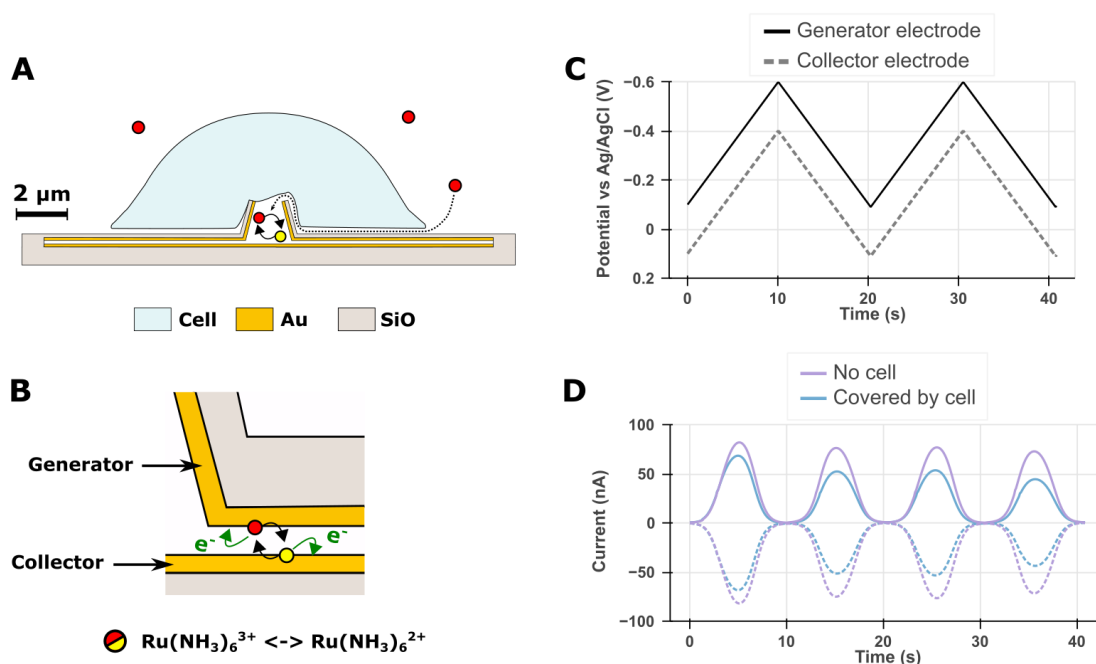
Figure 4.8: Redox probe diffusion inside a cell-covered nanovolcano determined by differential cyclic voltammetry. (A) Depiction of the detection scheme. Cells covering a nanovolcano might hinder the diffusion of molecules from the bath to the inside of the nanovolcano. Adding a cell impermeant redox probe to the bath a few days after cell plating allows to assess whether molecules can find their way to the nanovocano. (B) Enlargement of the nanogap sketching the redox cycling amplification mechanism. Without redox cycling the experiment could run into i) too small current and ii) uncertainty of the origin of the redox current. By using redox cycling the current measured are amplified several hundreds time and is selective toward molecules susceptible to reversible oxidoreduction reactions like the probe used (hexaammine(III) ruthenium, 100 µM). (C) Potential waveform applied to each electrode and (D) Resulting currents measured for a cell without (blue) or with (purple) a cell covering the nanovolcano. The data presented in (D) is representative of 6 cells investigated.

5 Conclusion

5.1 Summary of results, significance and limitations

5.1.1 Impedance spectroscopy of the cell/nanovolcano interface enables optimization for electrophysiology

Summary of results

In chapter 2, we applied impedance spectroscopy to characterize the interface of embryonic kidney cells and rodent primary neurons on nanovolcanoes (volcano-shaped nanostructures). In the case of neurons, we recorded their spontaneous electrophysiological activity as well and found a good correlation to seal resistance. The method was able to resolve the impact of the nanostructure geometry and chemical functionalization on the interface.

This was made possible by several technological developments. First, we developed a new fabrication process to build nanovolcanoes independently of an underlying electrode. Second, the electrode itself was designed to reach low impedance to enable measurement of the seal resistance at moderate frequencies. Third, the electrode design made the cell/nanostructure fully transparent which we could use to select relevant measurement sites (covered by a cell). We concluded with a feasibility study of access resistance measurement.

Significance of the work

This work is expected to have a lasting impact in the field of electrophysiology. It should be of interest to investigators developing micro- nano-electrodes for intracellular electrophysiology for which there exists a limited set of tools to optimize the yield of intracellular access. Optimization of the electrode geometry and chemical functionalization could be achieved using the technique we described. Furthermore, the electroporation waveform used to obtain intracellular access by many micro- nano-structures could be pitched on a site-to-site basis. This could be critical given that cell-to-cell transmembrane voltage threshold for electroporation is variable (Towhidi et al., 2008). We therefore anticipate that the measurement of seal

resistance through impedance spectroscopy may start to be routinely implemented especially for multi-electrode arrays (MEA) built on top of complementary metal-oxide-semiconductor where the necessary electrical circuitry is already available (Abbott et al., 2020; Lee et al., 2022).

Limitations

The nanostructure geometry optimization attempted in this study was unfortunately not fruitful with seal resistance and action potentials signal-to-noise ratio similar across the different geometries investigated. This may be due to the fact that the nanostructures investigated were all variants of the nanovolcano built with varying diameter, height and wall texture. It could have been more ambitious to fabricate a wider range of nanostructures including nanostraws, nanoporous membranes or arrays of one of these nanostructures addressed by the same electrode.

A limitation of impedance spectroscopy itself is that the duration of the measurement depends on the frequency range under study. With our devices, seal resistance was best resolved between 10 and 1000 Hz which can result in measurement times of a couple of seconds due to averaging needed to level down noise.

Another limitation is that depending on the electrode impedance, stray impedance and the magnitude of the seal resistance itself, the range of frequency that has to be covered can differ by one to two orders of magnitude. This can make our method not equally suitable for any devices. For example, we discussed the impact of the junctional membrane capacitance on the measurement which was found to largely affect electrodes of large impedance when resolving moderate seal resistances (few megaohms). In consequence our method may not be readily implementable for micro- nano-electrodes of large impedance and moderate seal resistance.

5.1.2 Design and implementation of a scalable intracellular electrochemical sensor

Summary of results

In chapter 3, we designed a sensor for intracellular electrochemical measurement of cytosolic catecholamines. Through theoretical and finite element modeling we defined the required sensor performance and resulting design rules. In particular, redox cycling within an electrochemical nanogap was devised as an approach to meet the sensitivity requirement. To bring the electrodes in contact with the cell cytosol, the electrochemical nanogap was built below a nanovolcano similar to that in chapter 2.

The fabrication of the electrochemical nanogap was realized with two different approaches. First with interdigitated electrodes and second with vertically stacked electrodes. The second strategy was found to result in more stable sensors and was selected for further characterization. We used mercapto propionic acid to limit fouling of the electrode and performed a

proof-of-concept detection of dopamine in whole cell lysate. The intracellular measurement of catecholamine should be the subject of further works focusing on optimization of the intracellular access through electroporation as was already achieved for another cell type (Desbiolles, de Coulon, et al., 2020).

Significance of the work

The work presented highlights a new framework of electrochemical sensor design for single-cell measurement. Few examples exist of intracellular electrochemical sensing (Liao et al., 2019; Mosharov et al., 2003; Rawson et al., 2015; P. Sun et al., 2008) none of which is well scalable. By using a multi-electrode array approach, this work poses the foundation of multi-site, intracellular, longitudinal monitoring of electroactive molecules. Longitudinal monitoring of electroactive molecules has for example significance to pathological conditions as for cytosolic dopamine in Parkinson disease(Mosharov et al., 2009). Accordingly, the sensor proposed poses the basis for an analytical research tool that would be useful to neuroscientists.

The fabrication process of the vertically stacked electrode presented improved upon previous reports by the incorporation of silicon dioxide pillars that markedly improved the yield of functional devices. This improvement should contribute to make electrochemical redox cycling detection schemes easier to implement and thus be more widely applicable.

The demonstration of the feasibility of dopamine detection in whole cell lysate by redox cycling with good selectivity is a significant achievement. If longitudinal sampling is not desired but single-cell precision is, a micro total analysis system combining cell lysis and redox cycling detection could constitute an interesting alternative to column separation based methods with downstream electrochemical measurement. Accordingly, redox cycling in whole cell lysate is a promising detection method.

Limitations

In this work, a careful analysis, modeling and design was undertaken. The theoretical analysis agrees well with the modeled data obtained from finite element modeling and where present, deviations highlight known phenomena (*i.e.*, adsorption) relevant to the device functioning. In particular, the known impact of dead volumes within the electrochemical nanogap was discussed. However, dead volumes in both implementations of the sensors were quite large and could have been reduced. For the interdigitated electrodes, a thinner layer of polyimide could have been used. In the case of the vertically stacked electrodes, the dead volume results from the alignment tolerance built in the design. Others have circumvented this problem by depositing both electrodes and the sacrificial layer at once and used ion beam etching together with selective wet etching to obtain well defined, tightly aligned electrodes (Kang et al., 2013). While this approach results in additional fabrication steps, it is expected to almost double the redox cycling current for the vertically stacked electrode design presented.

A limitation of having taken an electrochemical approach is the ensuing concerns about electrode stability and fouling. These common pitfalls in electrochemistry are not unsolvable, but typically require long iterative work to choose the correct solution from an extensive literature on the subject. Taking electrode fouling as an example, anti-fouling coating solutions include: carbon nanotubes either vertically aligned (Xiang et al., 2014) or embedded in a polyethylenimine matrix (Zestos et al., 2014), oxidized polypyrrole film (Sasso et al., 2013), Nafion or cellulose acetate membrane (Trouillon et al., 2009), S-layer protein SbpA (Damiati & Schuster, 2020), gold nanoparticles embedded in sol-gel network (Adams et al., 2011) or nanoporous structured gold (Patel et al., 2013) and many more.

Another limitation is the choice to rely on semiconductor manufacturing techniques. While this is an enabling factor in developing scalable solutions, semiconductor fabrication lines typically do not offer the possibility to work with the electrode material of choice for neurotransmitter electrochemistry: carbon. We have tried to circumvent this problem by using glassy carbon which can be obtained by pyrolysis of photoresist directly at wafer scale (Kim et al., 1998). Preliminary results not published in this thesis have however shown that glassy carbon is etched by the wet chromium etchant used in the vertically stacked electrode fabrication. Accordingly, the pursuit of scalability necessarily limited us to work with noble metals as electrode material. Notable exceptions include carbon nanotubes that are IC compatible and graphene which is increasingly more widespread in academic clean rooms (Ruhl et al., 2017).

Finally, we note that detection of a few picoamps of current from a large electrode as those used (7000 μm^2) is necessarily dependent on the quality of the electronic instrument used. This was highlighted in the characterization of the vertically stacked electrode where the limit of detection was underestimated because of the bias current of the input amplifier whose fluctuations results in a large background noise (proportional to the electrode surface area as discussed by Yao and Gillis, 2012). We did take care of designing our sensor to meet the required limit of detection for cytosolic neurotransmitter while using commonly available instruments (*i.e.*, patch clamp amplifier). Nonetheless, it is a drawback that the limit of detection will change depending on the instruments used.

5.1.3 Rapid exocytosis kinetics measured by amperometry within nanovolcano electrodes

Summary of results

In chapter 4 we used the sensor developed in chapter 3 for another application, the amperometric measurement of exocytosis. We demonstrated the ability of the vertically stacked electrode sensor to resolve pharmacological manipulation of exocytosis in rat pheochromocytoma cells. Against our expectation, we found out that exocytosis proceeds roughly ten times faster at the nanovolcano/cell interface compared to the traditional carbon fiber electrode/cell artificial synapse. We studied this phenomenon with finite element modeling of mass transport within nanovolcanoes following exocytosis and formulated the hypothesis that

faster exocytosis kinetics arise because of membrane tension and cytoskeleton reorganization brought by the nanovolcano sharp walls.

Significance of the work

The work performed is expected to contribute significantly to the field of electrochemistry for which it addresses two prominent topics. First, it addresses the throughput limitations of the traditional measurement method (carbon fiber microelectrode). Secondly, it proposes an implementation of a volume-confined sensor to address the escape of molecules from the detection site; still with the consideration of being scalable for improved throughput.

On the other hand, the discovery of a plausible mechanism of regulation of exocytosis by membrane deformation on nanotopography is expected to appeal to a broader audience. If this hypothesis is corroborated, nanostructures like the nanovolcano could be used as a platform to investigate the link between cytoskeleton organization and cell secretion mechanism. It may also have implications for brain-machine interface design.

Limitations

The goal set for this work was to develop a scalable, volume-confined amperometric sensor for exocytosis. This implies that the sensor *per se* should not affect the phenomenon being studied. We however found that exocytosis takes place with faster kinetics at the cell/nanovolcano interface compared to the cell/carbon fiber microelectrode artificial synapse and have argued for a possible fundamental discovery of the exocytosis mechanism rather than a measurement artifact/issue. This turn of event is not necessarily a limitation but could be seen as an opportunity to study the fundamental mechanisms of exocytosis as possibly being impacted by membrane tension and cytoskeleton reorganization. To be fair, it is reasonable to state that the impact of the nanovolcano on exocytosis kinetics is a limitation to its applicability as a sensor but an opportunity for fundamental investigations.

Another point open to discussion is whether the nanovolcano array improves the throughput when measuring exocytosis compared to the conventional method: carbon fiber microelectrode amperometry. While the method to fabricate the nanovolcano in itself is scalable, the scalability of the instrumentation needed to record from individual nanovolcanoes is realistically a limiting factor. In this study we have used a single patch clamp amplifier which we have connected sequentially to different nano volcanoes. Considering the cost of such amplifiers, another solution is needed to realize the potential of the device presented to enable high throughput experimentation. A sound approach would be to integrate the nanovolcano on top of complementary metal-oxide-semiconductor circuitry as described by others (M. Huang et al., 2018).

5.2   Perspectives for the future

The motivation of this thesis has been discussed in the introduction and summarize to the tenet: scalable, single-cell, longitudinal methods are lacking in electrophysiology and electrochemistry. The three core chapters of this thesis have presented efforts that were addressed to overcoming this limitation at different levels and for different applications. Ultimately, however, the goal is the same: to build new technologies to empower investigators. Because new technologies realized today foster the development of tomorrow's advances, we discuss below opportunities and promising leads of investigation put forth by the outputs of this thesis.

5.2.1   Bidirectional framework in intracellular electrophysiology recording from micro- nano-electrodes

The impedance based method to measure seal resistance presented in chapter 2 was motivated by the need for a scalable tool to quantify and thereby optimize cell/nanostructure coupling. This method could however be useful during the electrophysiological recording itself. Intracellular electrophysiology recording by micro- nano-electrodes having disrupted the cell membrane (*e.g.*, by electroporation) is limited in time due to membrane resealing. Furthermore, the quality of the signal recorded depends on the seal resistance and access resistance which will typically vary from recording site to recording site. This is a source of variability in electrophysiological data collected from micro- nano-electrodes and is a weakness compared to patch clamp recording in which these parameters are systematically assessed and largely controllable to satisfactory values for a skilled operator.

The method described in chapter 2 can measure both seal resistance and access resistance given that the former is in the hundred megaohm range. This measurement can be anticipated to have minimal impact on electrophysiological activity since impedance spectroscopy waveforms applied were typically 10 mV in amplitude peak-to-peak. A promising improvement for recording with micro- nano-electrodes would thereby consist in monitoring the seal and access resistance in parallel to the electrophysiology recording itself. This would enable i) to normalize the obtained data by correcting the recorded signal based on the cell/electrode interface and ii) pitch the electroporation waveform amplitude and frequency. For example, relating to i), the amplitude of the signal amplitude registered at the input amplifier is decreased by the voltage divider bridge formed by the access resistance in series with the seal resistance (see Desbiolles, de Coulon, et al., 2020, Supp. Figure S4 for equivalent circuit model). On the other hand, relating to point ii), the voltage experienced by the cell's plasma membrane is a function of the seal resistance and junctional membrane impedance (see Desbiolles, de Coulon, et al., 2020, Figure 1).

So far, there hasn't been a description of such a bidirectional framework. Furthermore, we can find evidence of the limitations mentioned (unknown seal and access resistance) in published research articles which our method could solve. In a prominent research article published

recently, pseudo voltage clamp of primary neurons was achieved using nanowire electrodes (Abbott et al., 2020, Figure 2). Interestingly, the holding voltage keeping the cell at rest (not emitting action potentials) is set at -650 mV. This is nearly ten times larger than the typical resting membrane potential of neurons which is typically around -70 mV. In order to depolarize the cell and trigger action potentials, the set potential was increased by 100 mV whereas in patch clamp voltage clamp experiments the relaxation of around 20 mV of the clamp voltage is enough. These oddly large values of the holding and stimulation voltage are likely the result of voltage drop across the access resistance (the portion of membrane that was permeabilized by electroporation). In this configuration, the study of ion channels properties like voltage gating would be impossible since the exact voltage applied across the cell membrane is unknown. If the access resistance was known however, the exact transmembrane potential resulting from a given holding potential could be calculated. This could be achieved from impedance spectroscopy as implemented in chapter 2 and would effectively make pseudo voltage clamp at micro- nano-electrodes comparable to voltage clamp using a patch clamp set up.

5.2.2 Improved electrophysiology recording from low impedance nanovolcano

Still in the scope of chapter 2, the new nanovolcano/buried electrode developed had markedly lower impedance compared to the previous implementation of the nanovolcano (Desbiolles, de Coulon, et al., 2020). This was also reflected in the inferred thermal noise being over 8 times lower at low frequencies (8.97 µV versus 1.03 µV between 100 mHz and 100 Hz).This is an advantage for intracellular electrophysiology dealing with signal of small amplitude and moderate characteristic frequencies like postsynaptic excitatory/inhibitory potentials. Postsynaptic excitatory/inhibitory potentials have duration of a few tens of milliseconds (Richardson & Silberberg, 2008) for which most of the signal power hence lies between 10 and 100 Hz . While their measured amplitudes can reach few hundreds of millivolts with conventional patch clamp, intracellular recording using nanowire arrays show a quantal distribution of 45 µV per excitatory input (Abbott et al., 2020) which can be on the same order of magnitude as the electrode thermal noise without proper impedance design. Similarly, the study of membrane oscillations characterized by typical frequency close to 10 Hz and amplitude of a few millivolts (Song et al., 2016) would be facilitated. Accordingly, the buried electrode strategy has great potential to widen the spectrum of electrophysiological signals that can be recorded from micro- nano-electrodes.

5.2.3 Optimize intracellular access and sampling for electrochemical recording

We described in chapter 3 a proof-of-concept detection of catecholamine by redox cycling in whole cell lysate. The electrochemical nanogap used was integrated below a nanovolcano, proposing that in a next step intracellular detection of cytosolic catecholamine could be pursued. Realizing this next step is not trivial as it will depend on i) the ability to permeabilize the junctional cell membrane enough to allow a detectable amount of analyte to diffuse to the sensor and ii) create a confined volume for detection in order to prevent loss by diffusion to

the bulk.

The optimization of ii) is very similar to the optimization of the seal resistance in electrophysiology and hence the seal resistance method reported in chapter 2 could be used to optimize the interface of catecholamine-containing cells (*e.g.*, chromaffin cells, pheochromocytoma cells) with the sensor developed in chapter 3. Essentially the approach would be the same as in chapter 2, the geometry of the nanovolcano and the chemical functionalization could be varied to find the configuration with the best insulation of the sensor from the extracellular bath when covered by a cell.

On the other hand the optimization of i) could leverage the same approach as that proposed for bidirectional electrophysiological recording proposed above. In particular, the access resistance could be monitored by impedance spectroscopy during electroporation and related to the pore size generated across the cell's junctional plasma membrane. Others have attempted this experimental measurement, not with impedance spectroscopy, but with the help of concomitant patch clamp and nano-electrode recording. In this experiment, the cell clamping voltage and passed current before/after electroporation was used to measure the access and seal resistance. The size of the pore generated by electroporation could be calculated from the access resistance (Lin et al., 2014). A total pore diameter of 23 nm was found in close agreement with the 25 nm generally accepted (Chang & Reese, 1990). This experiment demonstrated the faithfulness of electroporation pore estimation from access resistance but suffers from the use of patch clamp for wide range applicability and throughput. Thankfully, the sensor presented in chapter 3 could make use of the impedance spectroscopy method reported in chapter 2 to perform a similar measurement of the access resistance and retrieve the pore diameter after electroporation (see Appendix Figure 4 demonstrating the applicability of cell/nanovolcano impedance sensing with the electrochemical nanogap electrode).

The development of electroporation parameters resulting in predictable pore size could be used to obtain a reproducible mass transport to the sensor and as a sieve allowing selective diffusion of biomolecules. The last point can be compared to recent reports on the intracellular sampling of biomolecules of different size through nanostraws (Cao et al., 2017; J.-A. Huang et al., 2019) or hollow atomic force microscopy cantilevers (Guillaume-Gentil et al., 2016). In the former case, sampling through nanostraws with a lumen diameter of 150 nm shows a threshold at 16000 nucleotides above which nucleic acids were less likely to be sampled and in the latter case a triangular opening of 400 nm (base and height) would result in soluble protein sampling but not mitochondria or histones.

The characterization/optimization of mass transport is anticipated to be critical and will rely on fine tuning of the electroporation process. In particular, the timescale over which mass transport results in a detectable amount of molecule reaching the sensor can be a limiting factor. Simulating the diffusion from a cell to a sensor through a nanopore of 25 nm in diameter highlights that mass transport at this scale and magnitude of concentration gradient has a characteristic time constant of minutes (Appendix Figure 3, C, top). The time

needed to reach equilibrium (95% of steady state redox cycling current) is 123 seconds. This may intuitively seem wrong for an electrochemist who has experience with exocytosis for which timescales of tens of milliseconds are observed. However, the spatial concentration gradient in exocytosis is much steeper than for cytosolic neurotransmitter diffusing out of the cell. Although this simulation ignores electrokinetic and electroosmosis mass transport that will arise during the application of the electroporation waveform (Movahed & Li, 2012), it is evident that mass transport needs to be characterized to obtain a relevant measurement. For example, determining a time threshold after which the concentration of analyte within the sensor cavity has reached a set threshold even for the worst case (*i.e.*, smallest pore diameter, shortest pore lifetime) could be sufficient.

Finally, it is important to realize that detecting cytosolic neurotransmitter concentration by breaking the plasma membrane to access the cytosol may run into the complication of vesicle diffusing and bursting onto the electrode resulting in spikes of the observed current as reported by others (Mosharov et al., 2003). This may be limiting for neurotransmitters with cytosolic concentrations in the tens of nanomolar range which corresponds to a few thousand of molecule within the whole cytosol. Taking large dense core catecholamine vesicles in pheochromocytoma cells as an example, a single vesicle contains typically 85000 thousands catecholamine and more (Omiatek et al., 2010). The rupture of a vesicle during cytosolic measurement would hence results in an increase of the measured concentration by an order of magnitude. Luckily, the release of catecholamine from bursting vesicle contacting the electrode has time scales somewhere between tens (Omiatek et al., 2010) and hundreds (Mosharov et al., 2003) of milliseconds which should be easily resolvable from the slow wave of rising redox cycling current taking place over tens of seconds depending on the electroporation pore size as just discussed. It seems reasonable that such a sudden step in the redox cycling current could be subtracted during analysis.

We conclude that moving on to the next step in the development of the intracellular electrochemical sensor will benefit from the other methods developed in the scope of the thesis. Having identified the critical point to address (confined volume and mass transport), this investigation lead is reasonable and very promising considering there exist today no such sensor for scalable, longitudinal sampling.

5.2.4 Study of membrane curvature impact on exocytosis using electrodes with nanotopography

The development of a volume confined amperometric sensor for exocytosis measurements in chapter 4 ran into the unexpected result of measuring exocytosis events roughly ten times faster than those reported so far for pheochromocytoma cells. We have argued that this faster kinetics may arise from membrane tension and cytoskeleton reorganization at the point of contact between the cell membrane and the nanovolcano rim and proposed potential experiments that may verify the causality of nanotopography on accelerated exocytosis.

Without duplicating this discussion here we suggest the most straightforward experiments to verify this hypothesis. Looking to ascertain the role of membrane tension first, subjecting cells growing on nanovolcanoes to different osmotic conditions would be a straight forward approach. Hypotonic conditions would be expected to further increase the kinetics of exocytosis (Schroeder et al., 1996) and the converse for hypertonic conditions. Secondly, Latrunculin A could be use to inhibit filamenteous actin polymerization (Wen et al., 2016) and hence ascertain the impact of cytoskeleton reorganization around nanostructures (Lou et al., 2019) on exocytosis kinetics.

This is a promising and straightforward lead of investigation that could be combined together with *Actb* knockout and electron microscopy of the nanovolcano/cell interface and would advance the fundamental understanding of exocytosis links to cell mechanosensing.

5.3   Closing words

To conclude on the work performed throughout this thesis, let us go back to our argument about technological advancements impact on human history discussed in the Introduction. The work described here is obviously far from being as groundbreaking as the invention of the printing press or the discovery of the cell. There is however a reminiscence of the enabling power of new technologies to scientific endeavors. A central theme of the works presented in this thesis is the use of microfabrication techniques with the goal to offer scalable solutions. It is foreseeable that microfabricated probes will become increasingly popular and gradually replace their macroscopic part equivalent (*e.g.*, glass micropipette, bulk electrodes). Another critical object of this work was the use of the nanovolcano to address a wide range of challenges (seal resistance, intracellular access and volume-confinement). In doing so, the nanovolcano has proven to be a versatile approach to interface single cells for different applications and is poised to become a classic of microtechnology applied to biological studies.

We discussed the immediate opportunities arising from this thesis outputs. On a more distant horizon, one could imagine to translate nanovolcano based devices to *in vivo* investigations by integration on microshafts like the Michigan probe combining both electrophysiology and electrochemical sensing abilities to enable multiplex studies (Drake et al., 1988). Jumping even further in time we can speculate about the applicability of nanovolcano arrays to train networks of neurons in view of implantation following trauma or pathological degradation of the central nervous system. The neurons trained could be synthetic (Fil et al., 2022) or patient derived from induced pluripotent stem cells (Hargus et al., 2010).

As a research experience comes to an end, it is important to reflect on the importance of the communication of the knowledge developed. Transversal skills and outreach may be rewarding at the individual level but they should first and foremost be remembered to be the responsibility of the investigator toward society who sponsors the individual's work. Disclosing one's work as part of peer review is also fundamental to science integrity and falls within the investigator's responsibilities as well. For both of these reasons, it is the author's hope that this dissertation work will, first, appeal to society and secondly enable peers critics and discussions that will advance the total knowledge of humankind; no matter how small the step.

Appendix

Electrode geometry	Intracellular access strategy	Cell tested	Signal amplitude (mV)	Intracellular access duration	Intracellular access yield (%)	Reference
Nanowire array	Electroporation	Rodent cortical/hippo/ventricular neurons	0.2-2.5	8 min	40	Abbot *et. al.*, 2020
		iPSC derived glutaminergic neurons	0.1-2	-	-	Abbot *et. al.*, 2020
		Rodent CMCs	20	20 min to days	30	Robinson *et. al.*, 2012
Nanopillar array	Electroporation	HL-1 (CMC cell line)	12	10 min to days	-	Xie *et. al.*, 2012
Nanotube array	Electroporation	Rodent CMCs	15	15 min to days	-	Lin *et. al.*, 2014
Nanocrown pillar array	Electroporation	HiPSC derived CMCs	25	15 min to days	99	Jahed *et. al.*, 2022
Nanoporous membrane	Electroporation	Rodent CMCs	7.5	10 min	-	Xu *et. al.*, 2022
Nanoporous platinum	Electroporation	HiPSCs derived CMCs	10	10s min	80	Lee *et. al.*, 2022
Kinked Nanowire gate FET	Mechanical/ Phospholipid coating	Rodent CMC	55	5 min	Single cell	Tian *et. al.*, 2010, Qing *et. al.*, 2014
		HiPSC CMCs	110	15 min	Single cell	Zhao *et. al.*, 2019
		Rodent DRG neurons	70	3 min	Single cell	Zhao *et. al.*, 2019
Nanotube gate FET	Mechanical/ Phospholipid coating	Chicken CMCs	80	-	Single cell	Duan *et. al.*, 2012, Gao *et. al.*, 2012
Micromushroom	Engulfement promoting peptide	Rodent CMCs	6	10 min to days	-	Fendyur and Spira, 2012
		Rodent hippocampal neurons	5	days	34.5	Shmoel *et. al.*, 2016
		Applysia neurons	25	days	-	Hai *et. al.*, 2010
plasmonic nanopillar array	Optoporation	HL-1 (CMC cell line)	2	90 min	-	Dipalo *et. al.*, 2017
plasmonic metasurface	Optoporation	Rodent and HiPSC derived CMCs	5	40 min	85	Dipalo *et. al.*, 2018
Single nanowire	Sharpness	GH3	10	0.15 min	Single cell	Lee *et. al.*, 2014
Single nanowire	Sharpness	Rodent cortical neurons	0.1-99	Days	Single cell	Liu *et. al.*, 2017
		HiPSC derived dopaminargic neuron	0.1-35	Days	Single cell	Liu *et. al.*, 2017
		iPSC CVPCs	5 mV	-	Single cell	Liu *et. al.*, 2022

Figure 1: Performance comparison of Micro- Nano-electrode arrays for intracellular electrophysiology. Electrodes with different geometries and intracellular enabling strategies are compared in term of cell measured from, action potential signal amplitude, duration of the intracellular recording and yield of recording site amenable to intracellular access.
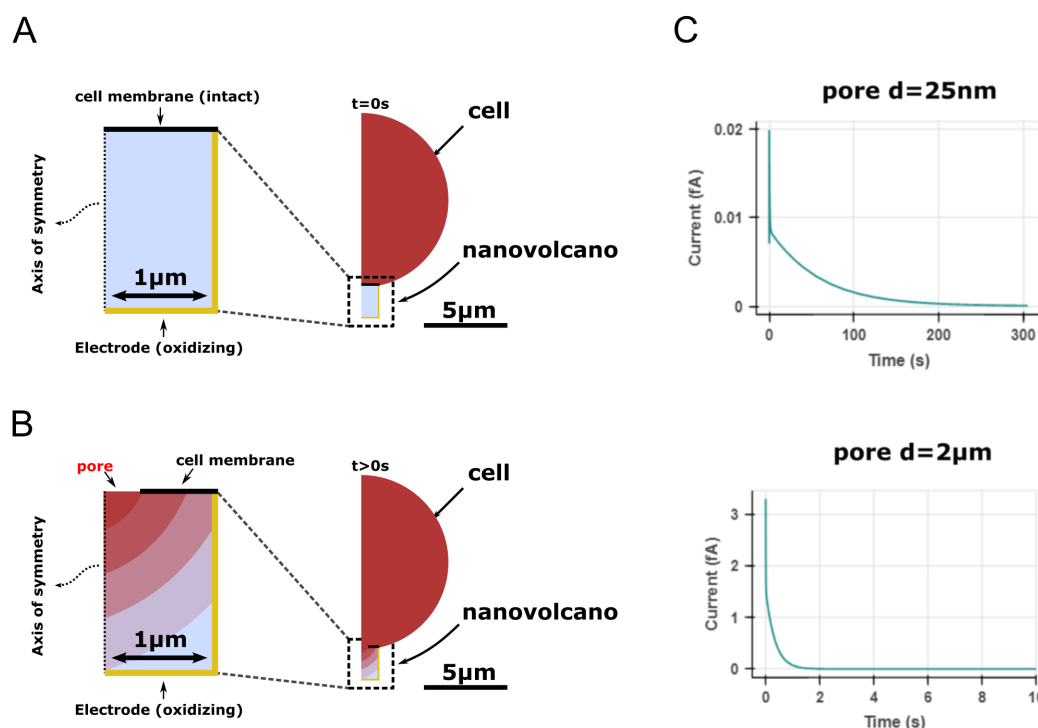
Figure 2: Finite element model of the electroporation-based sampling and on site detection using the underlying NV electrode. (A) Axisymmetric model of a cell on top of a NV before electroporation, the cell has a concentration of 10 nM of an electroactive molecule. The floor and wall of the NV are electrodes set to an oxidizing potential. For details about the implementation of the electrode process see Chapter 3, Materials and Methods 3.4.1 (B) After electroporation, mass-transport from the inside of the cell to the NV electrode occurs through the electroporation pore. For simplicity we assume there can be no leakage of molecule out of the NV into the extracellular bath. (C) The molecules reaching the electrodes are oxidized resulting in an amperometric trace which amplitude and timescale depends on the diameter of the electroporation pore (top vs bottom plot correspond to pore diameter of 25nm and 2µm). A pore of 2µm in diameter corresponds to total disruption of the cell membrane portion delimited by the NV. In practice, the electroporation pores are expected to be distributed between 10 and 160nm (Chang & Reese, 1990).
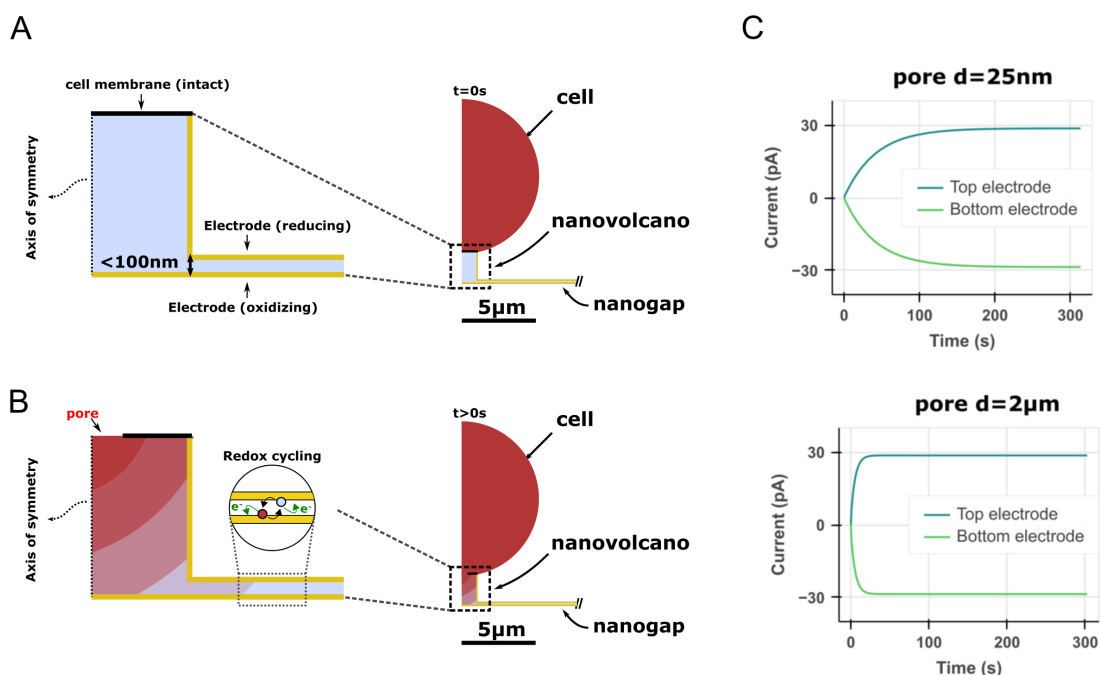
Figure 3: Finite element model of the electroporation-based sampling and on site electro-chemical redox cycling (ROc) detection using the underlying nanogap electrode pair. (A) Axisymmetric model of a cell on top of a NV before electroporation, the cell has a concentration of 10 nM of an electroactive molecule whose oxidoreduction reaction is reversible. The NV houses a pair of individually addressable electrode that are biased symmetrically apart from the redox couple formal potential. For details about the implementation of the electrode process see Chapter 3, Materials and Methods 3.4.1 (B) After electroporation, mass-transport from the inside of the cell to the NV nanogap electrodes occurs through the electroporation pore. For simplicity we assume there can be no leakage of molecule out of the NV into the extracellular bath. (C) The molecules reaching the electrodes are continuously cycled between their reduced and oxidized form resulting in an amperometric trace with an initial transient rising to a steady-state. Notice the magnitude of the steady-state current is in the tens of pico-amps, about 1000 times larger than without ROc 2. The timescale of the rise toward steady-state still depends on the diameter of the electroporation pore (top vs bottom plot correspond to pore diameter of 25nm and 2µm).
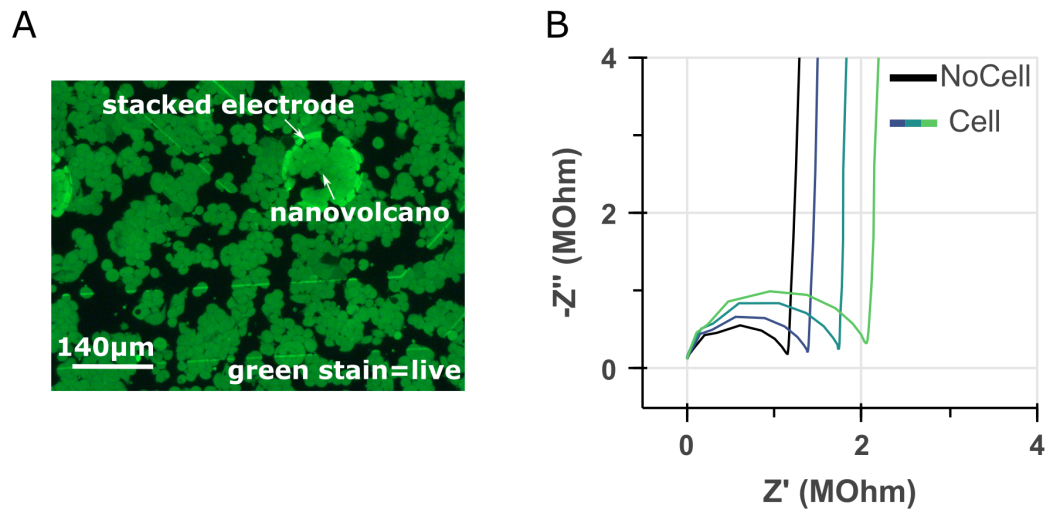
Figure 4: The seal resistance of human embryonic kidney (HEK) cells can be determined by impedance spectroscopy using the vertically stacked gold electrode configuration. (A) Fluorescence microscopy of HEK cells stained with calcein-AM viability stain. HEK cells cover the substrate homogeneously and do not seem to be distrubed or impaired on/close to the nanovolcano. (B) Nyquist plot of the impedance spectra measured from nanovolcanoes covered by a/several cells (colored lines) or not covered by any cell (black line). The spread in the colored curves indicates cell/nanovolcano characterized by different seal resistances. See chapter 2, section 2.2.2 for a discussion of seal resistance measurement from the impedance spectrum.

Bibliography

Abbott, J., Ye, T., Krenek, K., Gertner, R. S., Ban, S., Kim, Y., Qin, L., Wu, W., Park, H., & Ham, D. (2020). A nanoelectrode array for obtaining intracellular recordings from thousands of connected neurons. *Nature Biomedical Engineering, 4*(2), 232–241. https://doi.org/10. 1038/s41551-019-0455-7

Abbott, J., Ye, T., Qin, L., Jorgolli, M., Gertner, R. S., Ham, D., & Park, H. (2017). CMOS nano-electrode array for all-electrical intracellular electrophysiological imaging. *Nature Nanotechnology, 12*(5), 460–466. https://doi.org/10.1038/nnano.2017.3

Adams, K. L., Jena, B. K., Percival, S. J., & Zhang, B. (2011). Highly Sensitive Detection of Exocytotic Dopamine Release Using a Gold-Nanoparticle-Network Microelectrode. *Analytical Chemistry, 83*(3), 920–927. https://doi.org/10.1021/ac102599s

Albillos, A., Dernick, G., Horstmann, H., Almers, W., de Toledo, G. A., & Lindau, M. (1997). The exocytotic event in chromaffin cells revealed by patch amperometry. *Nature, 389*(6650), 509–512. https://doi.org/10.1038/39081

Amatore, C., Arbault, S., Bonifas, I., Bouret, Y., Erard, M., & Guille, M. (2003). Dynamics of Full Fusion During Vesicular Exocytotic Events: Release of Adrenaline by Chromaffin Cells. *ChemPhysChem, 4*(2), 147–154. https://doi.org/10.1002/cphc.200390024 _eprint: https://onlinelibrary.wiley.com/doi/pdf/10.1002/cphc.200390024

Amatore, C., Bouret, Y., Travis, E. R., & Wightman, R. M. (2000). Interplay between membrane dynamics, diffusion and swelling pressure governs individual vesicular exocytotic events during release of adrenaline by chromaffin cells. *Biochimie, 82*(5), 481–496. https://doi.org/10.1016/S0300-9084(00)00213-3

Amatore, C., Oleinick, A. I., & Svir, I. (2010). Reconstruction of Aperture Functions during Full Fusion in Vesicular Exocytosis of Neurotransmitters. *ChemPhysChem, 11*(1), 159–174. https://doi.org/10.1002/cphc.200900647 _eprint: https://onlinelibrary.wiley.com/doi/pdf/10.1002/cphc.200900647

Asmild, M., Oswald, N., Krzywkowski, K. M., Friis, S., Jacobsen, R. B., Reuter, D., Taboryski, R., Kutchinsky, J., Vestergaard, R. K., Schrøder, R. L., Sørensen, C. B., Bech, M., Korsgaard, M. P. G., & Willumsen, N. J. (2003). Upscaling and Automation of Electrophysiology: Toward High Throughput Screening in Ion Channel Drug Discovery. *Receptors and Channels, 9*(1), 49–58. https://doi.org/10.3109/10606820308258 _eprint: https://doi.org/10.3109/10606820308258

Bibliography

Bando, Y., Grimm, C., Cornejo, V. H., & Yuste, R. (2019). Genetic voltage indicators. *BMC Biology*, *17*(1), 71. https://doi.org/10.1186/s12915-019-0682-0

Berthing, T., Bonde, S., Rostgaard, K. R., Madsen, M. H., Sørensen, C. B., Nygård, J., & Martinez, K. L. (2012). Cell membrane conformation at vertical nanowire array interface revealed by fluorescence imaging. *Nanotechnology*, *23*(41), 415102. https://doi.org/10.1088/0957-4484/23/41/415102

Bond, A. M., Luscombe, D., Oldham, K. B., & Zoski, C. G. (1988). A comparison of the chronoamperometric response at inlaid and recessed disc microelectrodes. *Journal of Electroanalytical Chemistry and Interfacial Electrochemistry*, *249*(1), 1–14. https://doi.org/10.1016/0022-0728(88)80345-0

Borges, R., Travis, E. R., Hochstetler, S. E., & Wightman, R. M. (1997). Effects of External Osmotic Pressure on Vesicular Secretion from Bovine Adrenal Medullary Cells *. *Journal of Biological Chemistry*, *272*(13), 8325–8331. https://doi.org/10.1074/jbc.272.13.8325

Braun, D., & Fromherz, P. (2004). Imaging Neuronal Seal Resistance on Silicon Chip using Fluorescent Voltage-Sensitive Dye. *Biophysical Journal*, *87*(2), 1351–1359. https://doi.org/10.1529/biophysj.104.039990

Bruns, D. (2004). Detection of transmitter release with carbon fiber electrodes. *Methods*, *33*(4), 312–321. https://doi.org/10.1016/j.ymeth.2004.01.004

Cajal, S. (1888). Estructura de los centros nerviosos de las aves. *Rev. Trim. Histol. norm. patol.*

Cao, Y., Hjort, M., Chen, H., Birey, F., Leal-Ortiz, S. A., Han, C. M., Santiago, J. G., Paşca, S. P., Wu, J. C., & Melosh, N. A. (2017). Nondestructive nanostraw intracellular sampling for longitudinal cell monitoring. *Proceedings of the National Academy of Sciences*, *114*(10), E1866–E1874. https://doi.org/10.1073/pnas.1615375114

Capozza, R., Caprettini, V., Gonano, C. A., Bosca, A., Moia, F., Santoro, F., & De Angelis, F. (2018). Cell Membrane Disruption by Vertical Micro-/Nanopillars: Role of Membrane Bending and Traction Forces. *ACS Applied Materials & Interfaces*, *10*(34), 29107–29114. https://doi.org/10.1021/acsami.8b08218

Carmeliet, E. (2019). From Bernstein's rheotome to Neher-Sakmann's patch electrode. The action potential. *Physiological Reports*, *7*(1), e13861. https://doi.org/10.14814/phy2.13861

Chanda, B., Blunck, R., Faria, L. C., Schweizer, F. E., Mody, I., & Bezanilla, F. (2005). A hybrid approach to measuring electrical activity in genetically specified neurons. *Nature Neuroscience*, *8*(11), 1619–1626. https://doi.org/10.1038/nn1558

Chang, D. C., & Reese, T. S. (1990). Changes in membrane structure induced by electroporation as revealed by rapid-freezing electron microscopy. *Biophysical Journal*, *58*(1), 1–12. https://doi.org/10.1016/S0006-3495(90)82348-1

Chen, P., Xu, B., Tokranova, N., Feng, X., Castracane, J., & Gillis, K. D. (2003). Amperometric Detection of Quantal Catecholamine Secretion from Individual Cells on Micromachined Silicon Chips. *Analytical Chemistry*, *75*(3), 518–524. https://doi.org/10.1021/ac025802m

Chen, W., Guillaume-Gentil, O., Rainer, P. Y., Gäbelein, C. G., Saelens, W., Gardeux, V., Klaeger, A., Dainese, R., Zachara, M., Zambelli, T., Vorholt, J. A., & Deplancke, B. (2022). Live-seq

enables temporal transcriptomic recording of single cells. *Nature, 608*(7924), 733–740. https://doi.org/10.1038/s41586-022-05046-9

Chien, J. B., Wallingford, R. A., & Ewing, A. G. (1990). Estimation of Free Dopamine in the Cytoplasm of the Giant Dopamine Cell of Planorbis corneus by Voltammetry and Capillary Electrophoresis. *Journal of Neurochemistry, 54*(2), 633–638. https://doi.org/10.1111/j.1471-4159.1990.tb01918.x

_eprint: https://onlinelibrary.wiley.com/doi/pdf/10.1111/j.1471-4159.1990.tb01918.x

Cole, K. (1949). Dynamic electrical characteristics of the squid axon membrane. *Arch Sci Physiol*, (3), 253–258.

Compton, R. G., & Banks, C. E. (2018, July 4). *Understanding Voltammetry: Simulation of electrode processess (Third Edition)*. World Scientific.

Cui, X., & Martin, D. C. (2003). Electrochemical deposition and characterization of poly(3,4-ethylenedioxythiophene) on neural microelectrode arrays. *Sensors and Actuators B: Chemical, 89*(1), 92–102. https://doi.org/10.1016/S0925-4005(02)00448-3

Dalby, M. J., Gadegaard, N., & Oreffo, R. O. C. (2014). Harnessing nanotopography and integrin–matrix interactions to influence stem cell fate. *Nature Materials, 13*(6), 558–569. https://doi.org/10.1038/nmat3980

Damiati, S., & Schuster, B. (2020). Electrochemical Biosensors Based on S-Layer Proteins. *Sensors, 20*(6), 1721. https://doi.org/10.3390/s20061721

Dernick, G., Alvarez de Toledo, G., & Lindau, M. (2003). Exocytosis of single chromaffin granules in cell-free inside-out membrane patches. *Nature Cell Biology, 5*(4), 358–362. https://doi.org/10.1038/ncb956

Desbiolles, B. X. E., Bertsch, A., & Renaud, P. (2019). Ion beam etching redeposition for 3D multimaterial nanostructure manufacturing. *Microsystems & Nanoengineering, 5*(1), 1–8. https://doi.org/10.1038/s41378-019-0052-7

Desbiolles, B. X. E., de Coulon, E., Bertsch, A., Rohr, S., & Renaud, P. (2019). Intracellular Recording of Cardiomyocyte Action Potentials with Nanopatterned Volcano-Shaped Microelectrode Arrays. *Nano Letters, 19*(9), 6173–6181. https://doi.org/10.1021/acs.nanolett.9b02209

Desbiolles, B. X. E., Hannebelle, M. T. M., de Coulon, E., Bertsch, A., Rohr, S., Fantner, G. E., & Renaud, P. (2020). Volcano-Shaped Scanning Probe Microscopy Probe for Combined Force-Electrogram Recordings from Excitable Cells. *Nano Letters, 20*(6), 4520–4529. https://doi.org/10.1021/acs.nanolett.0c01319

Desbiolles, B. X. E., de Coulon, E., Maïno, N., Bertsch, A., Rohr, S., & Renaud, P. (2020). Nano-volcano microelectrode arrays: toward long-term on-demand registration of transmembrane action potentials by controlled electroporation. *Microsystems & Nanoengineering, 6*(1), 1–12. https://doi.org/10.1038/s41378-020-0178-7

Dipalo, M., Amin, H., Lovato, L., Moia, F., Caprettini, V., Messina, G. C., Tantussi, F., Berdondini, L., & De Angelis, F. (2017). Intracellular and Extracellular Recording of Spontaneous Action Potentials in Mammalian Neurons and Cardiac Cells with 3D Plasmonic Nanoelectrodes. *Nano Letters, 17*(6), 3932–3939. https://doi.org/10.1021/acs.nanolett.7b01523

Dipalo, M., McGuire, A. F., Lou, H.-Y., Caprettini, V., Melle, G., Bruno, G., Lubrano, C., Matino, L., Li, X., De Angelis, F., Cui, B., & Santoro, F. (2018). Cells Adhering to 3D Vertical Nanostructures: Cell Membrane Reshaping without Stable Internalization. *Nano Letters*, *18*(9), 6100–6105. https://doi.org/10.1021/acs.nanolett.8b03163

Dragas, J., Viswam, V., Shadmani, A., Chen, Y., Bounik, R., Stettler, A., Radivojevic, M., Geissler, S., Obien, M. E. J., Müller, J., & Hierlemann, A. (2017). In Vitro Multi-Functional Microelectrode Array Featuring 59 760 Electrodes, 2048 Electrophysiology Channels, Stimulation, Impedance Measurement, and Neurotransmitter Detection Channels. *IEEE Journal of Solid-State Circuits*, *52*(6), 1576–1590. https://doi.org/10.1109/JSSC.2017.2686580

Drake, K., Wise, K., Farraye, J., Anderson, D., & BeMent, S. (1988). Performance of planar multisite microprobes in recording extracellular single-unit intracortical activity. *IEEE Transactions on Biomedical Engineering*, *35*(9), 719–732. https://doi.org/10.1109/10.7273

Dunlop, J., Bowlby, M., Peri, R., Vasilyev, D., & Arias, R. (2008). High-throughput electrophysiology: an emerging paradigm for ion-channel screening and physiology. *Nature Reviews Drug Discovery*, *7*(4), 358–368. https://doi.org/10.1038/nrd2552

Fil, J., Dalchau, N., & Chu, D. (2022). Programming Molecular Systems To Emulate a Learning Spiking Neuron. *ACS Synthetic Biology*, *11*(6), 2055–2069. https://doi.org/10.1021/acssynbio.1c00625

Fischer, L. M., Tenje, M., Heiskanen, A. R., Masuda, N., Castillo, J., Bentien, A., Émneus, J., Jakobsen, M. H., & Boisen, A. (2009). Gold cleaning methods for electrochemical detection applications. *Microelectronic Engineering*, *86*(4), 1282–1285. https://doi.org/10.1016/j.mee.2008.11.045

Gao, R., Strehle, S., Tian, B., Cohen-Karni, T., Xie, P., Duan, X., Qing, Q., & Lieber, C. M. (2012). Outside Looking In: Nanotube Transistor Intracellular Sensors. *Nano Letters*, *12*(6), 3329–3333. https://doi.org/10.1021/nl301623p

Gerhardt, G., & Adams, R. N. (1982). Determination of diffusion coefficients by flow injection analysis. *Analytical Chemistry*, *54*(14), 2618–2620. https://doi.org/10.1021/ac00251a054

Gong, J., Lai, Y., Li, X., Wang, M., Leitz, J., Hu, Y., Zhang, Y., Choi, U. B., Cipriano, D., Pfuetzner, R. A., Südhof, T. C., Yang, X., Brunger, A. T., & Diao, J. (2016). C-terminal domain of mammalian complexin-1 localizes to highly curved membranes. *Proceedings of the National Academy of Sciences*, *113*(47), E7590–E7599. https://doi.org/10.1073/pnas.1609917113

Grall, S., Alić, I., Pavoni, E., Awadein, M., Fujii, T., Müllegger, S., Farina, M., Clément, N., & Gramse, G. (2021). Attoampere Nanoelectrochemistry. *Small*, *17*(29), 2101253. https://doi.org/10.1002/smll.202101253
_eprint: https://onlinelibrary.wiley.com/doi/pdf/10.1002/smll.202101253

Greene, L. A., & Rein, G. (1977). Release, storage and uptake of catecholamines by a clonal cell line of nerve growth factor (NGF) responsive pheochromocytoma cells. *Brain Research*, *129*(2), 247–263. https://doi.org/10.1016/0006-8993(77)90005-1

Grienberger, C., & Konnerth, A. (2012). Imaging Calcium in Neurons. *Neuron, 73*(5), 862–885. https://doi.org/10.1016/j.neuron.2012.02.011

Gubernator, N. G., Zhang, H., Staal, R. G. W., Mosharov, E. V., Pereira, D. B., Yue, M., Balsanek, V., Vadola, P. A., Mukherjee, B., Edwards, R. H., Sulzer, D., & Sames, D. (2009). Fluorescent False Neurotransmitters Visualize Dopamine Release from Individual Presynaptic Terminals. *Science, 324*(5933), 1441–1444. https://doi.org/10.1126/science.1172278

Guillaume-Gentil, O., Grindberg, R. V., Kooger, R., Dorwling-Carter, L., Martinez, V., Ossola, D., Pilhofer, M., Zambelli, T., & Vorholt, J. A. (2016). Tunable Single-Cell Extraction for Molecular Analyses. *Cell, 166*(2), 506–516. https://doi.org/10.1016/j.cell.2016.06.025

Hai, A., Kamber, D., Malkinson, G., Erez, H., Mazurski, N., Shappir, J., & Spira, M. E. (2009). Changing gears from chemical adhesion of cells to flat substrata toward engulfment of micro-protrusions by active mechanisms. *Journal of Neural Engineering, 6*(6), 066009. https://doi.org/10.1088/1741-2560/6/6/066009

Hai, A., Shappir, J., & Spira, M. E. (2010). In-cell recordings by extracellular microelectrodes. *Nature Methods, 7*(3), 200–202. https://doi.org/10.1038/nmeth.1420

Hamill, O. P., Marty, A., Neher, E., Sakmann, B., & Sigworth, F. J. (1981). Improved patch-clamp techniques for high-resolution current recording from cells and cell-free membrane patches. *Pflügers Archiv, 391*(2), 85–100. https://doi.org/10.1007/BF00656997

Hanssen, B. L., Siraj, S., & Wong, D. K. Y. (2016). Recent strategies to minimise fouling in electrochemical detection systems. *Reviews in Analytical Chemistry, 35*(1), 1–28. https://doi.org/10.1515/revac-2015-0008

Hargus, G., Cooper, O., Deleidi, M., Levy, A., Lee, K., Marlow, E., Yow, A., Soldner, F., Hockemeyer, D., Hallett, P. J., Osborn, T., Jaenisch, R., & Isacson, O. (2010). Differentiated Parkinson patient-derived induced pluripotent stem cells grow in the adult rodent brain and reduce motor asymmetry in Parkinsonian rats. *Proceedings of the National Academy of Sciences, 107*(36), 15921–15926. https://doi.org/10.1073/pnas.1010209107

Harris, K. D., Quiroga, R. Q., Freeman, J., & Smith, S. L. (2016). Improving data quality in neuronal population recordings. *Nature Neuroscience, 19*(9), 1165–1174. https://doi.org/10.1038/nn.4365

Haynes, W. M. (Ed.). (2016, July 31). *CRC Handbook of Chemistry and Physics* (97th ed.). CRC Press. https://doi.org/10.1201/9781315380476

Herculano-Houzel, S. (2012). The remarkable, yet not extraordinary, human brain as a scaled-up primate brain and its associated cost. *Proceedings of the National Academy of Sciences, 109*, 10661–10668. https://doi.org/10.1073/pnas.1201895109

Hierlemann, A., Frey, U., Hafizovic, S., & Heer, F. (2011). Growing Cells Atop Microelectronic Chips: Interfacing Electrogenic Cells In Vitro With CMOS-Based Microelectrode Arrays. *Proceedings of the IEEE, 99*(2), 252–284. https://doi.org/10.1109/JPROC.2010.2066532

Higgins, E. S., & George, M. S. (2019). *The neuroscience of clinical psychiatry: the pathophysiology of behavior and mental illness* (Third edition). Wolters Kluwer OCLC: 1048335337.

Hochbaum, D. R., Zhao, Y., Farhi, S. L., Klapoetke, N., Werley, C. A., Kapoor, V., Zou, P., Kralj, J. M., Maclaurin, D., Smedemark-Margulies, N., Saulnier, J. L., Boulting, G. L., Straub,

C., Cho, Y. K., Melkonian, M., Wong, G. K.-S., Harrison, D. J., Murthy, V. N., Sabatini, B. L., ... Cohen, A. E. (2014). All-optical electrophysiology in mammalian neurons using engineered microbial rhodopsins. *Nature Methods*, *11*(8), 825–833. https://doi.org/10.1038/nmeth.3000

Hodgkin, A. L., & Huxley, A. F. (1952). Currents carried by sodium and potassium ions through the membrane of the giant axon of Loligo. *The Journal of Physiology*, *116*(4), 449–472.

Hodgkin, A. L., Huxley, A. F., & Katz, B. (1952). Measurement of current-voltage relations in the membrane of the giant axon of Loligo. *The Journal of Physiology*, *116*(4), 424. https://doi.org/10.1113/jphysiol.1952.sp004716

Huang, J.-A., Caprettini, V., Zhao, Y., Melle, G., Maccaferri, N., Deleye, L., Zambrana-Puyalto, X., Ardini, M., Tantussi, F., Dipalo, M., & De Angelis, F. (2019). On-Demand Intracellular Delivery of Single Particles in Single Cells by 3D Hollow Nanoelectrodes. *Nano Letters*, *19*(2), 722–731. https://doi.org/10.1021/acs.nanolett.8b03764

Huang, M., Delacruz, J. B., Ruelas, J. C., Rathore, S. S., & Lindau, M. (2018). Surface-modified CMOS IC electrochemical sensor array targeting single chromaffin cells for highly parallel amperometry measurements. *Pflügers Archiv - European Journal of Physiology*, *470*(1), 113–123. https://doi.org/10.1007/s00424-017-2067-y

Jahed, Z., Yang, Y., Tsai, C.-T., Foster, E. P., McGuire, A. F., Yang, H., Liu, A., Forro, C., Yan, Z., Jiang, X., Zhao, M.-T., Zhang, W., Li, X., Li, T., Pawlosky, A., Wu, J. C., & Cui, B. (2022). Nanocrown electrodes for parallel and robust intracellular recording of cardiomyocytes. *Nature Communications*, *13*(1), 2253. https://doi.org/10.1038/s41467-022-29726-2

Jankowski, J. A., Finnegan, J. M., & Wightman, R. M. (1994). Extracellular Ionic Composition Alters Kinetics of Vesicular Release of Catecholamines and Quantal Size During Exocytosis at Adrenal Medullary Cells. *Journal of Neurochemistry*, *63*(5), 1739–1747. https://doi.org/10.1046/j.1471-4159.1994.63051739.x _eprint: https://onlinelibrary.wiley.com/doi/pdf/10.1046/j.1471-4159.1994.63051739.x

Jeng, J.-Y., Sun, L., Wang, J.-C., Lin, C.-Y., Hung, C.-P., Chu, L.-A., Chang, H.-Y., Chiang, A.-S., & Sang, T.-K. (2020, September 4). *CyDAP–A fluorescent probe for cytosolic dopamine detection* (preprint). Neuroscience. https://doi.org/10.1101/2020.09.04.283911

Jensen, M. B., Bhatia, V. K., Jao, C. C., Rasmussen, J. E., Pedersen, S. L., Jensen, K. J., Langen, R., & Stamou, D. (2011). Membrane curvature sensing by amphipathic helices: a single liposome study using alpha-synuclein and annexin B12. *Journal of Biological Chemistry*, *286*(49), 42603–42614. https://doi.org/10.1074/jbc.M111.271130

Jeon, H.-J., Kim, K. H., Baek, Y.-K., Kim, D. W., & Jung, H.-T. (2010). New Top-Down Approach for Fabricating High-Aspect-Ratio Complex Nanostructures with 10 nm Scale Features. *Nano Letters*, *10*(9), 3604–3610. https://doi.org/10.1021/nl1025776

Jill Venton, B., & Cao, Q. (2020). Fundamentals of fast-scan cyclic voltammetry for dopamine detection. *Analyst*, *145*(4), 1158–1168. https://doi.org/10.1039/C9AN01586H

Johnson, S. L., Marcotti, W., & Kros, C. J. (2005). Increase in efficiency and reduction in Ca2+ dependence of exocytosis during development of mouse inner hair cells. *The Journal*

of Physiology, *563*(1), 177–191. https://doi.org/10.1113/jphysiol.2004.074740
_eprint: https://onlinelibrary.wiley.com/doi/pdf/10.1113/jphysiol.2004.074740

Kaiser, K. M. M., Zilberter, Y., & Sakmann, B. (2001). Back-propagating action potentials mediate calcium signalling in dendrites of bitufted interneurons in layer 2/3 of rat somatosensory cortex. *The Journal of Physiology*, *535*, 17. https://doi.org/10.1111/j.1469-7793.2001.t01-1-00017.x

Kang, S., Nieuwenhuis, A. F., Mathwig, K., Mampallil, D., & Lemay, S. G. (2013). Electrochemical Single-Molecule Detection in Aqueous Solution Using Self-Aligned Nanogap Transducers. *ACS Nano*, *7*(12), 10931–10937. https://doi.org/10.1021/nn404440v

Kim, J., Song, X., Kinoshita, K., Madou, M., & White, R. (1998). Electrochemical Studies of Carbon Films from Pyrolyzed Photoresist. *Journal of The Electrochemical Society*, *145*(7), 2314. https://doi.org/10.1149/1.1838636

Kruss, S., Salem, D. P., Vuković, L., Lima, B., Vander Ende, E., Boyden, E. S., & Strano, M. S. (2017). High-resolution imaging of cellular dopamine efflux using a fluorescent nanosensor array. *Proceedings of the National Academy of Sciences*, *114*(8), 1789–1794. https://doi.org/10.1073/pnas.1613541114

Larsson, A., Majdi, S., Oleinick, A., Svir, I., Dunevall, J., Amatore, C., & Ewing, A. G. (2020). Intracellular Electrochemical Nanomeasurements Reveal that Exocytosis of Molecules at Living Neurons is Subquantal and Complex. *Angewandte Chemie*, *132*(17), 6777–6780. https://doi.org/10.1002/ange.201914564
_eprint: https://onlinelibrary.wiley.com/doi/pdf/10.1002/ange.201914564

Lavacchi, A., Bardi, U., Borri, C., Caporali, S., Fossati, A., & Perissi, I. (2009). Cyclic voltammetry simulation at microelectrode arrays with COMSOL Multiphysics®. *Journal of Applied Electrochemistry*, *39*(11), 2159. https://doi.org/10.1007/s10800-009-9797-2

Lee, J., Gänswein, T., Ulusan, H., Emmenegger, V., Saguner, A. M., Duru, F., & Hierlemann, A. (2022). Repeated and On-Demand Intracellular Recordings of Cardiomyocytes Derived from Human-Induced Pluripotent Stem Cells. *ACS Sensors*. https://doi.org/10.1021/acssensors.2c01678

Leopold, A. V., Shcherbakova, D. M., & Verkhusha, V. V. (2019). Fluorescent Biosensors for Neurotransmission and Neuromodulation: Engineering and Applications. *Frontiers in Cellular Neuroscience*, *13*.

Liao, Q.-L., Jiang, H., Zhang, X.-W., Qiu, Q.-F., Tang, Y., Yang, X.-K., Liu, Y.-L., & Huang, W.-H. (2019). A single nanowire sensor for intracellular glucose detection. *Nanoscale*, *11*(22), 10702–10708. https://doi.org/10.1039/C9NR01997A

Limongi, T., Cesca, F., Gentile, F., Marotta, R., Ruffilli, R., Barberis, A., Dal Maschio, M., Petrini, E. M., Santoriello, S., Benfenati, F., & Di Fabrizio, E. (2013). 3D Cell Cultures: Nanostructured Superhydrophobic Substrates Trigger the Development of 3D Neuronal Networks (Small 3/2013) [_eprint: https://onlinelibrary.wiley.com/doi/pdf/10.1002/smll.201370016]. *Small*, *9*(3), 334–334. https://doi.org/10.1002/smll.201370016

Lin, Z. C., Xie, C., Osakada, Y., Cui, Y., & Cui, B. (2014). Iridium oxide nanotube electrodes for sensitive and prolonged intracellular measurement of action potentials. *Nature Communications*, *5*(1), 3206. https://doi.org/10.1038/ncomms4206

Bibliography

Liu, R., Chen, R., Elthakeb, A. T., Lee, S. H., Hinckley, S., Khraiche, M. L., Scott, J., Pre, D., Hwang, Y., Tanaka, A., Ro, Y. G., Matsushita, A. K., Dai, X., Soci, C., Biesmans, S., James, A., Nogan, J., Jungjohann, K. L., Pete, D. V., ... Dayeh, S. A. (2017). High Density Individually Addressable Nanowire Arrays Record Intracellular Activity from Primary Rodent and Human Stem Cell Derived Neurons. *Nano Letters*, *17*(5), 2757–2764. https://doi.org/10.1021/acs.nanolett.6b04752

Liu, R., Lee, J., Tchoe, Y., Pre, D., Bourhis, A. M., D'Antonio-Chronowska, A., Robin, G., Lee, S. H., Ro, Y. G., Vatsyayan, R., Tonsfeldt, K. J., Hossain, L. A., Phipps, M. L., Yoo, J., Nogan, J., Martinez, J. S., Frazer, K. A., Bang, A. G., & Dayeh, S. A. (2022). Ultra-Sharp Nanowire Arrays Natively Permeate, Record, and Stimulate Intracellular Activity in Neuronal and Cardiac Networks. *Advanced Functional Materials*, *32*(8), 2108378. https://doi.org/10.1002/adfm.202108378
_eprint: https://onlinelibrary.wiley.com/doi/pdf/10.1002/adfm.202108378

Liu, X., Tian, M., Gao, W., & Zhao, J. (2019). A Simple, Rapid, Fluorometric Assay for Dopamine by In Situ Reaction of Boronic Acids and cis-Diol. *Journal of Analytical Methods in Chemistry*, *2019*, e6540397. https://doi.org/10.1155/2019/6540397

Liu, X., Barizuddin, S., Shin, W., Mathai, C. J., Gangopadhyay, S., & Gillis, K. D. (2011). Microwell Device for Targeting Single Cells to Electrochemical Microelectrodes for High-Throughput Amperometric Detection of Quantal Exocytosis. *Analytical Chemistry*, *83*(7), 2445–2451. https://doi.org/10.1021/ac1033616

Loftus, J. C., Smith, J. W., & Ginsberg, M. H. (1994). Integrin-mediated cell adhesion: the extracellular face. *Journal of Biological Chemistry*, *269*(41), 25235–25238. https://doi.org/10.1016/S0021-9258(18)47235-3

López-Muñoz, F., Boya, J., & Alamo, C. (2006). Neuron theory, the cornerstone of neuroscience, on the centenary of the Nobel Prize award to Santiago Ramón y Cajal. *Brain Research Bulletin*, *70*(4), 391–405. https://doi.org/10.1016/j.brainresbull.2006.07.010

Lou, H.-Y., Zhao, W., Li, X., Duan, L., Powers, A., Akamatsu, M., Santoro, F., McGuire, A. F., Cui, Y., Drubin, D. G., & Cui, B. (2019). Membrane curvature underlies actin reorganization in response to nanoscale surface topography. *Proceedings of the National Academy of Sciences*, *116*(46), 23143–23151. https://doi.org/10.1073/pnas.1910166116

Maloney, T. R., Dilkes-Hall, I. E., Vlok, M., Oktaviana, A. A., Setiawan, P., Priyatno, A. A. D., Ririmasse, M., Geria, I. M., Effendy, M. A. R., Istiawan, B., Atmoko, F. T., Adhityatama, S., Moffat, I., Joannes-Boyau, R., Brumm, A., & Aubert, M. (2022). Surgical amputation of a limb 31,000 years ago in Borneo. *Nature*, *609*(7927), 547–551. https://doi.org/10.1038/s41586-022-05160-8

Manica, D. P., Mitsumori, Y., & Ewing, A. G. (2003). Characterization of Electrode Fouling and Surface Regeneration for a Platinum Electrode on an Electrophoresis Microchip. *Analytical Chemistry*, *75*(17), 4572–4577. https://doi.org/10.1021/ac034235f

Marmont, G. (1949). Studies on the axon membrane. I. A new method. *J Cell Comp Physiol*, (34), 351–382.

Mazzarello, P. (1999). A unifying concept: the history of cell theory. *Nature Cell Biology*, *1*(1), E13–E15. https://doi.org/10.1038/8964

McCarty, G. S., Dunaway, L. E., Denison, J. D., & Sombers, L. A. (2022). Neurotransmitter Readily Escapes Detection at the Opposing Microelectrode Surface in Typical Amperometric Measurements of Exocytosis at Single Cells. *Analytical Chemistry, 94*(27), 9548–9556. https://doi.org/10.1021/acs.analchem.2c00060

McCormick, H. K., & Dick, J. E. (2021). Nanoelectrochemical quantification of single-cell metabolism. *Analytical and Bioanalytical Chemistry, 413*(1), 17–24. https://doi.org/10.1007/s00216-020-02899-9

McMahon, H. T., & Boucrot, E. (2015). Membrane curvature at a glance. *Journal of Cell Science, 128*(6), 1065–1070. https://doi.org/10.1242/jcs.114454

Mohrmann, R., & Sørensen, J. B. (2012). SNARE Requirements En Route to Exocytosis: from Many to Few. *Journal of Molecular Neuroscience, 48*(2), 387–394. https://doi.org/10.1007/s12031-012-9744-2

Mosharov, E. V., Gong, L.-W., Khanna, B., Sulzer, D., & Lindau, M. (2003). Intracellular Patch Electrochemistry: Regulation of Cytosolic Catecholamines in Chromaffin Cells. *Journal of Neuroscience, 23*(13), 5835–5845. https://doi.org/10.1523/JNEUROSCI.23-13-05835.2003

Mosharov, E. V., Larsen, K. E., Kanter, E., Phillips, K. A., Wilson, K., Schmitz, Y., Krantz, D. E., Kobayashi, K., Edwards, R. H., & Sulzer, D. (2009). Interplay between Cytosolic Dopamine, Calcium, and alpha-Synuclein Causes Selective Death of Substantia Nigra Neurons. *Neuron, 62*(2), 218–229. https://doi.org/10.1016/j.neuron.2009.01.033

Mosharov, E. V., Staal, R. G. W., Bové, J., Prou, D., Hananiya, A., Markov, D., Poulsen, N., Larsen, K. E., Moore, C. M. H., Troyer, M. D., Edwards, R. H., Przedborski, S., & Sulzer, D. (2006). Alpha-Synuclein Overexpression Increases Cytosolic Catecholamine Concentration. *Journal of Neuroscience, 26*(36), 9304–9311. https://doi.org/10.1523/JNEUROSCI.0519-06.2006

Mosharov, E. V., & Sulzer, D. (2005). Analysis of exocytotic events recorded by amperometry. *Nature Methods, 2*(9), 651–658. https://doi.org/10.1038/nmeth782

Movahed, S., & Li, D. (2012). Electrokinetic transport through the nanopores in cell membrane during electroporation. *Journal of Colloid and Interface Science, 369*(1), 442–452. https://doi.org/10.1016/j.jcis.2011.12.039

Mulder, W. H., Sluyters, J. H., Pajkossy, T., & Nyikos, L. (1990). Tafel current at fractal electrodes: Connection with admittance spectra. *Journal of Electroanalytical Chemistry and Interfacial Electrochemistry, 285*(1), 103–115. https://doi.org/10.1016/0022-0728(90)87113-X

Neher, E., & Sakmann, B. (1976). Single-channel currents recorded from membrane of denervated frog muscle fibres. *Nature, 260*(5554), 799–802. https://doi.org/10.1038/260799a0

Nosov, G., Kahms, M., & Klingauf, J. (2020). The Decade of Super-Resolution Microscopy of the Presynapse. *Frontiers in Synaptic Neuroscience, 12*.

Ojovan, S. M., Rabieh, N., Shmoel, N., Erez, H., Maydan, E., Cohen, A., & Spira, M. E. (2015). A feasibility study of multi-site,intracellular recordings from mammalian neurons by

extracellular gold mushroom-shaped microelectrodes. *Scientific Reports*, *5*(1), 14100. https://doi.org/10.1038/srep14100

Omiatek, D. M., Dong, Y., Heien, M. L., & Ewing, A. G. (2010). Only a Fraction of Quantal Content is Released During Exocytosis as Revealed by Electrochemical Cytometry of Secretory Vesicles. *ACS Chemical Neuroscience*, *1*(3), 234–245. https://doi.org/10.1021/cn900040e

Pachitariu, M., Stringer, C., Dipoppa, M., Schröder, S., Rossi, L. F., Dalgleish, H., Carandini, M., & Harris, K. D. (2017, July 20). Suite2p: beyond 10,000 neurons with standard two-photon microscopy. https://doi.org/10.1101/061507

Palmer, L. M., & Stuart, G. J. (2009). Membrane Potential Changes in Dendritic Spines during Action Potentials and Synaptic Input. *Journal of Neuroscience*, *29*(21), 6897–6903. https://doi.org/10.1523/JNEUROSCI.5847-08.2009

Pan, N., Rao, W., Kothapalli, N. R., Liu, R., Burgett, A. W. G., & Yang, Z. (2014). The Single-Probe: A Miniaturized Multifunctional Device for Single Cell Mass Spectrometry Analysis. *Analytical Chemistry*, *86*(19), 9376–9380. https://doi.org/10.1021/ac5029038

Pantoja, R., Nagarah, J. M., Starace, D. M., Melosh, N. A., Blunck, R., Bezanilla, F., & Heath, J. R. (2004). Silicon chip-based patch-clamp electrodes integrated with PDMS microfluidics. *Biosensors and Bioelectronics*, *20*(3), 509–517. https://doi.org/10.1016/j.bios.2004.02.020

Patel, J., Radhakrishnan, L., Zhao, B., Uppalapati, B., Daniels, R. C., Ward, K. R., & Collinson, M. M. (2013). Electrochemical Properties of Nanostructured Porous Gold Electrodes in Biofouling Solutions. *Analytical Chemistry*, *85*(23), 11610–11618. https://doi.org/10.1021/ac403013r

Pine, J. (2006). A History of MEA Development. In M. Taketani & M. Baudry (Eds.), *Advances in Network Electrophysiology* (pp. 3–23). Springer US. https://doi.org/10.1007/0-387-25858-2_1

Pires, R. H., Shree, N., Manu, E., Guzniczak, E., & Otto, O. (2019). Cardiomyocyte mechanodynamics under conditions of actin remodelling. *Philosophical Transactions of the Royal Society B: Biological Sciences*, *374*(1786), 20190081. https://doi.org/10.1098/rstb.2019.0081

Pothos, E., Desmond, M., & Sulzer, D. (1996). L-3,4-Dihydroxyphenylalanine Increases the Quantal Size of Exocytotic Dopamine Release In Vitro. *Journal of Neurochemistry*, *66*(2), 629–636. https://doi.org/10.1046/j.1471-4159.1996.66020629.x _eprint: https://onlinelibrary.wiley.com/doi/pdf/10.1046/j.1471-4159.1996.66020629.x

Pouzat, C., Delescluse, M., Viot, P., & Diebolt, J. (2004). Improved Spike-Sorting By Modeling Firing Statistics and Burst-Dependent Spike Amplitude Attenuation: A Markov Chain Monte Carlo Approach. *Journal of Neurophysiology*, *91*(6), 2910–2928. https://doi.org/10.1152/jn.00227.2003

Qian, C.-G., Zhu, S., Feng, P.-J., Chen, Y.-L., Yu, J.-C., Tang, X., Liu, Y., & Shen, Q.-D. (2015). Conjugated Polymer Nanoparticles for Fluorescence Imaging and Sensing of Neurotransmitter Dopamine in Living Cells and the Brains of Zebrafish Larvae. *ACS Applied Materials & Interfaces*, *7*(33), 18581–18589. https://doi.org/10.1021/acsami.5b04987

Qing, Q., Jiang, Z., Xu, L., Gao, R., Mai, L., & Lieber, C. M. (2014). Free-standing kinked nanowire transistor probes for targeted intracellular recording in three dimensions. *Nature Nanotechnology*, *9*(2), 142–147. https://doi.org/10.1038/nnano.2013.273

Radivojevic, M., Franke, F., Altermatt, M., Müller, J., Hierlemann, A., & Bakkum, D. J. (2017). Tracking individual action potentials throughout mammalian axonal arbors. *eLife*, *6*, e30198. https://doi.org/10.7554/eLife.30198

Rawson, F. J., Hicks, J., Dodd, N., Abate, W., Garrett, D. J., Yip, N., Fejer, G., Downard, A. J., Baronian, K. H. R., Jackson, S. K., & Mendes, P. M. (2015). Fast, Ultrasensitive Detection of Reactive Oxygen Species Using a Carbon Nanotube Based-Electrocatalytic Intracellular Sensor. *ACS Applied Materials & Interfaces*, *7*(42), 23527–23537. https://doi.org/10.1021/acsami.5b06493

Richardson, M. J. E., & Silberberg, G. (2008). Measurement and Analysis of Postsynaptic Potentials Using a Novel Voltage-Deconvolution Method. *Journal of Neurophysiology*, *99*(2), 1020–1031. https://doi.org/10.1152/jn.00942.2007

Robinson, J. T., Jorgolli, M., Shalek, A. K., Yoon, M.-H., Gertner, R. S., & Park, H. (2012). Vertical nanowire electrode arrays as a scalable platform for intracellular interfacing to neuronal circuits. *Nature Nanotechnology*, *7*(3), 180–184. https://doi.org/10.1038/nnano.2011.249

Rothe, J., Frey, O., Madangopal, R., Rickus, J., & Hierlemann, A. (2017). Robust Functionalization of Large Microelectrode Arrays by Using Pulsed Potentiostatic Deposition. *Sensors*, *17*(1), 22. https://doi.org/10.3390/s17010022

Ruhl, G., Wittmann, S., Koenig, M., & Neumaier, D. (2017). The integration of graphene into microelectronic devices. *Beilstein Journal of Nanotechnology*, *8*, 1056–1064. https://doi.org/10.3762/bjnano.8.107

Sabatini, B. L., Oertner, T. G., & Svoboda, K. (2002). The Life Cycle of Ca2+ Ions in Dendritic Spines. *Neuron*, *33*(3), 439–452. https://doi.org/10.1016/S0896-6273(02)00573-1

Sakmann, B., & Neher, E. (1983). Geometric Parameters of Pipettes and Membrane Patches. In B. Sakmann & E. Neher (Eds.), *Single-Channel Recording* (pp. 37–51). Springer US. https://doi.org/10.1007/978-1-4615-7858-1_2

Santoro, F., Zhao, W., Joubert, L.-M., Duan, L., Schnitker, J., van de Burgt, Y., Lou, H.-Y., Liu, B., Salleo, A., Cui, L., Cui, Y., & Cui, B. (2017). Revealing the Cell–Material Interface with Nanometer Resolution by Focused Ion Beam/Scanning Electron Microscopy. *ACS Nano*, *11*(8), 8320–8328. https://doi.org/10.1021/acsnano.7b03494

Sasso, L., Heiskanen, A., Diazzi, F., Dimaki, M., Castillo-León, J., Vergani, M., Landini, E., Raiteri, R., Ferrari, G., Carminati, M., Sampietro, M., E. Svendsen, W., & Emnéus, J. (2013). Doped overoxidized polypyrrole microelectrodes as sensors for the detection of dopamine released from cell populations. *Analyst*, *138*(13), 3651–3659. https://doi.org/10.1039/C3AN00085K

Scanziani, M., & Häusser, M. (2009). Electrophysiology in the age of light. *Nature*, *461*(7266), 930–939. https://doi.org/10.1038/nature08540

Bibliography

Schiller, C. A., & Strunz, W. (2001). The evaluation of experimental dielectric data of barrier coatings by means of different models. *Electrochimica Acta*, *46*(24), 3619–3625. https://doi.org/10.1016/S0013-4686(01)00644-2

Schindler, S., & Bechtold, T. (2019). Mechanistic insights into the electrochemical oxidation of dopamine by cyclic voltammetry. *Journal of Electroanalytical Chemistry*, *836*, 94–101. https://doi.org/10.1016/j.jelechem.2019.01.069

Schmoranzer, J., Goulian, M., Axelrod, D., & Simon, S. M. (2000). Imaging Constitutive Exocytosis with Total Internal Reflection Fluorescence Microscopy. *Journal of Cell Biology*, *149*(1), 23–32. https://doi.org/10.1083/jcb.149.1.23

Schroeder, T. J., Borges, R., Finnegan, J. M., Pihel, K., Amatore, C., & Wightman, R. M. (1996). Temporally resolved, independent stages of individual exocytotic secretion events. *Biophysical Journal*, *70*(2), 1061–1068. https://doi.org/10.1016/S0006-3495(96)79652-2

Schroeder, T. J., Jankowski, J. A., Senyshyn, J., Holz, R. W., & Wightman, R. M. (1994). Zones of exocytotic release on bovine adrenal medullary cells in culture. *Journal of Biological Chemistry*, *269*(25), 17215–17220. https://doi.org/10.1016/S0021-9258(17)32542-5

Shafer, T. J. (1998). Effects of Cd2+, Pb2+ and CH3Hg+ on high voltage-activated calcium currents in pheochromocytoma (PC12) cells: potency, reversibility, interactions with extracellular Ca2+ and mechanisms of block. *Toxicology Letters*, *99*(3), 207–221. https://doi.org/10.1016/S0378-4274(98)00225-2

Shin, W., Ge, L., Arpino, G., Villarreal, S. A., Hamid, E., Liu, H., Zhao, W.-D., Wen, P. J., Chiang, H.-C., & Wu, L.-G. (2018). Visualization of Membrane Pore in Live Cells Reveals a Dynamic-Pore Theory Governing Fusion and Endocytosis. *Cell*, *173*(4), 934–945.e12. https://doi.org/10.1016/j.cell.2018.02.062

Singh, P. S., Chan, H.-S. M., Kang, S., & Lemay, S. G. (2011). Stochastic Amperometric Fluctuations as a Probe for Dynamic Adsorption in Nanofluidic Electrochemical Systems. *Journal of the American Chemical Society*, *133*(45), 18289–18295. https://doi.org/10.1021/ja2067669

Song, S. C., Beatty, J. A., & Wilson, C. J. (2016). The ionic mechanism of membrane potential oscillations and membrane resonance in striatal LTS interneurons. *Journal of Neurophysiology*, *116*(4), 1752–1764. https://doi.org/10.1152/jn.00511.2016

Sparreboom, W., Eijkel, J. C. T., Bomer, J., & van den Berg, A. (2008). Rapid sacrificial layer etching for the fabrication of nanochannels with integrated metal electrodes. *Lab on a Chip*, *8*(3), 402–407. https://doi.org/10.1039/B716382G

Spégel, C., Heiskanen, A., Acklid, J., Wolff, A., Taboryski, R., Emnéus, J., & Ruzgas, T. (2007). On-Chip Determination of Dopamine Exocytosis Using Mercaptopropionic Acid Modified Microelectrodes. *Electroanalysis*, *19*(2-3), 263–271. https://doi.org/10.1002/elan.200603720

_eprint: https://onlinelibrary.wiley.com/doi/pdf/10.1002/elan.200603720

Spira, M. E., Huang, S.-H., Shmoel, N., & Erez, H. (2019). Multisite Intracellular Recordings by MEA. In M. Chiappalone, V. Pasquale, & M. Frega (Eds.), *In Vitro Neuronal Networks:*

From Culturing Methods to Neuro-Technological Applications (pp. 125–153). Springer International Publishing. https://doi.org/10.1007/978-3-030-11135-9_5

Spira, M. E., Kamber, D., Dormann, A., Cohen, A., Bartic, C., Borghs, G., Langedijk, J., Yitzchaik, S., Shabthai, K., & Shappir, J. (2007). Improved Neuronal Adhesion to the Surface of Electronic Device by Engulfment of Protruding Micro-Nails Fabricated on the Chip Surface. *TRANSDUCERS 2007 - 2007 International Solid-State Sensors, Actuators and Microsystems Conference*, 1247–1250. https://doi.org/10.1109/SENSOR.2007.4300363

Staal, R. G. W., Mosharov, E. V., & Sulzer, D. (2004). Dopamine neurons release transmitter via a flickering fusion pore. *Nature Neuroscience*, *7*(4), 341–346. https://doi.org/10.1038/nn1205

Sulzer, D., & Pothos, E. N. (2000). Regulation of Quantal Size by Presynaptic Mechanisms. *Reviews in the Neurosciences*, *11*(2-3), 159–212. https://doi.org/10.1515/REVNEURO.2000.11.2-3.159

Sun, P., Laforge, F. O., Abeyweera, T. P., Rotenberg, S. A., Carpino, J., & Mirkin, M. V. (2008). Nanoelectrochemistry of mammalian cells. *Proceedings of the National Academy of Sciences*, *105*(2), 443–448. https://doi.org/10.1073/pnas.0711075105

Sun, X., & Gillis, K. D. (2006). On-Chip Amperometric Measurement of Quantal Catecholamine Release Using Transparent Indium Tin Oxide Electrodes. *Analytical Chemistry*, *78*(8), 2521–2525. https://doi.org/10.1021/ac052037d

Taylor, S. C., & Peers, C. (1998). Hypoxia Evokes Catecholamine Secretion from Rat Pheochromocytoma PC-12 Cells. *Biochemical and Biophysical Research Communications*, *248*(1), 13–17. https://doi.org/10.1006/bbrc.1998.8905

Thomas, C. A., Springer, P. A., Loeb, G. E., Berwald-Netter, Y., & Okun, L. M. (1972). A miniature microelectrode array to monitor the bioelectric activity of cultured cells. *Experimental Cell Research*, *74*(1), 61–66. https://doi.org/10.1016/0014-4827(72)90481-8

Tian, B., Cohen-Karni, T., Qing, Q., Duan, X., Xie, P., & Lieber, C. M. (2010). Three-Dimensional, Flexible Nanoscale Field-Effect Transistors as Localized Bioprobes. *Science*, *329*(5993), 830–834. https://doi.org/10.1126/science.1192033

Tian, L., Hires, S. A., Mao, T., Huber, D., Chiappe, M. E., Chalasani, S. H., Petreanu, L., Akerboom, J., McKinney, S. A., Schreiter, E. R., Bargmann, C. I., Jayaraman, V., Svoboda, K., & Looger, L. L. (2009). Imaging neural activity in worms, flies and mice with improved GCaMP calcium indicators. *Nature Methods*, *6*(12), 875–881. https://doi.org/10.1038/nmeth.1398

Towhidi, L., Kotnik, T., Pucihar, G., Firoozabadi, S. M. P., Mozdarani, H., & Miklavčič, D. (2008). Variability of the Minimal Transmembrane Voltage Resulting in Detectable Membrane Electroporation. *Electromagnetic Biology and Medicine*, *27*(4), 372–385. https://doi.org/10.1080/15368370802394644
_eprint: https://doi.org/10.1080/15368370802394644

Trouillon, R., Combs, Z., Patel, B. A., & O'Hare, D. (2009). Comparative study of the effect of various electrode membranes on biofouling and electrochemical measurements. *Electrochemistry Communications*, *11*(7), 1409–1413. https://doi.org/10.1016/j.elecom.2009.05.018

Bibliography

VanDersarl, J. J., & Renaud, P. (2016). Biomimetic surface patterning for long-term transmembrane access. *Scientific Reports, 6*(1), 32485. https://doi.org/10.1038/srep32485

van Megen, M. J. J., Odijk, M., Wiedemair, J., Olthuis, W., & van den Berg, A. (2012). Differential cyclic voltammetry for selective and amplified detection. *Journal of Electroanalytical Chemistry, 681*, 6–10. https://doi.org/10.1016/j.jelechem.2012.05.021

Viswam, V., Obien, M. E. J., Franke, F., Frey, U., & Hierlemann, A. (2019). Optimal Electrode Size for Multi-Scale Extracellular-Potential Recording From Neuronal Assemblies. *Frontiers in Neuroscience, 13.*

Wang, J., & G. Ewing, A. (2014). Simultaneous study of subcellular exocytosis with individually addressable multiple microelectrodes. *Analyst, 139*(13), 3290–3295. https://doi.org/10.1039/C4AN00058G

Wang, Y., & Ewing, A. (2021). Electrochemical Quantification of Neurotransmitters in Single Live Cell Vesicles Shows Exocytosis is Predominantly Partial. *ChemBioChem, 22*(5), 807–813. https://doi.org/10.1002/cbic.202000622 _eprint: https://onlinelibrary.wiley.com/doi/pdf/10.1002/cbic.202000622

Wen, P. J., Grenklo, S., Arpino, G., Tan, X., Liao, H.-S., Heureaux, J., Peng, S.-Y., Chiang, H.-C., Hamid, E., Zhao, W.-D., Shin, W., Näreoja, T., Evergren, E., Jin, Y., Karlsson, R., Ebert, S. N., Jin, A., Liu, A. P., Shupliakov, O., & Wu, L.-G. (2016). Actin dynamics provides membrane tension to merge fusing vesicles into the plasma membrane. *Nature Communications, 7*(1), 12604. https://doi.org/10.1038/ncomms12604

Westerink, R. H. S., & Ewing, A. G. (2008). The PC12 cell as model for neurosecretion. *Acta Physiologica, 192*(2), 273–285. https://doi.org/10.1111/j.1748-1716.2007.01805.x _eprint: https://onlinelibrary.wiley.com/doi/pdf/10.1111/j.1748-1716.2007.01805.x

Westerink, R. H. S., de Groot, A., & Vijverberg, H. P. M. (2000). Heterogeneity of Catecholamine-Containing Vesicles in PC12 Cells. *Biochemical and Biophysical Research Communications, 270*(2), 625–630. https://doi.org/10.1006/bbrc.2000.2470

Wightman, R. M., Jankowski, J. A., Kennedy, R. T., Kawagoe, K. T., Schroeder, T. J., Leszczyszyn, D. J., Near, J. A., Diliberto, E. J., & Viveros, O. H. (1991). Temporally resolved catecholamine spikes correspond to single vesicle release from individual chromaffin cells. *Proceedings of the National Academy of Sciences, 88*(23), 10754–10758. https://doi.org/10.1073/pnas.88.23.10754

Wrobel, G., Hller, M., Ingebrandt, S., Dieluweit, S., Sommerhage, F., Bochem, H. P., & Offenhusser, A. (2007). Transmission electron microscopy study of the cellsensor interface. *Journal of The Royal Society Interface.* https://doi.org/10.1098/rsif.2007.1094

Xiang, L., Yu, P., Hao, J., Zhang, M., Zhu, L., Dai, L., & Mao, L. (2014). Vertically Aligned Carbon Nanotube-Sheathed Carbon Fibers as Pristine Microelectrodes for Selective Monitoring of Ascorbate in Vivo. *Analytical Chemistry, 86*(8), 3909–3914. https://doi.org/10.1021/ac404232h

Xie, X., Xu, A. M., Angle, M. R., Tayebi, N., Verma, P., & Melosh, N. A. (2013). Mechanical Model of Vertical Nanowire Cell Penetration. *Nano Letters, 13*(12), 6002–6008. https://doi.org/10.1021/nl403201a

Xu, D., Fang, J., Wang, H., Wei, X., Yang, J., Li, H., Yang, T., Li, Y., Liu, C., & Hu, N. (2022). Scalable Nanotrap Matrix Enhanced Electroporation for Intracellular Recording of Action Potential. *Nano Letters, 22*(18), 7467–7476. https://doi.org/10.1021/acs.nanolett.2c02398

Yang, Y., Wang, K., Gu, X., & Leong, K. W. (2017). Biophysical Regulation of Cell Behavior—Cross Talk between Substrate Stiffness and Nanotopography. *Engineering, 3*(1), 36–54. https://doi.org/10.1016/J.ENG.2017.01.014

Yao, J., & Gillis, K. D. (2012). Quantification of noise sources for amperometric measurement of quantal exocytosis using microelectrodes. *Analyst, 137*(11), 2674–2681. https://doi.org/10.1039/C2AN35157A

Ying, Y.-L., Hu, Y.-X., Gao, R., Yu, R.-J., Gu, Z., Lee, L. P., & Long, Y.-T. (2018). Asymmetric Nanopore Electrode-Based Amplification for Electron Transfer Imaging in Live Cells. *Journal of the American Chemical Society, 140*(16), 5385–5392. https://doi.org/10.1021/jacs.7b12106

Young, J. Z. (1936). Structure of nerve fibres and synapses in some invertebrates. *Cold Spring Harbor Symp Quant Biol,* (4), 1–6.

Zanetti, C., Spitz, S., Berger, E., Bolognin, S., Smits, L. M., Crepaz, P., Rothbauer, M., Rosser, J. M., Marchetti-Deschmann, M., Schwamborn, J. C., & Ertl, P. (2021). Monitoring the neurotransmitter release of human midbrain organoids using a redox cycling microsensor as a novel tool for personalized Parkinson's disease modelling and drug screening. *Analyst, 146*(7), 2358–2367. https://doi.org/10.1039/D0AN02206C

Zeck, G., & Fromherz, P. (2003). Repulsion and Attraction by Extracellular Matrix Protein in Cell Adhesion Studied with Nerve Cells and Lipid Vesicles on Silicon Chips. *Langmuir, 19*(5), 1580–1585. https://doi.org/10.1021/la0263209

Zestos, A. G., Jacobs, C. B., Trikantzopoulos, E., Ross, A. E., & Venton, B. J. (2014). Polyethylenimine Carbon Nanotube Fiber Electrodes for Enhanced Detection of Neurotransmitters. *Analytical Chemistry, 86*(17), 8568–8575. https://doi.org/10.1021/ac5003273

Zhang, A., Lee, J.-H., & Lieber, C. M. (2021). Nanowire-enabled bioelectronics. *Nano Today, 38,* 101135. https://doi.org/10.1016/j.nantod.2021.101135

Zhang, C., Li, J., Belianinov, A., Ma, Z., Renshaw, C. K., & Gelfand, R. M. (2020). Nanoaperture fabrication in ultra-smooth single-grain gold films with helium ion beam lithography. *Nanotechnology, 31*(46), 465302. https://doi.org/10.1088/1361-6528/abae99

Zhang, J., Fu, D., Chan-Park, M. B., Li, L.-J., & Chen, P. (2009). Nanotopographic Carbon Nanotube Thin-Film Substrate Freezes Lateral Motion of Secretory Vesicles. *Advanced Materials, 21*(7), 790–793. https://doi.org/10.1002/adma.200801586 _eprint: https://onlinelibrary.wiley.com/doi/pdf/10.1002/adma.200801586

Zhang, P.-C., Keleshian, A. M., & Sachs, F. (2001). Voltage-induced membrane movement. *Nature, 413*(6854), 428–432. https://doi.org/10.1038/35096578

Zhou, T., Perry, S. F., Ming, Y., Petryna, S., Fluck, V., & Tatic-Lucic, S. (2015). Separation and assisted patterning of hippocampal neurons from glial cells using positive dielectrophoresis. *Biomedical Microdevices, 17*(3), 62. https://doi.org/10.1007/s10544-015-9965-6

Bibliography

Zhu, F., Yan, J., Lu, M., Zhou, Y., Yang, Y., & Mao, B. (2011). A strategy for selective detection based on interferent depleting and redox cycling using the plane-recessed microdisk array electrodes. *Electrochimica Acta*, *56*(24), 8101–8107. https://doi.org/10.1016/j.electacta.2011.05.129

Publication list

Related to this thesis

- **N. Maïno**, A. Bertsch, P. Renaud (2022). Impedance spectroscopy of the cell/nanovolcano interface enables optimization for electrophysiology. *Submitted*

- **N. Maïno**, A. Bertsch, P. Renaud (2022). Rapid exocytosis kinetics measured by amperometry within nanovolcano electrodes. *Submitted*

- B. Desbiolles, E. de Coulon, **N. Maïno**, A. Bertsch, S. Rohr, P. Renaud (2020). Nanovolcano microelectrode arrays: toward long-term on-demand registration of transmembrane action potentials by controlled electroporation. *microsys. & nanoeng.*, 6(1), 1–12.
  https://doi.org/10.1038/s41378-020-0178-7

Others

- **N. Maïno**, T. Hauling, G. Cappi, N. Madaboosi, D. G. Dupouy, M. Nilsson (2019). A microfluidic platform towards automated multiplexed *in situ* sequencing. *Scientific Reports*, 9(1), 1-10.
  https://doi.org/10.1038/s41598-019-40026-6

- C. Bovigny, G. Tamò, T. Lemmin, **N. Maïno**, M. Dal Peraro (2015). *LipidBuilder*: A Framework To Build Realistic Models for Biological Membranes. *J. Chem. Inf. Model*, 2491-2499.
  https://doi.org/10.1021/acs.jcim.5b00501

Nicolas **Maïno**

Microengineer · Biotechnologist

20, Ch de la Sauge, 1030 Bussigny, Switzerland

(+41) 78-796-43-65 | ✉ maino.nicolas@gmail.com | in nicolasmaino

"Passionate about technologies and their application to the biomedical field"

Skills

Microfabrication	Photo- DUV- Ebeam-litography, Wet/Dry etching, Thin films, Stress budget, Dicing,Electron microscopy, Iso5 clean room accreditation
Electroanalytical	Electrophysiology (multi-electrode array, calcium imaging), Electrochemistry (amperometry/voltammetry impedance spectroscopy, electrodepostion), Dielectrophoresis (cell manipulation/patterning), Low noise (picoamps, microvolts, noise reduction design/strategy)
Light microscopy	Epifluorescence, Confocal, Fluorometry, Absorbance
Molecular biology	Sequencing by ligation, Immunohistochemistry, in situ Fluorescence hybridization, cDNA library prep., Rolling circle amplification, Cloning, Protein extraction
Cell culture	Mammalian cell lines (human,rodent), primary rodent neurons (cortex, hippocampus), bacteria
Programming	Python, Comsol (FEM), Matlab, C++
Languages	French (mother tongue), English (C1 level), Italian (A1)
Softskills	Leadership, Communication, Presentation, Outreach

Education

Ecole Polytechnique Fédérale de Lausanne (EPFL) *Lausanne, Switzerland*

Phd in in Bioengineering, , Defended on 07/12/2022 *Aug. 2018 - Dec. 2022*

- Novel multi-electrode array development for electrophysiology and electrochemistry
- Work published in peer reviewed journals and presented at an international conference
- Outreach during public events (EPFL open days, EPFL Scientastic)
- Students supervision and teaching in the laboratory

Ecole Polytechnique Fédérale de Lausanne (EPFL) *Lausanne, Switzerland*

Master in Bioengineering, specialization in regenerative medecine *Sep. 2015 - Mar. 2018*

- Master thesis in Prof. Nilson lab in Stockholm, Sweden
- Work published in a peer reviewed journal article

Ecole Polytechnique Fédérale de Lausanne (EPFL) *Lausanne, Switzerland*

Bachelor in Life Sciences *Sep. 2012 - Aug. 2015*

- Bachelor thesis in Prof. Dal Peraro lab in Lausanne
- Work published in a peer reviewed journal article

Experience

Lunaphore Technologies *Lausanne, Switzerland*

R&D Intern *Mar. 2017 - Sep. 2017*

- Microfluidic assay development

Techspark Academy *Lausanne, Switzerland*

Python instructor *Aug. 2015 - Sep. 2015*

- Developed course materials and teaching

ⓘ orcid.org/0000-0002-1159-2318

Main Publications

Impedance spectroscopy of the cell/nanovolcano interface enables optimization for electrophysiology

Submited - 2022

N. Maïno, A. Bertsch, P. Renaud

View xxxx - Cit. xx

• Developed new low impedance microelectrode and scalable impedance spectroscopy method

Rapid exocytosis kinetics measured by amperometry within nanovolcano electrodes

Submited - 2022

N. Maïno, A. Bertsch, P. Renaud

View xxxx - Cit. xx

• Developed new amperometric sensor for volume-confined, multi-site measurement of exocytosis

Nanovolcano microelectrode arrays: toward long-term on-demand registration of transmembrane action potentials by controlled electroporation

microsys. & nanoeng. - 2020

B. Desbiolles, E. de Coulon, N. Maïno, *et. al.*

View 2649 - Cit. 10
(31/10/22)

• Microfabrication and optimization of multi-electrode array for intracellular electrophysiology

A microfluidic platform towards automated multiplexed *in situ* sequencing

Scientific Reports - 2019

N. Maïno, T. Hauling, G. Cappi, N. Madaboosi, D. G. Dupouy, M. Nilsson

View 5613 - Cit. 23
(31/10/22)

• Implementation of a spatial transcriptomic assay on a microfluidic platform

LipidBuilder: A Framework To Build Realistic Models for Biological Membranes

J. Chem. Inf. Model - 2015

C. Bovigny, G. Tamò, T. Lemmin, N. Maïno, M. Dal Peraro

View 1215 - Cit. 19
(31/10/22)

• Development of a lipidome library for molecular dynamics

Hobbies

Competition	3rd place Swiss ski touring championship 2017, vertical race
Leisure	Running, Bouldering, Badminton
Outdoor	Hiking, Ski touring, Nordic ski

150